1-1-1983

Quantitative small-angle light scattering studies of semi-crystalline polymers.

Ronald J. Tabar
University of Massachusetts Amherst

Recommended Citation

Tabar, Ronald J., "Quantitative small-angle light scattering studies of semi-crystalline polymers." (1983). *Doctoral Dissertations 1896 - February 2014*. 679.
https://doi.org/10.7275/tczc-0n93 https://scholarworks.umass.edu/dissertations_1/679

QUANTITATIVE SMALL-ANGLE LIGHT SCATTERING STUDIES OF SEMI-CRYSTALLINE POLYMERS

A Dissertation Presented

By

RONALD J. TABAR

Submitted to the Graduate School of the
University of Massachusetts in partial fulfillment
of the requirements for the degree of

DOCTOR OF PHILOSOPHY

May 1983

Polymer Science and Engineering

QUANTITATIVE SMALL-ANGLE LIGHT SCATTERING STUDIES
OF SEMI-CRYSTALLINE POLYMERS

A Dissertation Presented

By

RONALD J. TABAR

Approved as to style and content by:

Richard S. Stein

Richard S. Stein, Chairperson of Committee

Richard J. Farris, Member

Julio M. Ottino, Member

Edwin L. Thomas

Edwin L. Thomas, Member

William J. MacKnight

William J. MacKnight,
Department Head
Polymer Science and Engineering

DEDICATION

To my mother, Eldora, my father, Max, and
my wife, Margaret, in grateful thanks and
with the hope that they will be proud of this achievement.

ACKNOWLEDGEMENTS

I wish to thank Professor Richard S. Stein for his guidance, patience and understanding throughout the course of this research. It has been a truly rewarding experience to have the opportunity to work with him. I also wish to thank the other members of my committee, Professor Richard J. Farris, Professor Julio M. Ottino and Professor Edwin L. Thomas for their helpful suggestions these past few years.

I would like to thank the many people who have made this endeavor more enjoyable by their help and friendship. In particular I would like to express my appreciation to Cam Murray, Wade Adams, Bill Harris, Marty Wai, Dale Handlin, Dave Anderson and Xiayu Wang for their assistance and, more importantly, for their companionship. I appreciate the assistance of Marshall Long in this research and Pat Barschenski in the preparation of this manuscript.

I wish to give my most gracious thanks to my wife, Margaret, for her long standing love, patience and assistance throughout this experience.

The financial support of the National Science Foundation, the Petroleum Research Fund of the American Chemical Society, the General Tire and Rubber Company and the Department of the Army is greatly appreciated.

ABSTRACT

Quantitative Small-Angle Light Scattering Studies of Semi-Crystalline Polymers

May 1983

Ronald J. Tabar, B.S., Northwestern University
M.S., University of Massachusetts
Ph.D., University of Massachusetts
Directed by: Professor Richard S. Stein

This dissertation presents studies of the advancement and utilization of the techniques of small-angle light scattering (SALS) to investigate the morphology of deformed and undeformed spherulitic semi-crystalline polymers. The technique advancements were made in the theoretical and instrumental aspects of SALS. The utilization of the latest techniques was made in four experimental SALS studies.

The major theoretical advancement of SALS made in this work was the determination, by computer simulation, of the effects of spherulitic truncation on H_v SALS. The changes in the H_v SALS patterns and equations due to these effects were determined. The method can be readily extended to the SALS study of several other morphological phenomena.

The major instrumental advancement made in this work was the development of a position sensitive SALS detector system. The device allows one to rapidly collect and analyze quantitative, two dimensional SALS data, which is essential to this and many other studies of polymers by SALS.

In a study of the melting of polyethylene terephthalate (PET), it was found that the spherulites melt over a range of about 20°C without change in spherulite size, number or internal disorder. In a study of PET crystallization, it was found that, as the spherulites grow, there was an initial decrease and then a levelling off of both the internal disorder and the spherulite crystallinity. The quantitative H_v SALS intensities, corrected for experimental and internal and external disorder effects, were in moderate agreement with those calculated from the sample crystallinities, for both the melting and the crystallization studies.

It was found in a study of low density polyethylene (LDPE) and polypropylene (PP) elongation that the van Aartsen and Stein affine model of spherulite deformation described the H_v SALS of LDPE and PP, but failed in the description of V_v and H_h SALS. The deformation mechanisms indicated by the H_v SALS were reasonable for LDPE and PP.

It was found, and explained in terms of the Debye-Bueche theory, that the haze from films of phase separated polymer blends does not increase monotonically with the size of the phase separated particles.

TABLE OF CONTENTS

ACKNOWLEDGEMENTS v

ABSTRACT vi

LIST OF TABLES xi

LIST OF FIGURES xiii

Chapter

I INTRODUCTION 1

II BACKGROUND AND THEORY 6

SALS from Unoriented Spherulitic Polymers 6
SALS from Deformed Spherulitic Polymers 17

III THE EFFECTS OF SPHERULITIC TRUNCATION ON SMALL-ANGLE LIGHT SCATTERING 23

Introduction 23
The Model and Principles of Calculation 27
Two dimensional spherulites 31
Three dimensional spherulites 41
Results and Discussion 46
Calculated intensities: two dimensional spherulites 46
Calculated intensities: three dimensional spherulites 61
Area, volume and radius measurements 64
Conclusions 68

IV A TWO DIMENSIONAL, POSITION SENSITIVE DETECTOR FOR SMALL-ANGLE LIGHT SCATTERING 73

Introduction 73
Device Description 73
Device Calibration 78
Device Applications 81
Conclusions 93

V STUDIES OF THE MELTING OF POLYETHYLENE TEREPHTHALATE 94

Introduction 94
Theory: Quantitative H_v SALS from PET 95
Experimental 104
Sample preparation 104
Characterization 104
Pressed films 107

SALS samples 107
DSC samples 107
Differential scanning calorimetry 108
Optical microscopy 108
H_v SALS 108
Transmission 109
Results 109
Differential scanning calorimetry 109
Optical microscopy 112
H_v SALS 112
Transmission 116
Discussion 119
Conclusions 128

VI STUDIES OF THE CRYSTALLIZATION OF POLYETHYLENE TEREPHTHALATE 131

Introduction 131
Theory 132
Experimental 134
Sample preparation 134
SALS 135
Transmission 135
Differential scanning calorimetry 136
Results 136
Optical microscopy 136
SALS 136
Transmission 146
Differential scanning calorimetry 146
Discussion 146
Conclusions 163

VII STUDIES OF THE ELONGATION OF LOW DENSITY POLYETHYLENE AND POLYPROPYLENE 168

Introduction 168
Experimental 169
Sample preparation 169
LDPE 169
PP 170
Sample characterization 170
Birefringence 171
Infrared dichroism 171
WAXD 172
Optical microscopy 172
SALS 172
Results 173
Birefringence and infrared dichroism 173
WAXD and optical microscopy 180
SALS 180

Discussion 185
Conclusions 193

VIII EFFECT OF PARTICLE SIZE ON POLYMER FILM HAZE . . . 194

Introduction 194
Experimental 195
Results 195
  Transmittance 195
  Photographic 197
  Position sensitive detector 200
Discussion 212
Conclusions 218

IX SUMMARY 220

General Conclusions 220
Suggestions for Further Research 224
  Theoretical studies 224
    Truncation of spherulites 224
    Internally disordered and truncated spherulites 225
    Deformed, truncated spherulites 225
    Other impinging growth studies 226
    Three dimensional internal disorder 226
    Radial variation of spherulite crystallinity 226
    Spherulite deformation 226
  Experimental studies 226
    Spherulite melting 227
    Crystallization 227
    Crystallinity measurement device 228
    Spherulite deformation of PP 228
    Spherulite deformation, orientation functions228

REFERENCES 230

APPENDIX 240

Polynomial Equations 240
OMA2 Analysis Software 253
Three Dimensional Internal Disorder 290

LIST OF TABLES

Table Page

III-1 Avrami Analysis of Computer Simulated Spherulite Growth 66

VII-1 Physical Properties of LDPE and PP 171

VII-2 SALS Analysis of the Deformation of LDPE and PP . 187

VIII-1 Sample Transmissions 197

VIII-2 Guinier Analysis of A-Position Specimens 206

VIII-3 Guinier Analysis of B- and C-Position Specimens . 209

A-1 Truncation Correction for Two Dimensional Spherulite Growth 242

A-2 Azimuthal H_v SALS Intensity Ratios for Two Dimensional Spherulite Growth and Simultaneous Nucleation 243

A-3 Azimuthal H_v SALS Intensity Ratios for Two Dimensional Spherulite Growth and Sporadic Nucleation 244

A-4 Area Fraction Spherulites for Two Dimensional Spherulite Growth 245

A-5 Truncation Correction for Three Dimensional Spherulite Growth and Simultaneous Nucleation . . 246

A-6 Azimuthal H_v SALS Intensity Ratios for Three Dimensional Spherulite Growth and Simultaneous Nucleation 247

A-7 Volume Fraction Spherulites for Three Dimensional Spherulite Growth and Simultaneous Nucleation 248

A-8 Average Spherulite Volume for Three Dimensional Spherulite Growth and Simultaneous Nucleation . . 249

A-9 Average Spherulite Area for Two Dimensional Spherulite Growth 250

A-10 Multiple Scattering Correction 251

A-11 Azimuthal H_v SALS Intensity Ratios for Internally Disordered, Nontruncated, Two Dimensional Spherulites 251

A-12 Azimuthal H_v SALS Intensity Ratios for Internally Disordered, Fully Grown, Three Dimensional Spherulites Resulting from Simultaneous Nucleation 252

A-13 Internal Disorder Correction for Two Dimensional Spherulites 252

A-14 Two and Three Dimensional Internal Disorder . . . 292

LIST OF FIGURES

Figure Page

II-1 Typical arrangement of the basic components in a photographic SALS experiment 9

II-2 H_v and V_v SALS photographs from PET crystallized from the melt for 10 minutes at 200°C 10

II-3 Diagram of the geometry used for the spherulite deformation model 19

II-4 H_v SALS isointensity contours for deformed spherulites from van Aartsen et al. 21

III-1 Optical micrograph of Marlex 50 polyethylene spherulites under crossed polars 24

III-2 Scanning transmission bright field electron micrograph of Marlex 6003 polyethylene spherulites 25

III-3 Diagram of the angular intervals for radii calculations for two dimensional spherulites . . . 29

III-4 Diagram of the angular intervals for radii calculations for three dimensional spherulites . . 30

III-5 Example of random location of 30 nuclei in the limiting circle 32

III-6 Two dimensional spherulites grown to 27.1% area fraction following simultaneous nucleation 33

III-7 Two dimensional spherulites grown to 60.1% area fraction following simultaneous nucleation 34

III-8 Two dimensional spherulites grown to 81.5% area fraction following simultaneous nucleation 35

III-9 Fully grown two dimensional spherulites grown following simultaneous nucleation 36

III-10 Two dimensional spherulites grown to 65.7% area fraction following sporadic nucleation 39

III-11 Scanning electron micrograph of polypropylene spherulites grown in mineral oil and fractured . . 42

III-12 Diagram of the scattering geometry for a three dimensional spherulite 44

III-13 H_v SALS profiles at $\mu = 45°$, for the two dimensional spherulitic system generated following simultaneous nucleation of 150 nuclei, at various area fractions of spherulites 47

III-14 H_v SALS profiles at $\mu = 45°$, for the two dimensional spherulitic system generated following simultaneous nucleation of 150 nuclei grown to area fraction = 0.57 and for the equivalent perfect, nontruncated disk system 48

III-15 H_v SALS profiles at $\mu = 45°$, for the fully grown two dimensional spherulitic system generated following simultaneous nucleation of 150 nuclei and for the equivalent perfect, nontruncated disk system 49

III-16 H_v SALS intensity profiles at $U = U_{max}$, for the two dimensional spherulitic system generated following simultaneous nucleation of 150 nuclei, at various area fractions of spherulites 50

III-17 H_v SALS intensity profiles at $U = U_{max}$, for the fully grown two dimensional spherulitic system generated following simultaneous nucleation of 150 nuclei and for the equivalent perfect, nontruncated disk system 51

III-18 Truncation correction factors for two dimensional spherulites, simultaneous and sporadic nucleation, as functions of the area fraction of spherulites. 53

III-19 Ratios of H_v intensities for several values of μ to that for $\mu = 45°$, at $U = U_{max}$, for two dimensional, simultaneously nucleated spherulites, as functions of the area fraction of spherulites. 55

III-20 Ratios of H_v intensities for several values of μ to that for $\mu = 45°$, at $U = U_{max}$, for two dimensional, sporadically nucleated spherulites, as functions of the area fraction of spherulites. . 56

III-21 Calibration curve of the area fraction of spherulites as functions of the ratio of the polar angle of maximum H_v intensity for full growth to the angle of maximum intensity for a particular stage of growth, two dimensional spherulites, simultaneous and sporadic nucleation 60

III-22 Truncation correction factor for three dimensional spherulites, simultaneous nucleation, as a function of the volume fraction of spherulites 62

III-23 Ratios of the H_v SALS intensities for several values of μ to that for $\mu = 45^\circ$, at $U = U_{max}$, for three dimensional spherulites, simultaneous nucleation, as functions of the volume fraction of spherulites . . . . , 63

III-24 Calibration curve of the volume fraction of spherulites as a function of the ratio of the polar angle of maximum H_v intensity for full growth to the angle of maximum intensity for a particular stage of growth, three dimensional spherulites, simultaneous nucleation 65

III-25 K_v as a function of the volume fraction of spherulites for three dimensional spherulites and simultaneous nucleation average spherulite volume $V = K_v\bar{R}_n^3$ 69

III-26 K_A as functions of the area fraction of spherulites for two dimensional spherulites and simultaneous and sporadic nucleation, average spherulite area $A = K_A\bar{R}_n^3$ 70

IV-1 Block diagram of the components of the Optical Multichannel Analyzer 2 75

IV-2 Diagram of the lens configuration for the OMA2 . . 76

IV-3 Sample three dimensional perspective plot of an H_v scattering pattern from PET 82

IV-4 Sample isointensity contour plot of the same pattern as in Figure IV-3 83

IV-5 Sample isointensity contour plot of a V_v scattering pattern from the same sample as in Figure IV-3 . . 84

IV-6 Single quadrant averaged H_v SALS isointensity contour plot for PET crystallized from the glass for 5 minutes at 130°C 86

IV-7 Single quadrant averaged H_v SALS isointensity contour plot from undeformed LDPE film 87

IV-8 Single quadrant averaged H_v SALS isointensity contour plot from LDPE film elongated 60% 88

IV-9 Full four quadrant SALS isointensity contour plot from a 60/40 blend of polystyrene/polyorthochlorostyrene 89

IV-10 Circularly averaged scattering profile for the data in Figure IV-9 91

V-1 Multiple scattering correction factors for fully truncated, internally disordered two dimensional spherulites 100

V-2 Effect of truncation and internal disorder on the shape of the H_v SALS azimuthal profile at $U = U_{max}$ 102

V-3 Ratios of the H_v SALS intensities for several values of μ to that for $\mu = 45°$, at $U = Umax$, for nontruncated, two dimensional spherulites as functions of the internal disorder parameter . . . 103

V-4 Determination of internal disorder, for fully truncated systems, from the H_v SALS intensity ratios $R_{H_v}(U_{max},45)/R_{H_v}(U_{max},\mu)$ 105

V-5 Correction factor for internal disorder in two dimensional spherulites for H_v SALS at $U = U_{max}$ and $\mu = 45°$ 106

V-6 Typical DSC trace for the melting of PET at a heating rate of 2.5°C per minute 110

V-7 Weight fraction crystallinity determined by DSC for the melting of PET at heating rates of 2.5 and 10°C per minute 111

V-8 Optical micrograph of PET, crystallized from the melt at 180°C for two hours; crossed polars 113

V-9 Single quadrant averaged H_v SALS isointensity contours for the melting of PET at 250, 255, 260 and 262°C at a heating rate of 2°C per minute 114

V-10 Polar scattering angle profiles at $\mu = 45°$, for several temperatures, of the H_v SALS intensity from the melting of PET at a heating rate of 2°C per minute 115

V-11 Azimuthal scattering angle profiles at $U = U_{max}$, for several temperatures, of the H_v SALS intensity from the melting of PET at a heating rate of 2°C per minute 117

V-12 τd as a function of temperature during the melting of PET at a heating rate of 2°C per minute . 118

V-13 Internal disorder as a function of temperature during the melting of PET at a heating rate of 2°C per minute 120

V-14 Comparison of the theoretically predicted H_v SALS intensity and the corrected experimental intensity at $U = U_{max}$ and $\mu = 45°$, during the melting of PET at a heating rate of 2°C per minute 125

VI-1 Optical micrograph of PET crystallized from the melt for 10 minutes at 200°C; crossed polars 137

VI-2 Isointensity contours of single quadrant averaged H_v SALS patterns from PET Crystallized from the melt at 200°C for 12, 18, 24 and 35 seconds 139

VI-3 H_v SALS intensity profiles at $\mu = 45°$, as functions of the magnitude of the scattering vector, for different crystallization times 140

VI-4 Average spherulite radius, determined by H_v SALS, as a function of crystallization time 141

VI-5 H_v SALS intensity profiles at $U = U_{max}$, as functions of the azimuthal angle, for different crystallization times 143

VI-6 Isointensity contours of four quadrant V_v SALS patterns from PET crystallized from the melt at 200°C for 2, 8, 13, 19, 25 and 36 seconds 144

VI-7 V_v SALS intensities at $H = 0.53$ and $1.06\ \mu m^{-1}$ and $\mu = 0$ and $90°$, as functions of the crystallization time 147

VI-8 τd as a function of crystallization time 149

VI-9 Volume fraction spherulites, determined by H_v SALS, as a function of crystallization time 152

VI-10 Internal disorder parameter as a function of crystallization time 154

VI-11 Volume fraction crystallinity within the spherulites as a function of crystallization time 156

VI-12 Overall degree of crystallinity as a function of crystallization time 160

VI-13 Corrected experimental V_v SALS intensity and V_v intensity calculated from the H_v SALS results, at $U = 4$ and $\mu = 0$ and 90°, as functions of the crystallization time 164

VII-1 Birefringences of LDPE and PP as functions of the elongation ratio 174

VII-2 Infrared dichroic ratios for LDPE as functions of the elongation ratio 176

VII-3 Crystallization and amorphous orientation functions of LDPE as functions of the elongation ratio, as determined by infrared dichroism 178

VII-4 Birefringence of LDPE as a function of the elongation ratio, as measured and as calculated from infrared dichroism 179

VII-5 Isointensity contour plots of H_v SALS from LDPE; undeformed and $\lambda_E = 1.3$ 181

VII-6 Azimuthal angles of maximum H_v SALS intensity for LDPE and PP, as functions of the elongation ratio 182

VII-7 Isointensity contour plots of V_v SALS from LDPE; undeformed and $\lambda_E = 1.3$ 183

VII-8 Isointensity contour plots of H_h SALS from LDPE; undeformed and $\lambda_E = 1.3$ 184

VII-9 Orientation functions as functions of the elongation ratio: crystalline c axis of LDPE as determined by infrared dichroism and the optic axis of a spherulite as calculated from SALS model with $\eta = 0.6$ and $\kappa = 0.0$ 190

VIII-1 Diagram of the positions of the A-, B-, and C-position specimens in the beverage cups 196

VIII-2 Photographic light scattering patterns from samples 1 and 2, A-, B-, and C-position specimens . 198

VIII-3 Two dimensional, single quadrant averaged SALS isointensity contours from the A-position specimens 201

VIII-4 Two dimensional, single quadrant averaged SALS isointensity contours from the B-position specimens 202

VIII-5 Two dimensional, single quadrant averaged SALS isointensity contours from the C-position specimens 203

VIII-6 Guinier type SALS plots from the A-position specimens at azimuthal angles 0 and 90° 207

VIII-7 Guinier type plots from circularly averaged SALS data from the B- and C-position specimens 210

VIII-8 Haze as a function of inhomogeneity size for various values of θ_{min} 216

A-1 Flow diagram of the computer programs for SALS data collection and analysis using the OMA2 254

A-2 Polar scattering angle profiles from three dimensional spherulites, at $\mu = 45°$, for various values of the internal disorder parameter 291

CHAPTER I

INTRODUCTION

The investigation of the microstructure of semi-crystalline polymers is useful to the advancement of the understanding of the relationships between polymer properties and their internal structure. Several techniques are available for this investigation. Each technique has its own advantages and disadvantages and offers only a partial description of the polymer microstructure. It is the complementary use of the various techniques by polymer scientists which unravels the complex nature of the behavior of semi-crystalline polymers. To that end, it is essential that each technique be advanced to the state where it contributes the maximum amount of information possible by that technique to the available information from the other methods.

Small-angle light scattering (SALS) from thin polymer films is a well established technique for the study of polymer microstructure. It is particularly useful for the investigation of structures in the size range of 0.5 - 50 µm. Thus SALS bridges the gap between small-angle x-ray scattering and light microscopy in the study of structures of various sizes in polymers. SALS has the advantages of being a method that is experimentally rapid, non-destructive, economical and requiring only small samples. It has the disadvantages of necessitating strict experimental care and involved theoretical interpretations. Besides its range of structure size applicability, SALS also has the feature of providing information about "average" properties in the illuminated

sample.

The SALS technique, when incorporating the use of a polarizer and an analyzer, is especially useful in the study of birefringent structures such as polymer crystals and spherulites. It can be utilized in the monitoring of the melting and crystallization of undeformed spherulitic semi-crystalline polymers. Such studies lead to information concerning: the changes in the number and size of the spherulites, their volume fraction, their growth kinetics, their anisotropy, their disorder, the crystallinity inside and outside the spherulites and the crystallization kinetics. Several of these features are best evaluated by utilizing quantitative SALS techniques. Quantitative SALS involves the use of absolute scattered intensities which necessitates several experimental and theoretical corrections. SALS studies of deformed spherulitic polymer samples can provide information similar to that from undeformed spherulites, as well as information concerning: the deformation of the spherulites, their deformation mechanisms and changes in molecular orientations.

The purpose of this dissertation is to advance and utilize the techniques of SALS to investigate the morphology of deformed and undeformed spherulitic semi-crystalline polymers. The technique advancements are made in both the theoretical and instrumental aspects of SALS. The utilization of the latest techniques, including quantitative SALS, as well as the theoretical and instrumental advances made here, are manifested in studies of the melting, crystallization and deformation of spherulitic semi-crystalline polymers and in a study of

the haze from films of phase separated polymer blends.

This dissertation is arranged into nine chapters and an appendix, this introductory section being Chapter I. Chapter II presents the background and current theories for SALS from spherulitic semi-crystalline polymers, both deformed and undeformed.

Chapter III presents the theoretical results of this dissertation: the effects of the truncation of spherulites on the SALS. Computer simulation of spherulitic growth in both two and three dimensions has been carried out. The changes in the H_v SALS patterns due to spherulitic truncation have been determined as functions of the volume (or area) fraction of spherulites and the type of nucleation. The computer simulation method is general and can be readily extended to several other studies of SALS from spherulites. These studies follow the original preliminary work of A. Wasiak, S.D. Hong and T. Yuasa. The three dimensional studies were done with the assistance of D.E. Rose.

Chapter IV presents the major instrumental advancement made in this dissertation: the development of a two dimensional, position sensitive detector system for SALS from polymer films. This microcomputer controlled device (OMA2) was developed to permit the experimenter to rapidly obtain two dimensional quantitative SALS data from a variety of polymer systems. It was essential for the experimental portions of this work and that of other workers in our laboratory. This instrument was developed with the assistance of M.B. Long of Yale University.

Chapter V gives the results of melting studies of polyethylene terephthalate (PET). H_v SALS results were combined with DSC studies to

examine the validity of the current SALS theories. The size, disorder and crystallinity of the PET spherulites were determined. This study is a continuation of the work of P. Leite-James.

Chapter VI gives the results of studies of the crystallization of PET from the melt. H_v and V_v SALS results were combined with DSC results to analyze the spherulitic changes in PET during crystallization and to follow the crystallization kinetics. The SALS theories were further examined. These studies are a continuation of the work initiated by T. Yuasa.

Chapter VII presents the results of studies of elongation of films of low density polyethylene (LDPE) and polypropylene (PP). SALS, birefringence, and infrared dichroism were combined to examine the deformation mechanisms of polymer spherulites and the differing mechanisms in these two polymers. The current SALS theories for spherulite deformation were examined. This work has been carried out with the assistance of J. Sheng and T. Masaoka.

Chapter VIII presents the results of a SALS study on noncrystalline polymers. The turbidity of phase separated high-impact polystyrene films was examined. New relationships were developed between polymer film haze and phase size. These studies were done with the assistance of C.T. Murray and S.R. Hu.

Chapter IX presents the general conclusions of these studies and suggestions for further research. The Appendix includes the coefficients determined from least squares fitting to polynomial equations of the curves from several of the figures in this

dissertation. It also includes the OMA2 analysis software. Some unpublished three dimensional internal disorder results of Yoon are documented as well in the Appendix.

CHAPTER II

BACKGROUND AND THEORY

SALS from Unoriented Spherulitic Polymers

SALS from polymer films has been analyzed principally according to two theoretical approaches: the statistical method of Debye and Bueche [1] and the model method pioneered by Stein and Rhodes [2]. The statistical method involves the use of a correlation function describing density fluctuations in an isotropic medium. The statistical method has been extended to include fluctuations in the orientation of anisotropic scatterers as well [3,4]. The statistical method has been further developed [5-9], but remains theoretically complex for spherulitic systems.

The model approach for undeformed spherulitic semi-crystalline polymers has been extended by Stein and coworkers [10-11]. The original work [2] modelled polymer spherulites as isolated spheres containing molecules with their optic axes aligned either parallel or perpendicular to the radius of the sphere. Equations describing the scattered intensity were developed for these models under the conditions of crossed polars (H_v) and parallel polars (V_v). These equations, corrected by Samuels [12,13], qualitatively agree with the observed experimental scattering intensity patterns [14-17]. The equations were later developed for two dimensional disk-like spherulites [11] and they were shown to predict scattering profiles qualitatively similar to those

from the three dimensional model.

According to the model, the scattered intensities for three-dimensional isolated spherulites in the H_v (polarization directions of the analyzer and polarizer are horizontal and vertical, respectively) and the V_v (polarization directions of the analyzer and polarizer are both vertical) modes are given by [17,18]:

$$R_{H_v}(U,\mu) = \frac{144\pi^4 N_s V^2}{\lambda_o^4}(\alpha_r - \alpha_t)^2[((\cos^2\theta/2)/\cos\theta)$$

$$\sin\mu \cos\mu \cos\rho_2(\Phi_{H_v})]^2 \qquad \text{(II-1)}$$

and

$$R_{V_v}(U,\mu) = \frac{144\pi^4 N_s V^2 \cos^2\rho_1}{\lambda_o^4}[(\alpha_r - \alpha_s)\Phi^A_{V_v}$$

$$+ (\alpha_t - \alpha_s)\Phi^B_{V_v} + (\alpha_r - \alpha_t)((\cos^2\theta/2)/\cos\theta)\cos^2\mu\Phi_{H_v}]^2 \qquad \text{(II-2)}$$

where:

U = magnitude of the reduced scattering vector ($= \frac{4\pi\bar{R}_s}{\lambda}\sin\theta/2$)

$\bar{R}_s$ = average spherulite radius

λ = wavelength of the light in the sample

θ = polar scattering angle in the sample

μ = azimuthal scattering angle

N_s = number of spherulites per unit volume

V = average volume of a spherulite

λ_o = wavelength of the light in vacuum

α_r = radial polarizability of the spherulites

α_t = tangential polarizability of the spherulites

α_s = polarizability of the surroundings of the spherulites

$\cos\rho_2 = \cos\theta/(\cos^2\theta + \sin^2\theta \, \sin^2\mu)^{1/2}$

$\cos\rho_1 = \cos\theta/(\cos^2\theta + \sin^2\theta \, \cos^2\mu)^{1/2}$

$\Phi_{H_v} = (1/U^3)(4\sin U - U\cos U - 3\mathrm{Si}U)$

$\mathrm{Si}U = \int_0^U \frac{\sin x}{x}\, dx$

$\Phi^A_{V_v} = (1/U^3)(\mathrm{Si}U - \sin U)$

$\Phi^B_{V_v} = (1/U^3)(2\sin U - U\cos U - \mathrm{Si}U)$

The geometry of the SALS experiment, including the polar and azimuthal scattering angles, is illustrated in Figure II-1.

The H_v pattern from an unoriented spherulitic polymer film is the familiar four-leaf clover pattern. An example H_v SALS photographic pattern from spherulitic PET is given in Figure II-2a. For the "usual" spherulites, scattering maxima are located at azimuthal angles having odd multiples of 45° [2]. There also exists "unusual" spherulites whose maxima occur at azimuthal angles having even multiples of 45° [19,20]. In either case the scattering angle of the maximum intensity (θ_{max}) is given by [2]:

$$U_{max} = \frac{4\pi \bar{R}_s}{\lambda} \sin \frac{\theta_{max}}{2} \qquad \text{(II-3)}$$

where the terms are as previously defined. For two dimensional spherulites, $U_{max} = 3.9$ [11]. For three dimensional spherulites, $U_{max} = 4.1$ [17]. Equation (II-3) provides a convenient means for the measurement of the average size of the spherulites in a film.

It is apparent from equation (II-1) that the H_v intensity depends on the number of spherulites per volume, the size of those spherulites and

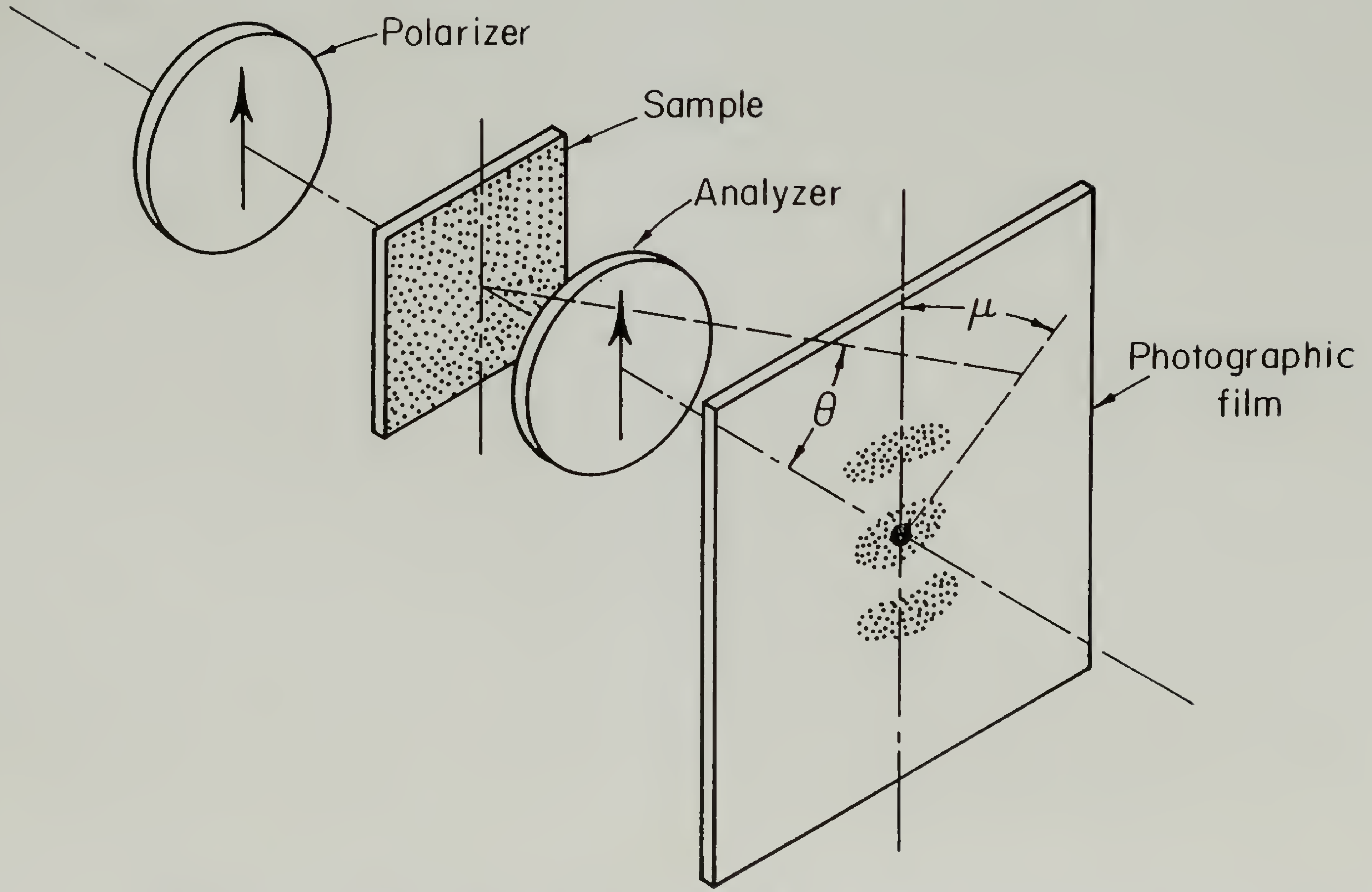

Fig. II-1. Typical arrangement of the basic components in a photographic SALS experiment.

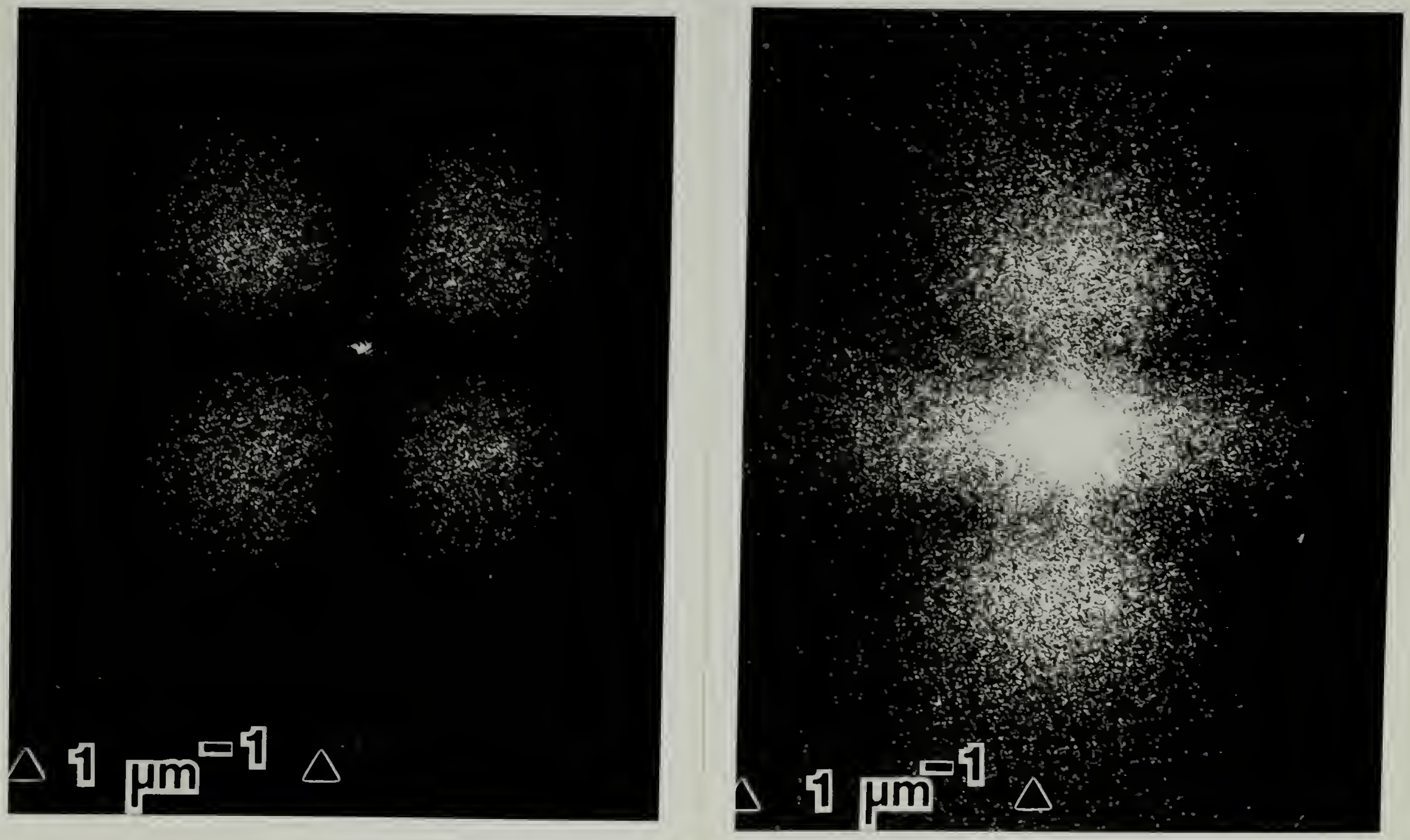

a)

b)

Fig. II-2 SALS photographs from PET crystallized from the melt for 10 minutes at 200°C: a) H_v and b) V_v.

their anisotropy. As will be discussed later, the anisotropy of the spherulites can be related to their crystallinity. Therefore, the H_v SALS experiment is an excellent experiment for monitoring the size, number and crystallinity of spherulites in a polymer film.

The V_v pattern from an unoriented spherulitic polymer film can contain a variety of combinations of horizontal lobes, vertical lobes and circularly symmetric portions, depending upon the relative values of the radial and tangential polarizabilities of the spherulites and the polarizability of the medium around the spherulites [12,13]. An example V_v SALS photographic pattern from spherulitic PET is given in Figure II-2b. The additional dependence of the V_v pattern on the polarizability of the spherulite's surroundings is in contrast to the H_v pattern's dependence only on the spherulite's anisotropy. The change of the V_v pattern with these polarizability changes makes the pattern a good indicator of these polarizabilities.

In comparing equations (II-1) and (II-2), it can be seen that the H_v scattering equation has one azimuthally dependent term which is proportional to $(\alpha_r - \alpha_t)^2$. The V_v equation, on the other hand, has two additional terms which are azimuthally independent and depend upon $(\alpha_r - \alpha_s)$ and $(\alpha_t - \alpha_s)$. The combination of these three terms makes the shape and intensity of the V_v pattern dependent on the volume fraction of spherulites in the sample.

During the crystallization of a spherulitic polymer film the V_v pattern undergoes several changes [2,9]. The shape changes in the pattern are best explained in terms of the changes in the relative

values of the polarizabilities, α_r, α_t and α_s, in equation (II-2). The polarizability of the surroundings depends upon the volume fraction spherulites according to the relationship [9]

$$\alpha_s = \phi_s \left(\frac{\alpha_r + 2\alpha_t}{3}\right) + (1 - \phi_s)\alpha_m \tag{II-4}$$

where ϕ_s = volume fraction spherulites and α_m = polarizability of the nonspherulitic medium. In the initial stages of crystallization, α_s is close to the value α_m. If all of the crystallinity is contained within the spherulites, α_m equals the polarizability of the amorphous material. Since the amorphous polarizability is generally significantly less than the spherulitic polarizabilities, the $(\alpha_r - \alpha_s)$ and $(\alpha_t - \alpha_s)$ terms dominate over the $(\alpha_r - \alpha_t)$ term and the pattern is circularly symmetric.

As the spherulites grow, the shape of the V_v pattern becomes more anisotropic due to the increasing importance of the $(\alpha_r - \alpha_t)$ term. The diminished relative importance of the first two terms is due to the increased value of α_s as ϕ_s increases. The anisotropy of the pattern is due to the cosμ dependence of the third term in equation (II-2). As the spherulites approach volume filling, the third term becomes so significant that the familiar anisotropic dumbbell pattern develops. This pattern shape is retained as secondary crystallization proceeds beyond the point of volume filling spherulites.

The intensity changes in the V_v pattern during cyrstallization are best explained using the relationships developed by Yoon and Stein [9] in a theory which combines the statistical and model approaches to SALS

from polymer spherulites. The theory leads to an equation similar to equation (II-2) for the V_v intensity from polymer spherulites:

$$R_{V_v}(U,\mu) = \frac{192\pi^5 \bar{R}_s^3 B(\phi_s)\cos^2\rho_1}{\lambda_o^4}$$

$$[(\alpha_r - \alpha_s)\,\Phi_{V_v}^{A} + (\alpha_r - \alpha_s)\,\Phi_{V_v}^{B}$$

$$+ (\alpha_r - \alpha_t)\,((\cos^2\theta/2)/\cos\theta)\cos^2\mu\;\Phi_{H_v}]^2 \qquad \text{(II-5)}$$

where

$$B(\phi_s) = \frac{\{\cos^2\rho_1[\phi_s(1 - \phi_s)(\alpha_t - \alpha_m)(2/3\alpha_r + 1/3\alpha_t - \alpha_m) + \phi_s(1/5 - \phi_s/9)(\alpha_r - \alpha_t)^2] + \sin^2\rho_1\phi_s/15(\alpha_r - \alpha_t)^2\}}{\{\cos^2\rho_1[(1 - \phi_s)^2(\alpha_t - \alpha_m)(2/3\alpha_r + 1/3\alpha_t - \alpha_m) + (\alpha_r - \alpha_t)^2(1/5 - 2\phi_s/9 + \phi_s^2/9)] + \sin^2\rho_1\,\phi_s/15(\alpha_r - \alpha_t)^2\}} \qquad \text{(II-6)}$$

and the other terms are as previously defined.

$B(\phi_s)$ is approximately equal to ϕ_s for small values of ϕ_s. In the case of volume filling spherulites, $B(\phi_s) = 1$ and equation (II-5) reduces to equation (II-2). The function $B(\phi_s)$ reaches a maximum at about $\phi_s = 0.6$ [9]. It is this function which explains why the V_v intensity during crystallization initially increases, reaches a maximum and then decreases.

Once the spherulites become volume filling, the intensity will again increase due to secondary crystallization. This increase can best be visualized by examining the V_v equations when $\phi_s = 1$. At this condition, equation (II-4) reduces to

$$\alpha_s = \frac{\alpha_r + 2\alpha_t}{3}. \qquad \text{(II-7)}$$

Combination of equation (II-7) with equation (II-2) or (II-5) leads to

$$R_{V_v}(U,\mu) = K\cos^2\rho_1(\alpha_r - \alpha_t)^2[2/3\,\Phi^A_{V_v} - 1/3\,\Phi^B_{V_v} + ((\cos^2\theta/2)/\cos\theta)\cos^2\mu\;\Phi_{H_v}]^2 \qquad \text{(II-8)}$$

where K represents a product of several constants. According to equation (II-8), for fixed values of U and μ, the V_v intensity will increase during secondary crystallization as the spherulite anisotropy, $(\alpha_r - \alpha_t)^2$, increases. The V_v intensity at this point has the same dependency on anisotropy as the H_v intensity (equation (II-1). Once the system is volume filled with spherulites, the H_v and V_v intensities should increase proportionately.

It is apparent that the V_v SALS experiment complements the H_v SALS experiment in providing information about the size, number, crystallinity and volume fraction of the spherulites in a polymer film. In addition, the V_v experiment provides information about the morphology of the nonspherulitic material. Chapter V presents the use of H_v SALS to follow these changes during the melting of polymer spherulites. Chapter VI combines H_v and V_v SALS in the studies of polymer crystallization via a spherulitic morphology.

Although these model equations predict well many of the features of H_v and V_v SALS patterns as functions of polymer morphology, experimentally measured scattering intensities were found to differ in detail from the two and three dimensional models [11,21,22]. The deviations between the experimental intensities and the intensities predicted by the perfect spherulitic models can be classified as being due to external and internal disorder within the polymeric sample.

The most probable forms of external disorder include a distribution of spherulite sizes, interspherulitic interference and the truncation of the spherulites. It has been shown [23,24] that the major effect of a distribution of spherulite size in a system is to remove the higher order peaks from the H_v scattering pattern. The effect of interspherulitic interference is to impose sinusoidal modulations upon the scattering profile [25-28]. These modulations become negligible when the scattering volume contains a larger number of spherulites. The truncation of the spherulites occurs as a result of the impingement of neighboring spherulites during their growth [29,30]. A recent study [29] employed a theoretical procedure to estimate the degree of truncation in a fully grown spherulitic polymer. The effects of truncation are: a lowering of the H_v scattered intensity at the maximum as compared to round spherulites, an increase of the intensity at low and high angles and a change in the meaning of the average spherulite radius determined from the angle of the scattering maximum. Corrections of the measured H_v intensity can be made to account for the effects of truncation. The effects of truncation have been examined further in this dissertation to include the cases of non-volume filling, two [31] and three dimensional spherulites and sporadic and simultaneous nucleation. These results are presented in Chapter III.

Internal spherulitic disorder may arise from variations in the optic axis orientation within the spherulites. The effects of such variations have been the subject of several studies [21,32-34]. The Yoon-Stein lattice theory [34] of orientational disorder in two dimensional

spherulites allows the optic axes direction in lattice cells to statistically deviate from its mean value in a manner which is correlated with the orientation in neighboring cells. The amount of disorder in the spherulites is described by a disorder parameter δ. $\delta = 0$ for undisordered spherulites, whereas highly disordered spherulites are described by a value of δ of 0.5 or larger.

The effects of this type of disorder are a lowering of the H_v intensity at the maximum and an increase in the scattered intensity at low and high angles. Procedures have been developed for modifying the measured H_v intensity, based on the shape of the scattering profile, to account for the effects of internal disorder. Recently the calculations have been carried out for three dimensional spherulites [35] and the effects of disorder have been found to be greater than that for two dimensional spherulites.

The procedures for the correction of the measured intensities for the effects of external and internal disorder were mostly developed independently. The corrections are applied with some attempts to combine the effects of the different types of disorder. A rigorous theoretical development would be necessary to develop the interdependent corrections of the intensity.

In addition to these theoretical factors, various experimental sources exist which produce deviations from the theoretically predicted intensities. Stein and Keane [36] have identified the sources of experimental deviation as reflection, refraction and multiple scattering of the light; they have described procedures for their correction. A

more recent theory [37,38] describes another method for the correction of the scattered intensity for the effects of multiple scattering in the H_v and V_v modes.

Quantitative SALS means the use of absolute intensities, not relative intensities, in the SALS experiment and analysis [39-41]. In order to obtain absolute intensity data, the SALS detection apparatus must be calibrated in terms of absolute intensity. The calibration of the OMA2 is presented in Chapter IV. The measured intensities must then be corrected for the experimental and theoretical effects as described above [22]. The fully corrected intensities can then be compared to the model equations both to evaluate the effectiveness of the theory and the morphology of spherulitic polymer films.

Fully corrected H_v SALS intensities were utilized in studies of the melting of PET (Chapter V) and the crystallization of PET (Chapter VI). The correction procedures for V_v SALS are not as well developed as those for H_v. Partially corrected V_v SALS were also used in the study of PET crystallization (Chapter VI).

SALS from Deformed Spherulitic Polymers

Extension of the Stein-Rhodes spherulitic models to models of two [11] and three [42,43] dimensional deformed spherulites has been made for the study of oriented systems by light scattering. These works, assuming an affine mode of deformation of the spherulites, developed theoretical equations for the H_v, H_h and V_v SALS from such systems. In

addition to assuming that the spherulites deform affinely, these models also assume that the deformation is uniaxial elongation, the system demonstrates cylindrical symmetry, there is no volume change during deformation and the change in the orientation of the optic axes can be described by two empirical equations. Also, one of the models assumes that there is a constant density of crystals preserved during deformation.

According to the three dimensional model [42,43], the orientation of the optic axis is described in terms of angles β and ω (Figure II-3). β is the angle between the optic axis and the spherulite radius. ω is the angle of rotation of the optic axis about the radius. Changes in β and ω are given by the following empirical equations

$$\beta = \beta_o \exp[-\kappa(\lambda_3^2 - \lambda_2^2)\cos^2\alpha'] \qquad \text{(II-9)}$$

$$2\langle\cos^2\omega\rangle - 1 = 1 - \exp[-\eta(\lambda_3^2 - \lambda_2^2)\sin^2\alpha'] \qquad \text{(II-10)}$$

where:

β_o = value of β for no deformation (assumed to be 90°)

κ = parameter of compliance toward optic axis tilting

λ_3 = extension ratio in the stretching direction

λ_2 = extension ratio in the transverse direction

α' = angle between the radial element and the stretching direction (Figure II-3)

$\langle\cos^2\omega\rangle$ = average value of $\cos^2\omega$

η = parameter of compliance toward optic axis rotation about the radius.

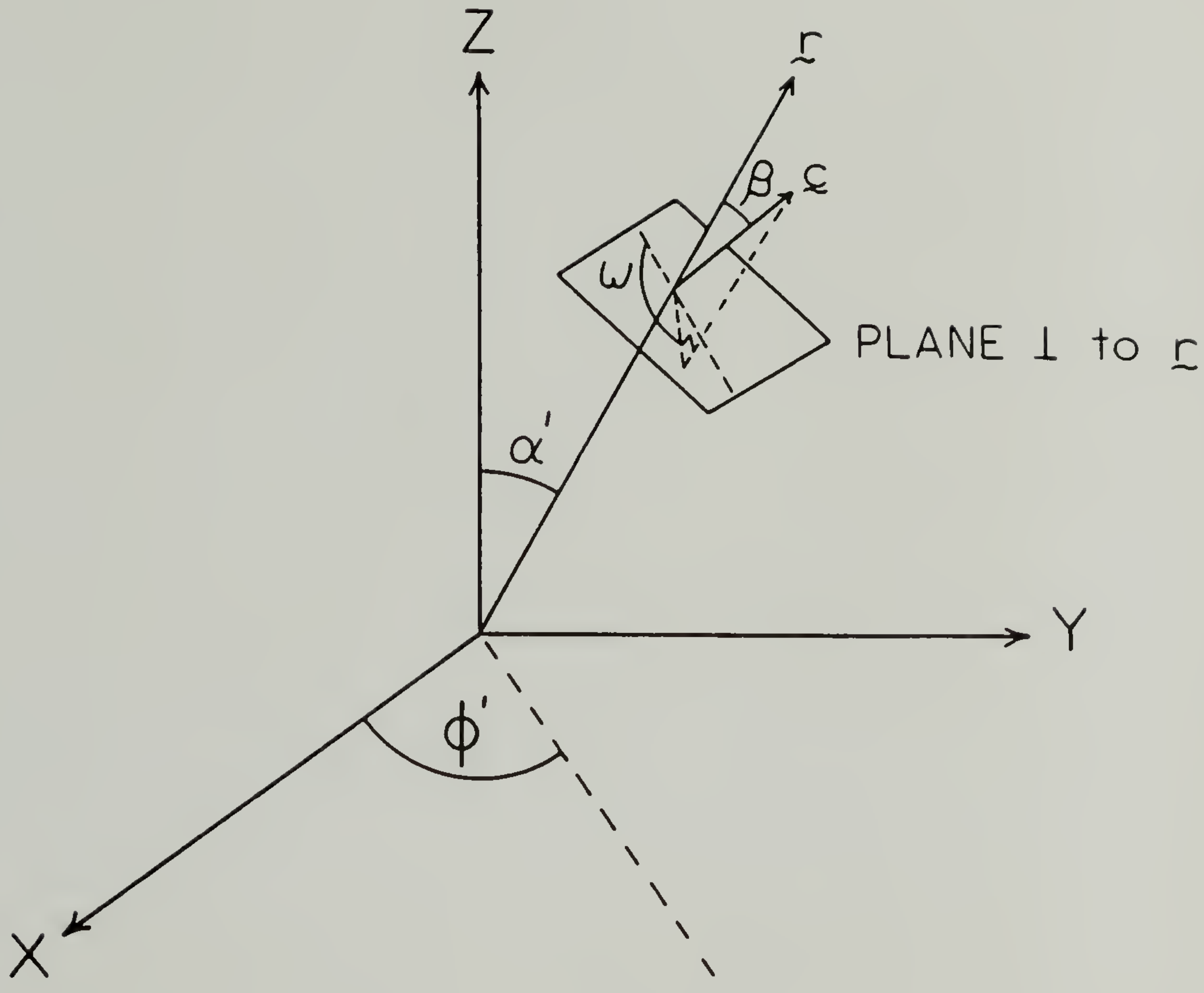

Fig. II-3 Diagram of the geometry used for the spherulite deformation model.

Equations (II-9) and (II-10) have the usual rubber elasticity type dependence upon the extension ratio [44-46]. It is apparent from the two equations that optic axis tilting is favored in the polar regions of the spherulite. Rotation of the optic axis about the radius is favored in the equatorial regions. The ease with which the orientation of the optic axes changes with elongation by these two mechanisms is described by the compliance parameters κ and η.

Using this model, van Aartsen and Stein [42,43] generated a series of H_v SALS isointensity contours as functions of the deformation and the compliance parameters. Examples of some of those contours for constant density of crystals are given in Figure II-4. As evident from Figure II-4, the azimuthal angle of maximum H_v intensity increases during deformation from its initial value of 45°. The lobes of the four-leaf clover pattern move toward the equator of the pattern. Also the polar angle of maximum intensity increases slightly with spherulite elongation. Experimental H_v scattering patterns from medium density polyethylene agree well with this affine model [11]. The data was not sufficiently sensitive to evaluate the deformation mechanisms.

Samuels has made a more simplified, non-rigorous derivation of the equations for SALS from affinely deformed spherulites [13,14,47]. A most significant result of this derivation is the prediction that the azimuthal angle of maximum intensity remains at 45° during uniaxial elongation. Samuels has found that experimental H_v and V_v SALS patterns from deformed isotactic polypropylene agree with his model, that is, the spherulites deform affinely up to $\lambda_3 = 5$ and that the azimuthal angle of

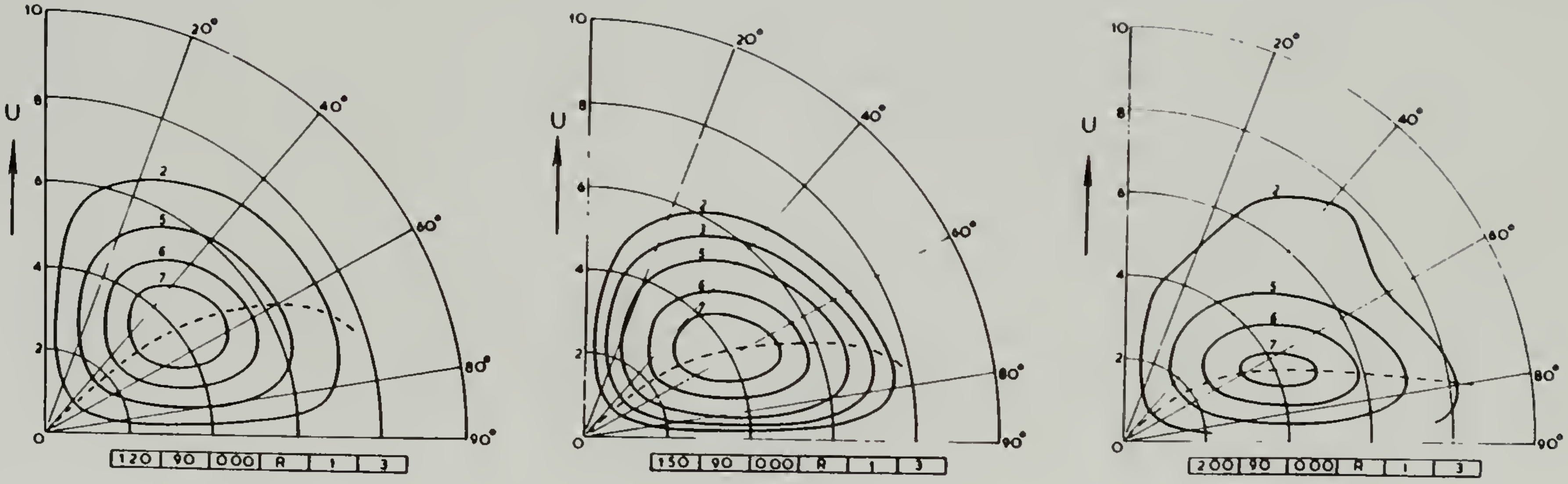

a)

b)

c)

Fig. II-4 H_v SALS isointensity contours from van Aartsen et al. [38]. $\beta_o = 90°$, ω is random, density of crystals is constant and elongation ratio is a) 1.20, b) 1.50 and c) 2.00.

maximum H_v intensity is constant at 45°.

Chapter VII of this dissertation presents results of deformation studies of low density polyethylene and isotactic polypropylene. These affine deformation theories are examined in relation to these results. The theories for SALS from deformed spherulites have not been developed to include the quantitative corrections developed for SALS from undeformed spherulites as previously outlined. Therefore, the studies presented in Chapter VII utilize only relative intensity values. The establishment of a valid deformation model must precede the theoretical development of quantitative SALS from deformed spherulites. The sensitivity of the van Aartsen and Stein model to the different spherulitic morphologies of different polymers is examined in this chapter.

CHAPTER III

THE EFFECTS OF SPHERULITIC TRUNCATION ON SMALL-ANGLE LIGHT SCATTERING

Introduction

In Chapter II an expression for the H_v scattering from polymer spherulites was given. Equation (II-1) was derived [2] for the spherulite model: the spherulites are isolated, perfect spheres whose optic axes are either parallel or perpendicular to the spherulite radius. A similar equation has been derived [11] for model two dimensional disk-like spherulites. As discussed in Chapter II, the experimental SALS from spherulitic polymer films deviates from the model due to spherulitic disorder, both internal and external. This chapter presents theoretical studies investigating the effects of one of the types of external disorder: the truncation of the spherulites.

The model equations assume that polymer spherulites are either perfect disks or perfect spheres. In practice, polymer spherulites are usually truncated due to the impingement of other spherulites during their growth. This truncation is apparent in Figures III-1 and III-2. The spherulites appear polygonal in shape in these micrographs. It is the purpose of this study to determine the effects on the H_v SALS patterns due to this spherulitic truncation.

So far all attempts to estimate the effects of truncation on light scattering consider either only a single isolated spherulite or a completely volume filled system [22,29,30,48,49]. In the case of a

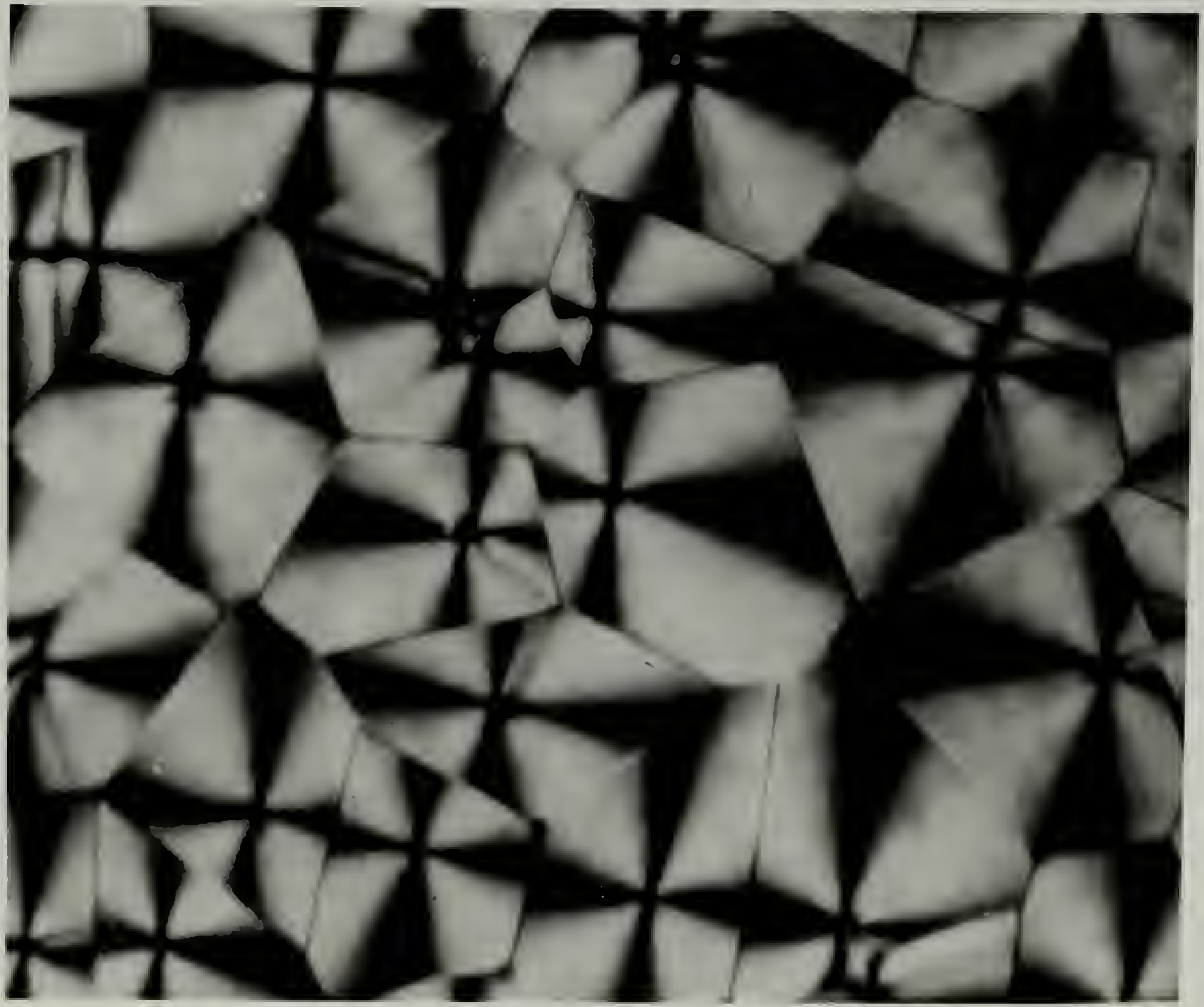

Fig. III-1 Optical micrograph of Marlex 50 polyethylene spherulites under crossed polars [29].

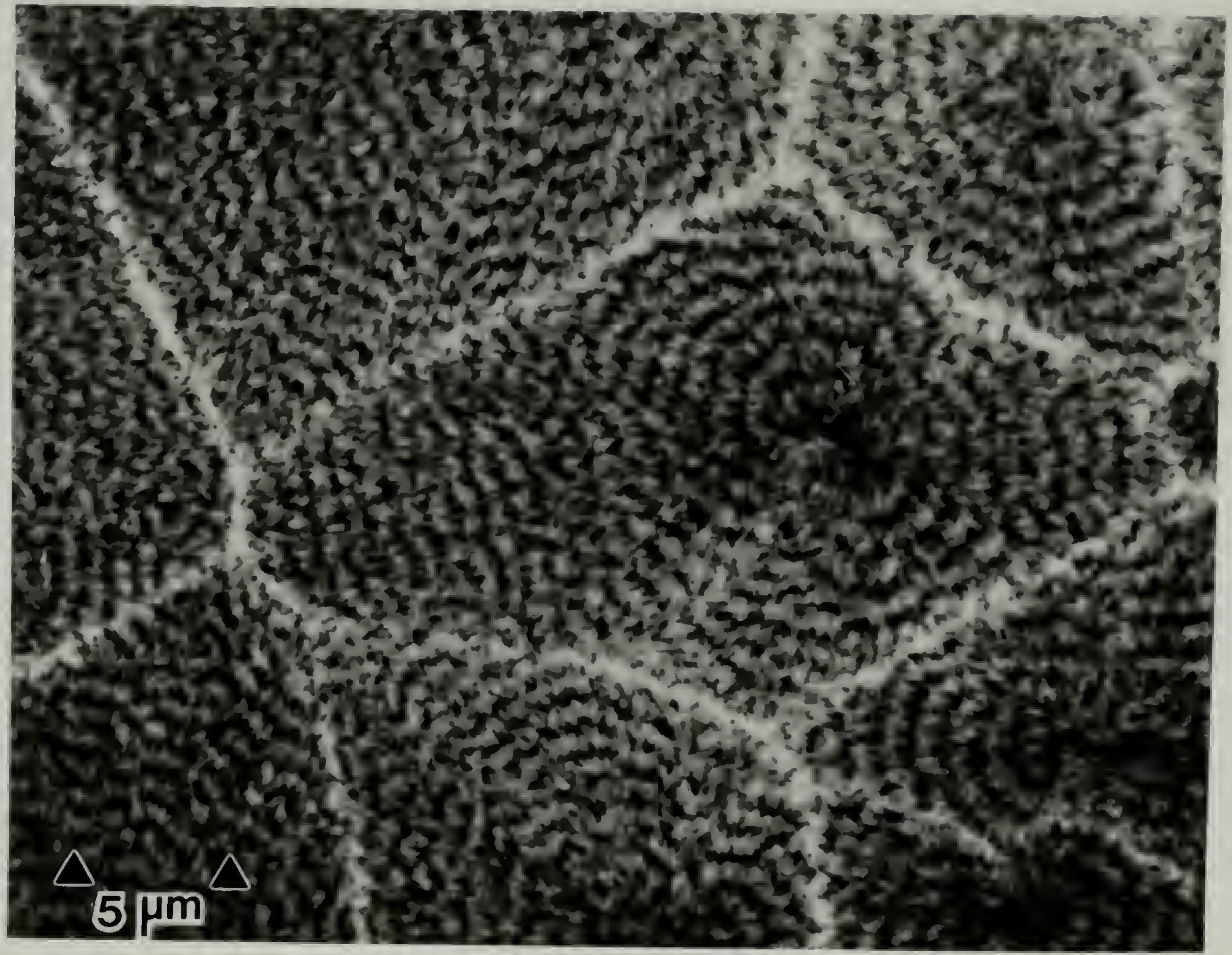

Fig. III-2 Scanning transmission bright field electron micrograph of Marlex 6003 polyethylene spherulites. Micrograph courtesy of W.W. Adams.

crystallizing polymer, various states of spherulite growth occur. In the early stages probably no spherulites impinge. As the spherulites continue to grow, more and more of them will impinge upon each other, and the extent of truncation for each individual spherulite also increases. This process of truncation will continue until the system becomes volume filled with spherulites. Recent Monte Carlo studies of the growth of two [50] and three [51] dimensional spherulites included the cases of non-volume filling, but did not calculate the effects on light scattering.

It is an unresolved question as to whether the disorder of optic axis orientation changes during spherulite growth. The results in Chapter VI indicate that internal disorder does change during spherulite growth. The approach in this study is that the effects of truncation can be determined separately from those of internal disorder. The two effects are combined in an additive manner in Chapters V and VI. The methods developed in this chapter can be readily extended to combine the effects of truncation and internal disorder on the SALS.

Recently, attempts have been made to apply quantitatively the small-angle scattering technique to the investigation of crystallization kinetics of polymers [39]. This procedure necessitates the estimation of the truncation effect on the scattering in the various states of spherulite growth. The study in this chapter uses computer simulation of spherulite growth to determine these effects.

The Model and Principles of Calculation

The computer simulation technique generated sets of random nucleation sites and times, calculated the shapes of the spherulites after a specified growth time, determined average features of the spherulite sets and calculated the H_v SALS intensity from such sets of spherulites. The intensities were compared to that predicted by the model equations. This simulation has been carried out for both simultaneous and sporadic nucleation in two dimensions and simultaneous nucleation in three dimensions.

The nuclei locations were generated using a random number generator. The nuclei were assigned nucleation times then randomly located in a sphere (circle for two dimensions). In order to avoid the case where two nuclei may occupy the same location, the minimum distance between two nuclei was restricted to be greater than 0.1 μm. This restriction had little, if any, effect on the randomness of placement of the nuclei since the random number generating routine rarely placed two nuclei closer than 0.1 μm. This feature of the computer simulation could be used in future studies of nucleation and growth where the proximity of the nuclei is restricted.

The shapes of the growing spherulites were determined by examining the system after various growth times. The growth rate of the spherulites was assumed constant. The radii of each spherulite were calculated at various angular increments around the nucleus. In two dimensions, the radii were calculated at 3° intervals around the nucleus

(Figure III-3). The shape of a spherulite is then described by 120 radius values. In three dimensions, the radii were calculated at 9° intervals in α and ϕ (Figure III-4). The shape of a spherulite is then described by 840 radius values.

The value of a radius at a particular angle in a spherulite at some growth time is the lesser of two values:

1. the growth rate multiplied by the elapsed growth time since the spherulite's nucleation or
2. the distance from the nucleus, along the particular angle, at which the spherulite impinges another spherulite.

Any spherulite, which upon full growth, penetrated the limiting sphere (or circle) in which the original nuclei were located was excluded from the statistics since its shape would be affected by the limiting sphere (or circle). However, such eliminated spherulites were still allowed to affect the growth of other spherulites. The dimensions of the limiting sphere (or circle) were chosen such that the average radius of fully grown spherulites was about 10 µm.

The type of nucleation was controlled by the growth rate relative to the nucleation rate. The nucleation rate was held constant at one nucleus per minute (units of time are arbitrary). Simultaneous nucleation was then effected by choosing an extremely slow growth rate, such as 1×10^{-12} µm per minute. In such cases, all of the spherulites have been nucleated before any significant spherulite growth occurs. Sporadic nucleation was effected by choosing a moderate growth rate value, such as 0.05 µm per minute. In sporadic nucleation some of the

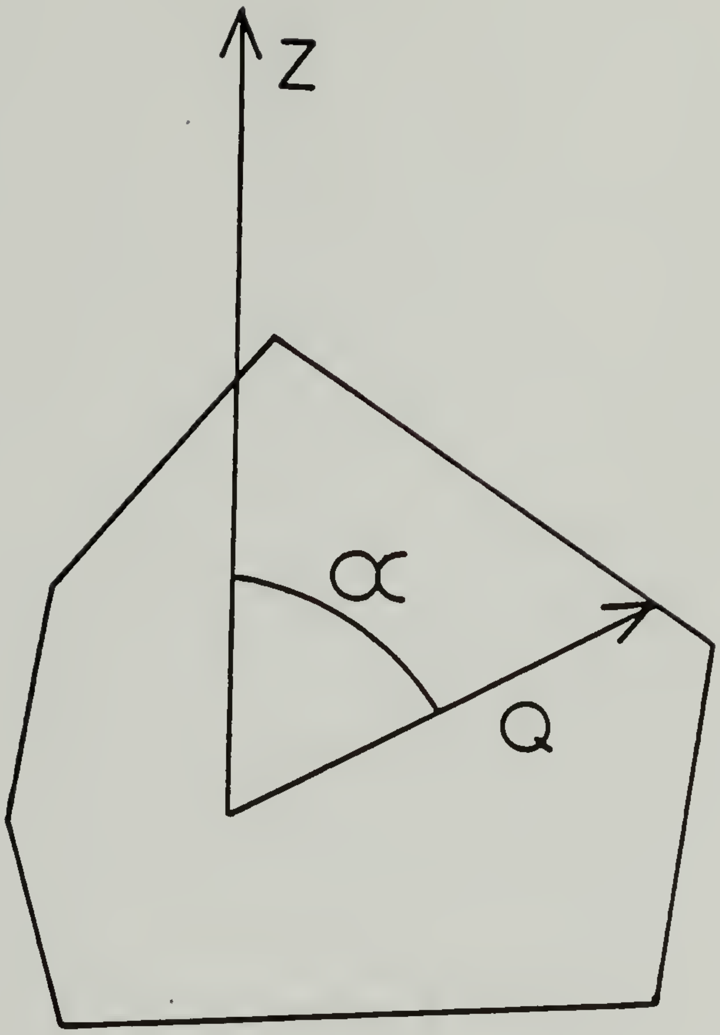

Fig. III-3 Diagram of the angular intervals for radii calculations for two dimensional spherulites.

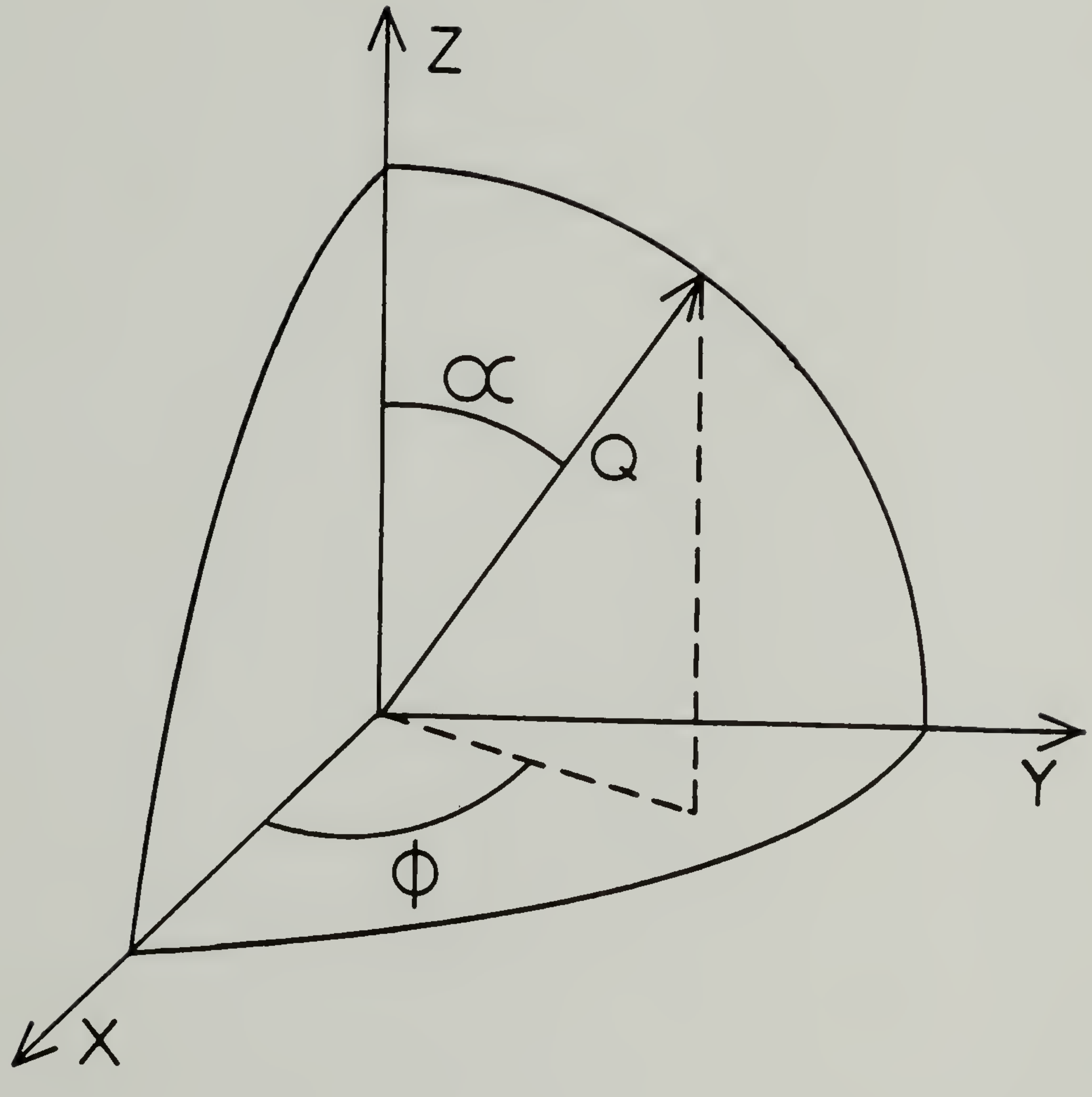

Fig. III-4 Diagram of the angular intervals for radii calculations for three dimensional spherulites.

potential spherulites were never nucleated since their nucleation sites were overgrown by a spherulite with an earlier nucleation time.

Two dimensional spherulites. The effects of the truncation of two dimensional spherulites were evaluated first because the computation time would be much less than for three dimensional spherulites. The effects were evaluated in two separate studies. In the first study [31], sets of 30 nuclei were randomly located in the limiting circle (30 - 40 µm in radius). Figure III-5 represents an example of one set of randomly located nuclei. The nuclei located by X's penetrated the limiting circle on full growth. Those located by O's were the remaining nuclei. Figures III-6 to III-9 show the shapes of the spherulites at various stages of growth, generated from the remaining nuclei following simultaneous nucleation. Note that the boundary between any two impinging spherulites is along the perpendicular bisector of the line segment connecting the two nuclei. This boundary is straight.

To characterize the extent of truncation, previous studies [29,48] of the subject were followed in the definitions of terms. For spherulite j, the average radius is defined as

$$\bar{Q}_j = \frac{1}{120} \sum_{i=1}^{120} Q_{ij} \tag{III-1}$$

where Q_{ij} is the radius value of spherulite j at angle i. The average truncation parameter for a system of N spherulites is defined as

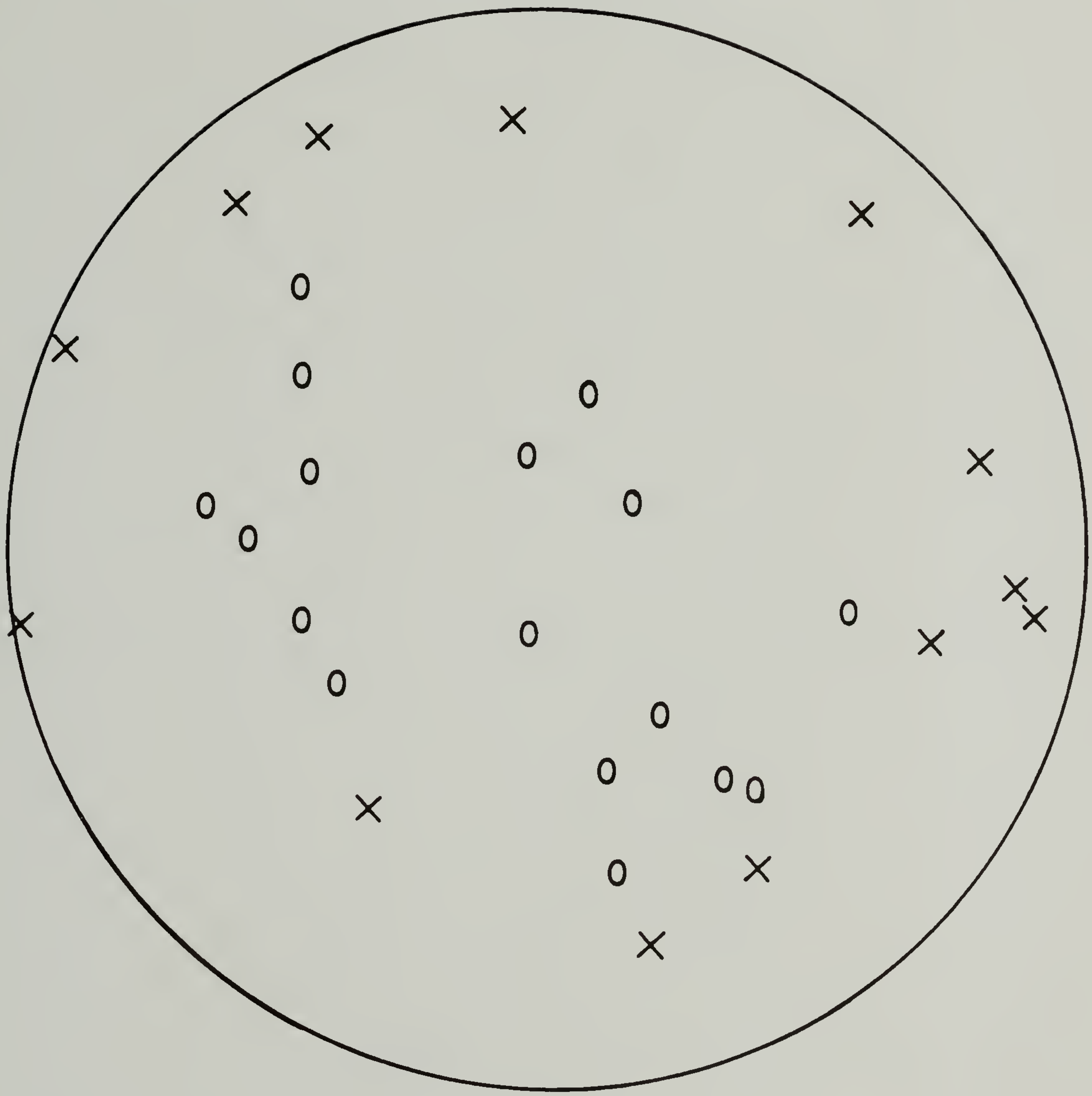

Fig. III-5 Example of random location of 30 nuclei in the limiting circle: (X) nuclei whose spherulites penetrate the circle upon full growth; (O) remaining nuclei.

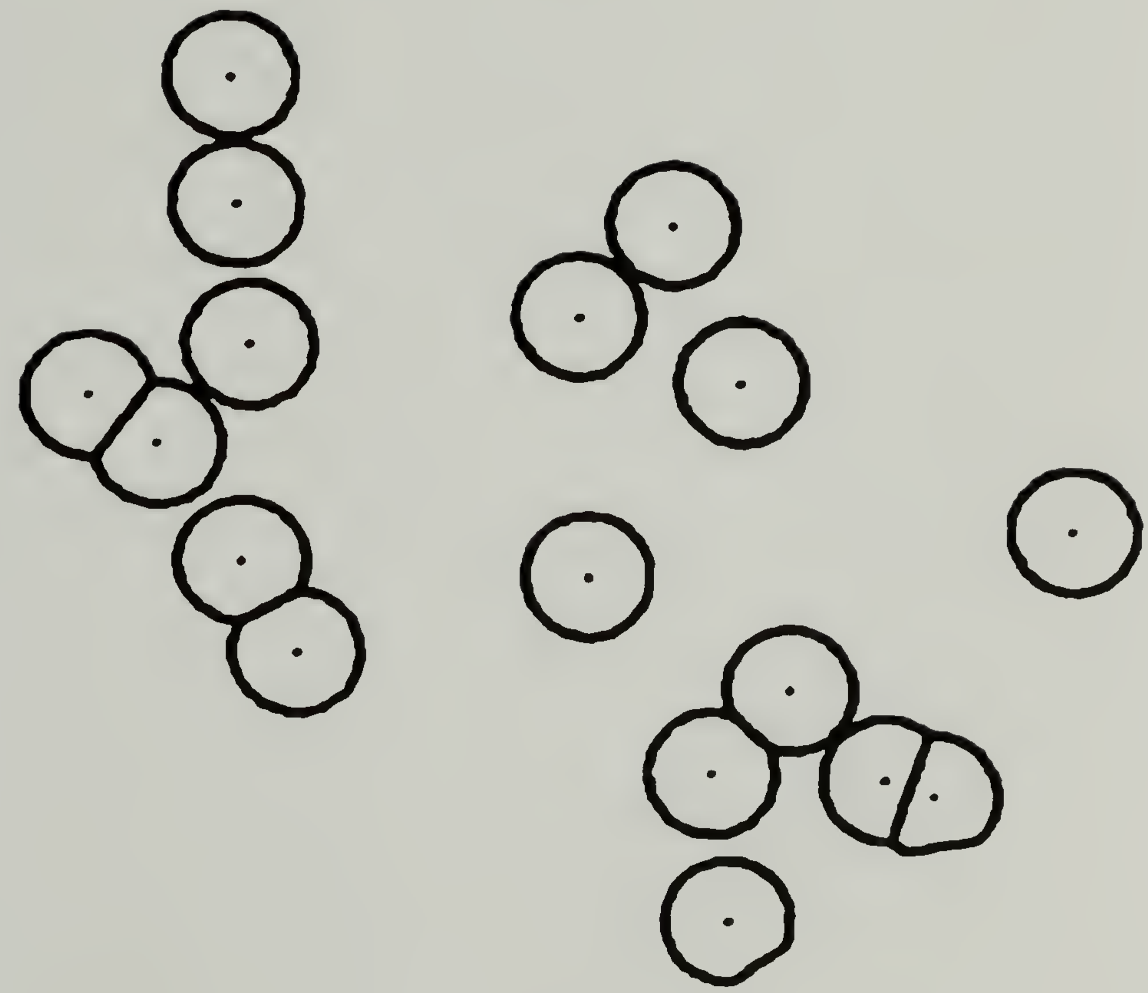

Fig. III-6 Two dimensional spherulites grown to 27.1% area fraction following simultaneous nucleation from the remaining nuclei in Figure III-5.

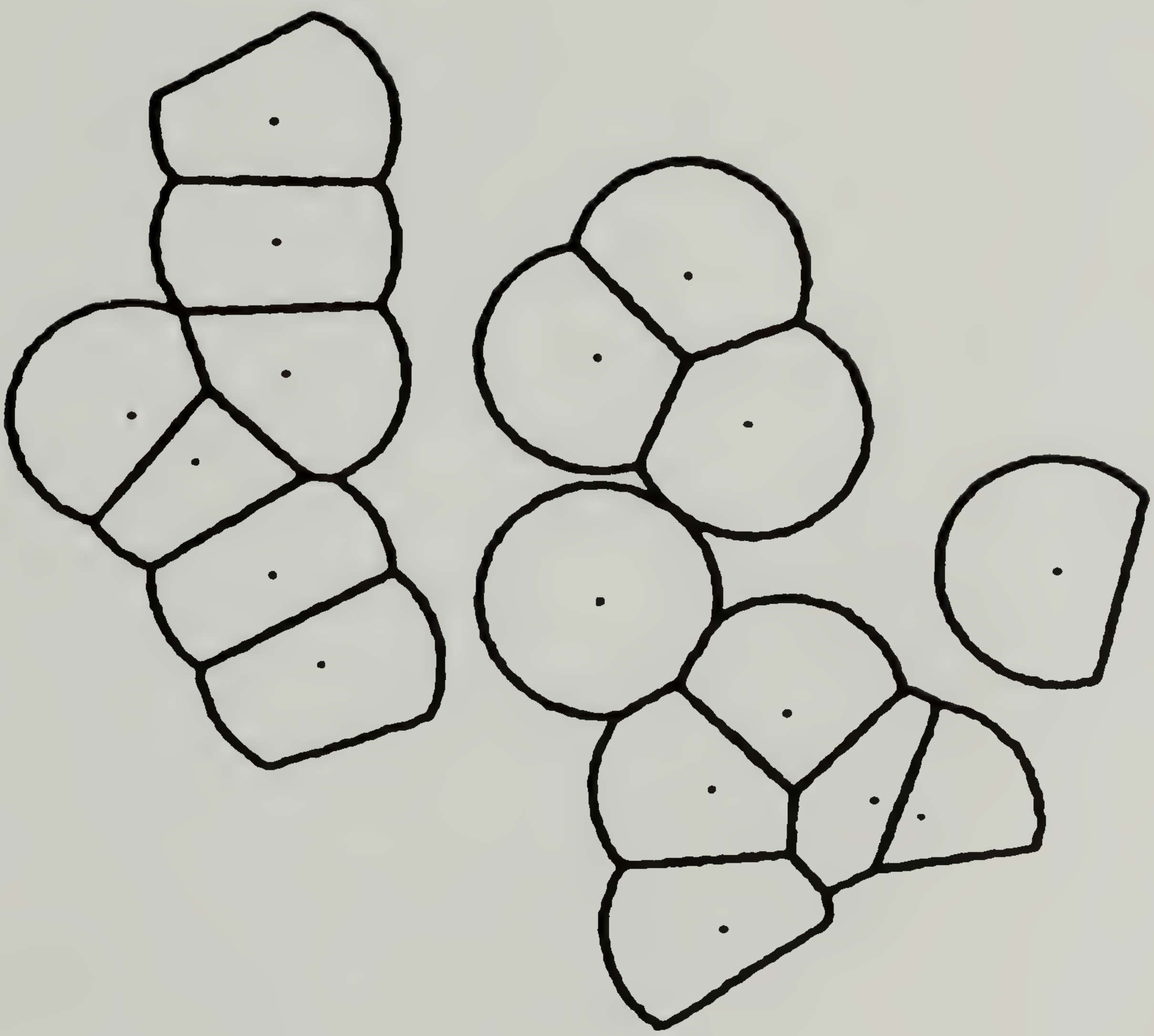

Fig. III-7 Two dimensional spherulites grown to 60.1% area fraction following simultaneous nucleation from the remaining nuclei in Figure III-5.

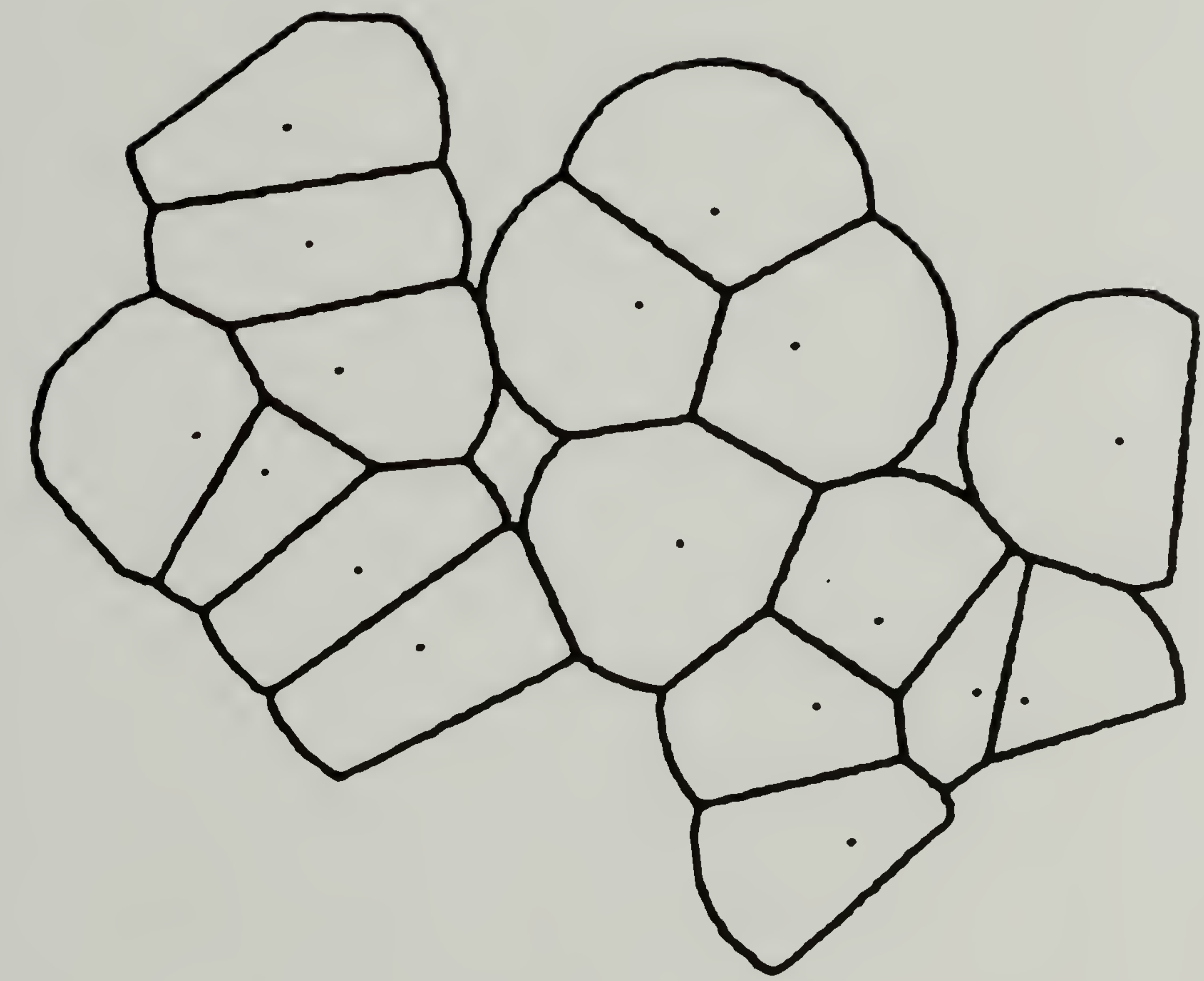

Fig. III-8 Two dimensional spherulites grown to 81.5% area fraction following simultaneous nucleation from the remaining nuclei in Figure III-5.

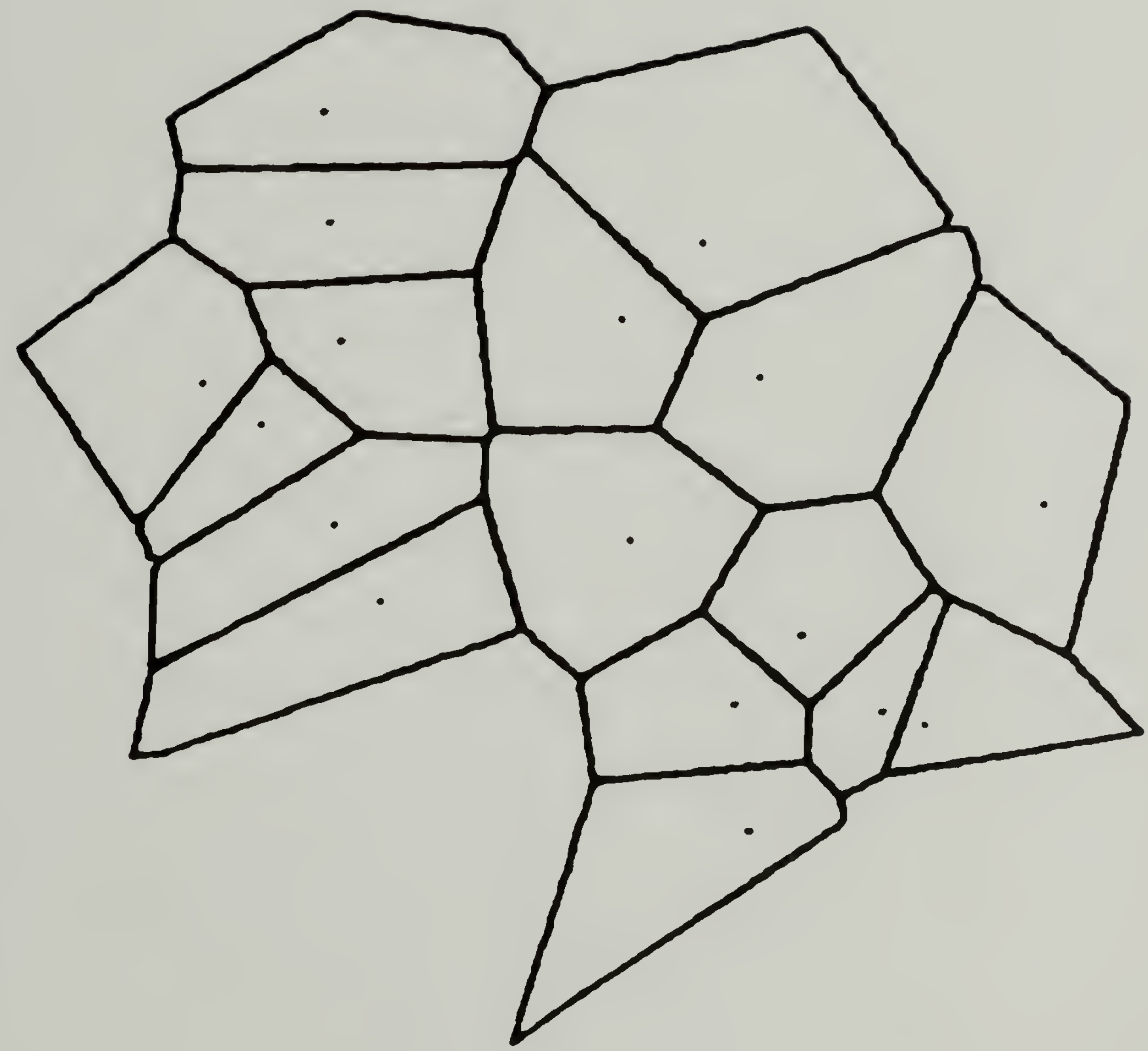

Fig. III-9 Fully grown two dimensional spherulites following simultaneous nucleation from the remaining nuclei in Figure III-5.

$$(TP) = (\frac{\sigma^2}{\bar{Q}^2}) = \sum_{j=1}^{N} \frac{\sigma^2}{\bar{Q}^2_j} N^{-1} \qquad \text{(III-2)}$$

where σ_j is the variance of the radii for spherulite j. An average truncation parameter weighted by the sixth power of the average size has also been defined as

$$\langle TP \rangle = \langle\frac{\sigma^2}{\bar{Q}^2}\rangle = \sum_{j=1}^{N} (\frac{\sigma^2}{\bar{Q}^2})_j \bar{Q}_j^6 / \sum_{j=1}^{N} \bar{Q}_j^6 \qquad \text{(III-3)}$$

In this first study, 40 sets of 30 spherulites each were investigated. Wide variations of the truncation parameters for the fully grown spherulites were observed. The average values for these 40 systems were (TP) = 0.236 and ⟨TP⟩ = 0.133, which are in excellent agreement with previously determined truncation parameters for randomly nucleated fully grown spherulites of (TP) = 0.228 and ⟨TP⟩ = 0.132 [48]. The value of (TP) is also in good agreement with a Monte Carlo method of spherulite growth which obtained a value of (TP) = 0.205 [50,52]. In this study of the various stages of growth, 10 of the 40 sets of spherulites with more narrow distributions of the truncation parameters and average values of (TP) = 0.235 and ⟨TP⟩ = 0.132 were chosen. The results of this study were averages from these 10 sets of spherulites.

In the second study of two dimensional spherulite growth, the methods of the first study were generalized to include the case of sporadic nucleation. In place of several sets of spherulites, the second study used one set of 150 nuclei located in a circle of radius 80 μm. The average truncation parameters for this set were (TP) = 0.257 and ⟨TP⟩ = 0.130. An example of the spherulites generated following

sporadic nucleation is given in Figure III-10. It should be noted that, in contrast to spherulites grown following simultaneous nucleation, many of the boundaries between impinging spherulites in Figure III-10 are curved in a hyperbolic shape. This curvature is a result of the impingement of two spherulites with differing nucleation times. The results from the first study and the simultaneous nucleation portion of the second study are in excellent agreement. Therefore, the two dimensional results presented in this chapter are from the second study only. The agreement among the two studies and the previous work [48] is indicative of the randomness of the nuclei and the repeatability of the results. Since the sporadic nucleation portion of the second study was based on the same nuclei set as the simultaneous nucleation section, the agreement with the other studies implies the sporadic study is also reliable.

The H_v light scattering intensity distributions were computed considering the spherulites as two-dimensional anisotropic disks whose anisotropic scattering elements orient along the radius of the disk. The anisotropy was assumed constant throughout the disk. In order to eliminate the modulation of intensity due to interspherulitic interference, the intensities from each of the spherulites in a system were merely added. One can write for the H_v scattering amplitude [29]

$$E_{H_v} = C(\alpha_r - \alpha_t)\cos\rho_2 \int_{\alpha=o}^{2\pi} \int_{r=o}^{Q} \sin\alpha \cos\alpha \\ \exp(i\ k\ r \sin\theta \cos(\mu - \alpha))r\, dr\, d\alpha \tag{III-4}$$

where C is a constant; α_r and α_t are the radial and tangential polarizabilities, respectively; α is the angle between a radial

Fig. III-10 Two dimensional spherulites grown to 65.7% area fraction following sporadic nucleation of 150 nuclei; (X) nuclei whose spherulites penetrate the limiting circle upon full growth.

direction of the disk and a reference z axis; r is a radial displacement magnitude; $k = 2\pi/\lambda$ is the wave number; λ is the wavelength of the light in the medium; θ is the polar scattering angle; μ is the azimuthal angle; and

$$\cos\rho_2 = \cos\theta/(\cos^2\theta + \sin^2\theta \sin^2\mu)^{1/2}. \qquad \text{(III-5)}$$

Equation (III-4) may be further simplified by integrating with respect to r, to give

$$E_{H_v} = K\int_{\alpha=o}^{2\pi} \sin\alpha \cos\alpha \, (T_R(\alpha) + iT_I(\alpha))d\alpha \qquad \text{(III-6)}$$

where

$$T_R(\alpha) = \cos(PQ)/P^2 + Q\sin(PQ)/P - 1/P^2 \qquad \text{(III-7)}$$

$$T_I(\alpha) = \sin(PQ)/P^2 - Q\cos(PQ)/P \qquad \text{(III-8)}$$

$$P = k\sin\theta \cos(\mu - \alpha) \text{ and} \qquad \text{(III-9)}$$

$$K = C \cos\rho_2 \, (\alpha_r - \alpha_t) \ . \qquad \text{(III-10)}$$

For a truncated disk, the magnitude of the radius Q depends on α. The integration with respect to α was carried out numerically using the radius values generated at 3° intervals of α for each spherulite. The scattered intensity was determined from

$$I_{H_v} = E_{H_v}E^*_{H_v} \qquad \text{(III-11)}$$

where $E^*_{H_v}$ is the complex conjugate of the scattering amplitude.

In a real polymer system, spherulites have various orientations with respect to a reference z axis. It is assumed that by using random nucleation and a large number of spherulites (150) that the arbitrary

choice of a reference z axis did not affect the results. Again, the agreement between the two studies helps substantiate this assmuption.

Three dimensional spherulites. The methods of the first two studies were further generalized to three dimensional growth. In this case 500 nuclei were randomly located in a sphere of radius 80 µm. Truncation parameters were not calculated since their meaning in three dimensions is not clear. In the interest of minimizing time spent, only the case of simultaneous nucleation was carried out for three dimensional growth. It is assumed that the calculated differences between simultaneous and sporadic nucleation cases in two dimensions can be extrapolated to three dimensions.

Due to the complexity of such illustrations, diagrams of the set of computer grown, three dimensional spherulites at varius stages of growth were not produced. A representation of typical three dimensional spherulites, fully grown following simultaneous nucleation, is given in Figure III-11 [53]. The polypropylene spherulites in this micrograph were grown in mineral oil and then fractured. The polyhedral shape of the spherulites is apparent. Similar polyhedral shapes were generated by the computer simulation.

The H_v light scattering amplitude is given for a noncentrosymmetric spherulite by [2,54]:

$$E_{H_v} = C\int(\underset{\sim}{M}\cdot\underset{\sim}{O})\exp(ik(\underset{\sim}{r}\cdot\underset{\sim}{S}))d^3\underset{\sim}{r} \qquad \text{(III-12)}$$

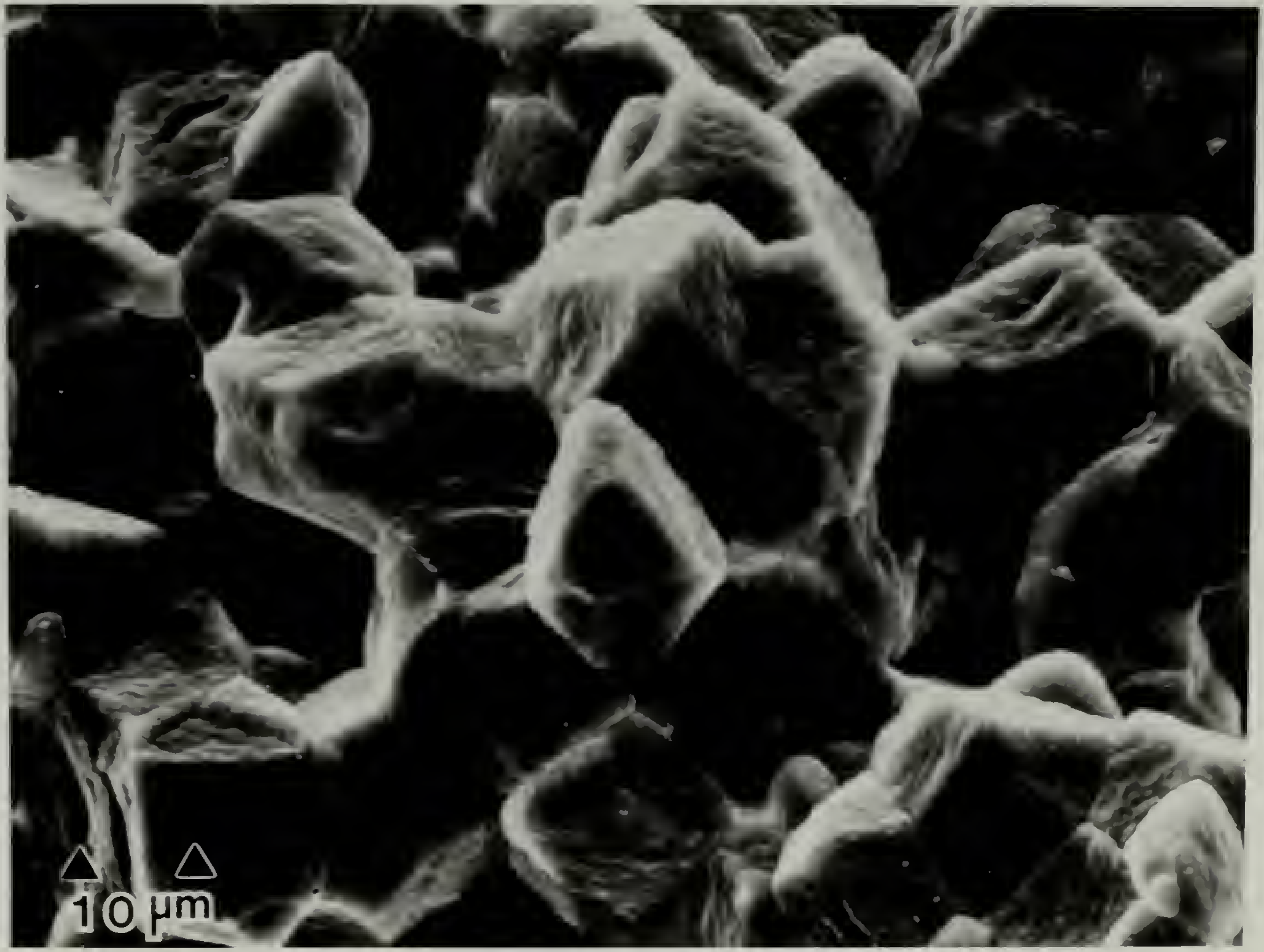

Fig. III-11 Scanning electron micrograph of polypropylene spherulites grown in mineral oil and fractured. Micrograph is the courtesy of R. Lutz and D.L. Handlin of Shell Development Company.

where C is constant, k is the wave number, $\mathbf{M}$ is the dipole moment induced by the incident electric field in the volume element of the spherulite located by the vector $\mathbf{r}$ relative to the nucleus of the spherulite, $\mathbf{O}$ is a unit vector in the direction of the electric vector of the scattered wave transmitted by the analyzer, $\mathbf{S} = \mathbf{S}_o - \mathbf{S}_1$, where $\mathbf{S}_o$ is a unit vector in the direction of the incident light beam, $\mathbf{S}_1$ is a unit vector in the direction of the scattered light beam and $d^3\mathbf{r}$ is the differential volume element.

Using the spherical coordinate system described in Figure III-12, equation (III-12) can be replaced by [2]:

$$E_{H_v} = C\int_{\phi=o}^{2\pi} \int_{\alpha=o}^{\pi} \int_{r=o}^{Q} [\delta(\mathbf{\varepsilon}\cdot\mathbf{a})(\mathbf{a}\cdot\mathbf{o}) + \alpha_t(\mathbf{\varepsilon}\cdot\mathbf{o})] \qquad \text{(III-13)}$$

$$\exp(ik(\mathbf{r}\cdot\mathbf{s}))r^2 \sin\alpha \, dr \, d\alpha \, d\phi$$

where

Q = the radius of the spherulite at angles α and

$\delta = \alpha_r - \alpha_t$ for a spherulite whose optic axis is parallel to the radius of the spherulite

$\mathbf{\varepsilon}$ = incident electric field vector

$\mathbf{a}$ = unit vector in the direction of the optic axis

and α_r and α_t are as previously defined.

For H_v scattering:

$\mathbf{\varepsilon} = \varepsilon_o\mathbf{k}$

$\mathbf{a} = \mathbf{r}/r = \sin\alpha \cos \mathbf{i} + \sin\alpha \sin \mathbf{j} + \cos\alpha\mathbf{k}$

$\mathbf{O} = -\sin\rho_2\mathbf{i} + \cos\rho_2\mathbf{j}$

$\mathbf{S} = (1-\cos\ )\mathbf{i} - \sin\ \sin\mu\mathbf{j} - \sin\ \cos\mu\mathbf{k}$

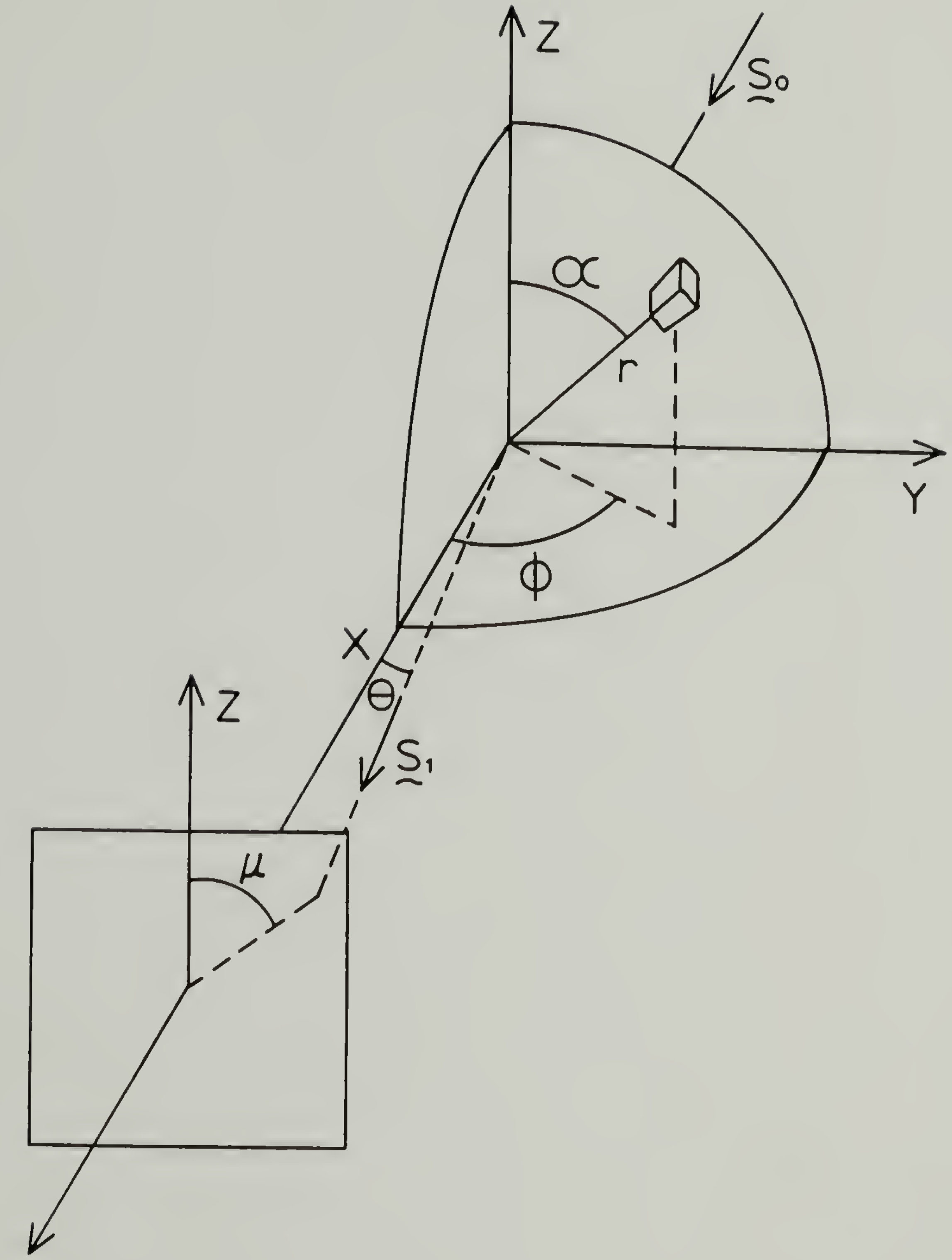

Fig. III-12 Diagram of the scattering geometry for a three dimensional spherulite.

where

ε_o = field strength of the incident light wave

$\sin\rho_2 = \sin /(\cos^2\theta + \sin^2\theta \sin^2\mu)^{1/2}$

$\mathbf{i}, \mathbf{j}, \mathbf{k}$ = unit vectors in the x, y and z directions, respectively, and $\cos\rho_2$ is as previously defined.

Therefore:

$$\boldsymbol{\varepsilon} \cdot \mathbf{a} = \varepsilon_o \cos\alpha$$

$$\mathbf{a} \cdot \mathbf{o} = -\sin\rho_2 \sin\alpha \cos\phi + \cos\rho_2 \sin\alpha \sin\phi$$

$$\boldsymbol{\varepsilon} \cdot \mathbf{o} = 0$$

$$rB = k\mathbf{r} \cdot \mathbf{s} = kr\,(\sin\alpha \cos\phi - \cos\theta \sin\alpha \cos\phi - \sin\theta \sin\mu \sin\alpha \sin\phi - \sin\theta \cos\mu \cos\alpha).$$

Combining terms, equation (III-13) becomes:

$$E_{H_v} = K\int_{\phi=o}^{2\pi} \int_{\alpha=o}^{\pi} \sin^2\alpha \cos\alpha\,(-\sin\rho_2 \cos\phi + \cos\rho_2 \sin\phi)\,d\alpha\, d\phi \int_{r=o}^{Q} r^2 \exp irB\, dr \qquad \text{(III-14)}$$

where $K = C\delta$.

Carrying out the integration over r, equation (III-14) becomes

$$E_{H_v} = K\int_{\phi=o}^{2\pi} \int_{\alpha=o}^{\pi} \sin^2\alpha \cos\alpha(-\sin\rho_2 \cos\phi + \cos\rho_2 \sin\phi)(F_R + iF_I)\,d\alpha\, d\phi \qquad \text{(III-15)}$$

where:

$$F_R = \frac{2Q \cos QB}{B_2} + \frac{Q^2B^2-2}{B_3} \sin QB$$

$$F_I = \frac{2Q \sin QB}{B^2} - \frac{Q^2B^2-2}{B^3} \cos QB \frac{-2}{B^3}$$

The integrations over α and ϕ were carried out numerically using the radius values generated at 9° intervals in α and ϕ. The intensity was calculated using equation (III-11).

Results and Discussion

Calculated intensities: two dimensional spherulites. As spherulites grow, the extent of truncation and its effect on the H_v SALS pattern increase. Figures III-13 to III-17 display the changes in the H_v SALS patterns during spherulitic growth and impingement. These figures are results from the set of 150 spherulites grown following simultaneous nucleation. Figure III-13 plots the H_v intensity at $\mu = 45°$ as a function of the reduced scattering vector, U_∞, for various stages of growth ($U_\infty = (4\pi/\lambda\ \bar{R}_\infty) \sin\theta/2$, where $\bar{R}_\infty$ is the average spherulite radius after infinite growth time). Figure III-13 shows the movement of the angle of maximum intensity to smaller values and the increase of the intensity of the scattering maximum with the increase in area fraction spherulites. Both effects are due to the increasing radii of the spherulites. The intensity increase is also due to the increasing total area of spherulites.

In Figures III-14 and III-15 the H_v scattering patterns at $\mu = 45°$ for 57.5% and 100% growth, respectively, are compared to the patterns of systems of nontruncated spherulites with the same total spherulite area and the same angle of maximum intensity. The effect of truncation is to lower the intensity of the scattering maximum and increase the intensity

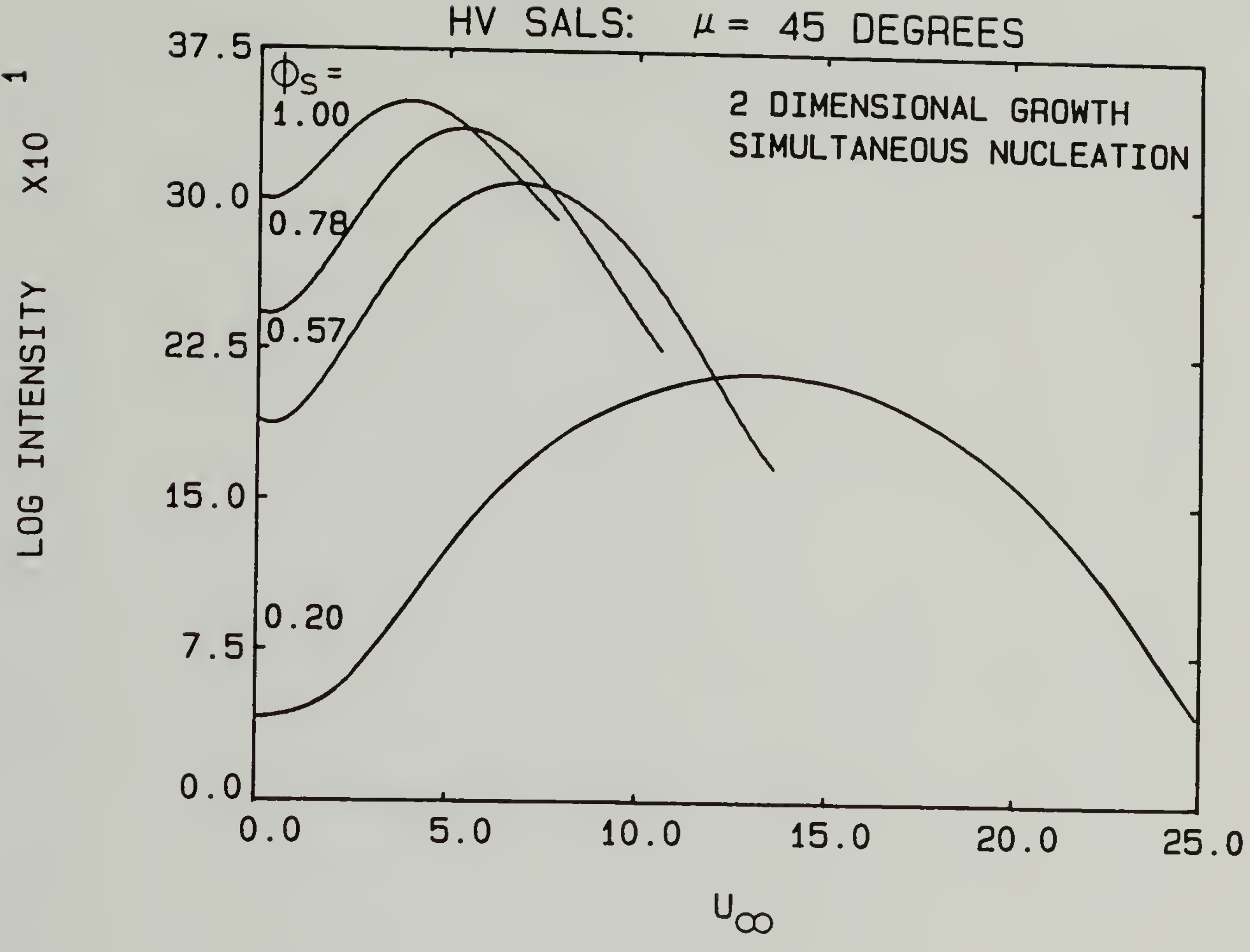

Fig. III-13 H_v SALS profiles at $\mu = 45°$, for the two dimensional spherulitic system generated following simultaneous nucleation of 150 nuclei, at various area fractions of spherulites (ϕ_s). $U_\infty = (4\pi/\lambda)\,\overline{R}_\infty \cdot \sin\theta/2$, where $\overline{R}_\infty$ is the average spherulite radius when $\phi_s = 1$. Arbitrary intensity units.

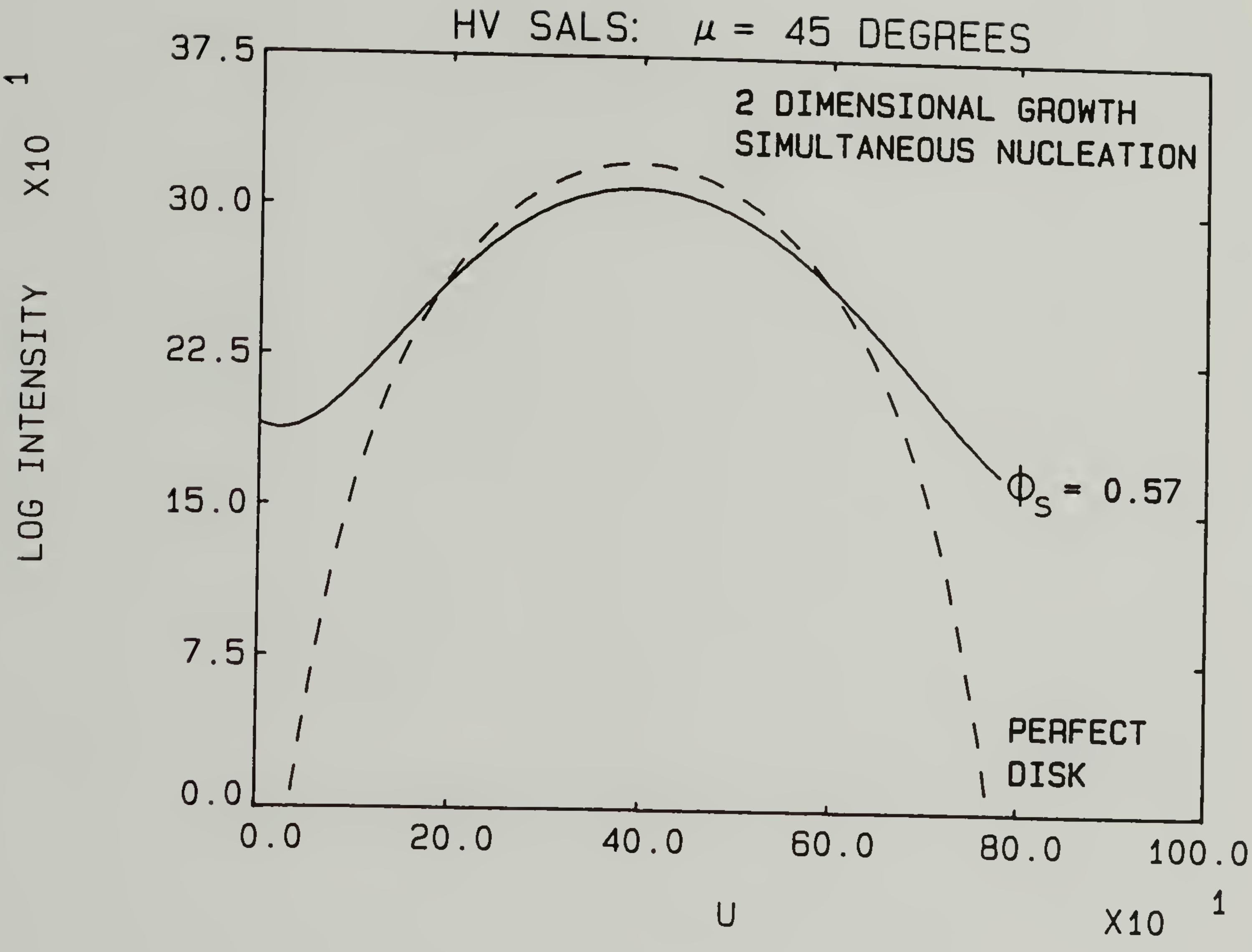

Fig. III-14 H_v SALS profiles at $\mu = 45°$, for the two dimensional spherulitic system generated following simultaneous nucleation of 150 nuclei grown to area fraction = 0.57 and for the equivalent perfect, nontruncated disk system. Arbitrary intensity units.

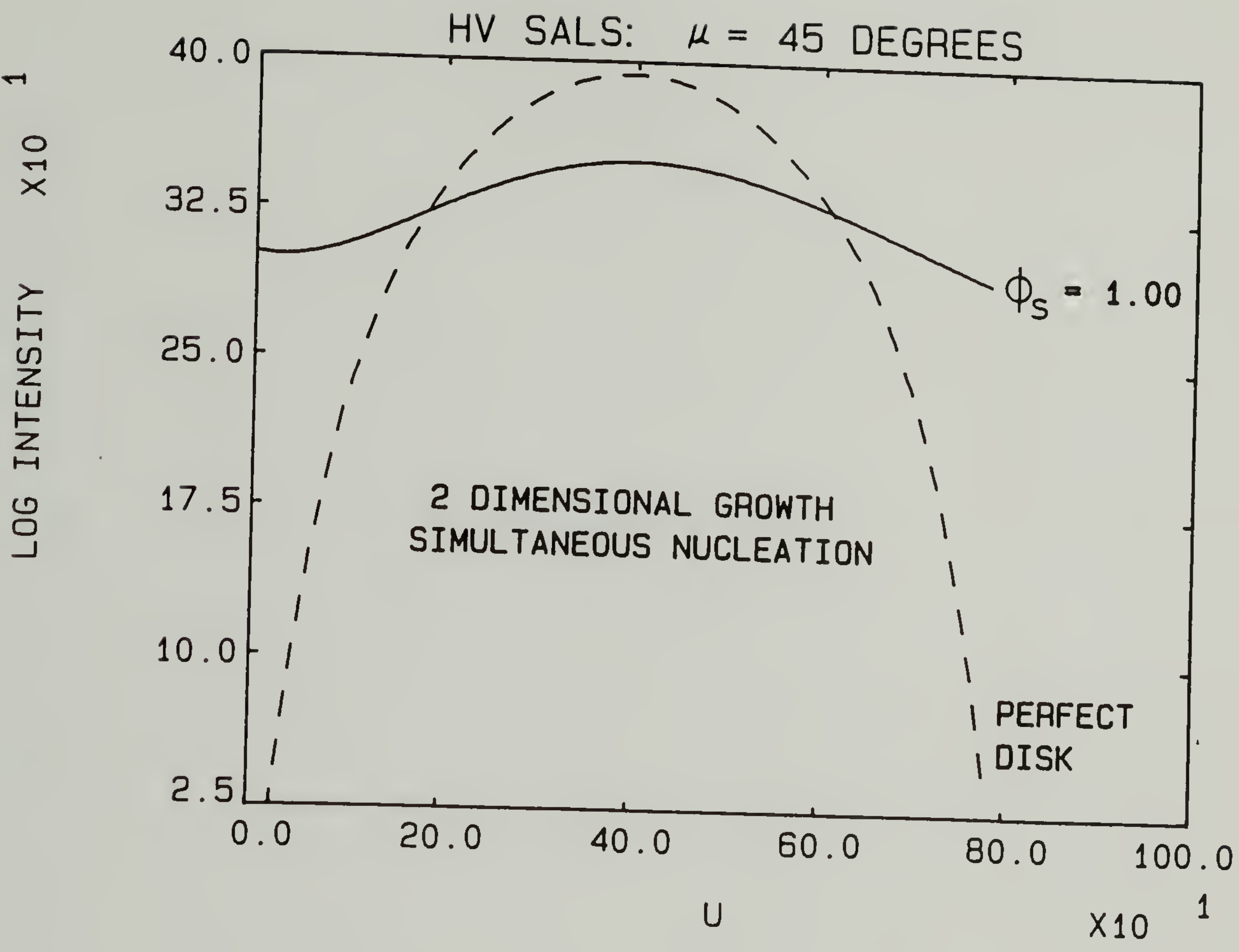

Fig. III-15 H_v SALS profiles at μ = 45°, for the fully grown two dimensional spherulitic system generated following simultaneous nucleation of 150 nuclei and for the equivalent perfect, nontruncated disk system. Arbitrary intensity units.

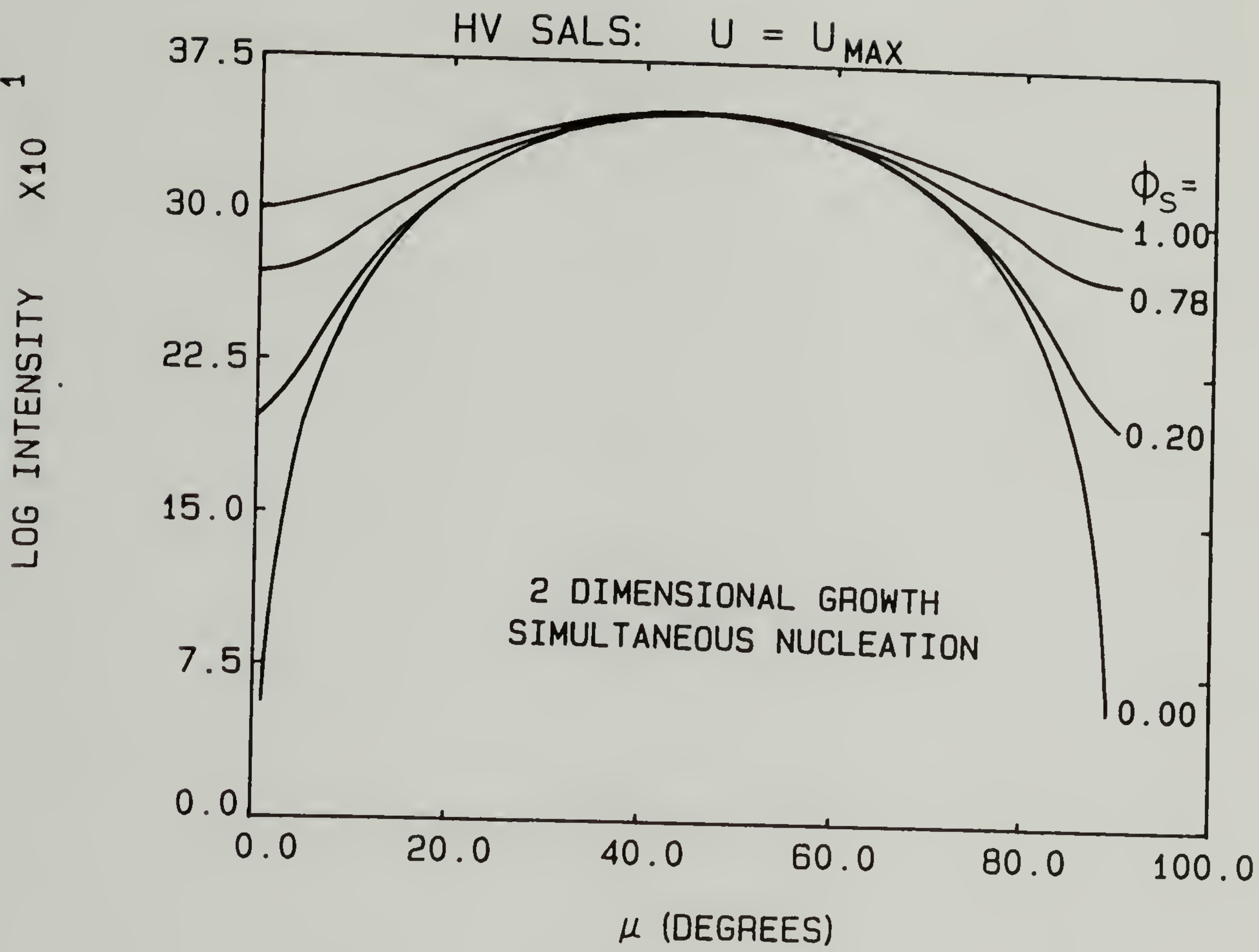

Fig. III-16 H_v SALS profiles at $U = U_{max}$, for the two dimensional spherulitic system generated following simultaneous nucleation of 150 nuclei, at various area fractions of spherulites (ϕ_s). Intensities are normalized to the same maximum value for each ϕ_s. Perfect, nontruncated spherulite represented by $\phi_s = 0.00$.

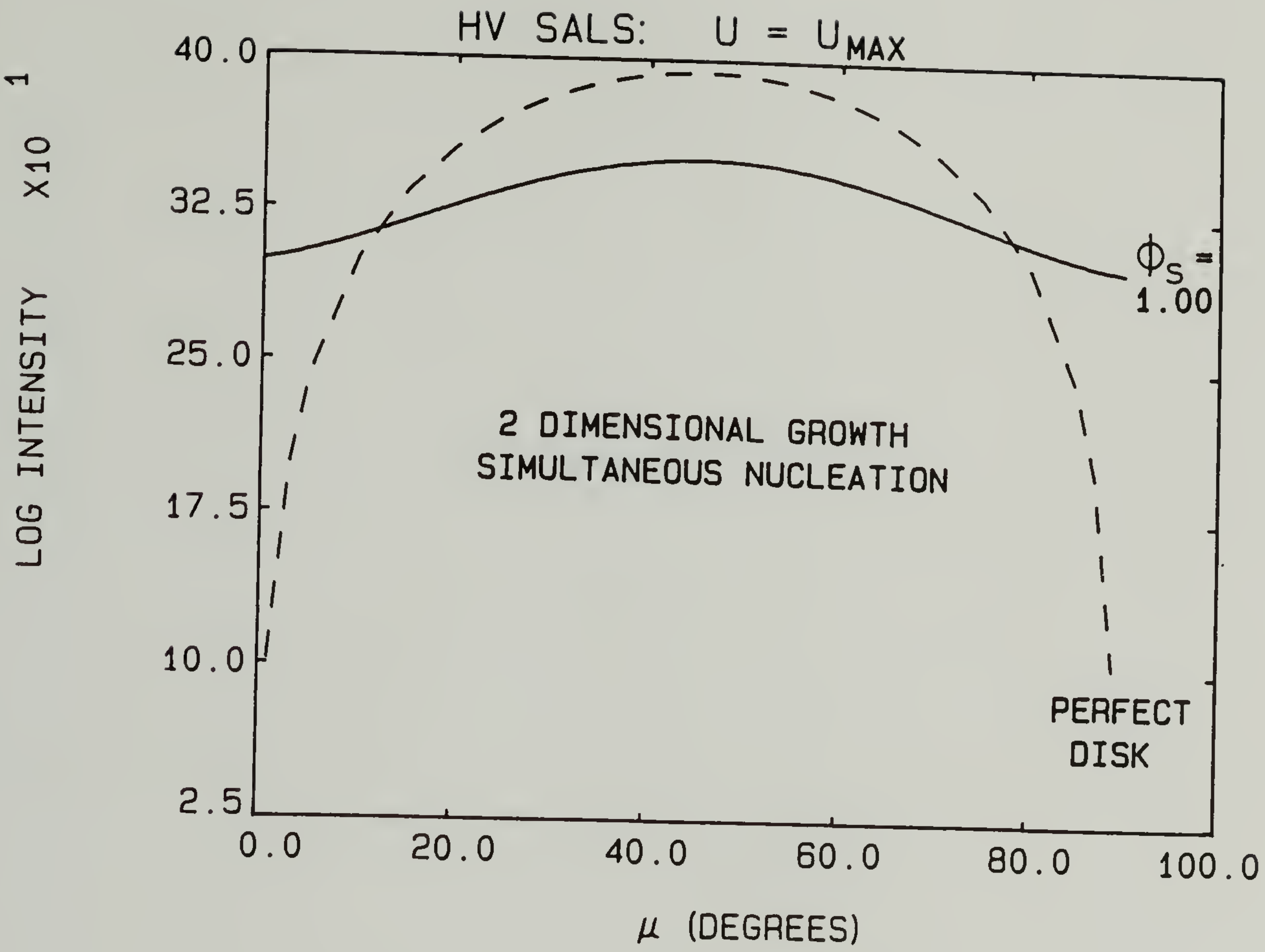

Fig. III-17 H_v SALS profiles at $U = U_{max}$, for the fully grown two dimensional spherulitic system generated following simultaneous nucleation of 150 nuclei and for the equivalent perfect, nontruncated disk system. Arbitrary intensity units.

at small and large angles. The scattering peak is made more diffuse, compared to nontruncated spherulites, as the area fraction increases. At very early stages of growth the patterns from the truncated and nontruncated spherulites become identical due to the lack of impingement.

Similarly, one can compare the H_v SALS profile as a function of the azimuthal angle where $U = U_{max}$. Figure III-16 plots the H_v intensity profiles, for two dimensional spherulites following simultaneous nucleation, for various stages of growth. To emphasize the broadening effect the truncation has on the scattering peak, each profile has been normalized to give the same maximum intensity. The profile labelled "$\phi_s = 0.00$" represents the scattering from a perfect disk-like spherulite. The broadening of the pattern due to truncation is apparent; it increases with the area fraction of spherulites.

Figure III-17 plots the H_v scattering profiles, as a function of azimuthal angle with $U = U_{max}$, for a simultaneously nucleated, fully grown, truncated system and the equivalent nontruncated spherulites. An equivalent nontruncated system has the same total spherulite area and the same polar scattering angle of maximum intensity as the truncated system. The scattering peak is lowered and broadened due to the truncation. Similar changes occur in the H_v patterns for two dimensional growth following sporadic nucleation.

By comparing the scattering profiles of truncated and equivalent nontruncated systems, one can calculate the effects on the H_v SALS patterns due to truncation. Figure III-18 plots the ratio of the H_v

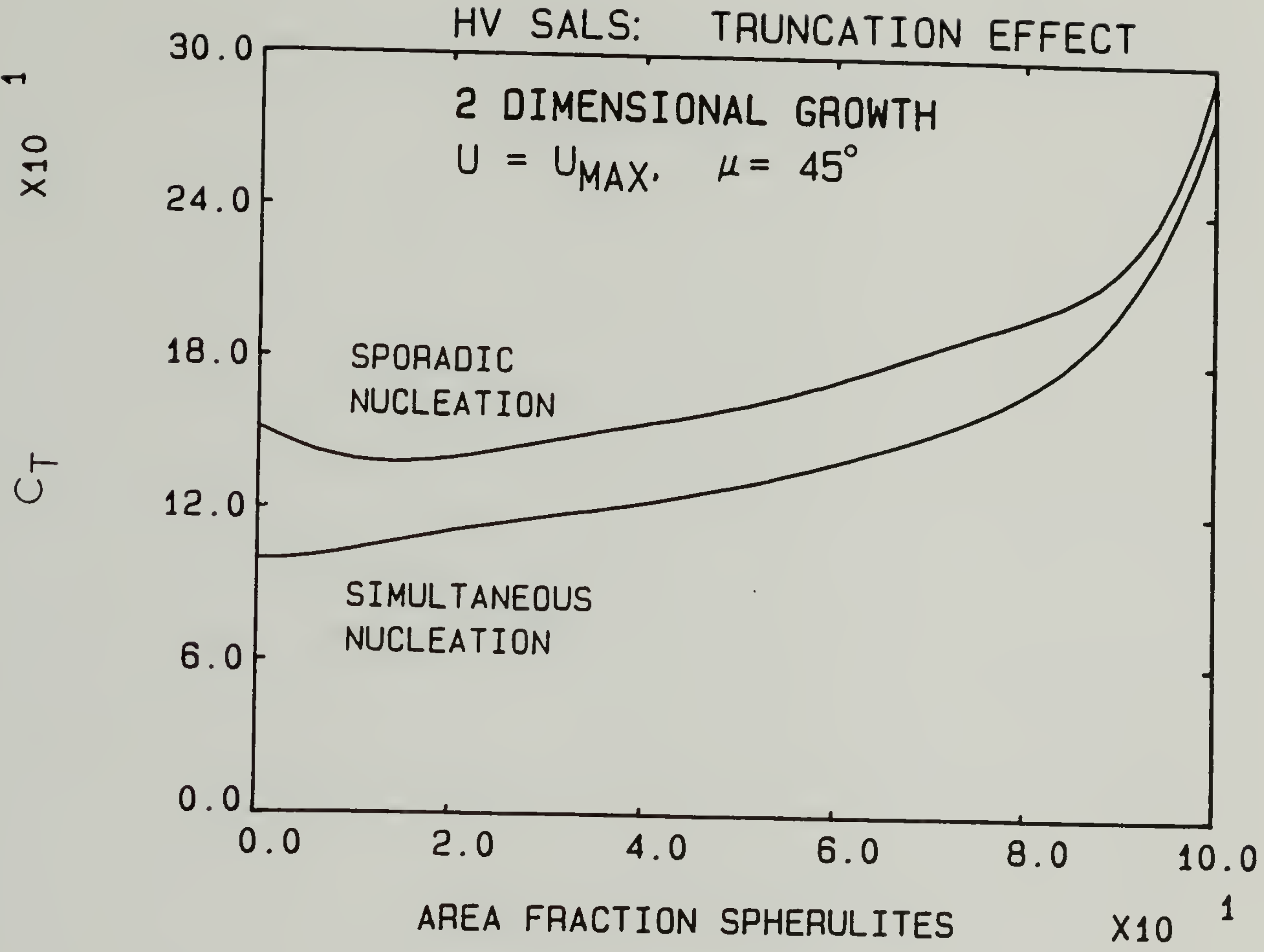

Fig. III-18 Truncation correction factors for two dimensional spherulites, simultaneous and sporadic nucleation, as functions of the area fraction of spherulites.

intensity for a nontruncated system to that for a truncated system, at $U = U_{max}$ and $\mu = 45°$, as functions of the area fraction of spherulites. The curves in Figure III-18 were calculated for simultaneously and sporadically nucleated two dimensional spherulites. This ratio will be referred to as C_T: the correction due to truncation of the H_v intensity at the maximum. In order to correct an experimental SALS pattern for the effects of truncation, one must multiply $R_{H_v}(U_{max},45)$ from the experiment by the appropriate values of C_T from Figure III-18.

A discussion of a method for combining the effects of truncation and internal disorder on the H_v SALS patterns is presented in Chapter V. In that method, the broadening effects due to truncation are added to those due to internal disorder. The resultant scattering profiles are examined by determining the ratios of the intensity at $\mu = 45°$ to the intensities at several other values of μ, all at $U = U_{max}$. Figures III-19 and III-20 plot these intensity ratios for undisordered, two dimensional spherulites, for simultaneous and sporadic nucleation, respectively, as functions of the area fraction of spherulites. These results can be combined with similar results for disordered, nontruncated spherulites. (Polynomial equations are given in the Appendix for the curves in Figures III-18, III-19, III-20 and several other analytical plots in this dissertation.)

Previous studies [18,29,34,37,38] have calculated the effects of truncation, internal disorder and multiple scattering in terms of the H_v intensity at $\mu = 45°$ and $U = U_{max}$, $2U_{max}$ and $3U_{max}$. Changes in the H_v intensity profiles in the U direction due to these effects are much more

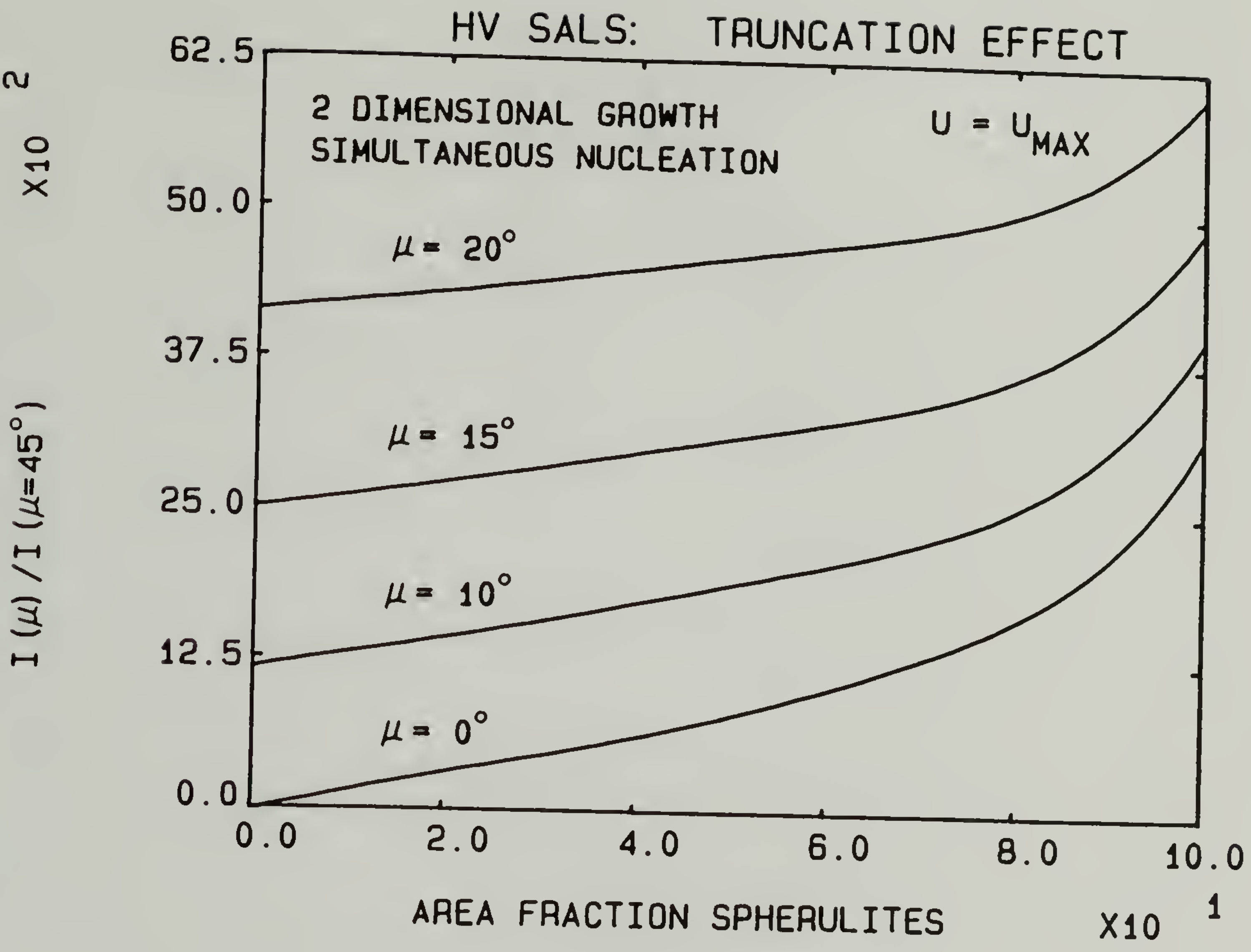

Fig. III-19 Ratios of H_v intensities for μ = 45° to that for several other values of μ, at $U = U_{max}$, for two dimensional, simultaneously nucleated spherulites, as functions of the area fraction of spherulites.

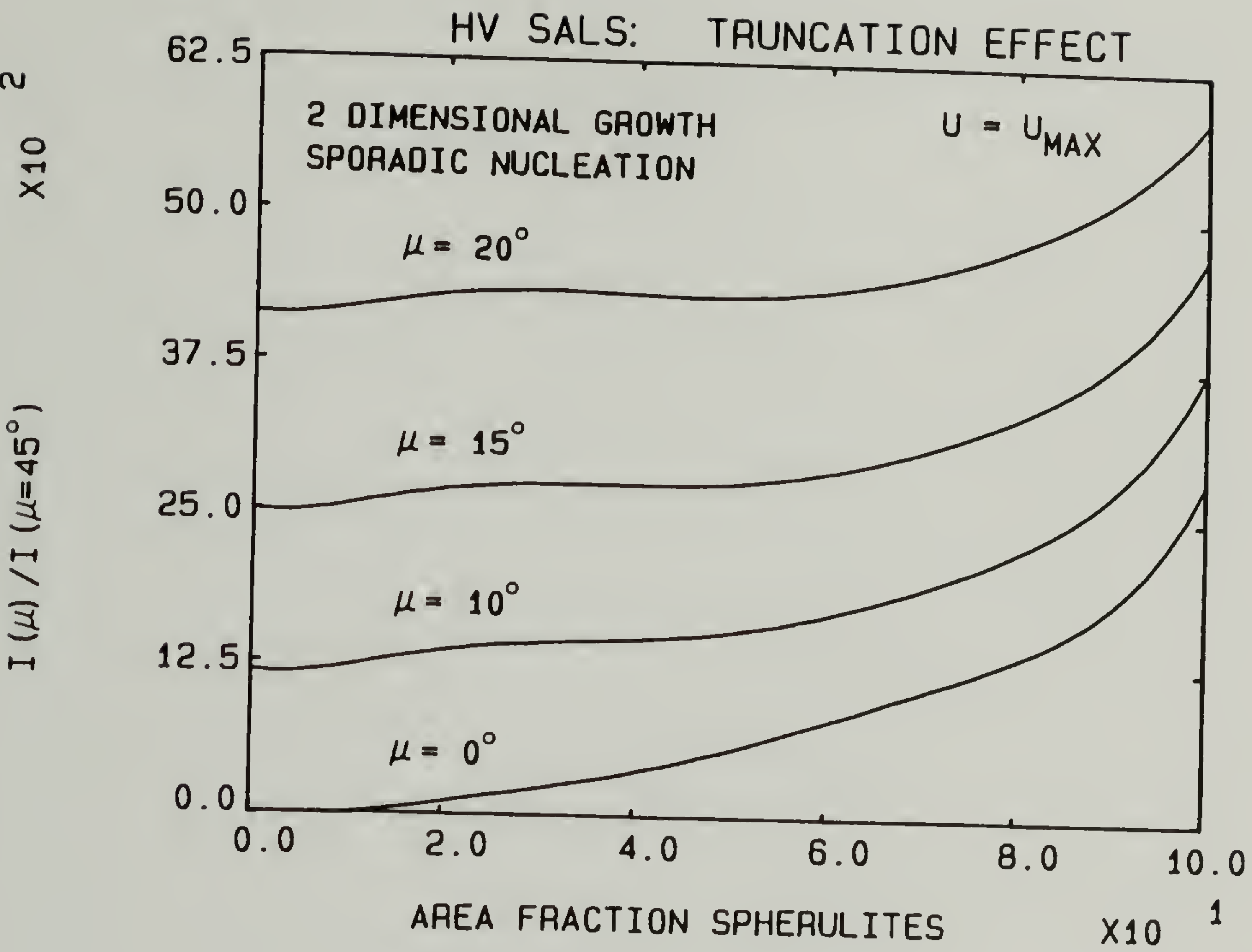

Fig. III-20 Ratios of H_v intensities for $\mu = 45°$ to that for several other values of μ, at $U = U_{max}$, for two dimensional, sporadically nucleated spherulites, as functions of the area fraction of spherulites.

difficult to describe than those in the μ direction. The deviations from the model spherulite tend to eliminate the high order maxima and minima. In fact, $U = 2U_{max}$ is very near the first minimum, so that a small change in internal disorder of any type increases the intensity there by orders of magnitude. Prud'homme [18] needed to assume a gaussian distribution of spherulite sizes as the nondisordered case to eliminate this problem. This procedure immediately eliminates the higher order maxima.

It appears that the azimuthal profiles are more well behaved and can be analyzed in a more general fashion. It has been shown that the azimuthal dependence can be factored out of the integration for calculating H_v intensities from a distribution of spherulite sizes [23]. Therefore one does not need to be restricted to a gaussian or other fixed distribution of spherulite sizes when using azimuthal profiles since a distribution of sizes does not affect the shape of the azimuthal profile. It was found that the intensity changes at $U = 2U_{max}$ and $U = 3U_{max}$ are not useful to describe the effects of truncation because of the elimination of the higher order maxima and minima by even a small amount of size disorder (size distribution or truncation). It is highly recommended that azimuthal profiles be utilized in quantitative SALS studies. The instrumentation described in Chapter IV greatly facilitates such analysis.

In Figure III-18 it can be seen that the correction factor for the truncation of two dimensional, simultaneously nucleated spherulites approaches unity for early stages of growth since there is little

truncation. This correction factor increases continuously from 1.0 for zero growth to 2.8 for 100% growth. The value of 2.8 for 100% growth is in good agreement with the correction value proposed by Prud'homme et al. [29] for these values of truncation parameters. Prud'homme et al. [29,41] evaluated the intensity correction at $U = U_{max}$ and $\mu = 45^{\circ}$ to be 1.39. However, they have also shifted the angle of maximum intensity by a factor of 1.3 to account for the apparent size effect of truncation. When one adjusts their correction factor for angle shift and the dependency of R_{H_v} on spherulite size, their correction factor becomes 2.4 in the terminology of this study, which is reasonable agreement. Further comment will be made later about the location of the scattering maximum and its relation to the size of truncated spherulites.

The correction factor for the truncation of two dimensional, sporadically nucleated spherulites does not approach unity for zero growth in Figure III-18. For sporadic nucleation and early stages of growth, there is little or no truncation but there is a distribution of spherulite sizes. It is this distribution of spherulite sizes which causes the H_v scattering peak to be lower at the early stages of growth than the model equations would predict. C_T for fully grown, two dimensional, sporadically nucleated spherulites equals 3.0.

It can be seen from equation (II-1) that the H_v intensity from model spherulites is proportional to $\sin^2\mu \cos^2\mu$. For model spherulites then, the ratios of the H_v intensity at $\mu = 45^{\circ}$ to that at other values of μ, for $U = U_{max}$, equals $4 \sin^2\mu \cos^2\mu$. Figure III-19 shows that, for two dimensional, simultaneously nucleated spherulites, the intensity ratios

approach 4 $\sin^2\mu \cos^2\mu$ for zero growth, indicating little truncation effects for the early stages of growth.

In Figure III-20, the intensity ratios for two dimensional, sporadically nucleated spherulites also approach 4 $\sin^2\mu \cos^2\mu$ for zero growth. Since C_T for sporadic nucleation does not approach unity at zero growth, it is apparent that the azimuthal profile is lowered, but not broadened at early growth for sporadic nucleation. These effects are due to the distribution of spherulite sizes resulting from sporadic nucleation, even in the absence of significant spherulite truncation. These spherulite size distribution effects are not seen for simultaneous nucleation at low growth. The intensity ratios at full growth are similar for simultaneous and sporadic nucleation.

The correction factors are plotted as functions of area fraction of spherulites. Since area fraction (or volume fraction) is not readily ascertainable from light scattering patterns, calibration curves (Figure III-21) of area fraction as functions of the movement of the scattering maximum during spherulitic growth have been established. The curves are given for both simultaneous and sporadic nucleation. The area fraction spherulites can therefore be calculated from the measured values of the polar angle of maximum intensity. One can then correct the experimental H_v intensity for truncation by knowing the type of nucleation and the polar scattering angle of maximum intensity (θ_{max}). The type of nucleation must be established by other means since the features of H_v SALS cannot distinguish nucleation types.

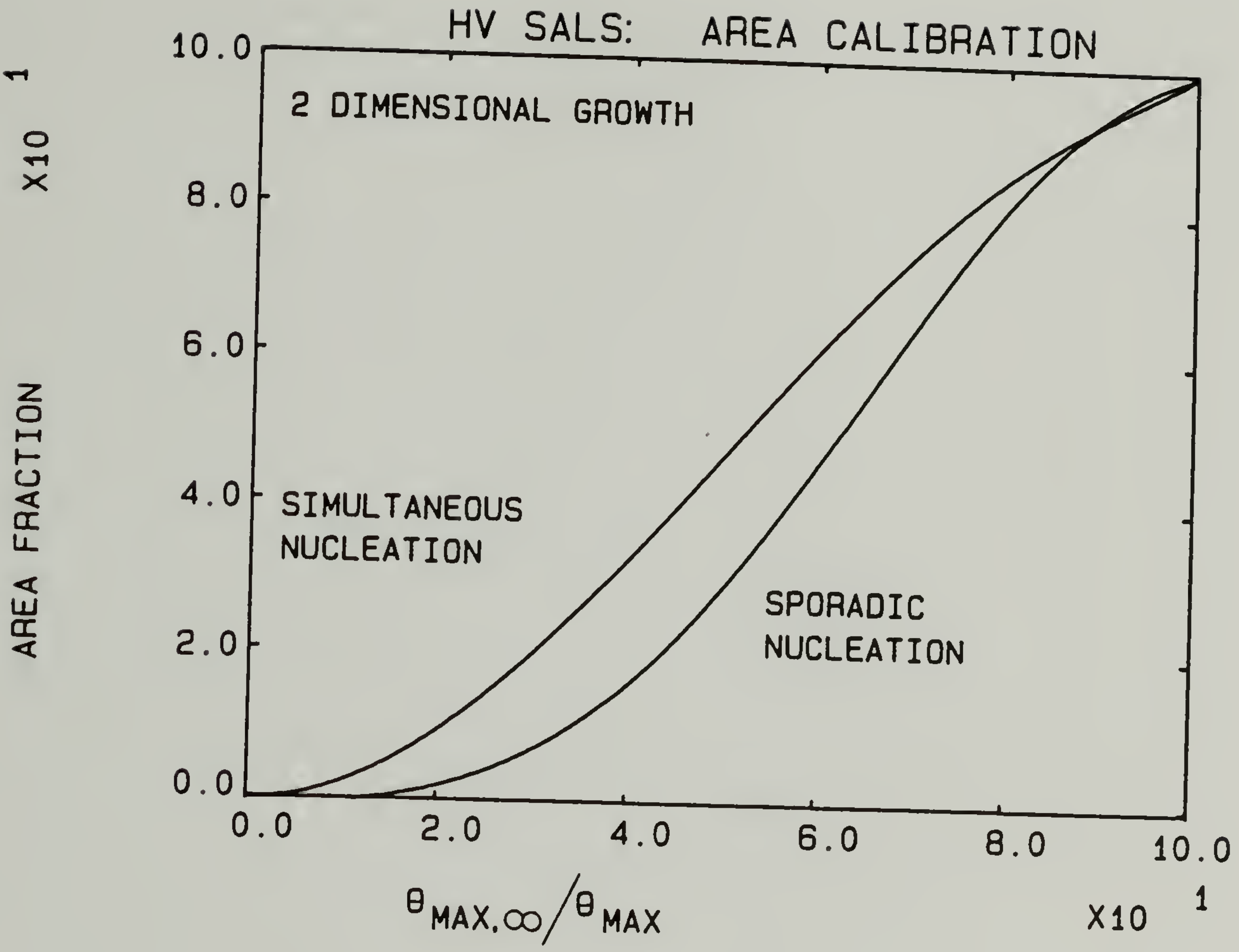

Fig. III-21 Calibration curve of the area fractions of spherulites as functions of the ratio of the polar angle of maximum intensity for full growth to the angle of maximum intensity for a particular stage of growth. Two dimensional spherulites, simultaneous and sporadic nucleation.

Calculated intensities: three dimensional spherulites. The H_v intensity calculations for three dimensional spherulites grown following simultaneous nucleation show effects similar to those from two dimensional growth: lowering of the H_v maximum intensity and broadening of the scattering peak with increasing volume fraction of spherulites. Figure III-22 plots the truncation correction factor, C_T, for three dimensional, simultaneously nucleated spherulites. C_T is the ratio of the H_v intensity for perfect spherical spherulites to that for truncated spherulites, at $U = U_{max}$ and $\mu = 45°$. An equivalent nontruncated system has the same total spherulite volume and the same polar scattering angle of maximum intensity as the truncated system. It is interesting to note that this correction factor has a maximum value of 2.2, in contrast to the value of 2.8 for simultaneous nucleation and two dimensional growth. It seems clear that the truncation of a disk which is perpendicular to the line of sight of an observer would be more noticeable than similar truncation of a sphere. Similarly the effects of truncation are greater for two dimensional spherulites than those of three dimensions. Again, for reasons similar to those given in the discussion of truncated two dimensional spherulites, it is recommended that azimuthal profiles be utilized when using such correction factors.

Figure III-23 is a plot similar to Figures III-19 and III-20. Figure III-23 plots the ratios of the H_v intensity at $\mu = 45°$ to that for other values of μ, at $U = U_{max}$, as functions of the volume fraction of spherulites. The intensity ratios approach $4 \sin^2\mu \cos^2\mu$ for early stages of growth, similar to the two dimensional spherulites. Figure

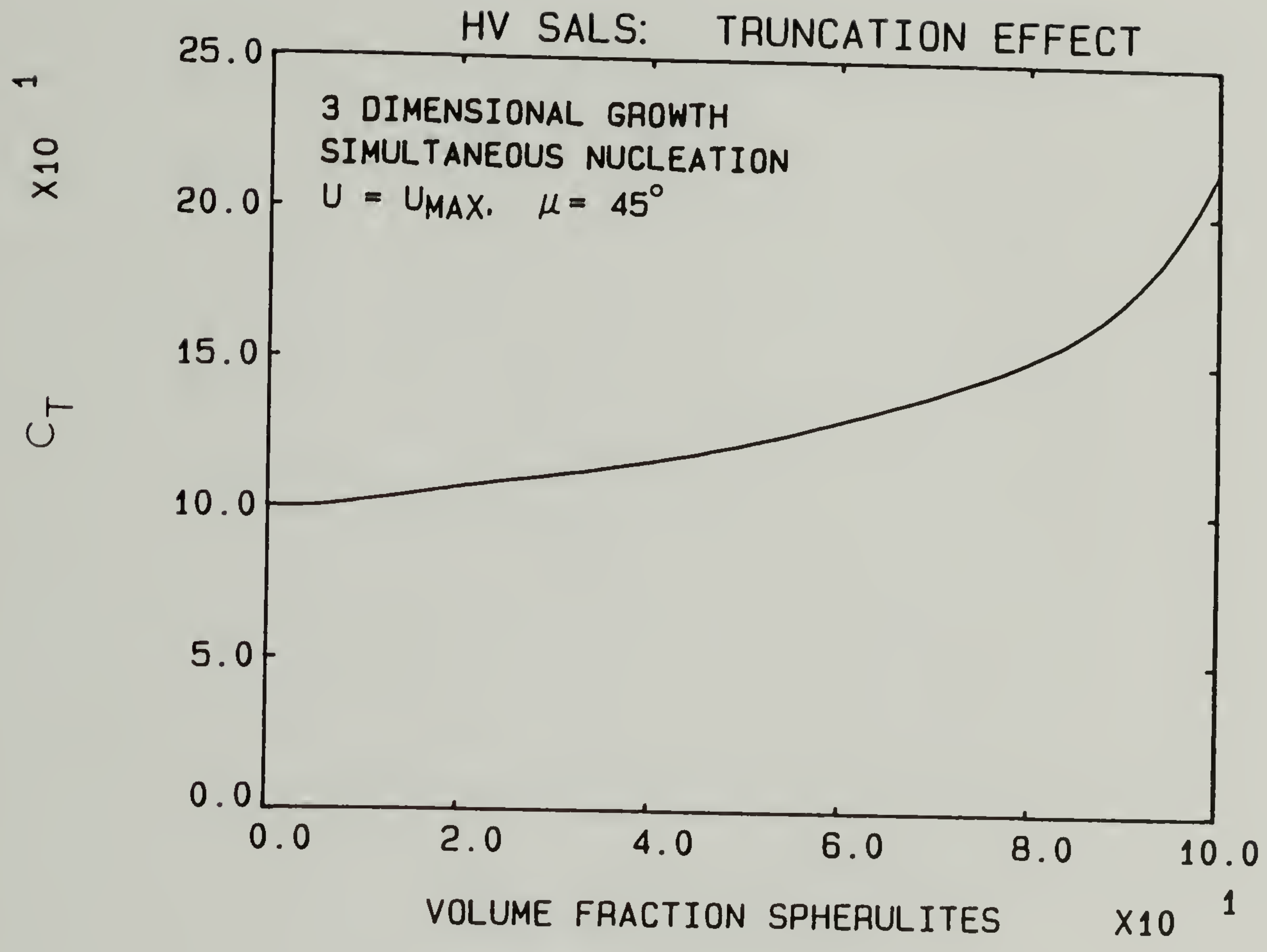

Fig. III-22 Truncation correction factor for three dimensional spherulites, simultaneous nucleation, as a function of the volume fraction of spherulites.

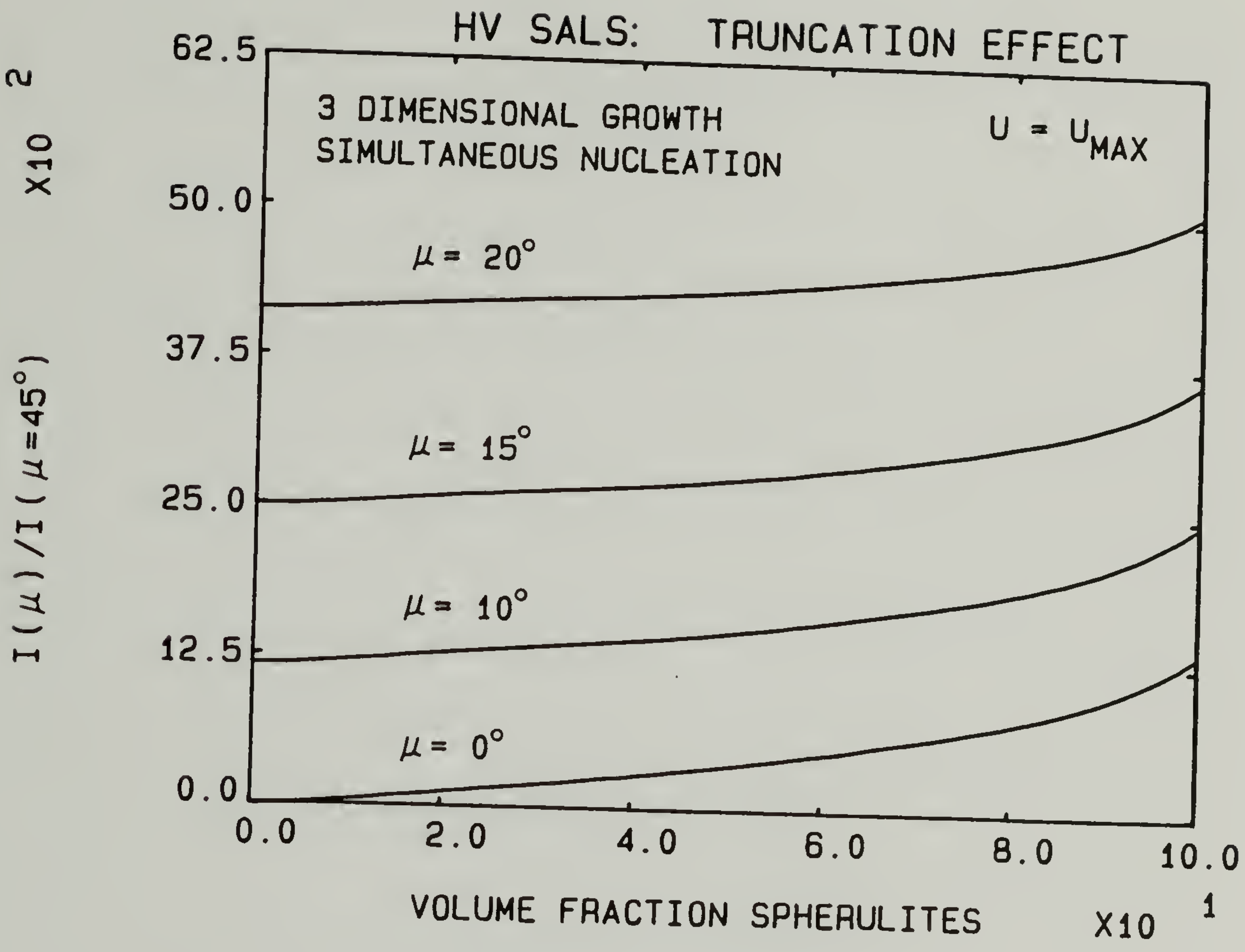

Fig. III-23 Ratios of the H_v intensities for μ = 45° to that for several other values of μ, at $\bar{U} = U_{max}$, for three dimensional spherulites, simultaneous nucleation, as functions of the volume fraction of spherulites.

III-23 was calculated for three dimensional, simultaneously nucleated spherulites and will be used in Chapter V to combine the effects of truncation and internal disorder on the H_V intensity profile.

Figure III-24 is a calibration plot similar to Figure III-21. Figure III-24 plots the volume fraction of spherulites as a function of the movement of the scattering maximum for three dimensional spherulites following simultaneous nucleation. One can use Figure III-24 along with the experimentally measured polar angle of maximum intensity to determine the volume fraction spherulites in a sample.

<u>Area, volume and radius measurements</u>. The spherulitic growths were examined according to the Avrami type analysis [55,56]. The Avrami analysis for spherulitic growth states that

$$1 - \phi_s = \exp(-kt^n) \tag{III-16}$$

where

ϕ_s = area or volume fraction spherulites

k = growth rate constant

t = time of growth

n = exponent characterizing the type of nucleation and growth.

Avrami analysis of the computer simulated growth has been used to determine the values of n listed in Table III-1.

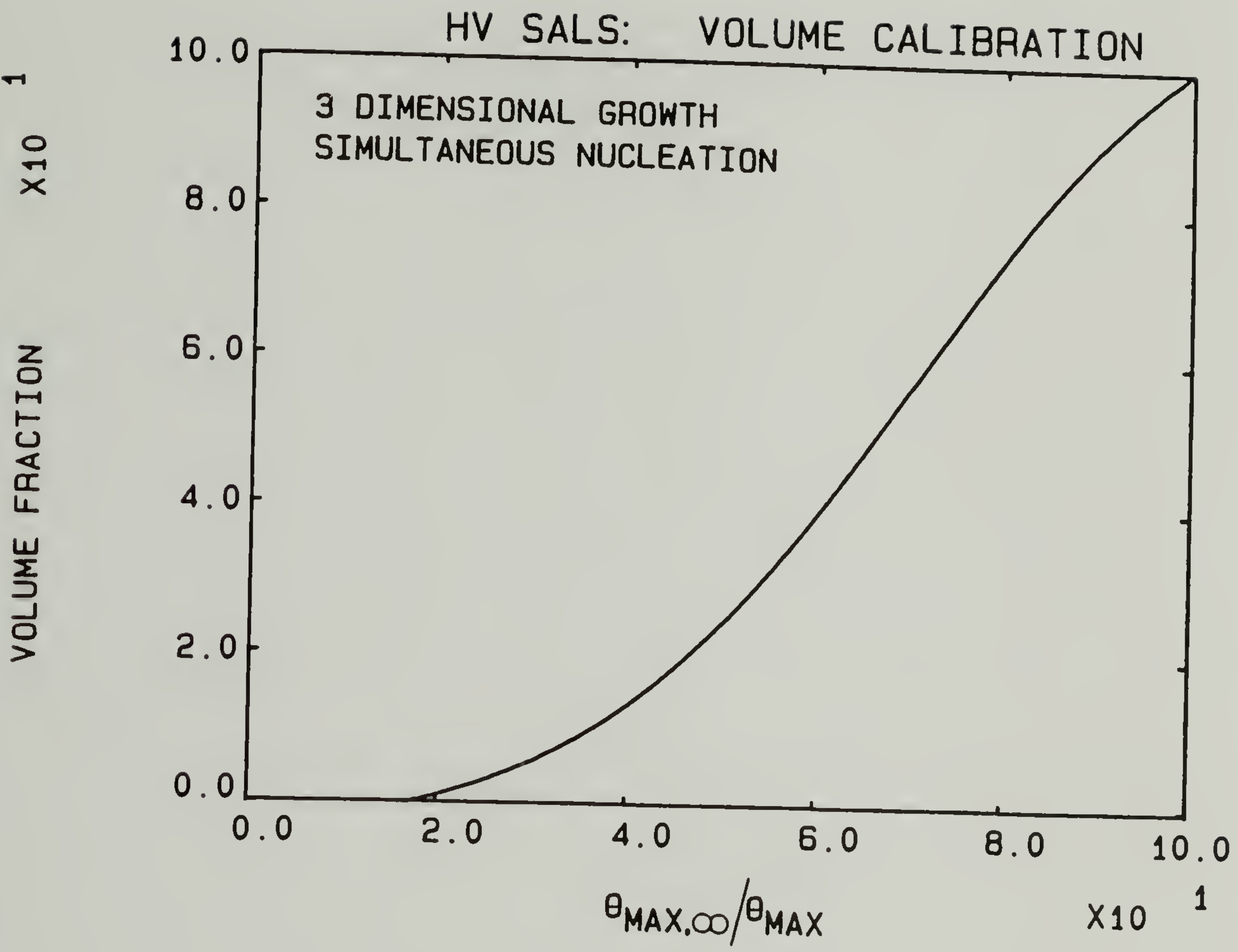

Fig. III-24 Calibration curve of the volume fraction of spherulites as a function of the ratio of the polar angle of maximum intensity for full growth to the angle of maximum intensity for a particular stage of growth. Three dimensional spherulites, simultaneous nucleation.

Table III-1

Avrami Analysis of Computer Simulated Spherulite Growth

Growth Dimensions	Nucleation	Calculated	Avrami Predicted
two dimensional	simultaneous	1.98	2
two dimensional	sporadic	2.94	3
three dimensional	simultaneous	3.02	3

The agreement between the values of n from the computer simulated spherulite growths and the Avrami analysis is excellent.

It was pointed out in Chapter II that, according to the perfect spherulite models, the average radius ($\bar{R}_n$) of a set of spherulites can be determined by H_v SALS from the equation [2]:

$$U_{max} = \frac{4\pi\bar{R}_n}{\lambda} \sin \frac{\theta_{max}}{2} \tag{III-17}$$

where $U_{max} = 3.9$ for two dimensional spherulites [11] and $U_{max} = 4.1$ for three dimensional spherulites [17]. For truncated spherulites the definition of the average radius must be considered. An n^th order average radius can be defined for a system of spherulites as:

$$\bar{R}_n = \frac{\sum\limits_{\text{spherulites}} \sum\limits_{\text{angles}} Q^n}{\sum\limits_{\text{spherulites}} \sum\limits_{\text{angles}} Q^{n-1}} \tag{III-18}$$

where Q is the radius of a particular spherulite at specified angles. It was found that for two-dimensional spherulites, equation (III-17) applies when n is in the range 4 - 5. For three dimensional spherulites, equation (III-17) applies when n is in the range 5 - 6.

(For the three dimensional geometry given in Figure III-4, the summations must be weighted by multiplying by $\sin\alpha$.) This high order average shows the predominance of the large spherulite segments in the SALS. Keijzers found that equation (III-17) applies for a distribution of sizes of nontruncated spherulites when a high moment of the distribution is used [57]. The weighting of SALS results toward the large spherulite segments must be kept in mind when comparing spherulite sizes measured by H_v SALS to that measured by other techniques, such as optical microscopy. At complete growth, these high order averages differ from the arithmetic average by 30 - 40%.

Prud'homme et al. [29,41] chose to correct for this apparent discrepancy in spherulite size measurement by multiplying the measured θ_{max} by 1.3. The redefinition of the average spherulite size here has a similar effect.

Equations (II-1), (II-2) and (II-5) in Chapter II involve the average volume of the spherulites (V) in a spherulitic sample. From the previous discussion, it is apparent that for truncated spherulites the equation

$$V = \frac{4}{3}\pi\overline{R}_n^3 \qquad \text{(III-19)}$$

is not necessarily valid. If one assumes that the average spherulite volume is related to the average spherulite radius, measured by H_v SALS according to equation (III-17), by the relationship

$$V = K_v\overline{R}_n^3, \qquad \text{(III-20)}$$

then K_v takes on values from $4/3\pi$ (= 4.19) for no truncation to a value

of 1.97 for 100% growth of three dimensional spherulites following simultaneous nucleation. Figure III-25 plots K_v as a function of the volume fraction of the spherulites for three dimensional growth. By using this plot one can use the correct value for V in the H_v and V_v equations in Chapter II.

Similarly, Figure III-26 plots K_A as a function of area fraction where the average spherulite area is given by

$$A = K_A \overline{R}_n^2 \ . \qquad \text{(III-21)}$$

For simultaneous nucleation, K_A ranges from a value of π for no growth to 1.27 for 100% growth. For sporadic nucleation, K_A does not approach π at low growth. The effect of spherulite size distribution is again reflected here.

Conclusions

Computer simulation of spherulite growth has led to the determination of the effects of spherulitic truncation on H_v SALS as well as some geometrical characteristics of truncated spherulites. The effect of truncation is to lower the H_v intensity at the maximum and broaden the scattering peak. Multiplicative factors have been derived for correcting experimental H_v SALS data, at $U = U_{max}$ and $\mu = 45°$, for the effects of truncation. These factors have been derived for two dimensional spherulites (both simultaneous and sporadic nucleation) and three dimensional spherulites (simultaneous nucleation) as functions of the area (or volume) fraction of spherulites. It was found that the corrections are greater for two dimensional spherulites. It was also

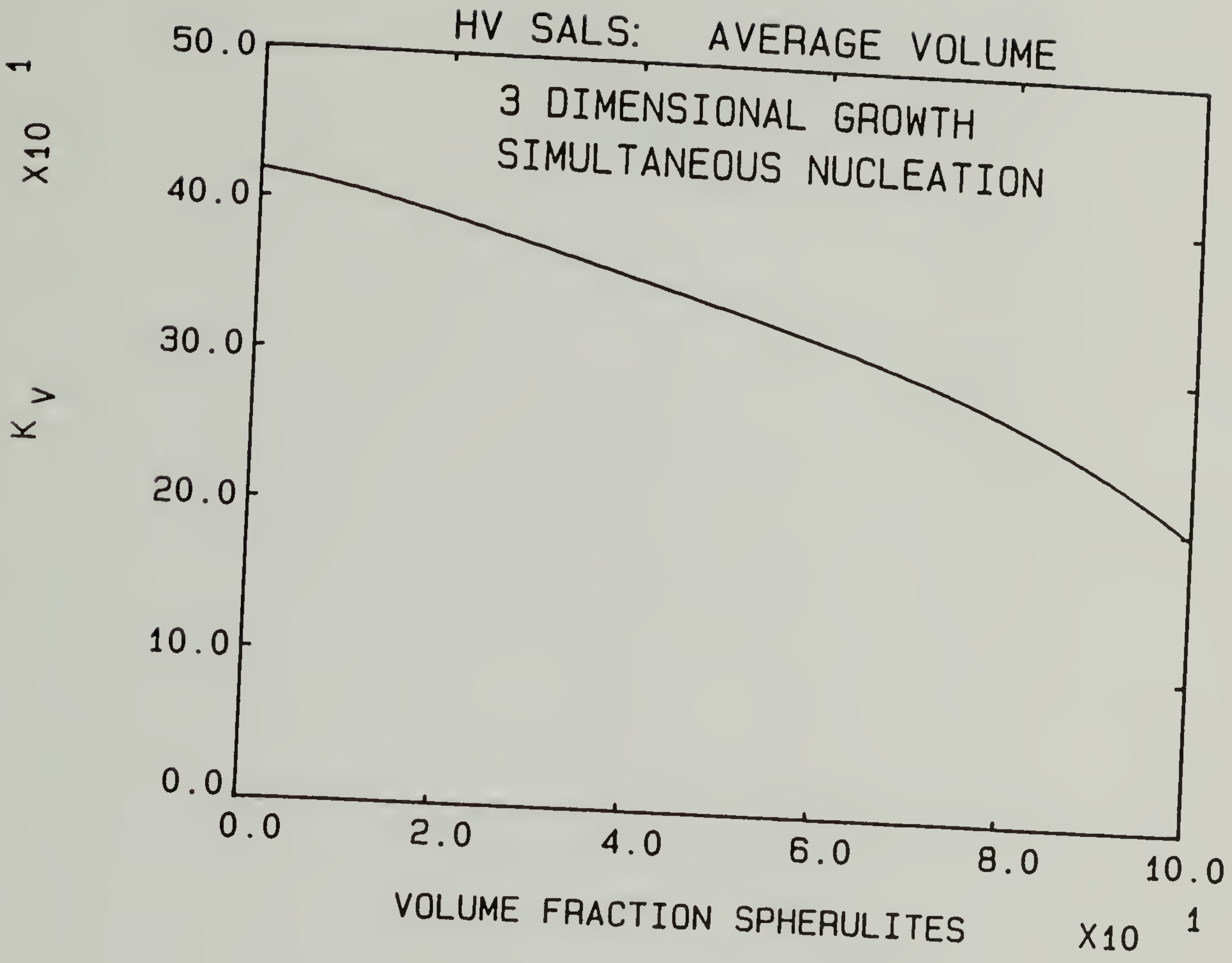

Fig. III-25 K_v as a function of the volume fraction of spherulites for three dimensional spherulites and simultaneous nucleation. Average spherulite volume $V = K_v \bar{R}_n^3$.

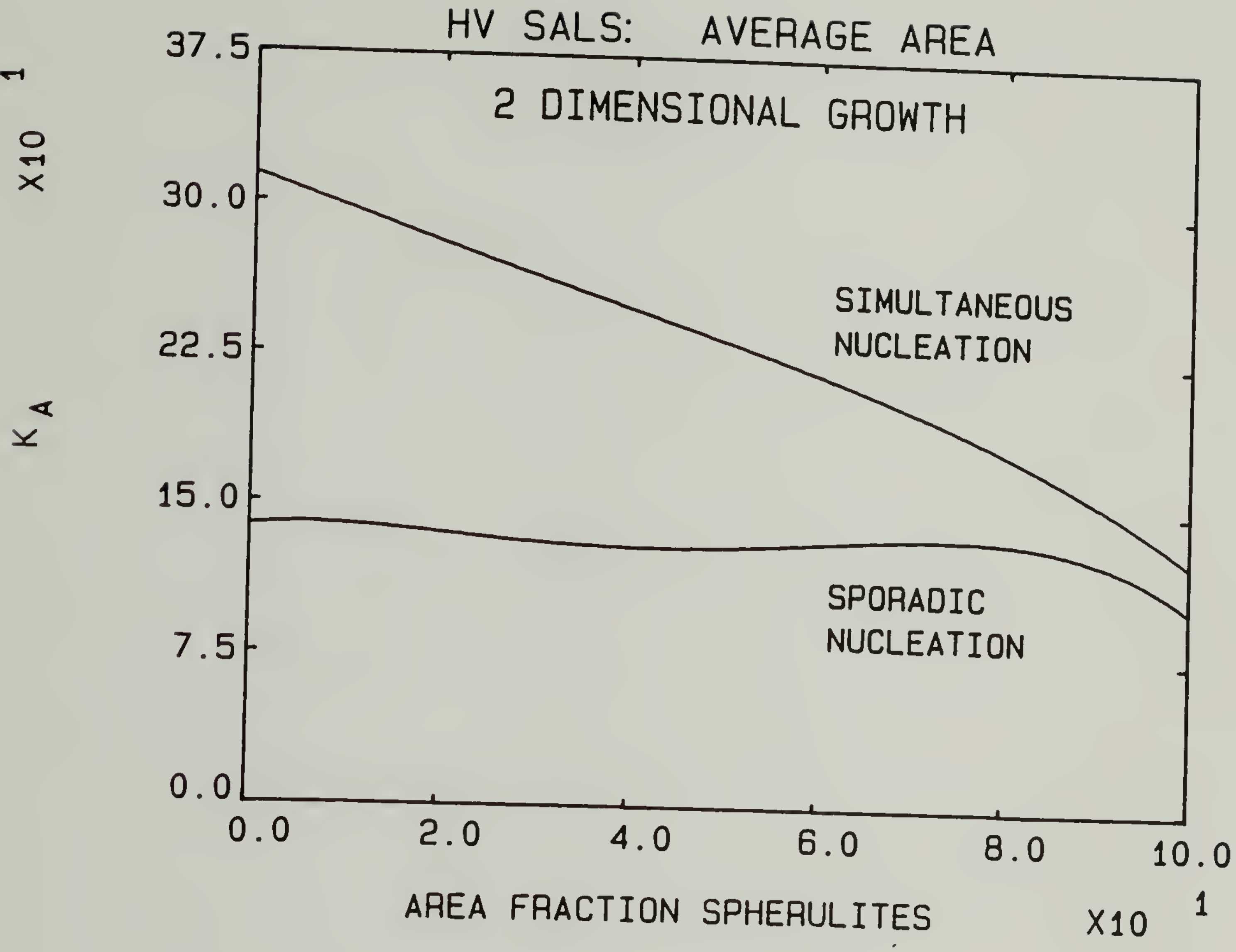

Fig. III-26 K_A as functions of the area fraction of spherulites for two dimensional spherulites and simultaneous and sporadic nucleation. Average spherulite area $A = K_A\bar{R}_n^3$.

found that spherulite size distribution effects are apparent for sporadically nucleated spherulites even at low growth.

Azimuthal H_v SALS profiles at $U = U_{max}$ have been determined for truncated spherulite systems. These profiles can be used with similar profiles for internally disordered spherulites to calculate the combined effects of truncation and disorder.

The meaning of the average radius of spherulites as measured by H_v SALS is now more well understood. The average is heavily weighted toward the large radius values. In conjunction with the meaning of the average radius, the actual average volume (or area) of the spherulites has also been defined. A method of experimental measurement of the volume (or area) fraction spherulites from the H_v SALS has been developed. Use of the H_v multiplicative factors, the azimuthal profiles, the average spherulite size, the volume (or area) fraction spherulites and the average volume (or area) are necessary for the quantitative use of the SALS equations developed for spherulitic scattering.

The computer simulation method developed is general and can be readily extended to examine several features of SALS from spherulitic polymers. A large data base and several programs have been developed. With only very minor changes to the data base or a program, one could examine: the effects of deformation on truncated spherulites, the combined effects of internal disorder and truncation, the effects on V_v and H_h SALS, or spherulitic growth under nonrandom nucleating conditions, for example. The method is also amendable to nonspherulitic

nucleation and growth studies. Copies of the programs can be obtained from the author.

CHAPTER IV

A TWO DIMENSIONAL, POSITION SENSITIVE DETECTOR FOR SMALL-ANGLE LIGHT SCATTERING

Introduction

Experimental techniques for small-angle light scattering (SALS) from solid polymer films have been improved steadily from the original photographic studies of Stein and Rhodes [2]. The use of laser light sources [58], novel light intensity measuring devices [59-62] and digital computers have improved the speed of data acquisition and permit more complete analysis of the data from SALS experiments.

Several position sensitive detector systems have been developed for x-ray scattering [63-67], including commercially available devices. Recently a one dimensional position sensitive detector (Optical Multichannel Analyzer 1 (OMA1)) was developed for SALS from polymer films [68]. This device includes a vidicon detector and a multichannel analyzer for the acquisition of position dependent intensity data. A two dimensional position sensitive detector system with improved speed of data acquisition has now been developed [69]. This chapter describes this device, its unique features, its calibration and some of its applications.

Device Description

A block diagram of the Optical Multichannel Analyzer 2 (OMA2) is

given in Figure IV-1. A 2 mw laser beam, filtered to control the intensity and polarized if desired, impinges upon a thin film polymer sample and is scattered by the film. A series of three converging lenses collects the scattered rays, sends them through an analyzer, if desired, and transmits a focused pattern of the appropriate size onto the face of the vidicon detector. The lenses are chosen to provide various polar scattering angular ranges up to 0 - 30°.

A diagram of the configuration of the lenses is given in Figure IV-2. Ray diagrams are indicated for the scattered rays and an unscattered incident beam. The lenses are numbered 1, 2, and 3, starting from the lens nearest the sample. Their focal lengths are f_1, f_2, and f_3, respectively. The location of the lenses is determined by their focal lengths.

The polar scattering angular range is selected by the choice of lens 1. Lenses 2 and 3 remain fixed. The angular range can be determined from simple geometry and Figure IV-2. A greater angular range is obtained by a smaller value of f_1. The scattered pattern is compressed in size by a ratio of 2:1 since $f_2 \approx 2f_3$. This arrangement allows a pattern which is 25 mm wide after lens 1 to be totally collected on the vidicon detector, which is 12.5 mm square. The 25 mm pattern may be viewed by insertion of a piece of paper after lens 1. The choice of the ratio of 2:1 was made as a compromise of obtaining a large pattern to be viewed visually after lens 1 and maintaining a reasonable sample to detector distance ($2f + 2f_2 + 2f_3$).

The vidicon detector and its controller (Princeton Applied Research

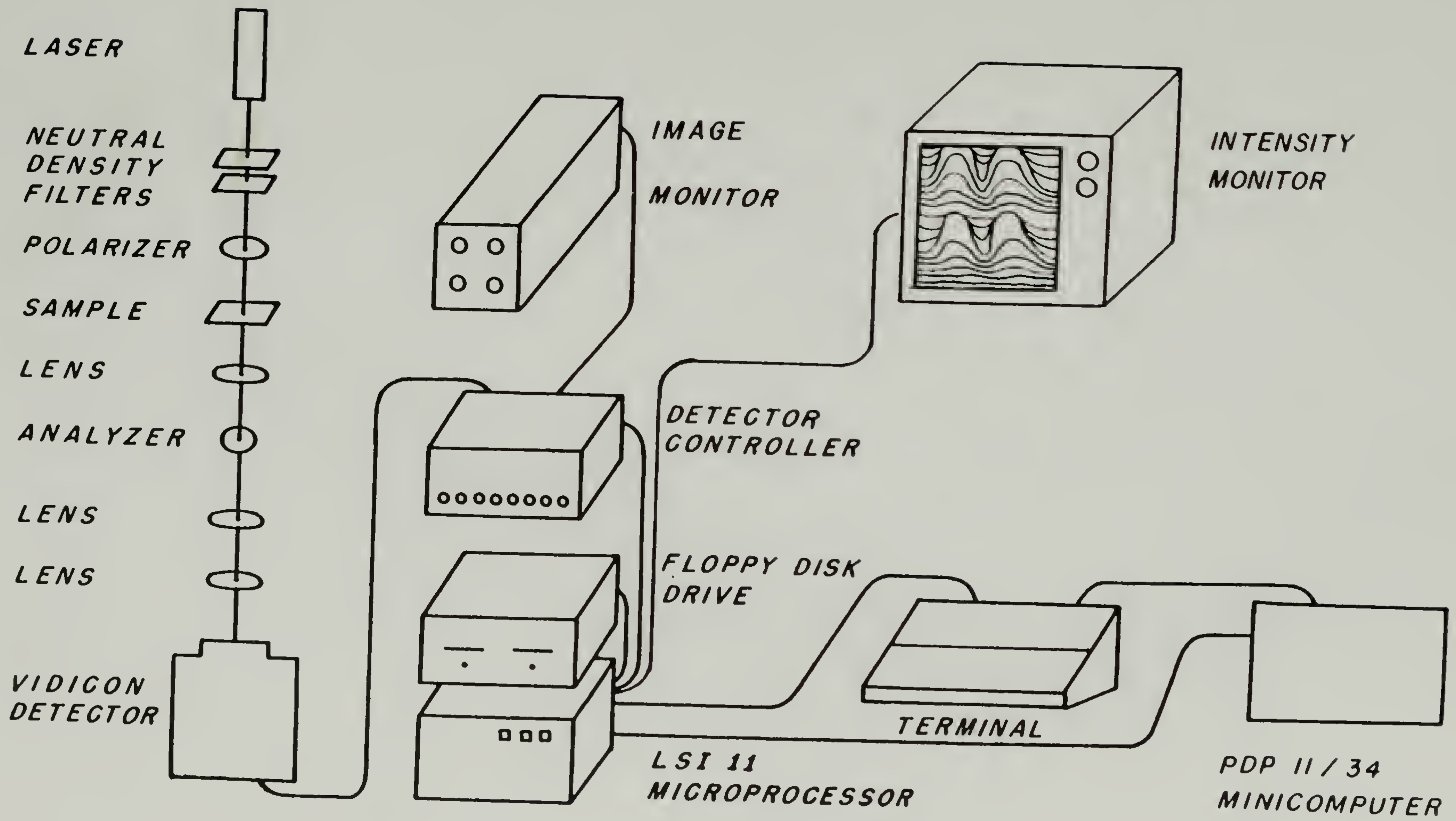

Fig. IV-1 Block diagram of the components of the Optical Multichannel Analyzer 2.

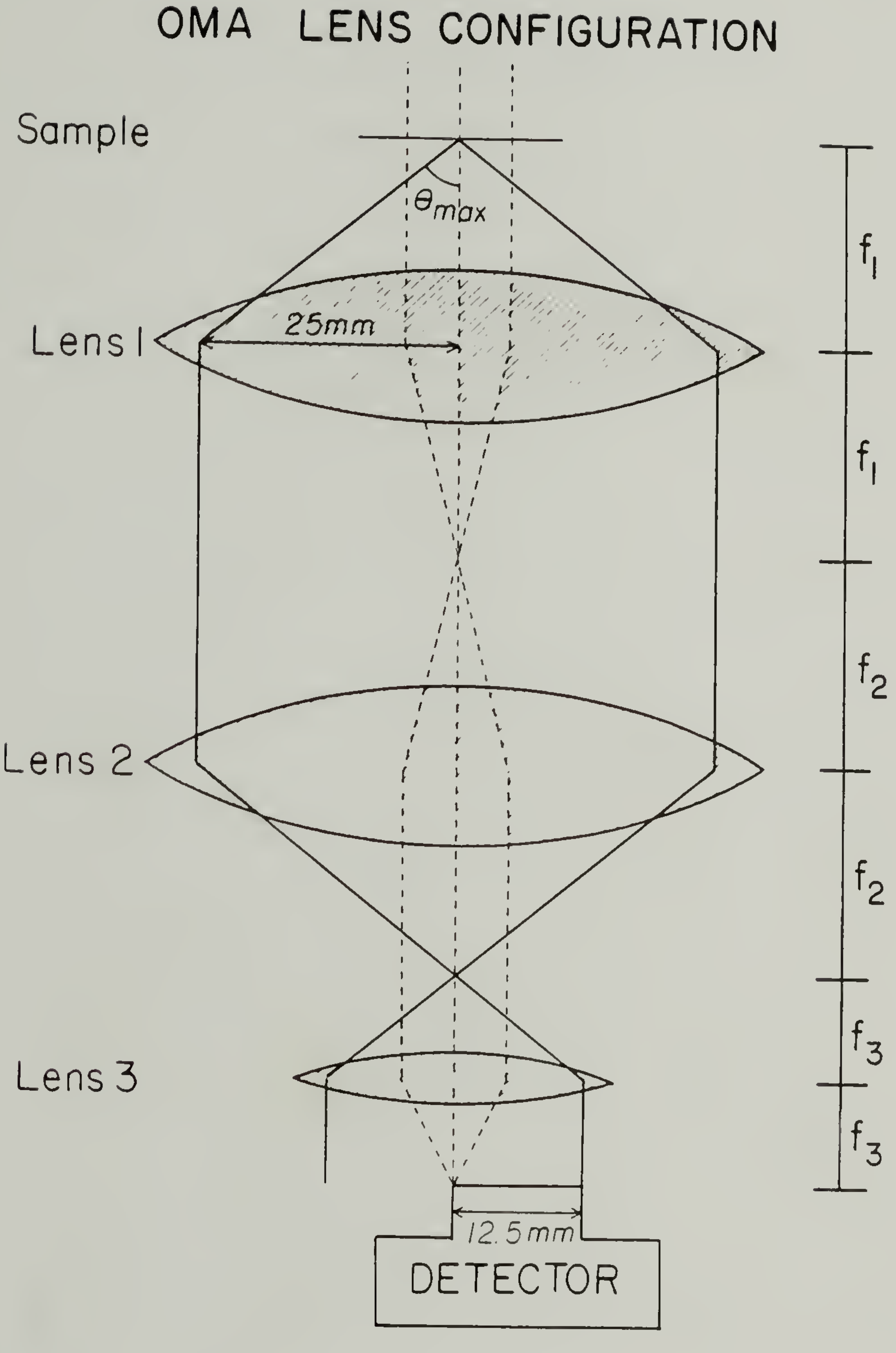

Fig. IV-2 Diagram of the lens configuration for the OMA2. Ray diagrams are indicated: solid line for a scattered ray at the largest detectable polar scattering angle (θ_{max}), dashed line for the unscattered incident ray from the laser and the lens center line.

Corp.) are capable of scanning the scattered pattern in two dimensions. The data is collected by the detector from an x-y grid of up to 500 x 500 data points and transmitted to a microprocessor (LSI 11/2, 64K byte RAM, Digital Equipment Corp., Charles River Data Systems, Inc.). The shape and time characteristics of the scans are controlled by the detector controller and the microprocessor. The data is stored on flexible disks and is analyzed using the microprocessor and a PDP 11/34 minicomputer (Digital Equipment Corp.). The image monitor displays the real time video image and the scanning operation. The intensity monitor displays a three dimensional image of intensity vs. x-y location.

This device is novel in its rapid, quantitative detection of one and two dimensional SALS patterns. The previously described [68] position sensitive detector (OMA1) measures scattered light intensities in only one dimension, at an appreciably slower rate. The OMA1 can collect and store linear scans of 500 data points at the rate of about 1 scan every 2 minutes. With the current manual timing and flexible disk storage procedures, the computer-controlled OMA2 can collect and store two dimensional scans of 2500 data points at the rate of about 1 scan every 4 seconds. Computer-controlled timing of the scans and random-access-memory data storage could improve the rate of the OMA2 to about 1 complete scan every 100 milliseconds. These rates could be further improved by taking scans of fewer data points, where the scans cover only a critical portion of the scattering pattern.

The one dimensional feature of the OMA1 limits its practical application to scans of intensities as a function of polar angle at a

constant azimuthal angle only. The two dimensional OMA2 simultaneously measures intensities as functions of both the polar and azimuthal angles. Whereas one dimensional scans are suitable for examining isotropic systems, the two dimensional detector is necessary to examine anisotropic systems. The scan parameters of the OMA2 can be adjusted to convert the OMA2 into a one dimensional detector, if desired. The measured intensities, from one or two dimensional scans of the OMA2, can be converted to absolute intensities (Rayleigh factors).

Device Calibration

The OMA2 is calibrated for each operating condition with respect to scattering angles, detector sensitivity and absolute intensity. Polar scattering angle θ calibration is obtained by recording the SALS diffraction pattern from a line grating. The detector x-y grid location of $\theta = 0$ is determined from the 0^{th} order diffraction intensity maximum. The x-y location of the first order intensity maximum is also determined. Simple geometry is then used to calibrate the x-y grid in terms of θ. The azimuthal angle is also calculated from geometry and some assignment of $\mu = 0$ based on sample and/or polarizer orientation.

The system is calibrated for sensitivity and absolute intensity by the use of a calibrated opal glass diffuser. This procedure uses the sensitivity calibration procedures used for the OMA1 by Russell et al. [70] without necessitating the involved angular calculations presented in their technique. The procedure presented here determines the

sensitivity calibration and the absolute intensity calibration with one standard. It does not require the secondary intensity calibration required by the technique of Prud'homme et al [18,41].

The sensitivity of the system for the detection of light intensity at any x-y grid location is affected by lens optics, lens reflection, air scatter, detector sensitivity, etc. The actual scattered intensity from the diffuser is compared to its known scattering behavior in order to calibrate the system for all of these effects for any particular system geometry. The scattered intensity from the diffuser should be that of a Lambertian diffuser [71]

$$I_g(\theta) = I_g(0)\cos\theta \qquad \text{(IV-1)}$$

where $I_g(\theta)$ is the intensity scattered by the diffuser glass at angle θ and $I_g(0)$ is the scattered intensity when $\theta = 0$. Equation (IV-1) was verified by measuring $I_g(\theta)$ on a photometric device.

Calibration of the system for absolute intensity is made by first calibrating the glass diffuser for absolute intensity. Absolute light scattering intensity for a material is given by the Rayleigh factor $R(\theta)$ [36]:

$$R(\theta) = \frac{I(\theta)\ r^2}{I_o V_o} \qquad \text{(IV-2)}$$

where $I(\theta)$ is the scattered intensity at angle θ, r is the distance from the sample to the detector, I_o is the total incident intensity and V_o is the volume of the scattering material. $R(\theta)$ is a material only

dependent value. V_o can be replaced by $A_o t$ where A_o is the illuminated area of the sample and t is its thickness.

Combination of equation (IV-2) for the glass diffuser with equation (IV-1) yields

$$t_g R_g(\theta) = \frac{I_g(0) r^2 \cos\theta}{I_o A_g} \tag{IV-3}$$

where the subscript g refers to the glass diffuser. Equation (IV-3) can be rewritten as

$$t_g R_g(\theta) = t_g R_g(0) \cos\theta \tag{IV-4}$$

where

$$t_g R_g(0) = \frac{I_g(0) r^2}{I_o A_g} \quad . \tag{IV-5}$$

$t_g R_g(0)$ was determined by measuring the parameters on the right side of equation (IV-5) using the OMA2 without lenses. (The factors in the term $t_g R_g(0)$ were never separated.)

The value of $t_g R_g(0)$ is then used along with the intensity scan of the glass diffuser to calibrate the intensity data from a sample scan $(I_s(\theta))$ for absolute intensity while also correcting for sensitivity. Rewriting equation (IV-2) for a sample

$$R_s(\theta) = \frac{I_s(\theta) r^{2'}}{I_o' t_s A_o'} \tag{IV-6}$$

and for the glass diffuser for the same system geometry

$$R_g(\theta) = \frac{I_g(\theta) r^{2'}}{I_o' t_g A_o'} \tag{IV-7}$$

where the s subscript refers to the sample and the primed values refer to the OMA2 geometry. Combination of equations (IV-4), (IV-6) and (IV-7) leads to

$$R_s(\theta) = \frac{I_s(\theta) t_g R_g(0) \cos\theta}{I_g(\theta) t_s} \qquad \text{(IV-8)}$$

which gives the absolute scattered intensity of the sample in terms of two easily obtained intensity data sets and three known parameters. Equation (IV-8) is included in the OMA2 analysis software, which makes acquisition of absolute intensity data from the OMA2 a simple and straightforward procedure. There is no need to measure the values of I_o, t_g or A_o on the OMA2 system once the glass diffuser is calibrated. Indeed, the definition of r in the lens system of the OMA2 may be unclear.

Device Applications

Rapid detection of one and two dimensional SALS intensity patterns is the principal advantage of the OMA2 over previous devices. The intensities are analyzed as a function of the polar and azimuthal scattering angles. A sample three dimensional perspective plot of H_v scattered intensity from a spherulitic polyethylene terephthalate (PET) thin film is shown in Figure IV-3. A contour plot of the same data is presented in Figure IV-4. (The contours in each of the contour plots in this chapter occur at linear intervals.) A contour plot of a V_v pattern from the same sample is shown in Figure IV-5.

The OMA2 can be utilized for studies of changing polymer morphology.

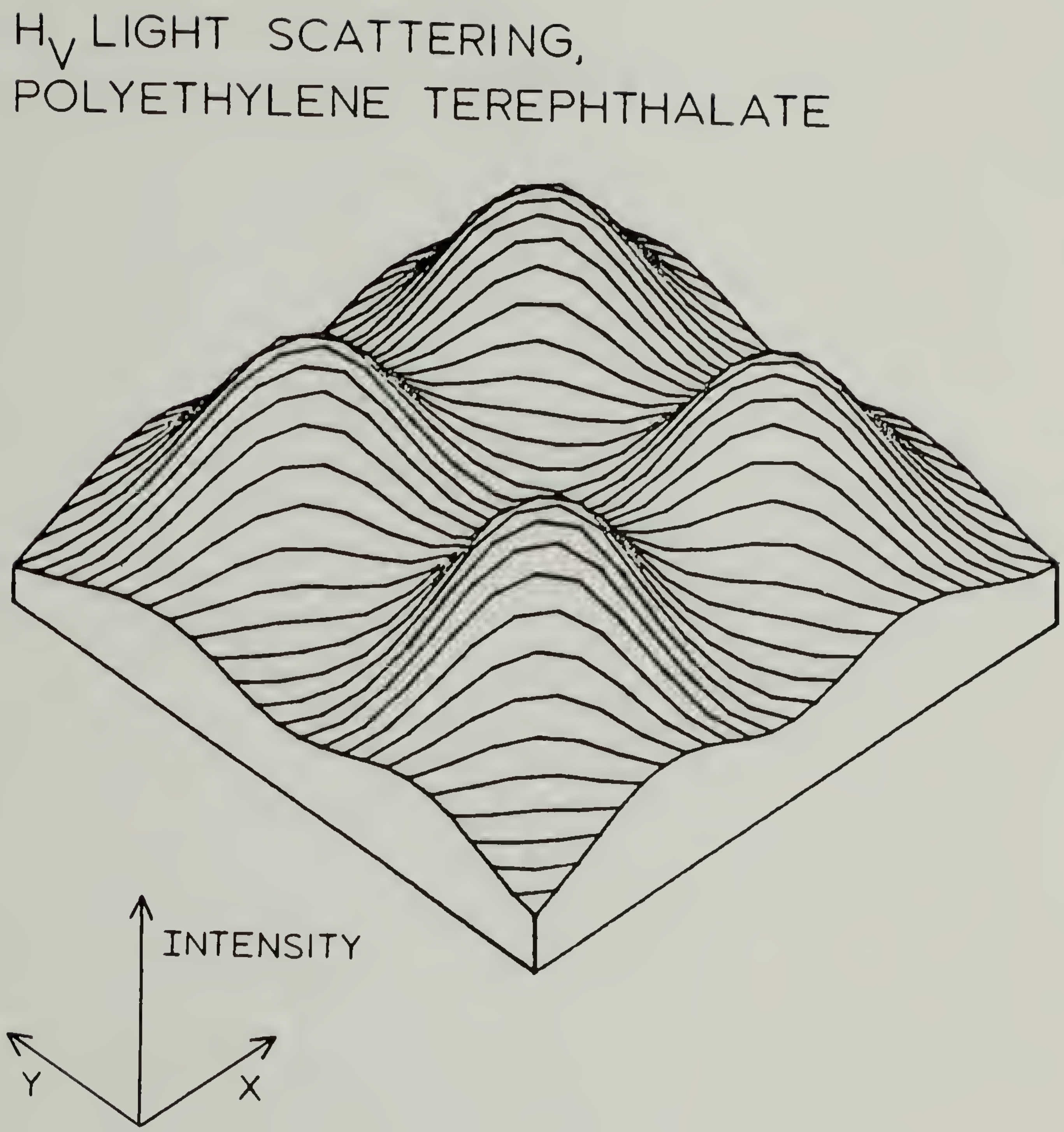

Fig. IV-3 Sample three dimensional perspective plot of an H_V scattering pattern from PET.

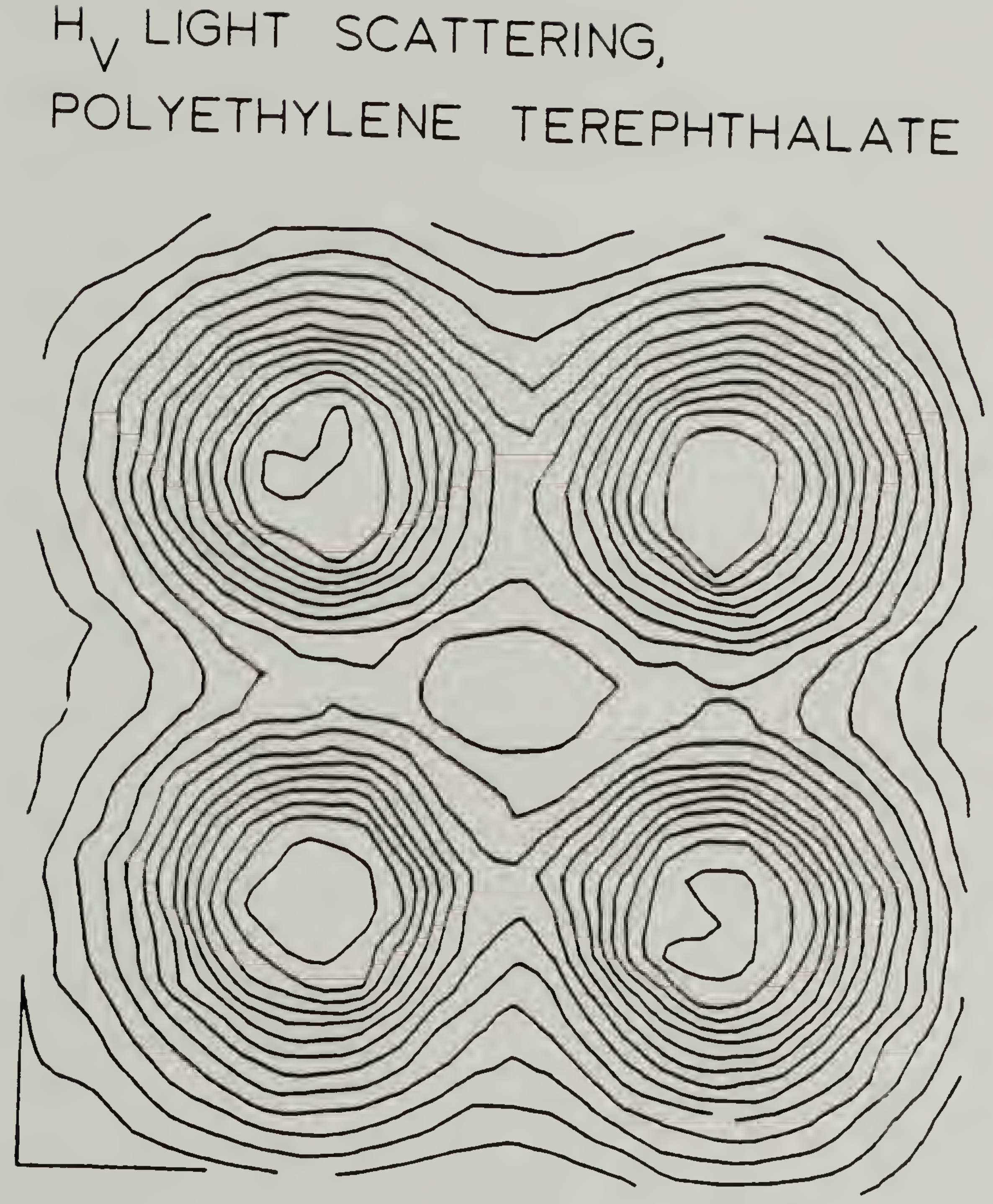

Fig. IV-4 Sample isointensity contour plot of the same pattern as in Figure IV-3.

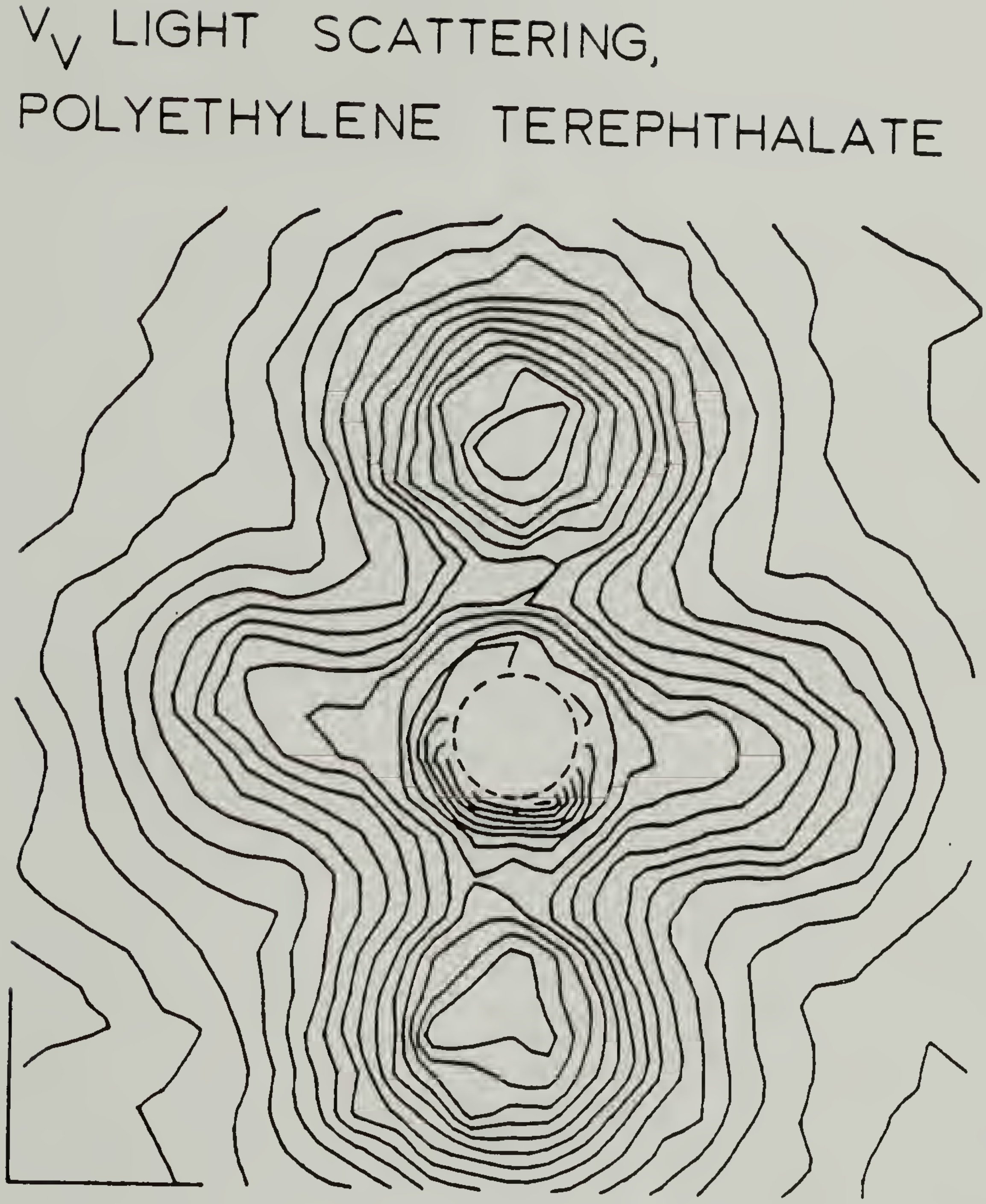

V_V LIGHT SCATTERING, POLYETHYLENE TEREPHTHALATE

Fig. IV-5 Sample isointensity contour plot of a V_v scattering pattern from the same sample as in Figure IV-3. (The main beam has been suppressed inside the dashed circle.)

Four quadrant light scattering patterns, such as Figure IV-3, are redundant in that each of the four quadrants provides the same information. Such light scattering data can be quadrant averaged to produce one quadrant of information with improved signal-to-noise (S/N) ratios. Figure IV-6 demonstrates the use of quadrant averaged intensity distributions for monitoring polymer crystallization. The single quadrant averaged H_V SALS contour pattern in Figure IV-6 is from a PET film crystallized from the glassy state for 5 minutes at 130°C. Intensity profiles at constant polar scattering angle or at constant azimuthal angle can be obtained from intensity data sets as represented in Figure IV-6.

The easy acquisition of azimuthal profiles using the OMA2 is a significant development over the earlier devices. Chapter V (PET melting) and Chapter VI (PET crystallization) make extensive use of OMA2 data and the constant angle profiles. Theoretical descriptions of this type of data are given in Chapter II and Chapter III. Details of the interpretation of such OMA2 data from unoriented spherulitic polymer samples can be found in those four chapters.

The two dimensional capabilities of this device make it suitable for the monitoring of polymer deformation morphology. Anisotropic polymer morphology leads to anisotropic light scattering patterns readily detectable by the OMA2. Figures IV-7 and IV-8 represent single quadrant averaged H_V SALS scattering patterns from low density polyethylene (LDPE), undeformed and elongated 60%, respectively. In Chapter VII, similar data and plots from deformed LDPE and polypropylene are

Fig. IV-6 Single quadrant averaged H_V SALS isointensity contour plot for PET crystallized from the glass for 5 minutes at 130°C.

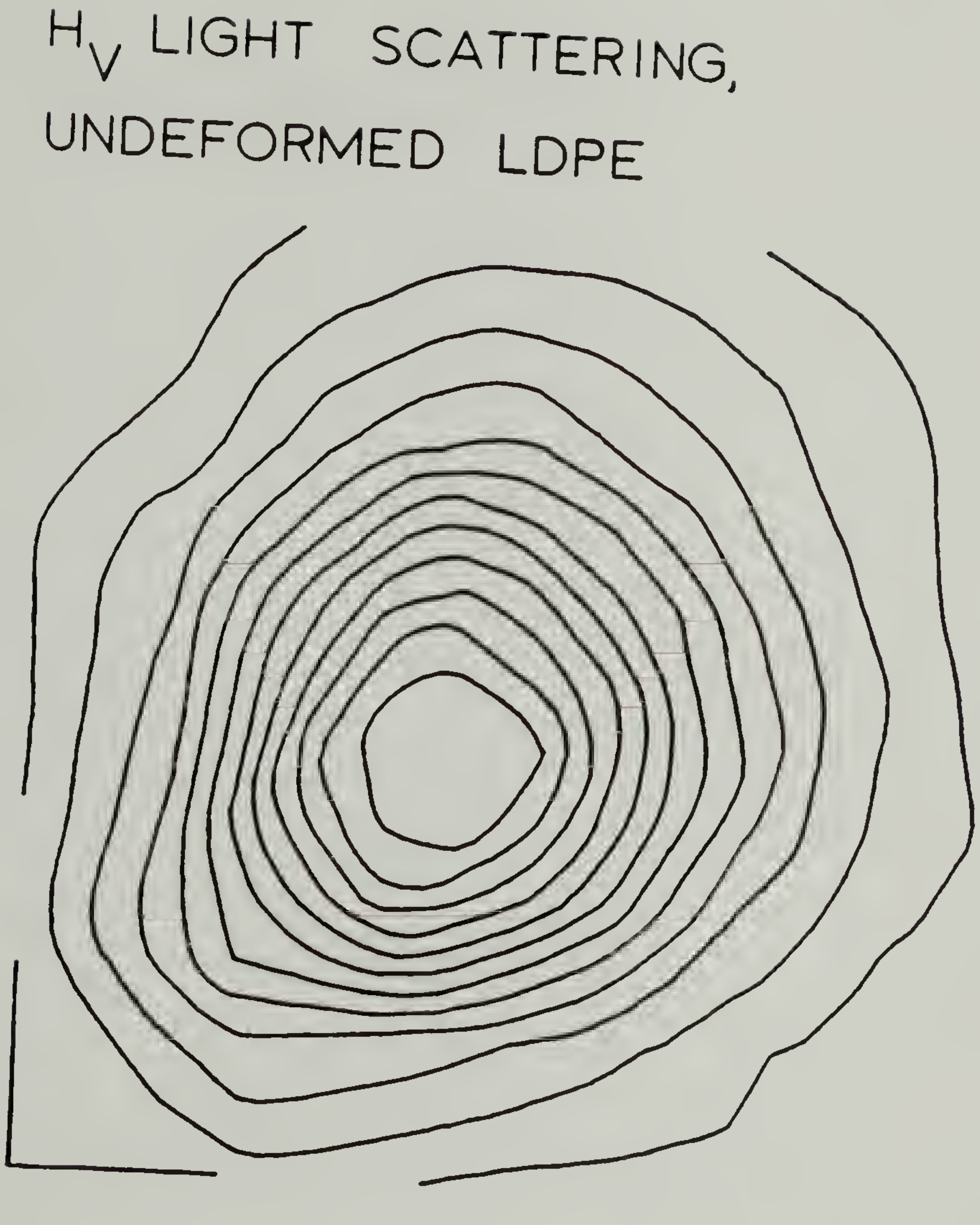

Fig. IV-7 Single quadrant averaged H_V SALS isointensity contour plot from undeformed LDPE film.

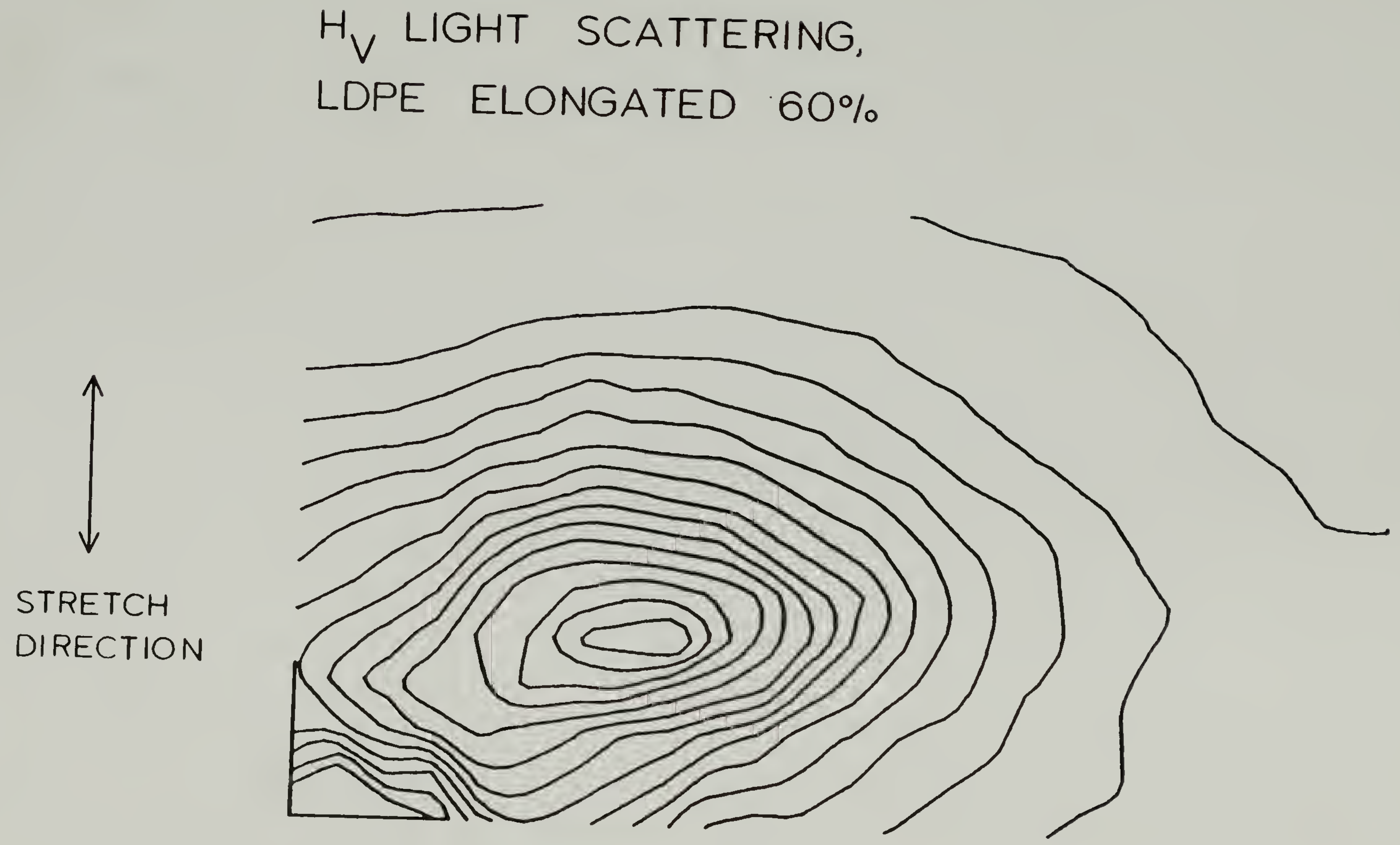

Fig. IV-8 Single quadrant averaged H_v SALS isointensity contour plot from LDPE film elongated 60%.

presented and discussed.

The OMA2 greatly facilitates the rapid detection of scattered light intensities in an anisotropic pattern. Single position photometric detection of a complete anisotropic pattern would be extremely slow. The previously developed one dimensional position sensitive detector [68] would require rotation and many scans to develop a full two dimensional pattern. The OMA2 quickly obtains a complete two dimensional pattern. In addition to making two dimensional pattern detection more convenient, the combination of the two dimensioanl capabilities and speed of the OMA2 allows one to examine SALS patterns from relaxation and moderate speed deformation studies of polymer films. The device could be used for dynamic SALS studies of polymer deformation with appropriate software development.

The OMA2 can also be used to monitor polymer phase separation. Figure IV-9 is a full four quadrant contour plot of SALS from a 60/40 polystyrene/polyorthochlorostyrene phase separated blend. In order to improve the signal-to-noise ratio from isotropic scattering patterns, the OMA2 data can be circularly averaged. Figure IV-10 is a plot of the data from Figure IV-9, circularly averaged to display the intensity as a function of scattering angle. Figures IV-9 and IV-10 display intensity maxima due to a spatial periodicity of the concentration profile of the blend [72]. Circular averaging makes the maximum more apparent in Figure IV-10. Light scattering invariant analysis can also be performed to determine the mean square average polarizability fluctuations [73]. Debye-Bueche analysis can also be carried out on circularly averaged

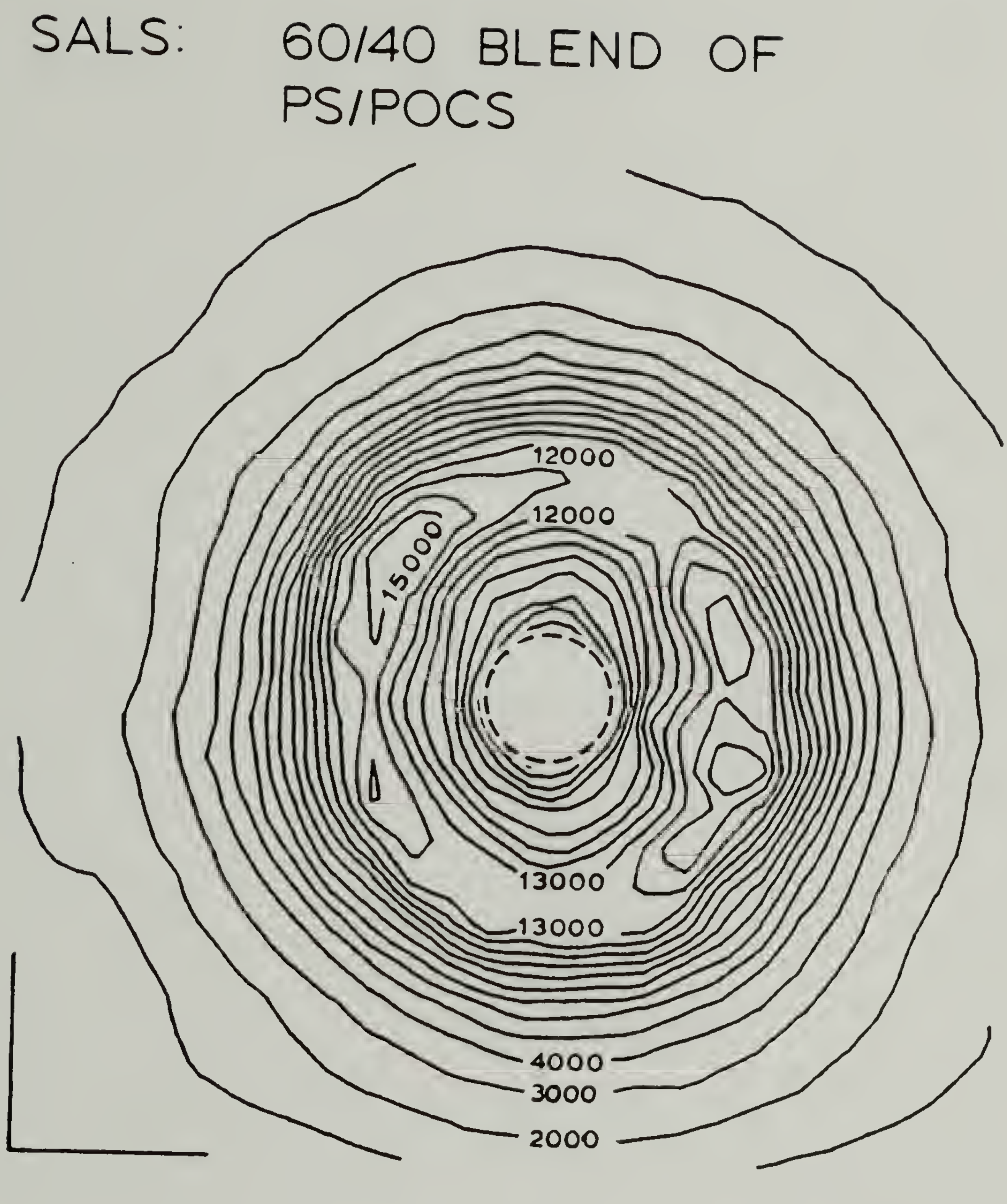

Fig. IV-9 Full four quadrant SALS isointensity contour plot from a 60/40 blend of polystyrene/polyorthochlorostyrene. (The main beam has been suppressed inside the dashed circle.)

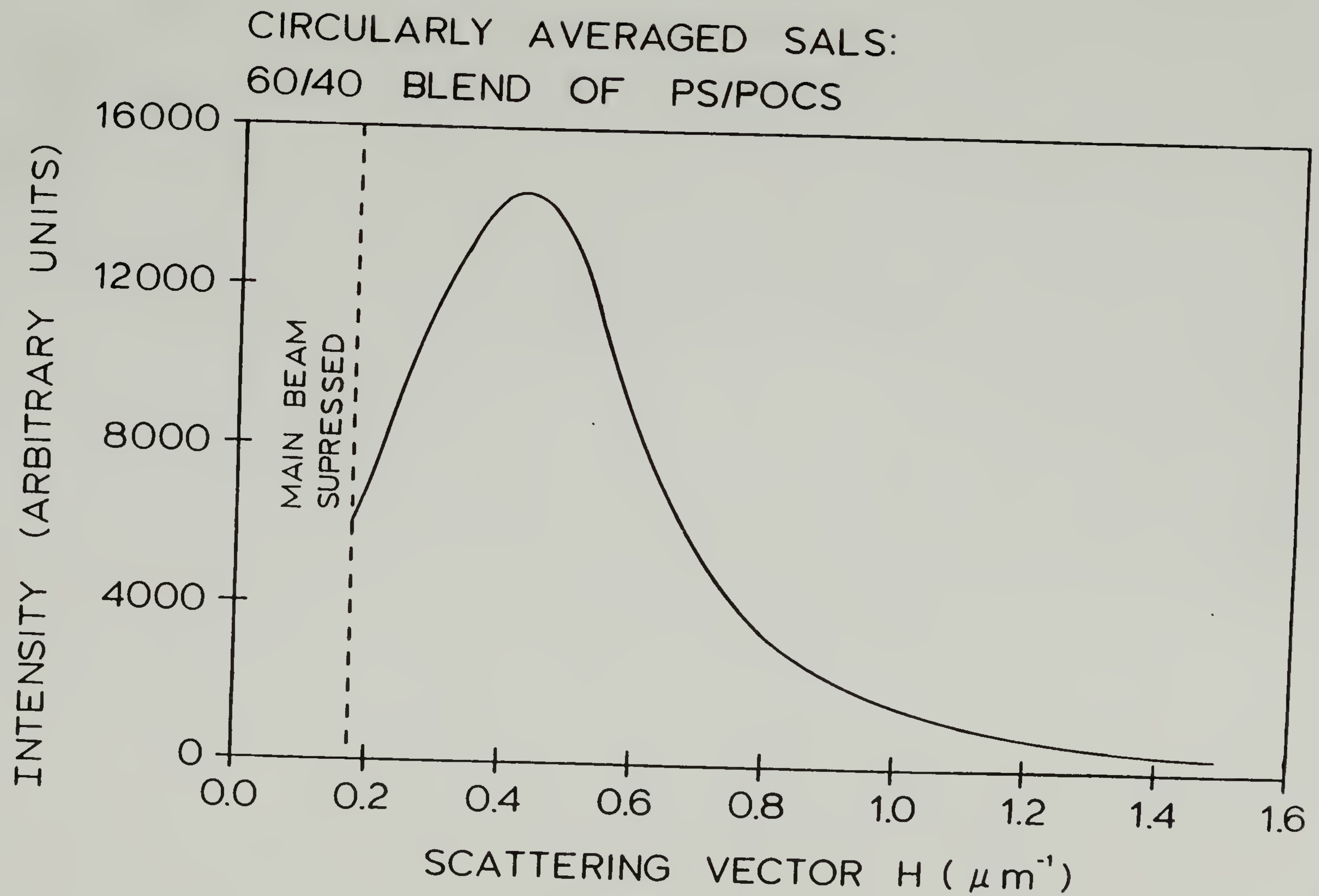

Fig. IV-10 Circularly averaged scattering profile for the data in Figure IV-9. $H = (4\pi/\lambda) \sin(\theta/2)$.

scattered light intensity profiles from random two phase mixtures to determine phase sizes [1]. The quantitative nature and speed of the OMA2 facilitate such measurements. A study of phase separated systems is presented in Chapter VIII. Other phase separated systems are being examined by SALS in our laboratory using the OMA2.

In applications utilizing the OMA2 one must work within the limitations of the device and design the experiments accordingly. Currently the device is limited to a total of 10,000 data points per scan. (This could be improved by software and hardware improvements.) A square grid of 100 x 100 data points in a two dimensional scan is limited in angular resolution. The angular resolution is dependent upon the area of the scattering pattern being examined. Scanning of only one quadrant of the pattern will increase the angular resolution.

Another consideration in experimental design is the desired S/N ratio. One can improve the S/N at the expense of data collection speed by collecting the data over longer times or averaging several scans. As previously mentioned, quadrant averaging of a four quadrant scan also improves S/N, but this improvement is at the expense of less angular resolution as compared to a single quadrant scan. Contour and three dimensional plotting routines, as well as polynomial fitting procedures of constant angle profiles, "smooth" the data.

In smoothing SALS data, particularly from spherulitic polymer films, one must consider the "speckles" present in most patterns. The speckles are due to the interparticle interference within the polymer film [25-28]. This speckling effect can be minimized by using a larger incident

beam (in order to scatter from more particles), by averaging the intensities from different locations in the sample or by quadrant averaging of the data. Since this speckling is an interference effect, it will not be affected by longer collection times.

Conclusions

The development of the OMA2 is a significant advancement in the instrumental aspects of SALS from polymer films. It permits one to rapidly obtain quantitative, two dimensional SALS data. It complements the previous theoretical advancements and those presented elsewhere in this dissertation. The OMA2 is essential for the experimental portions of this work and that of several other workers in our laboratory.

Extensive software has been developed for the operation of the OMA2 and the analysis of the data. The operations software is written principally in macro assembly language, whereas the analysis programs are written in fortran. The operations software can be obtained from M.B. Long of the Department of Engineering and Applied Science at Yale University. The analysis programs are included in the Appendix.

CHAPTER V

STUDIES OF THE MELTING OF POLYETHYLENE TEREPHTHALATE

Introduction

The equations for H_v SALS from model polymer spherulites were given in Chapter II. Equation (II-1) relates the scattered intensity to the number and size of the spherulites, their anisotropy and the scattering angles. It was also explained in Chapter II how experimentally measured intensities differ from the models due to internal disorder, external disorder and experimental conditions. The studies made to develop the modifications for these effects were mentioned. Chapter III presented the effects of one kind of external disorder on H_v SALS: spherulitic truncation.

One can use equation (II-3) and the relationships presented in Chapter III to measure spherulite size by H_v SALS. By correcting equation (II-1) for the multiple scattering, truncation and experimental effects, one can analyze the anisotropy of the spherulites. The anisotropy is related to the spherulitic crystallinity and its internal disorder.

The melting of a fully grown spherulitic polymer is a convenient process for examining these theories and the spherulitic morphology of the polymer. During melting, the number and size of the spherulites are not expected to change. The anisotropy should change during the melting process. The melting process is less complicated than crystallization

(Chapter VI) which involves changes in the number and size of the spherulites, as well as possible anisotropy changes.

Polyethylene terephthalate (PET) is a good polymer to examine for melting and crystallization studies since its crystallization is easily controlled and it is a well studied polymer in our laboratory [39,40,74]. Although quenching will not be utilized in this study, the ability to control PET's morphology by quenching it to below its glass transition temperature has made it a popular choice in previous studies.

This chapter presents a study of the melting of PET by H_v SALS and differential scanning calorimetry (DSC). It is a continuation of a similar study in our laboratory [40]. The quantitative H_v SALS theories are examined and applied to assess the spherulite size, number, internal disorder and crystallinity as functions of temperature during melting. The DSC results are used for comparison.

Theory: Quantitative H_v SALS from PET

The model equation for H_v scattering from isolated three dimensional spherulites was given in Chapter II as

$$R_{H_v}(U, \mu) = \frac{144\pi^4 N s V^2}{\lambda_o^4}(\alpha_r - \alpha_t)^2[((\cos^2\theta/2)/\cos\theta) \quad \text{(V-1)}$$

$$\sin\mu \cos\mu \cos\rho_2 \, \Phi_{H_v}]^2$$

where the terms are as previously defined. The anisotropy of a spherulite is given by [75]

$$(\alpha_r - \alpha_t) = (\alpha_r - \alpha_t)_c^o \phi_{cs} f_{cs} + (\alpha_r - \alpha_t)_a^o (1 - \phi_{cs}) f_{as} \quad \text{(V-2)}$$

$$+ (\Delta\alpha)F$$

where:

$(\alpha_r - \alpha_t)_c^o$ = intrinsic anisotropy of a pure crystal

$(\alpha_r - \alpha_t)_a^o$ = intrinsic anisotropy of the amorphous material

ϕ_{cs} = volume fraction crystallinity within the spherulite

f_{cs} = orientation function of the crystals within the spherulites with respect to the spherulite radius

f_{as} = orientation function of the amorphous segments with the spherulites with respect to the spherulite radius

$(\Delta\alpha)F$ = form anisotropy of the crystalline-amorphous boundary

and the orientation function is given by [76-78]

$$f = \frac{3\langle\cos^2\phi\rangle - 1}{2} \qquad \text{(V-3)}$$

where ϕ is the angle between the axis of a structure and a reference axis. In the case of spherulites, the reference axis is the spherulite radius. The averaging of $\cos^2\phi$ is performed over the distribution of orientations in the system. The limiting values of the orientation function are:

1: perfect alignment along the reference axis,

-1/2: perfect alignment perpendicular to the reference axis and

0: completely random orientation.

In the model spherulites [2,11], the crystals are assumed to have perfect alignment ($f_{cs} = 1$) and the amorphous orientation is random ($f_{as} = 0$). (Imperfect crystal orientation ($f_{cs} \neq 1$) will be treated in terms of internal disorder [34].) If it is also assumed that the form anisotropy is negligible, then equation (V-2) reduces to

$$(\alpha_r - \alpha_t) = (\alpha_r - \alpha_t)_c^o \phi_{cs} . \tag{V-4}$$

The overall volume fraction crystallinity is given by

$$\phi_c = \phi_s\phi_{cs} + (1 - \phi_s)\phi_{cm} \tag{V-5}$$

where:

ϕ_s = volume fraction spherulites and

ϕ_{cm} = volume fraction crystallinity in the nonspherulitic material.

For volume filling spherulites, $\phi_s = 1$ and therefore

$$(\alpha_r - \alpha_t) = (\alpha_r - \alpha_t)_c^o\phi_c . \tag{V-6}$$

Spherulite anisotropy is related to the spherulite birefringence by the differential of the Lorenz-Lorentz equation [46]:

$$n_r - n_t = \frac{2\pi}{9} (\frac{\bar{n}^2 + 2)^2}{\bar{n}}) (\alpha_r - \alpha_t) \tag{V-7}$$

where n_r and n_t are the radial and tangential refractive indices of the spherulite and $\bar{n}$ is the average refractive index given by

$$\bar{n} = \frac{n_r + 2n_t}{3} \tag{V-8}$$

By combining equations (V-1), (V-6), (V-7) and (V-8) one can relate the absolute H_v intensity to the degree of crystallinity of a sample volume filled with spherulites. The necessary modifications must first

be made to the measured intensities, and then the experimental and the theoretically predicted H_v intensities can be compared. Only the intensity at $U = U_{max}$ and $\mu = 45°$ is fully corrected. The intensities for other values of μ are partially corrected and then used to complete the correction at $U = U_{max}$ and $\mu = 45°$.

The modifications to the experimentally measured intensities can be made as described in Chapter II. The corrected experimental intensity is given by

$$R^{c}_{H_{v,exp}}(U_{max},45) = R_{H_{v,exp}}(U_{max},45) C_{refl} C_{refr} C_M C_T C_D \qquad \text{(V-9)}$$

where

$R^{c}_{H_{v,exp}}(U_{max},45)$ = corrected experimental intensity

$R_{H_{v,exp}}(U_{max},45)$ = uncorrected experimental intensity

C_{refl} = reflection correction

C_{refr} = refraction correction

C_M = correction for multiple scattering

C_T = correction for truncation

C_D = correction for internal disorder.

$C_{refl} \approx 1.05$ for a thin film sample sealed by glass on both sides [36]. $C_{refr} \approx n^2$ for small scattering angles [36]. For PET, with a crystalline refractive index of 1.64 [79,80], $C_{refr} = 2.69$.

The correction for multiple scattering is dependent upon the truncation and the internal disorder. A most complete treatment would involve an iterative process including [18,41]:

a) choosing a value for the internal disorder for a level of truncation,

b) calculating the multiple scattering effects for that internal disorder and truncation,

c) correcting the intensities for multiple scattering and the other effects,

d) determining a new value of internal disorder and

e) restarting at a) until the starting and determined values of internal disorder are the same.

Such a process is tedious and was not used in these studies. Instead, the multiple scattering correction for a fully truncated system with a moderate value of internal disorder was used. The corrections were made at $U = U_{max}$ and azimuthal angles of 45, 20, 10, and 0 degrees. The corrections are functions of the value τd of the samples as defined in [37]

$$\frac{I_t}{I_o} = \exp(-\tau d) \tag{V-10}$$

where I_t is the intensity transmitted by a sample of thickness d when the incident intensity is I_o. τ is the sample turbidity. Modifications of the intensity due to multiple scattering in the H_v mode, for an internal disorder parameter $\delta = 0.2$ (δ is described in Chapter II) are given as functions of τd for various values of (U, μ) in Figure V-1 [39,41]. Polynomial fitting coefficients for the curves in Figures V-1, V-3 and V-4 are given in the Appendix.

Upon modifying the intensities for reflection, refraction and multiple scattering, one can then make the modifications for the effects of spherulitic truncation and internal disorder. The effects of

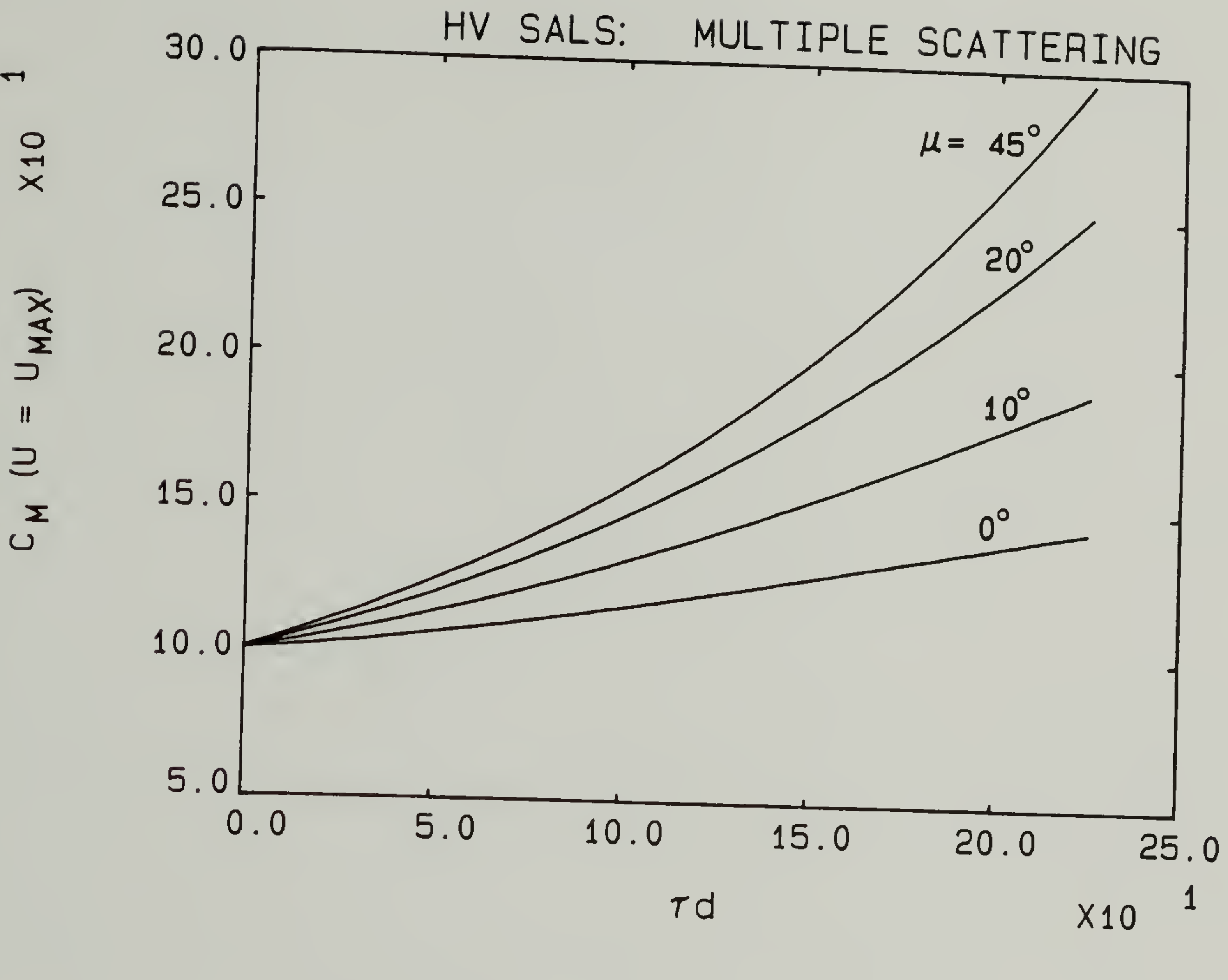

Fig. V-1 Multiple scattering correction factors for fully truncated, disordered two dimensional spherulites (δ = 0.2) [39,41].

truncation and internal disorder are combined in a procedure described by Prud'homme et al. [18,41]. In this procedure the broadening effects on the azimuthal intensity profile due to truncation and internal disorder are combined as illustrated in Figure V-2. Curve (a) in the figure is the H_v scattering azimuthal profile from a perfect, nontruncated, undisordered, three dimensional spherulite. Curve (b) is the profile from an undisordered, fully grown, three dimensional set of spherulites resulting from simultaneous nucleation (from Chapter III). Curve (c) is the profile from two dimensional (three dimensional effects are not available), nontruncated spherulites with $\delta = 0.2$ All three curves are normalized to a maximum intensity of 1000.

The effects of truncation and internal disorder are assumed additive. An example of the calculation of the combined effects is given here for $U = U_{max}$ and $\mu = 15°$. The effect of truncation can be measured as the difference between curves (b) and (a): $366 - 250 = 116$. The effect of internal disorder is the difference between curves (c) and (a): $340 - 250 = 90$. The profile due to the combined effects is the sum of the individual effects and the original profile: $116 + 90 + 250 = 456$. Such procedures were carried out for several values of μ leading to the combined effects of truncation and internal disorder represented in curve (d).

Similar curves can be developed for several values of δ. To assist in the development of these curves, Figure V-3 plots the H_v intensity ratios $I(U_{max},\mu)/I(U_{max},45)$ as functions of the internal disorder parameter, δ, for four values of μ [34]. Figure V-3 can be used with

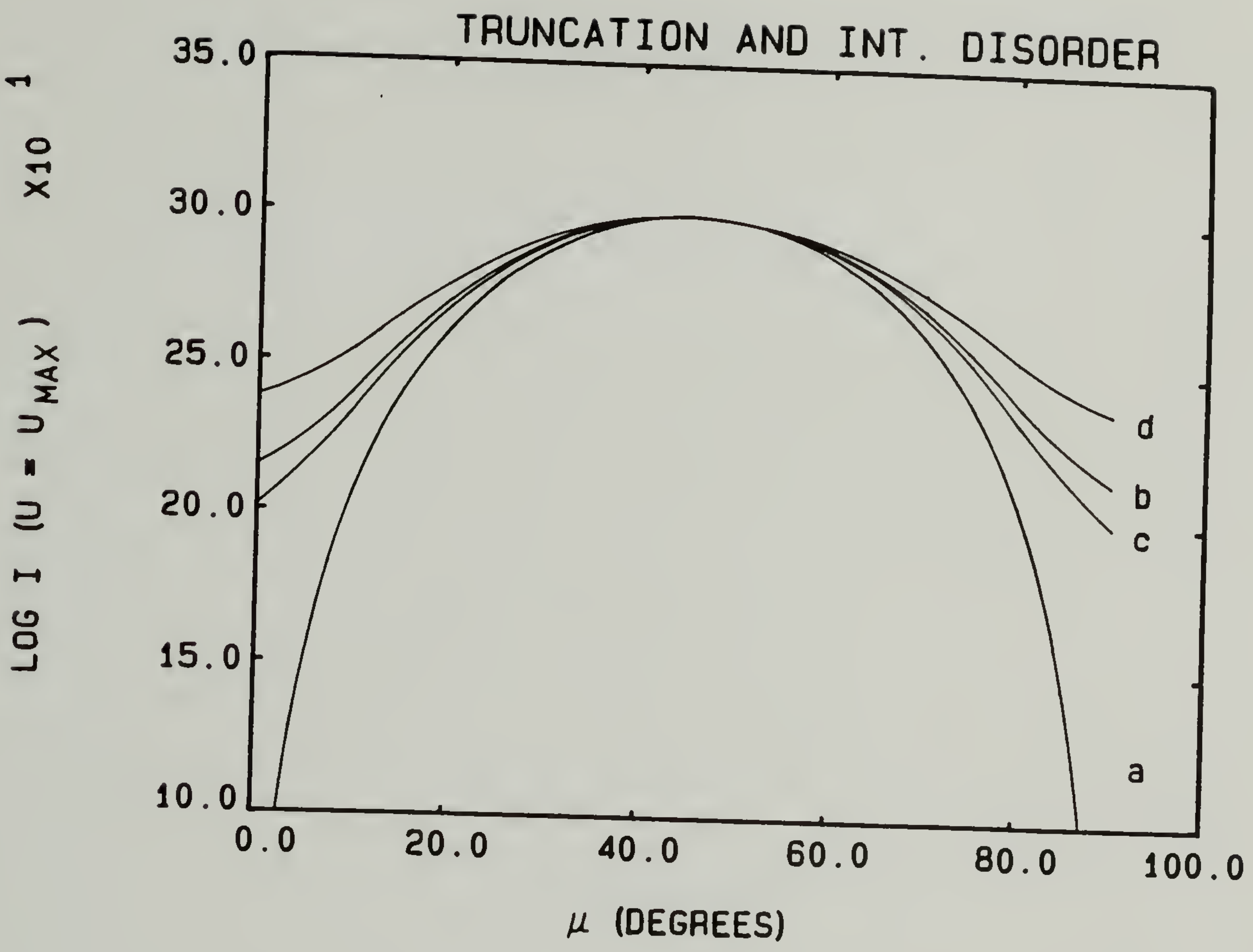

Fig. V-2 Effect of truncation and internal disorder on the shape of the H_v SALS azimuthal profile at $U = U_{max}$:

a) nontruncated, undisordered, three dimensional spherulites;

b) fully truncated, undisordered, three dimensional, simultaneously nucleated spherulites;

c) nontruncated, disordered, two dimensional spherulites ($\delta = 0.2$);

d) combined effects of truncation and internal disorder.

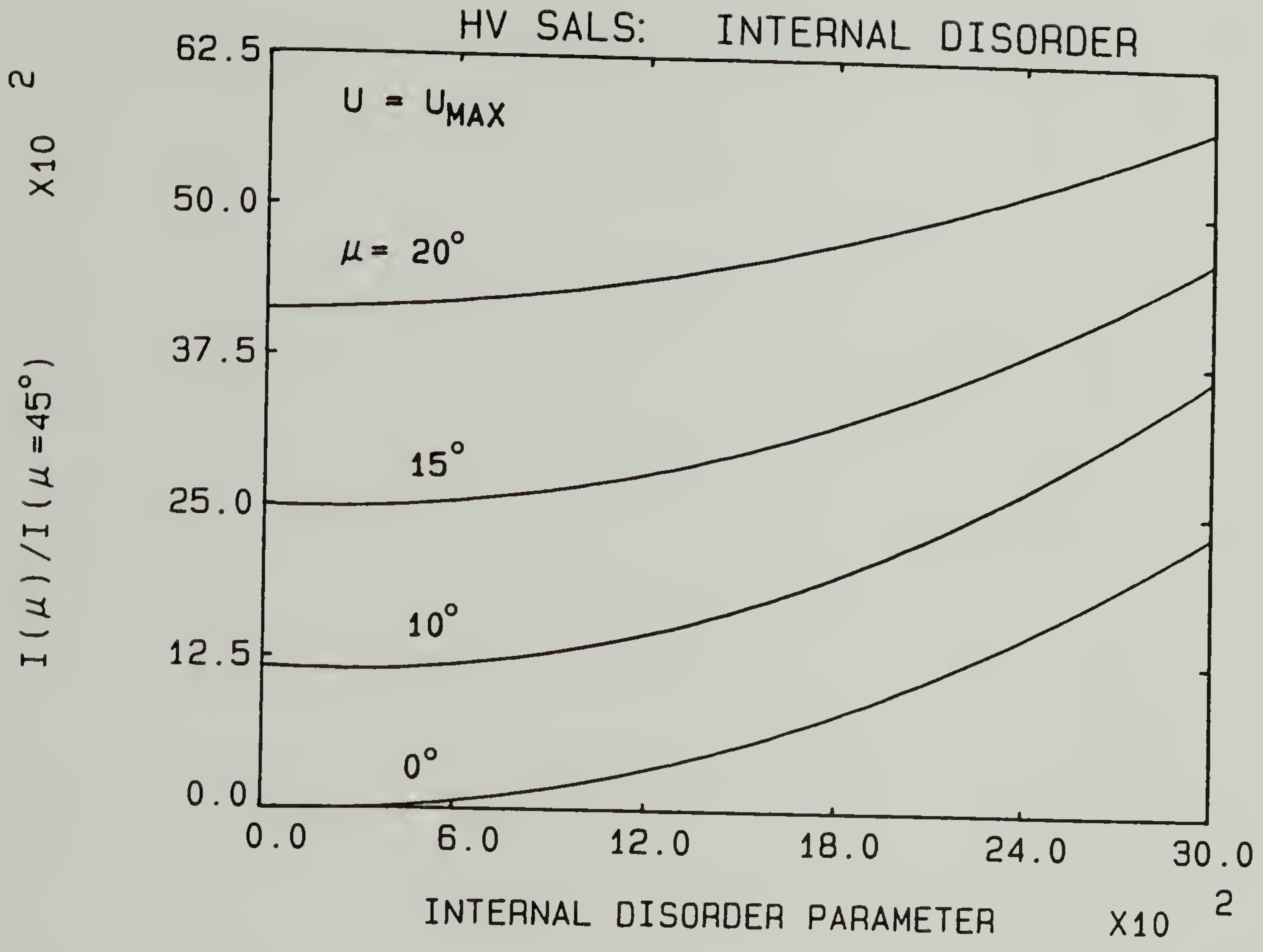

Fig. V-3 Ratios of the H_v intensities for several values of μ to that for μ = 45°, at $U = U_{max}$, for nontruncated, two dimensional spherulites as functions of the internal disorder parameter, δ [34].

Figures III-19, III-20 or III-23 to combine the effects of internal disorder and spherulitic truncation as outlined in Figure V-2. Figure V-2 represents fully grown spherulites, but the process can be carried out, as will be demonstrated in Chapter VI, for any value of volume (or area) fraction spherulites.

The H_v intensity ratios $I(U_{max},45)/I(U_{max},\mu)$ are used as measures of the internal disorder. Such ratios, determined by calculations similar to that represented in Figure V-2, are plotted in Figure V-4 for various values of μ, at $U = U_{max}$, for fully grown, three dimensional, simultaneously nucleated spherulites.

One determines the values of δ from Figure V-4 and the experimental intensity ratios, which have been corrected for reflection, refraction and multiple scattering. From the value of δ, one can determine the correction for internal disorder C_D, at $U = U_{max}$ and $\mu = 45°$ by the use of Figure V-5 [34]. This correction and C_T ($C_T = 2.2$ for full growth, from Chapter III) are applied according to equation (V-9) to determine $R^c_{H_{v,exp}}(U_{max},45)$. This value will be used in Equation (V-1) to examine the polymer morphology during melting.

Experimental

Sample preparation.

Characterization. PET pellets were obtained from the General Electric Company. The pellets were dried under vacuum for 24 hours at 100°C and stored in a desiccator until use. The molecular weight of the PET was determined by intrinsic viscosity at 45.00 ± 0.05°C using

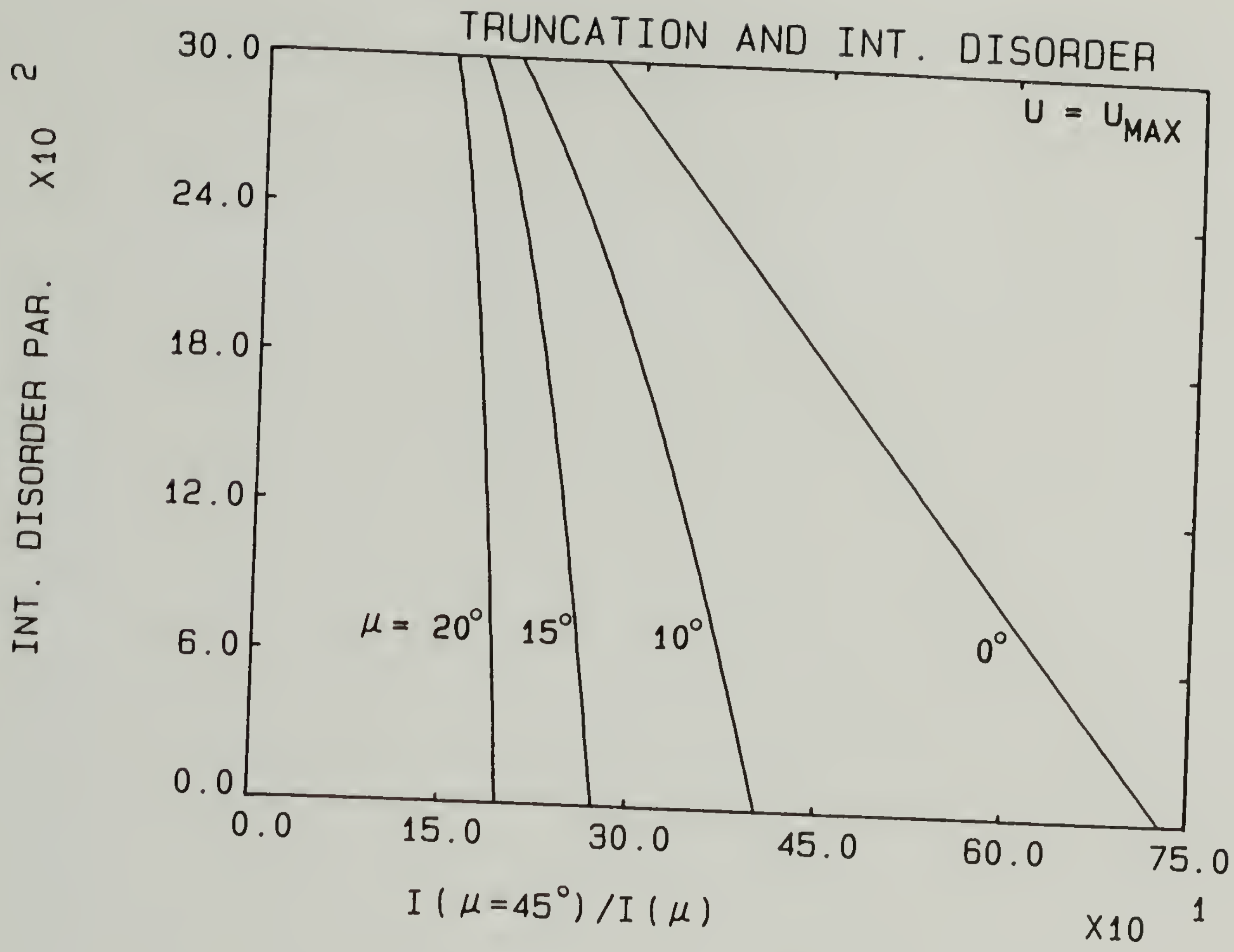

Fig. V-4 Determination of internal disorder, for fully truncated systems, from the H_v SALS intensity ratios $I(U_{max},45)/I(U_{max},\mu)$.

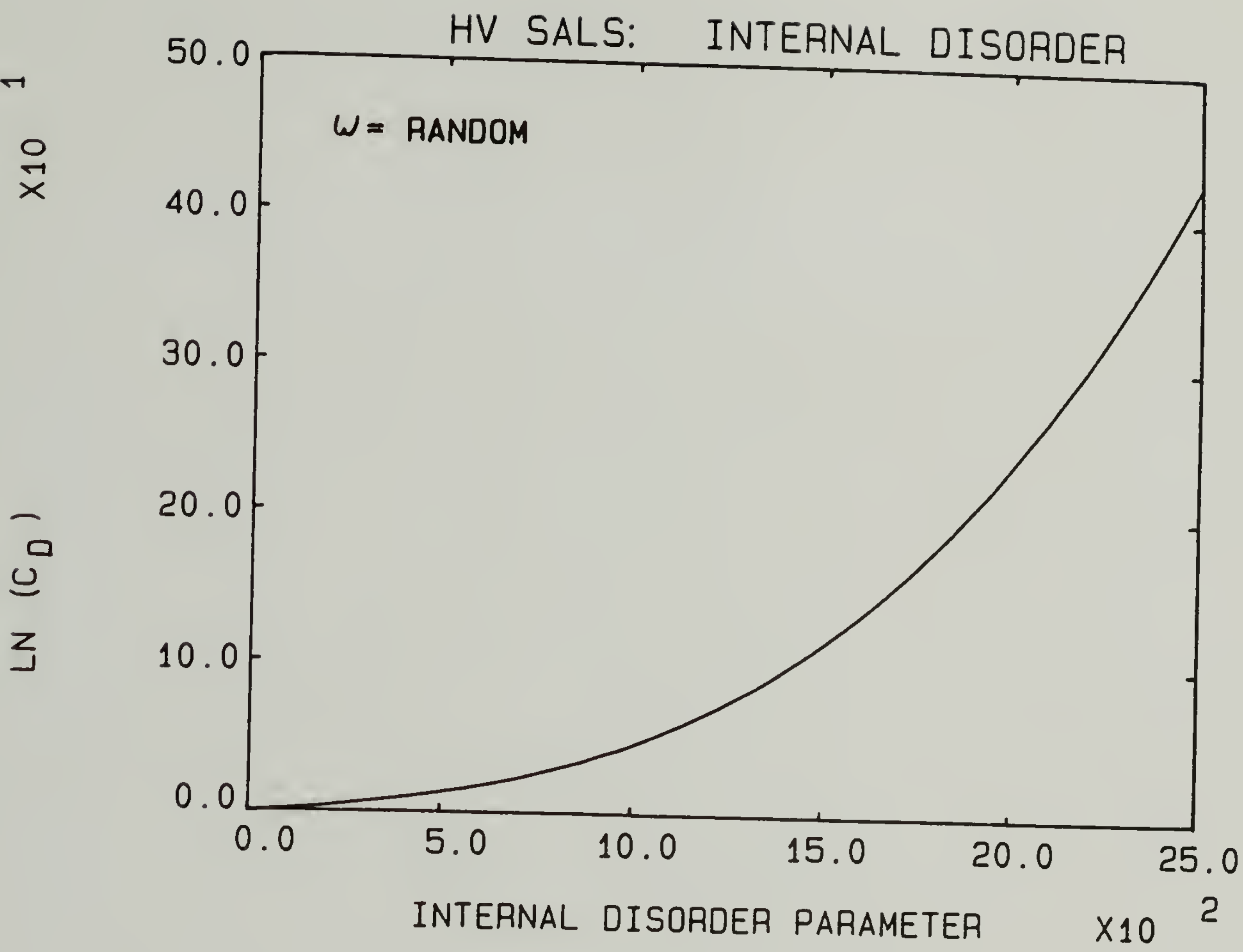

Fig. V-5 Correction factor for internal disorder for H_v SALS at $U = U_{max}$ and $\mu = 45°$ [34].

dichloroacetic acid as the solvent and the relationship [81]

$$[\eta] = 0.4\ M_v^{0.50} \tag{V-11}$$

where $[\eta]$ is the intrinsic viscosity (in ml/g) and M_v is the viscosity average molecular weight. It was found that $[\eta] = 54$ ml/g, which indicates that $M_v = 18{,}000$.

Pressed films. Smooth thin films were prepared using a Pasadena hydraulic press operating at 280°C. Ferro-type plates were coated with a thin film of 1-2531 Release Coating (Dow Corning Corporation) and cured 15 minutes on the press. The pellets were pressed between the plates, using 25 µm brass shim spacers. The sandwich was heated in the press with gentle pressure for 1 minute, under about 1500 psi for 5 minutes, then no pressure for one minute to relieve stress. The sample was then quenched in an ice-water bath, dried and stored in the desiccator.

SALS samples. Films approximately 1 mm square were cut for the SALS studies. They were each placed between a microscope slide and a cover glass and gently held in place by paper clips. The assembly was placed in an oil bath at 278 ± 3°C for 10 minutes, then quickly moved to a crystallizing oil bath at 180 ± 0.5°C for 2 hours. After crystallization the samples were allowed to cool slowly in air to room temperature, then stored in a desiccator until use.

DSC samples. Samples for differential scanning calorimetry (DSC) were prepared from the pressed films, crystallized between sheets of

aluminum foil according to the same oil bath cycle as the SALS samples. The films were removed from the foil by dissolving the foil in HCl.

Differential scanning calorimetry. The DSC (Perkin Elmer DSC2) was calibrated for temperature and heat of fusion using tin and lead standards. PET samples were about 5 mg each in mass. The samples were heated from room temperature to 227°C at 320°C per minute. They were then heated at 2.5 and 10°C per minute through 265°C. The data was averaged over three samples for the 2.5° per minute heating rate and over two samples for the 10° per minute heating rate. The curves were analyzed by tracing with an area integration device (Bitpad One).

Optical microscopy. Optical micrographs were obtained from the SALS samples prior to melting. The micrographs were obtained using a Zeiss polarizing microscope under the crossed polars condition.

H_v SALS. The SALS experiments were performed using the OMA2 described in Chapter IV. The geometry of the OMA2 was chosen such that slightly more than one quadrant of the scattering pattern was collected by the detector. The system was calibrated in terms of scattering angles, sensitivity and absolute intensity according to procedures outlined in Chapter IV. The sample assembly (microscope slide, sample and cover glass) was placed in a Mettler hot stage for the melting study. The temperature was raised quickly to 180° and then heated at 2 and 10°C per minute up to 265°C. One H_v scan (2450 data points each) per degree was collected over the temperature range 240 to 265°C.

Transmission. The transmission of the samples was also measured as a function of temperature using the OMA2 and equation (V-10). The transmission of the samples used in the H_v experiments was measured at room temperature. The transmission of separate samples was measured during melting. The transmission results of the separate samples were normalized to the same value at room temperature as the samples used in the H_v experiment. All of the OMA2 data was collected and stored on flexible disks for later analysis.

Results

Differential scanning calorimetry. A typical DSC trace of a PET melting endotherm is given in Figure V-6. The area under the endotherm is proportional to the total heat absorbed during the melting, being calibrated by the melting of a tin standard. The weight fraction crystallinity, w_c, is calculated for any temperature from the area under the curve between that temperature and the temperature of complete melting. The heat of fusion value used for PET was 30. cal/g [82].

The DSC measured w_c's for heating rates of 2.5 and 10°C per minute are given as functions of temperature in Figure V-7. There is a continuous decrease in crystallinity over the temperature range 240 to 265°C. There are no further signs of crystallinity beyond 265°C. A higher degree of crystallinity was determined for the 2.5° per minute heating rate. This difference is most likely due to an annealing effect in the DSC during the slower heating rate. The change in crystallinity with temperature will be used in conjunction with the H_v SALS data and

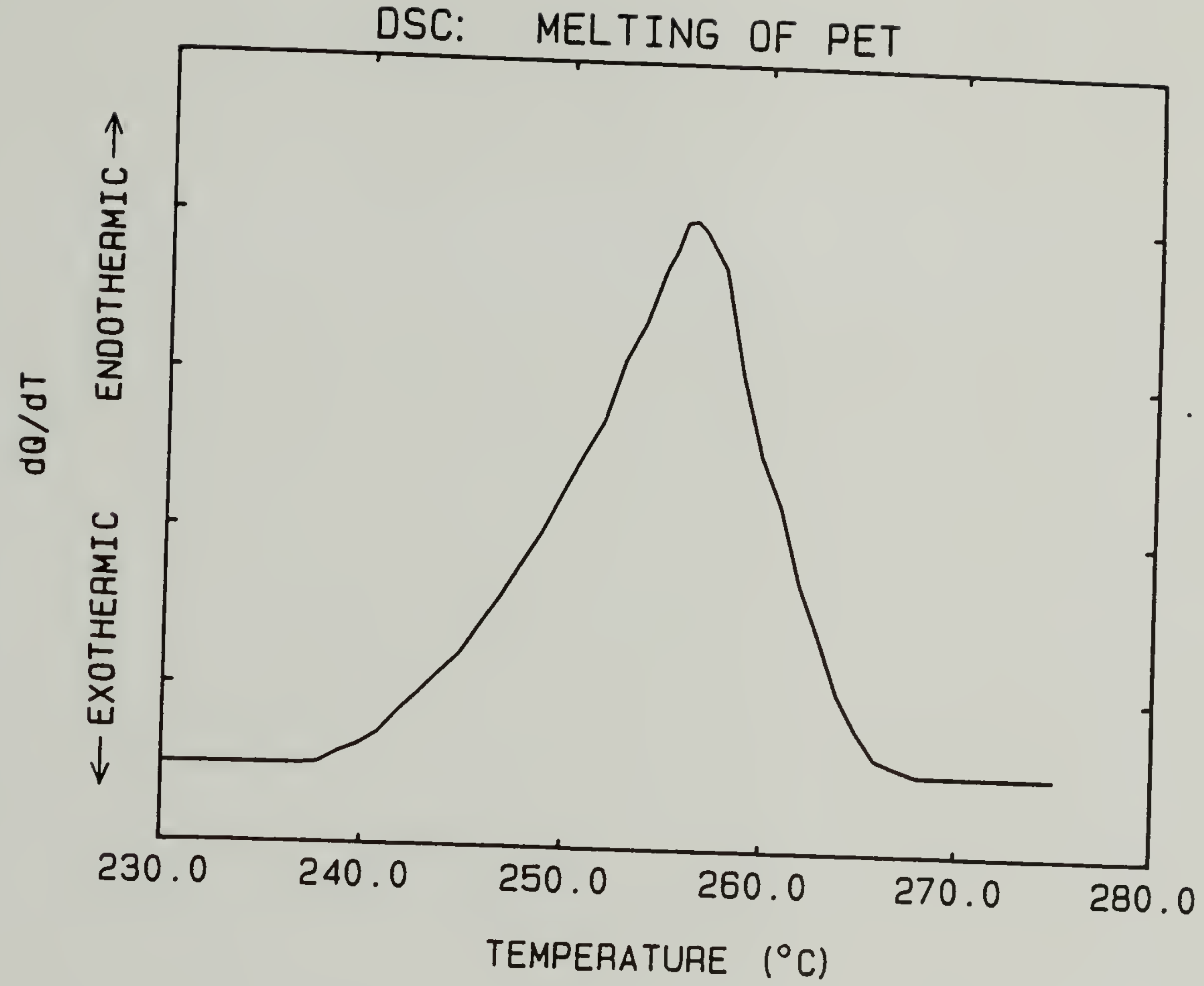

Fig. V-6 Typical DSC trace for the melting of PET at a heating rate of 2.5°C per minute.

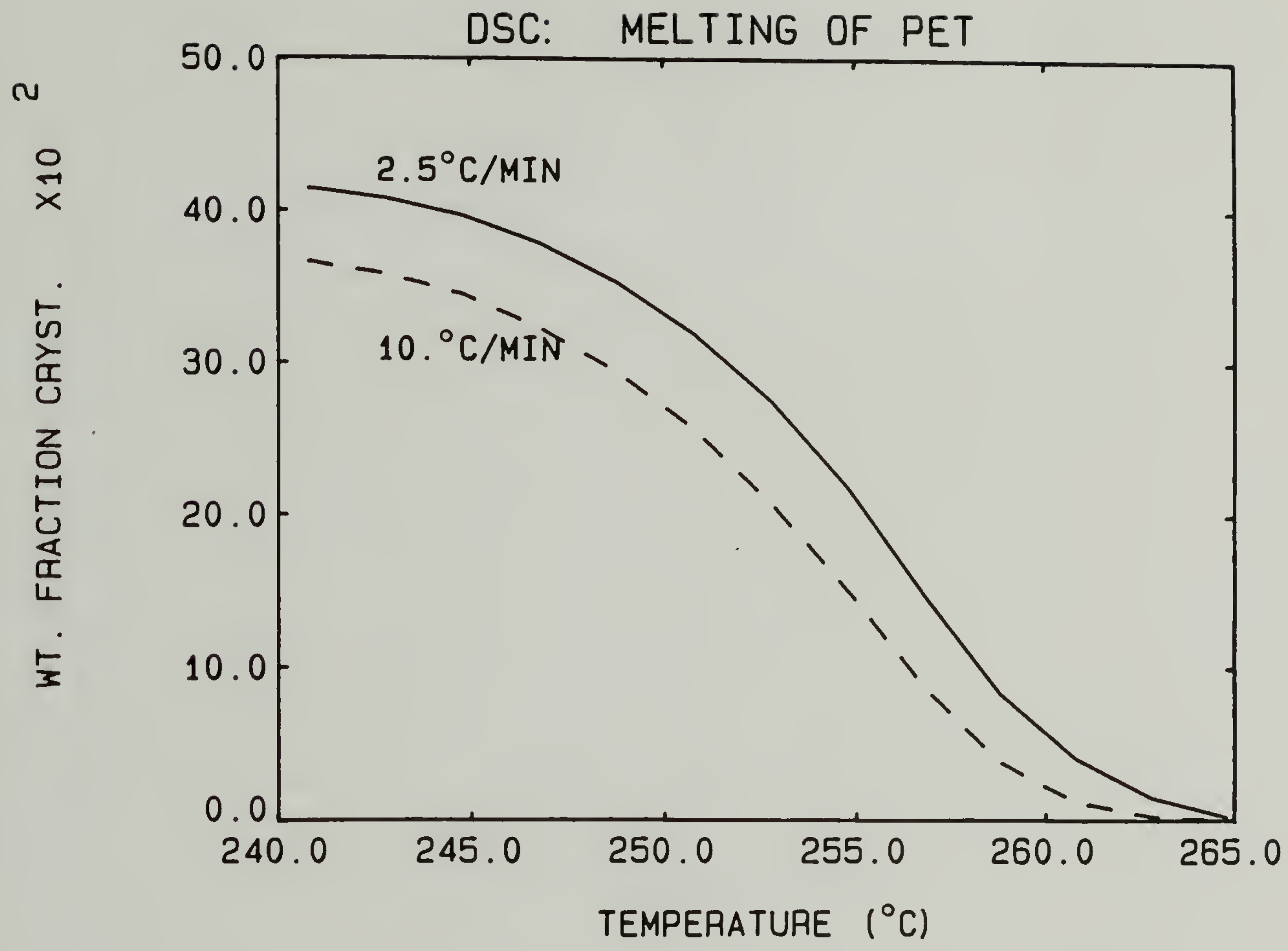

Fig. V-7 Weight fraction crystallinity determined by DSC for the melting of PET at heating rates of 2.5 and 10°C per minute.

the modified model equations.

Optical microscopy. A crossed polar micrograph of a SALS sample prior to melting is given in Figure V-8. Although the sample is too thick to distinguish the spherulites, the birefringent nature of the sample is apparent.

H_v SALS. The intensity data was collected from scattering patterns similar in appearance to Figure II-2a. The measured H_v intensities at the various temperatures were converted to absolute intensities as functions of the scattering angles ($R(\theta,\mu)$) using the OMA2 analysis software and the calibration standards as described in Chapter IV.

The intensity data has been single quadrant averaged (although most of the data was contained in the first quadrant of the scattering pattern). Sample isointensity contours of the H_v SALS at 250, 255, 260 and 262°C, heating rate of 2°C per minute, are given in Figure V-9. The contours are at the same intensity levels for all four patterns in Figure V-9. It is apparent that there was a decrease in intensity with temperature increase. It also appears that the angular location of the intensity maximum did not change with temperature. Similar patterns were detected for the 10°C per minute heating rate.

To examine these H_v SALS patterns according to the theories presented earlier, profiles at a constant azimuthal angle of $\mu = 45°$, as a function of the magnitude of the scattering vector, H, were determined from each data set. Some of these intensity profiles are given in Figure V-10, again for the heating rate of 2° per minute. Experimental fluctuations and interspherulitic interference effects [25-28] were

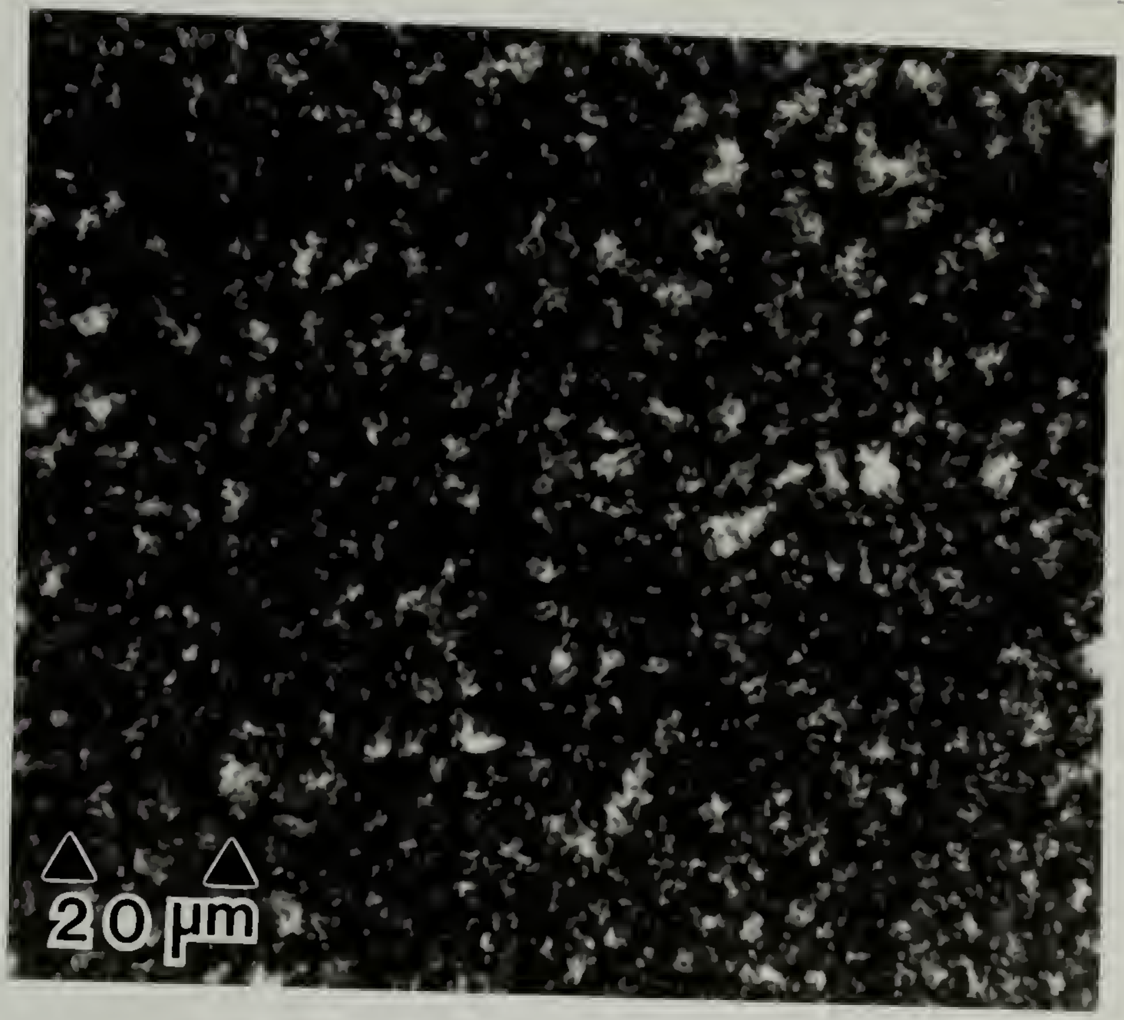

Fig. V-8 Optical micrograph of PET, crystallized from the melt at 180°C for two hours, crossed polars.

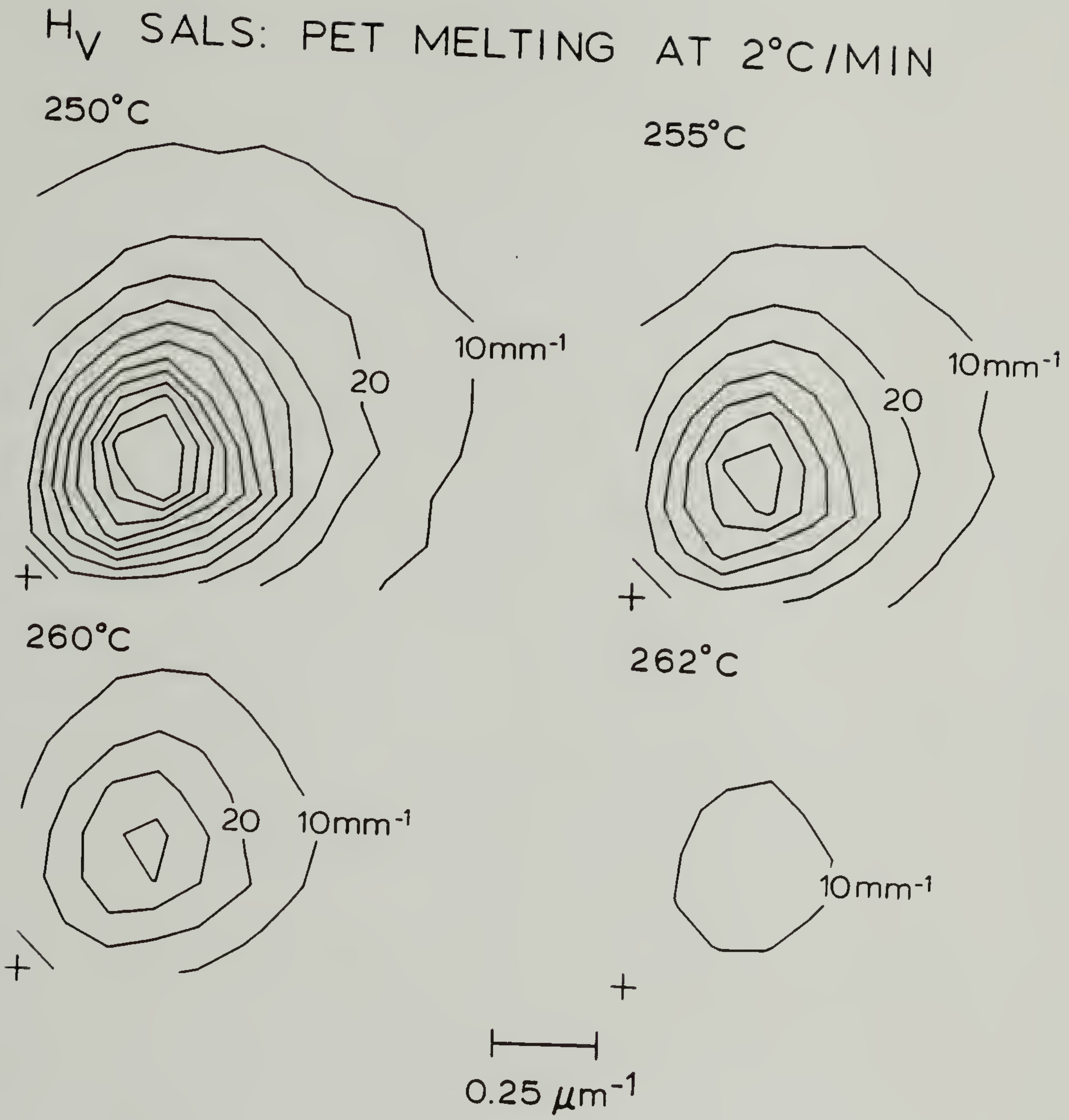

Fig. V-9 Single quadrant averaged H_v SALS isointensity contours for the melting of PET at a heating rate of 2°C per minute: 250, 255, 260 and 262°C. The contour levels for each pattern at intervals of 10 mm^{-1}.

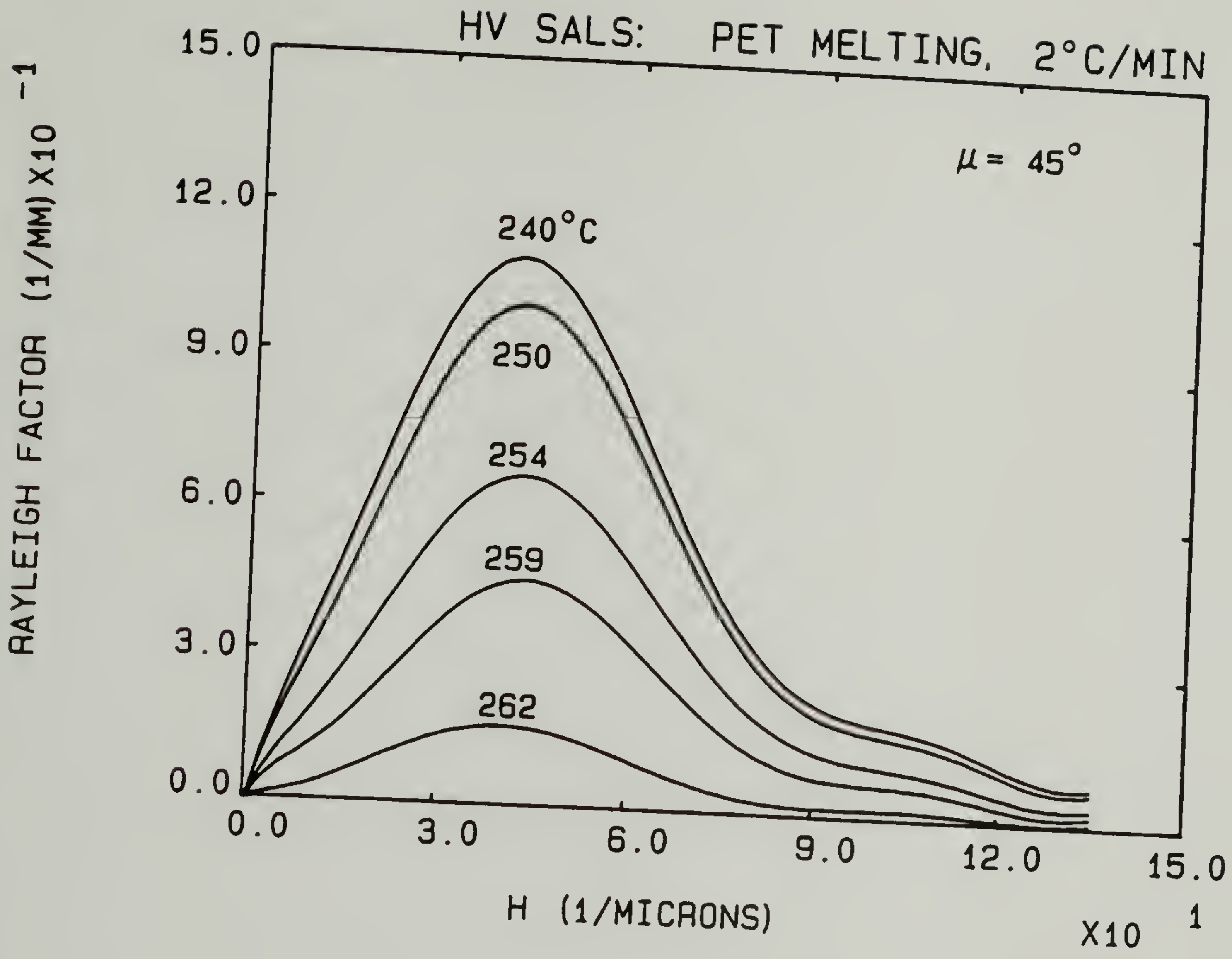

Fig. V-10 Polar scattering angle profiles at μ = 45°, for several temperatures, of the H_v SALS intensity from the melting of PET at a heating rate of 2°C per minute.

removed from the profiles by a least squares fitting of the data to 8th order polynomials. It is clear from this figure how the intensity decreased with increasing temperature. There was also no significant change in the polar scattering angle where the intensity was maximum; the constant average spherulite radius was about 9.6 μm. Similar results were determined for the heating rate of 10° per minute.

To further examine the H_v SALS theories, intensity profiles as functions of the azimuthal angle at the polar angle of maximum intensity are given in Figure V-11. Each profile is a 4th order polynomial least squares fit of the data. Again the intensity decrease with temperature is apparent. The maxima of course occurred near $\mu = 45°$. (The slight deviation of the maxima from $\mu = 45°$ may be due to a slight rotation of the polarizer and analyzer in the SALS set up. The polarizer and analyzer directions remained perpendicular.) The breadth of the profiles is related to the multiple scattering of the sample, the internal disorder and the truncation. These effects will be examined in the discussion section.

Transmission. The values of τd are plotted in Figure V-12 as a function of the temperature during melting for the heating rate of 2°C per minute. The samples became more clear as τd decreased with increasing temperature. Similar results were found for the heating rate of 10°C per minute. The values of τd were used to evaluate the effects of multiple scattering.

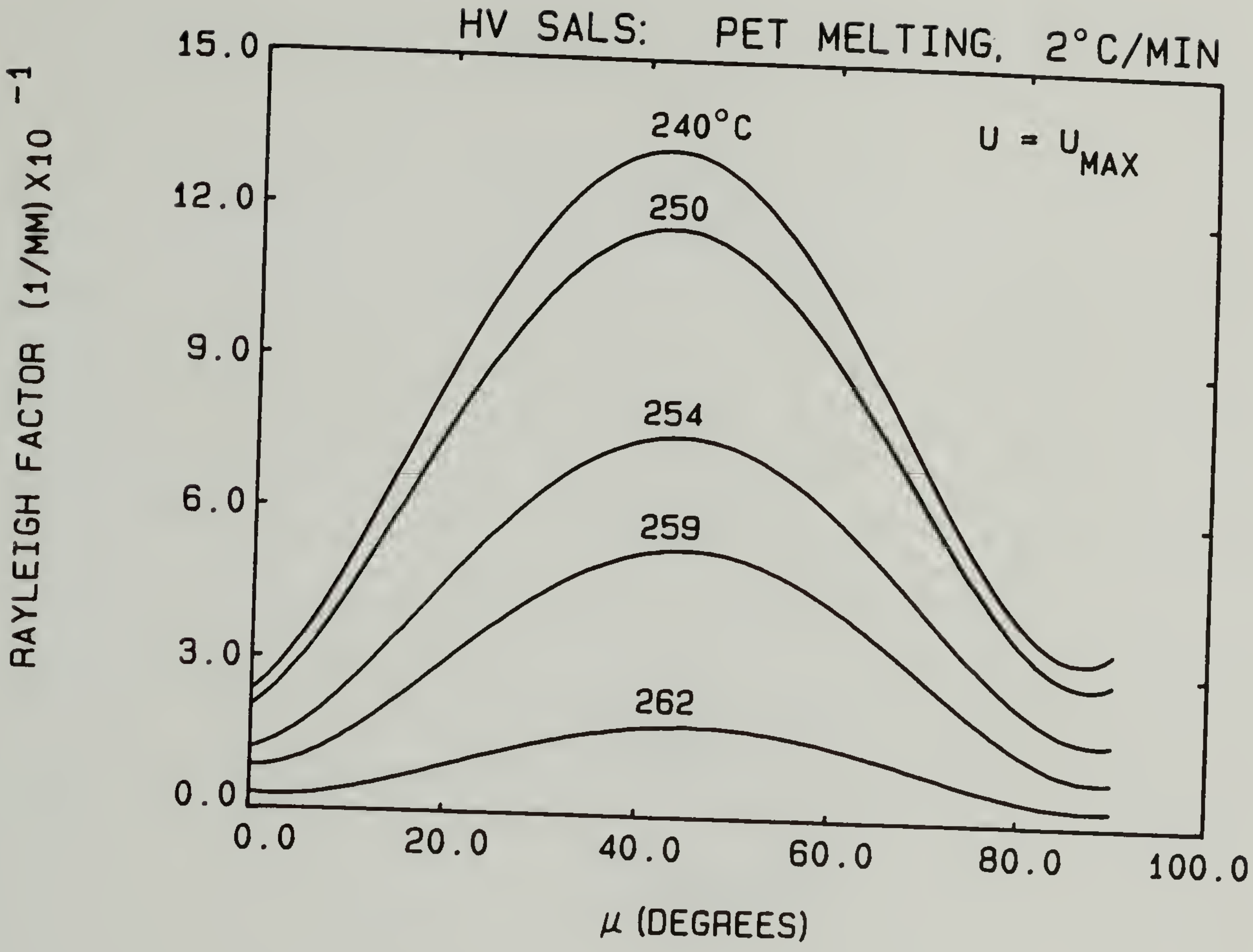

Fig. V-11 Azimuthal scattering angle profiles at $U = U_{max}$, for several temperatures, of the H_v SALS intensity from the melting of PET at a heating rate of 2°C per minute.

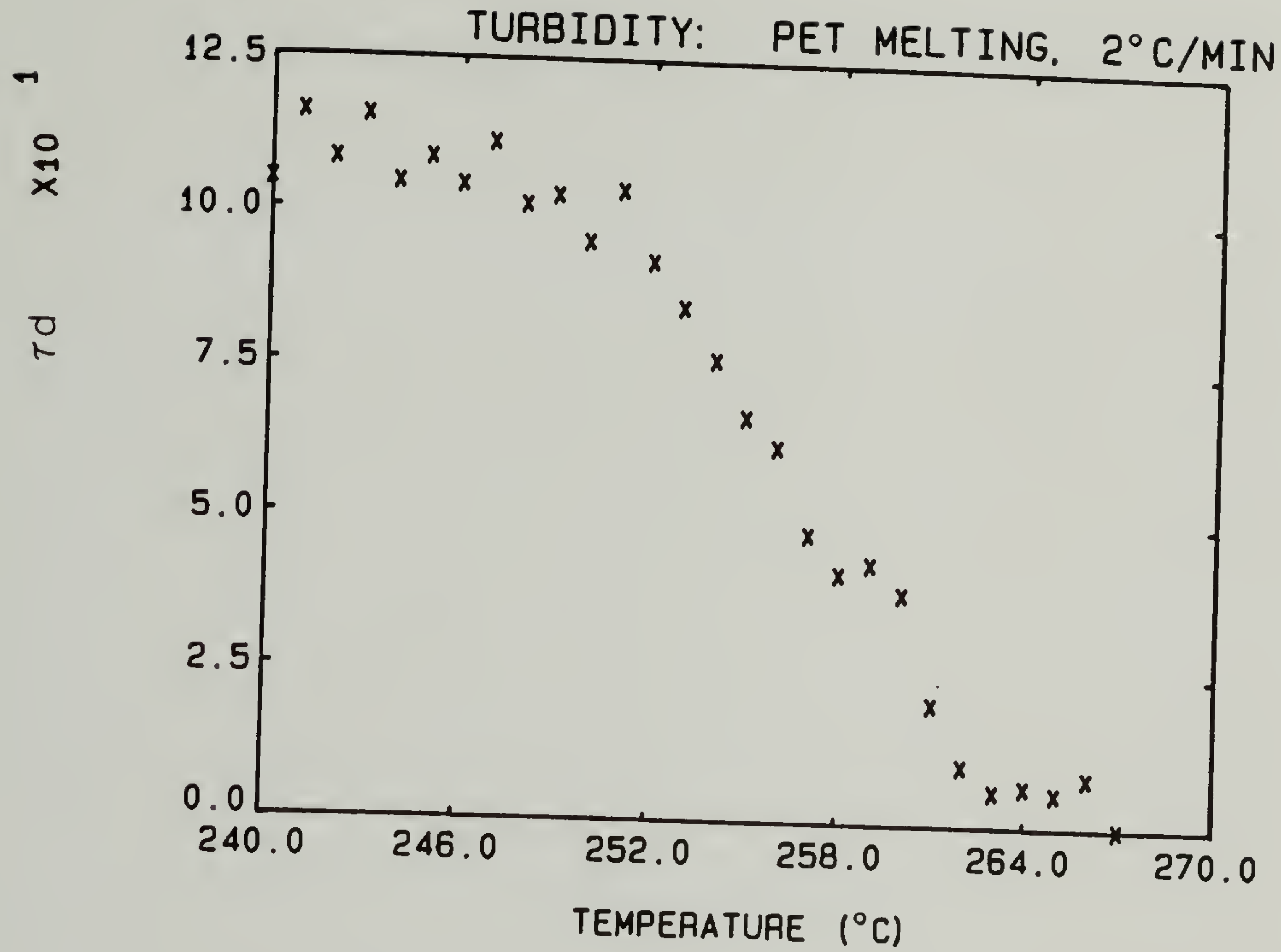

Fig. V-12 τd as a function of temperature during the melting of PET at a heating rate of 2°C per minute.

Discussion

It is apparent from Figure V-10 that the PET spherulites did not change in size during melting since the polar angle of maximum intensity did not change with temperature. Since the system was volume filled with spherulites, it can be assumed that the number of spherulites per volume, N_s, also did not change.

It is also apparent in Figures V-9, 10 and 11 that the H_v intensity decreased with temperature. Since the size (and therefore the average volume V) and number of spherulites did not change during melting, the anisotropy must have changed in order to account for the decrease in intensity. The anisotropy is related to the crystallinity of the spherulites (equation (V-4)) and the internal disorder [34]. Quantitative analysis of the H_v SALS was made and combined with the DSC results to discriminate between the effects of crystallinity and internal disorder and to examine the H_v SALS theories.

For the reasons presented in Chapter III, the azimuthal intensity profiles, rather than the polar profiles, were analyzed. The intensities at $U = U_{max}$ and μ = 45, 20, 10 and 0° were corrected for reflection, refraction and multiple scattering as described earlier in this chapter. Internal disorder parameters for fully grown spherulites were determined from $R_{H_v}(U_{max},45)/ R_{H_v}(U_{max},20)$, $R_{H_v}(U_{max},45)/R_{H_v}(U_{max},10)$ and $R_{H_v}(U_{max},45/ R_{H_v}(U_{max},0)$ and Figure V-4. The average internal disorder parameter, δ, is plotted as a function of temperature during melting for the heating rate of 2°C per minute in Figure V-13. The internal disorder was relatively constant over the whole melting

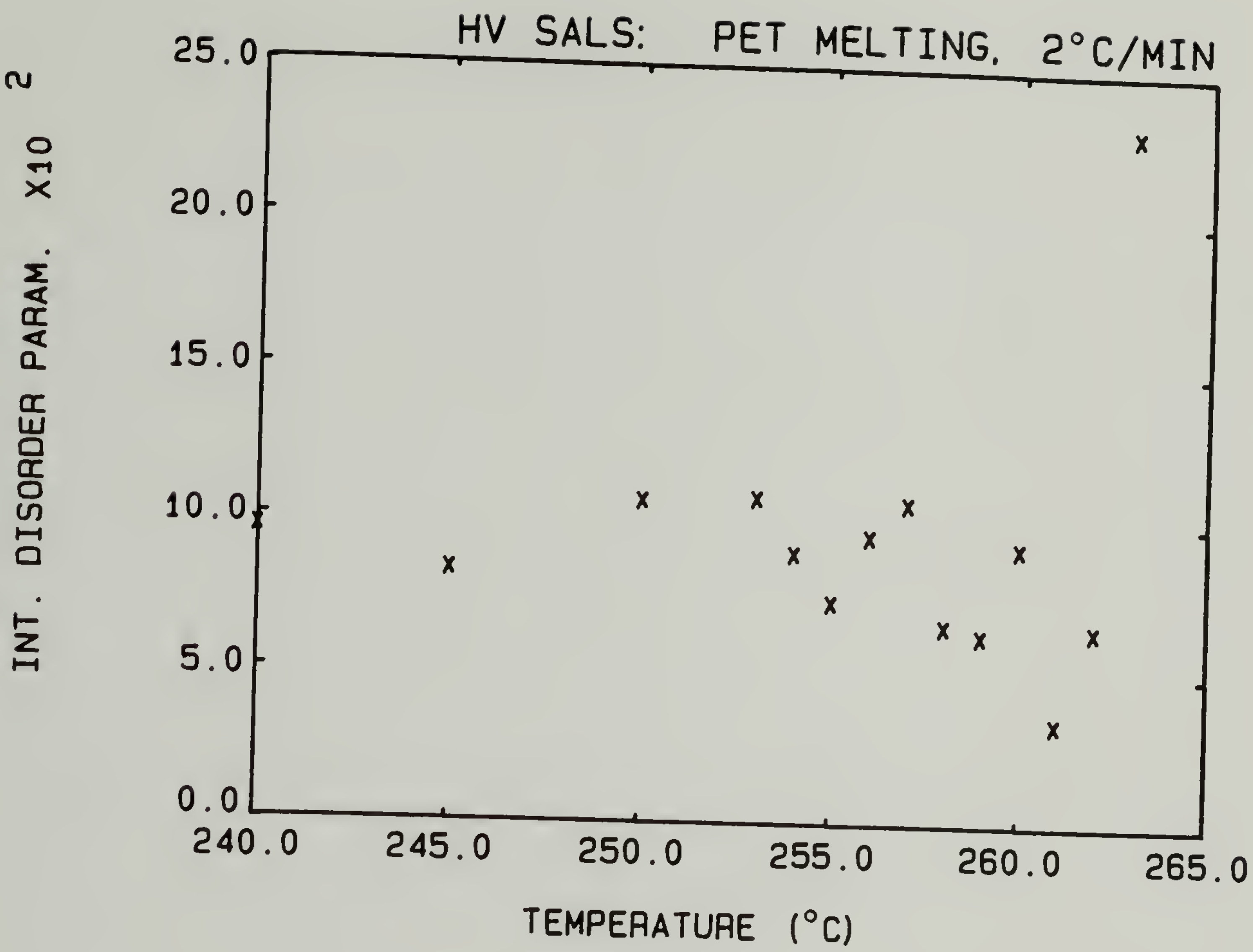

Fig. V-13 Spherulitic disorder as a function of temperature during the melting of PET at a heating rate of 2°C per minute.

range until the very final stages of melting. At 263°C and above the internal disorder parameter apparently increased sharply as the intensity profile became flat. The scattered intensities were so small at these temperatures that analysis of the data beyond 262°C is not reasonable.

The constant value of the internal disorder parameter was about 0.8. This value is relatively low compared to other studies of PET [39,40] and a study of polyethylene [41]. In fact, the determined internal disorder parameters for the heating rate of 10°C per minute were often less than 0. However, the intensity ratios $R_{H_v}(U_{max},45)/R_{H_v}(U_{max},20)$, $R_{H_v}(U_{max},45)/R_{H_v}(U_{max},10)$ and $R_{H_v}(U_{max},45)/R_{H_v}(U_{max},0)$ were constant over the melting range for the higher heating rate. This fact indicates that the internal disorder remained constant as well for this heating rate. The actual value of the internal disorder parameter for both heating rates may have been underestimated due to a possible overestimate of the effects of truncation. These possibilities are discussed later.

The DSC results showed that the crystallinity of the samples diminished continuously from 240 to 265°C. When this fact is combined with the results that the size, number and disorder of the spherulites were unchanged over the temperature range of 240 to 262°C, it is concluded that the H_v intensity decrease during the melting process can be attributed solely to a decrease in spherulite crystallinity.

The predicted H_v SALS intensity at $U = U_{max}$ and $\mu = 45°$ from the crystallinity determined by DSC was compared to the corrected

experimentally measured intensities over the melting range.

Substitution of equation (V-6) into equation (V-1) at the conditions of $U = U_{max}$ and $\mu = 45^\circ$ leads to

$$R_{H_v}(U_{max},45) = \frac{144\pi^4 N_s V^2 \phi_c{}^2 (\alpha_r - \alpha_t)_c^{o\,2} (.25)}{\lambda_o{}^4} \qquad \text{(V-12)}$$

$$[((\cos^2\theta/2)/\cos\theta)\ \cos\rho_2\ \Phi_{H_v}]^2$$

For PET at $\phi_s = 1$, the following values can be substituted into equation (V-12):

$N_s V = 1$

$V = 1.97\overline{R}_n^{3}$ (from Chapter III)

$\Phi^2_{H_v} = 7.9 \times 10^{-3}$

$\lambda_o = 0.6328\ \mu m$

$(\cos^2\theta/2)/\cos\theta \simeq 1$ and

$\cos\rho_2 \simeq 1$

where $\overline{Rn}^{3}$ is the average spherulite size as determined from the polar angle of maximum H_v intensity and equation (III-17). The necessity of the $\cos\rho_2$ correction is removed (even though the correction is small) by the lens geometry of the OMA2 since the scattered rays are parallel when they reach the analyzer (see Figure IV-2).

Even though PET is a commercially important polymer which has received much study, its spherulitic structure is not clearly understood. Several studies have indicated that PET, when crystallized from the melt at 180°C, generally forms positively birefringent spherulites, with the molecular chain axis tending toward orientations

perpendicular to the spherulite radius [83-86]. The unit cell of PET is triclinic with the following values [87,88].

$a = 4.57$ Å $\quad b = 5.95$ Å $\quad c = 10.75$ Å

$\alpha = 98.5°$ $\quad \beta = 118°$ $\quad \gamma = 112°$.

One study has assigned the crystal refractive indices as [88]

$n_c = 1.806$

$n_b' = 1.733$

$n_a' = 1.398$

where n_c is the refractive index along the chain axis and n_b' and n_a' are refractive indices along mutually perpendicular directions. These refractive indices lead to an average refractive index of 1.646 and an intrinsic crystal birefringence of 0.240. These values are in reasonable agreement with other reported values of 1.64 for the average refractive index [79,80] and 0.220 for the intrinsic crystal birefringence [89].

Use of these refractive indices in equation (V-7) yields a crystalline anisotropy of [40]

$$((\alpha_r - \alpha_t)_c^o)^2 = 1.94 \times 10^{-4}.$$

Substitution of all of these values in equation (V-12) leads to

$$R_{H_v}(U_{max},45) = 65.9\ \phi_c^2\ \overline{Rn}^3 \qquad \text{(V-13)}$$

where $R_{H_v}(U_{max},45)$ is in the units of mm^{-1} and $\overline{R}_n^3$ is in μm. Volume fraction crystallinity, ϕ_c, was calculated from the DSC-determined weight fraction crystallinity, w_c, according to

$$\phi_c = \frac{w_c \rho_a}{\rho_c - w_c (\rho_c - \rho_a)} \qquad \text{(V-14)}$$

where ρ_a and ρ_c are the amorphous and crystalline densities, respectively. For PET, $\rho_a = 1.335$ g/cm³ and $\rho_c = 1.455$ g/cm³ [87].

The theoretical intensities were calculated using equations (V-13) and (V-14), the DSC results and the measured values of $\bar{R}_n$. The theoretical intensities are compared, as functions of temperature, to the corrected experimental intensities from the melting at 2°C per minute in Figure V-14. In consideration of all the assumptions and modifications which were carried out, not only in the analysis, but also in the derivations of the correction theories, the experimental and theoretical intensity agreement is quite gratifying. Additivity of the effects of internal disorder and spherulitic truncation is a particularly significant, and unproven, assumption in this procedure. The comparison between experimental and theoretical intensity becomes unsatisfactory in the very late states of melting, i.e. at temperatures greater than 262°C.

Before the onset of melting (at temperatures at or below 240°C), the experimental intensity is lower than the theoretical intensity by about a factor of 5. This difference could be due to the use of the two dimensional internal disorder theory and/or an overestimation of the truncation effects. The internal disorder effects recently calculated for three dimensional spherulites [35] show that the correction for internal disorder, C_D, is larger for three dimensional spherulites than for two dimensional spherulites with the same polar angle scattering

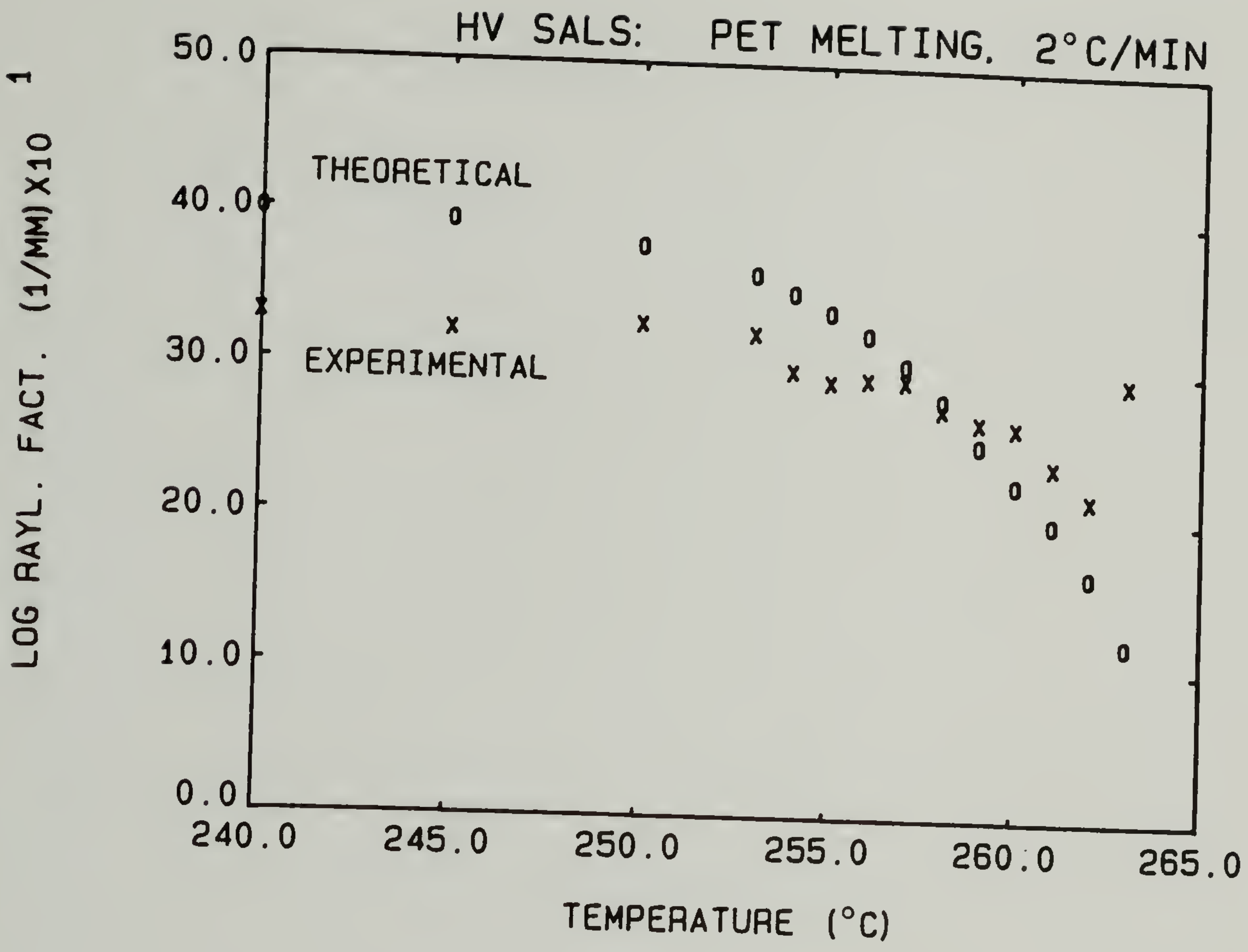

Fig. V-14 Comparison of the theoretically predicted H_v SALS intensity (O) and the corrected experimental intensity (X) during the melting of PET at a heating rate of 2°C per minute.

profile breadth. Unfortunately, the theory is not available for azimuthal profiles and the problems generated by polar angle profiles were discussed in Chapter III.

The preliminary, unpublished work of Yoon on three dimensional internal disorder is summarized in the Appendix [35]. Only polar scattering angle profiles are available in this work.

C_D for three dimensional internal disorder is about 4 times as large as C_D for two dimensional internal disorder for the same, moderately broad, polar angle scattering profile [35]. If one were to suppose that this factor of 4 should be applied to the experimental intensity curve in Figure V-14, the experimental and theoretical curves would be in excellent agreement at 240°C. However, the experimental intensity decrease with increasing temperture would be less rapid than the predicted intensity decrease. This slower intensity decrease may be due to nonrandom amorphous orientation. As one melts crystals, which have a strong tendency to be radially oriented, into amorphous material, it would not be surprising for the converted material to be nonrandom in orientation. Equation (V-6) assumes random amorphous orientation. The slower intensity decrease may be due to such nonrandom amorphous scattering contributions.

Another possible cause of the low value of the corrected experimental intensities may be due to an overestimation of the effects of truncation. In effect, the correction procedures removed all of the other correctable effects, including that due to truncation, and then assigned the remaining deviation in azimuthal profile breadth from the

model as being due to internal disorder. For the same amount of azimuthal profile broadening, the internal disorder correction is larger than the truncation correction. As an example, Figure V-2 plots the azimuthal profile for undisordered, fully truncated spherulites (curve (b)) and for untruncated, disordered, $\delta = 0.2$, spherulites (curve (c)). The breadth of the two profiles are similar. However, the correction factor for truncation, C_T, equals 2.2 for fully grown spherulites, whereas the correction factor for internal disorder, C_D, equals about 10 (see Figure V-5) for $\delta = 0.2$. If too much of the profile breadth was assigned as truncation effects, then the overall correction factor would be less and the internal disorder parameter, δ, would be lower. The results presented here for the melting of PET had low values of δ and low values for the corrected experimental intensities, thus implying the possibility of over correction for truncation.

The possibility of over correction from truncation is a result of the assumptions used in the truncation analysis in Chapter III. In the derivation of the effects of truncation, the nuclei were randomly located. In a study by Misra et al [48], it was found that polyethylene spherulites tend to develop as though the nuclei were not randomly located. They found that, if an artificial restriction on the minimum distance between nuclei was imposed, that the truncation parameters of computer simulated, fully grown, two dimensional spherulites more closely matched those measured from a polyethylene micrograph. Application of the restriction in the computer simulation lowered the truncation parameter. Therefore, application of the theory of the

effects of truncation from randomly nucleated spherulites may overestimate the effects of truncation, underestimate the effects of internal disorder and therefore under correct the intensities, leading to corrected experimental intensities which are lower than theoretically predicted intensities, as was found in this study.

No clear explanations of why heterogeneously nucleated spherulites would nucelate nonrandomly were presented in the Misra study [48]. Therefore, the truncation study presented in Chapter III used the widely accepted notion of randomly nucleated spherulites. The nuclei generating routines were developed to include a restriction on the minimum distance between two nuclei. The restriction was not applied due to a lack of convincing evidence such restrictions are justified.

Conclusions

This chapter presented the results of melting studies of PET made by H_v SALS and DSC. The studies were performed to investigate the morphology of the melting behavior of PET and to examine the validity of quantitative SALS techniques as applied to spherulitic polymer films.

It was found that the fully grown spherulites melt over a temperature range of about 20°C without change in spherulite size, number or internal disorder. The decrease in H_v SALS intensity was due to a decrease in spherulitic crystallinity over the melting range. The corrected experimental intensities are lower than, but in reasonable agreement with, the theoretically predicted intensities. The differences between the intensities may be attributable to the lack of a

suitable three dimensional spherulite internal disorder theory, nonrandom amorphous orientation following the melting of crystals and/or an overestimation of the effects of spherulitic truncation.

The procedures have been presented for correcting H_v SALS intensity data from three dimensional, simultaneously nucleated spherulites for experimental, external disorder and internal disorder effects. These procedures, along with the relevant chapter figures and Appendix tables in this dissertation, are summarized in the following steps:

1) Measure $R_{H_{v,exp}}(\theta,\mu)$ from at least one quadrant of the pattern;
2) Measure τd for the sample;
3) Determine θ_{max}, $\bar{R}_n$, $(\theta_{max},\infty)/\theta_{max}$ and ϕ_s (Figure III-24 and Table A-7);
4) Correct $R_{H_{v,exp}}(U_{max},\mu)$ at $\mu = 45, 20, 10$ and 0° for multiple scattering by multiplying by $C_M(U_{max},\mu)$ (Figure V-1 and Table A-10);
5) Combine theoretical H_v intensities, at $U = U_{max}$ and $\mu = 45, 20,$ 10 and 0°, due to internal disorder and spherulitic truncation for the calculated value of ϕ_s (Figures III-23, V-2 and V-3 and Tables A-6 and A-11);
6) Determine H_v intensity ratios $I(U_{max},45)/I(U_{max},\mu)$ from the results of step 5 for several values of δ;
7) Determine the internal disorder parameter, δ, from the intensity ratios in step 6 (Figure V-4 and Table A-12, for example);
8) Determine internal disorder correction, C_D, from the value of δ (Figure V-5 and Table A-13);

9) Determine truncation correction, C_T, from the value of ϕ_s (Figure III-22 and Table A-5);

10) Correct $R_{H_{v,exp}}$ $(U_{max}, 45)$ by multiplying by $C_{refl}\ C_{refr}\ C_T\ C_D$;

11) Determine average spherulite volume, V, from the value of ϕ_s (Figure III-25 and Table A-8);

12) Apply values in equation (V-1).

Similar procedures could also be carried out for two dimensional spherulites, either simultaneously or sporadically nucleated, using the figures and tables presented in this dissertation.

CHAPTER VI

STUDIES OF THE CRYSTALLIZATION OF POLYETHYLENE TEREPHTHALATE

Introduction

Chapter V presented the results of a study of the melting of PET. In that chapter the theories and procedures necessary for quantitative H_v SALS from spherulitic polymer films were developed for the volume filling spherulites encountered during the melting process. The size, number and internal disorder of the spherulites did not change over the melting range.

Crystallization is a more complicated process to examine by SALS due to the concurrent changes in the size, number and anisotropy of the spherulites possible during the process. The SALS equations must be used in the more general form of non-volume filling spherulites.

Several studies have used a rather empirical relationship between the total depolarized light scattering intensity and crystallinity to follow polymer crystallization [90-93]. A recent theoretical development relates the degree of crystallinity in a spherulitic system to the crossed polars light scattering invariant [73]. This theory is based on model type spherulites. Corrections for the effects of internal disorder, which have not been developed, are necessary to employ this theory to follow practical polymer spherulite growth. The approach outlined in Chapter V for following crystallinity through quantitative analysis of the H_v SALS maximum intensity is a more fully

developed technique to follow crystallization by SALS.

This chapter presents a study of the crystallization of PET from the melt by SALS. Sample turbidity and quantitative H_v and V_v SALS techniques will be used to examine the SALS theories and the effect of crystallization on the spherulite size, the number of spherulites, the volume fraction spherulites, the spherulitic and nonspherulitic crystallinities and the internal disorder. DSC results will be used as a comparison to the SALS results. This study is a continuation of a similar study in our laboratory [39].

Theory

Chapter V presented the development of the theory and procedures for quantitative H_v SALS from volume filling PET spherulites. For crystallization, these theories and procedures must be generalized to the non-volume filling case. In addition, V_v SALS will also be used in the crystallization study.

Equation (V-1) can be rewritten for non-volume filling spherulites as

$$R_{H_v}(U,\mu) = \frac{144\pi^4\phi_s V}{\lambda_o^4}(\alpha_r - \alpha_t)^2\left[(\cos^2\frac{\theta}{2}/\cos\theta)\sin\mu\cos\mu\cos\rho_2\Phi_{H_v}\right]^2 \qquad \text{(VI-1)}$$

where N_sV has been replaced by the volume fraction spherulites, ϕ_s, and the other terms are as previously defined. Again, assuming that the amorphous orientation and the form anisotropy are negligible, the

spherulite anisotropy is given by

$$(\alpha_r - \alpha_t) = (\alpha_r - \alpha_t)_c^o \phi_{cs} \qquad \text{(VI-2)}$$

where the terms are all as previously defined. Combination of equations (VI-1) and (VI-2) at $U = U_{max}$ and $\mu = 45°$ with the relationships presented in Chapter V yields for PET

$$R_{H_v} (U_{max}, 45) = 33.5 \, \phi_{cs}^2 \, \phi_s \, K_v \, \bar{R}_n^{-3} \qquad \text{(VI-3)}$$

where $R_{H_v} (U_{max}, 45)$ is in the units of mm^{-1} and $\bar{R}_n$ is in μm. Equation (VI-3) reduces to equation (V-13) for the case of ϕ_s equal to unity. ϕ_s is calculable from $\theta_{max,\infty}/\theta_{max}$, assuming three dimensional, simultaneously nucleated spherulites, and $\bar{R}_n$ is determined from θ_{max}. Both calculation methods were presented in Chapter III.

The H_v SALS intensity data can therefore be used to determine the changes in the size of the spherulites, the volume fraction spherulites and the volume fraction crystallinity of the spherulites as functions of time during crystallization. This type of analysis of course necessitates the use of quantitative H_v SALS, including the calibrations and corrections outlined in Chapters IV and V. The spherulite growth rate, the number of spherulites per volume and the internal disorder can also be determined from the H_v SALS data.

The V_v SALS intensity measured during crystallization can be analyzed according to equation (II-5). For PET crystallization, the following values can be substituted into equations (II-5) and (II-6):

$\cos\rho_1 \approx 1.$

$\sin\rho_1 \approx 0.$

$\lambda_o = 0.6328$ µm and

$(\cos^2\theta/2)/\cos\theta \simeq 1$.

Using the spherulite truncation results of Chapter III, the factor $4/3\ \pi\bar{R}_s$ in equation (II-5) can be replaced by $K_v\ \bar{R}_n^3$. Substitution of these values into equation (II-5) leads to

$$R_{V_v}\ (U,\mu) = 8.75 \cdot 10^7\ K_v\ \bar{R}_n^{-3}\ B(\phi_s)\ [(\alpha_r - \alpha_s)\ \Phi_{V_v}^A + (\alpha_t - \alpha_s)\ \Phi_{V_v}^B + (\alpha_r - \alpha_t)\cos^2\mu\ \Phi_{H_v}]^2 \qquad \text{(VI-4)}$$

where $R_{V_v}\ (U,\mu)$ is the units of mm^{-1} and $\bar{R}_n$ is in µm. The terms are as previously defined. The values of the polarizabilities, $\bar{R}_n$ and ϕ_s can be determined as functions of the crystallization time from the H_v SALS. One can then apply these values in equation (VI-4), calculate the V_v SALS intensities and compare them to the measured intensities. In this method the V_v SALS complements the H_v SALS. In contrast to H_v SALS, the V_v intensities are dependent upon the value of the polarizability of the spherulite's surroundings, α_s. These calculations and comparisons are made later in this chapter.

Experimental

Sample preparation. The characterization of the PET used, the preparation of the pressed films and the optical microscopy of the crystallized films were the same as that given in Chapter V. The samples for SALS were prepared in a fashion similar to that used for the melting studies. The films were 35 µm in thickness. They were melted in the microscope slide/cover glass assembly for 3 minutes at 278 ± 3°C

in the oil bath and then allowed to cool slowly in air to room temperature. The samples were stored in a desiccator until use.

SALS. The H_v and V_v SALS experiments were performed using the OMA2 described in Chapter III. The geometry of the OMA2 was chosen such that all four quadrants of the scattering pattern were collected by the detector. The system was calibrated in terms of scattering angles, sensitivity and absolute intensity according to the procedures outlined in Chapter IV.

The sample assembly (microscope slide, sample and cover glass) was heated on a Kofler hot stage for three minutes at 275 ± 3°C. The assembly was quickly moved to a Mettler hot stage, temperature controlled at 200 ± 0.5°C, for the SALS study of crystallization. For H_v and V_v SALS, scans (2450 data points each) were collected every 5.6 seconds, up to 160 seconds. For H_v SALS, time = 0 was assumed to be the time when the extrapolated spherulite size equalled zero. For V_v SALS, time = 0 was assumed to be the time when the extrapolated intensities at $\mu = 0°$ and $U_\infty = 4$ and 8 equalled zero. (U_∞ is defined in terms of the maximum spherulite size.)

Transmission. The transmission of the samples was also measured as a function of time during crystallization using the OMA2 and equation (V-10). The thermal cycle for the transmission measurements was the same as that for the SALS studies. The transmission of a separate sample was measured during crystallization. The values of τd were normalized to the same values after complete crystallization as the samples used for H_v and V_v SALS. For the transmission tests, time = 0

was assumed to be the time when the extrapolated value of τd equalled zero. All of the OMA2 data was collected and stored on flexible disks for later analysis.

Differential scanning calorimetry. The DSC was calibrated for temperature and heat of fusion using tin and lead standards. The samples used were removed from the glass slide assembly after crystallization in the OMA2. The crystallinity of the samples was determined by melting. The samples were heated from room temperature to 177°C at 320°C per minute. They were then heated at 20°C per minute through the melting point. The endotherms were analyzed gravimetrically. The results represent the average of two samples.

Results

Optical microscopy. A crossed polars micrograph of a SALS sample following crystallization is given in Figure VI-1. Although the sample is too thick to distinguish the spherulites, the birefringent nature of the sample is apparent.

SALS. Photographic H_v and V_v SALS patterns from the samples after crystallization were given in Figures II-2a and II-2b, respectively. These patterns display the typical four-leaf clover pattern and the anisotropic dumbbell pattern expected from spherulitic PET.

The H_v and V_v SALS intensities, measured on the OMA2 as functions of the crystallization time, were converted to absolute intensities as functions of the scattering angle ($R(\theta,\mu)$) using the OMA2 analysis

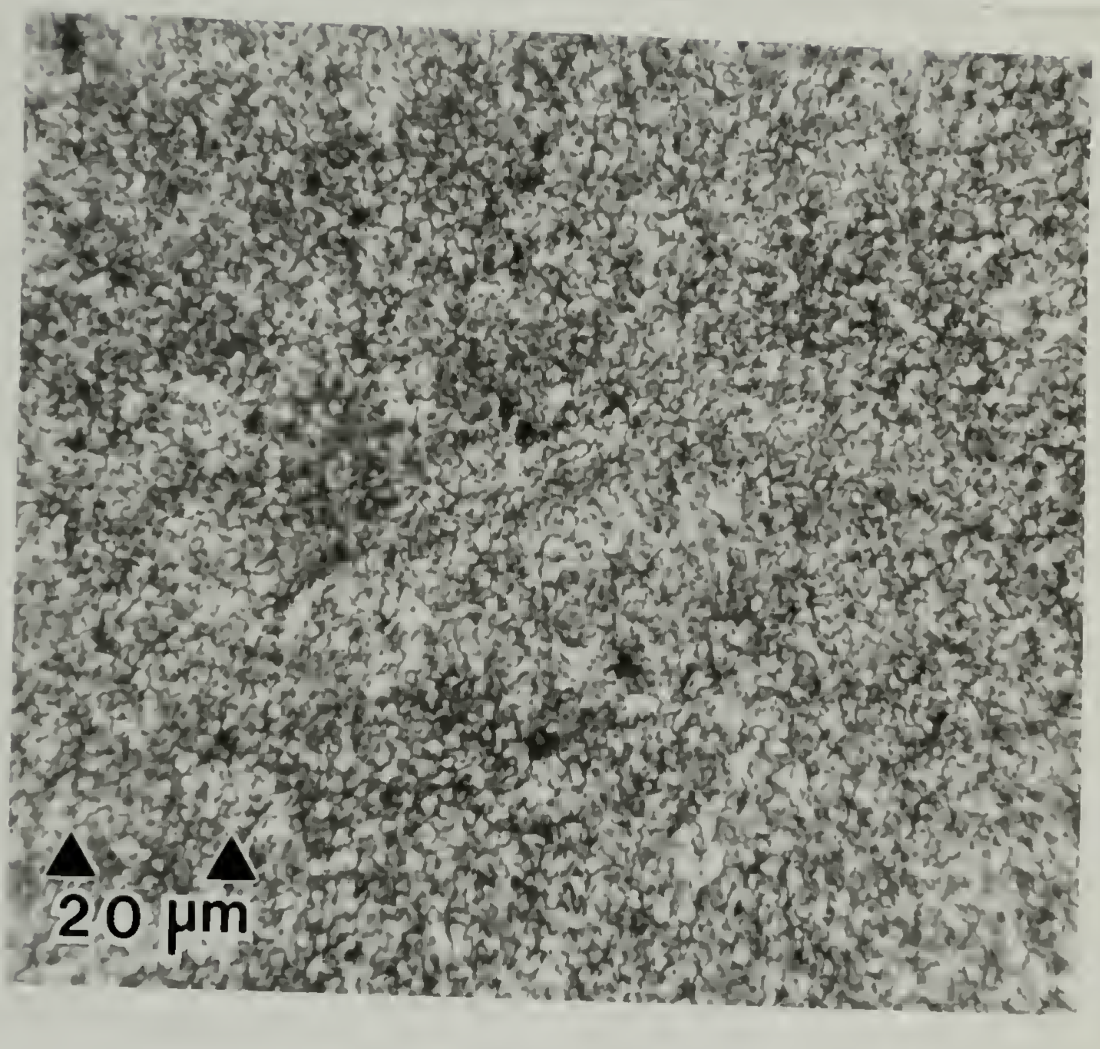

Fig. VI-1 Optical micrograph of PET crystallized from the melt for 10 minutes at 200°C; crossed polars.

software and the calibration standards as described in Chapter IV.

The H_v intensity data has been single quadrant averaged. Sample isointensity contours of the H_v SALS at time = 12, 18, 24 and 35 seconds are given in Figure VI-2. The contours are at the same intensity levels for all four patterns in Figure VI-2. It is apparent that there is an increase in intensity with crystallization time. It is also apparent that the polar angle of maximum intensity decreases with crystallization time, indicating an increase in spherulite size.

To examine these H_v SALS patterns according to the theories presented earlier, profiles at a constant azimuthal angle of $\mu = 45°$, as functions of the magnitude of the scattering vector, H, were determined at each crystallization time. Some of these intensity profiles are given in Figure VI-3. The profiles are more smooth than the original profiles obtained at $\mu = 45°$ for the melting study. (The melting study profiles were fit to 8th order polynomials to smooth them.) This fact is likely due to the collection of the SALS data during crystallization over all four quadrants of the scattering pattern, whereas the SALS scans during the melting covered only one quadrant. As described in Chapter IV, collecting data over all four quadrants improves the signal-to-noise ratio at the expense of angular resolution.

The average radius of the spherulites, $\bar{R}_n$, was determined from the H_v SALS profiles at $\mu = 45°$ and equation (III-17). $\bar{R}_n$ as a function of crystallization time is given in Figure VI-4. It can be seen from this figure that the spherulites grow rapidly and reach full growth early in the experiment. The spherulite growth rate was determined from the

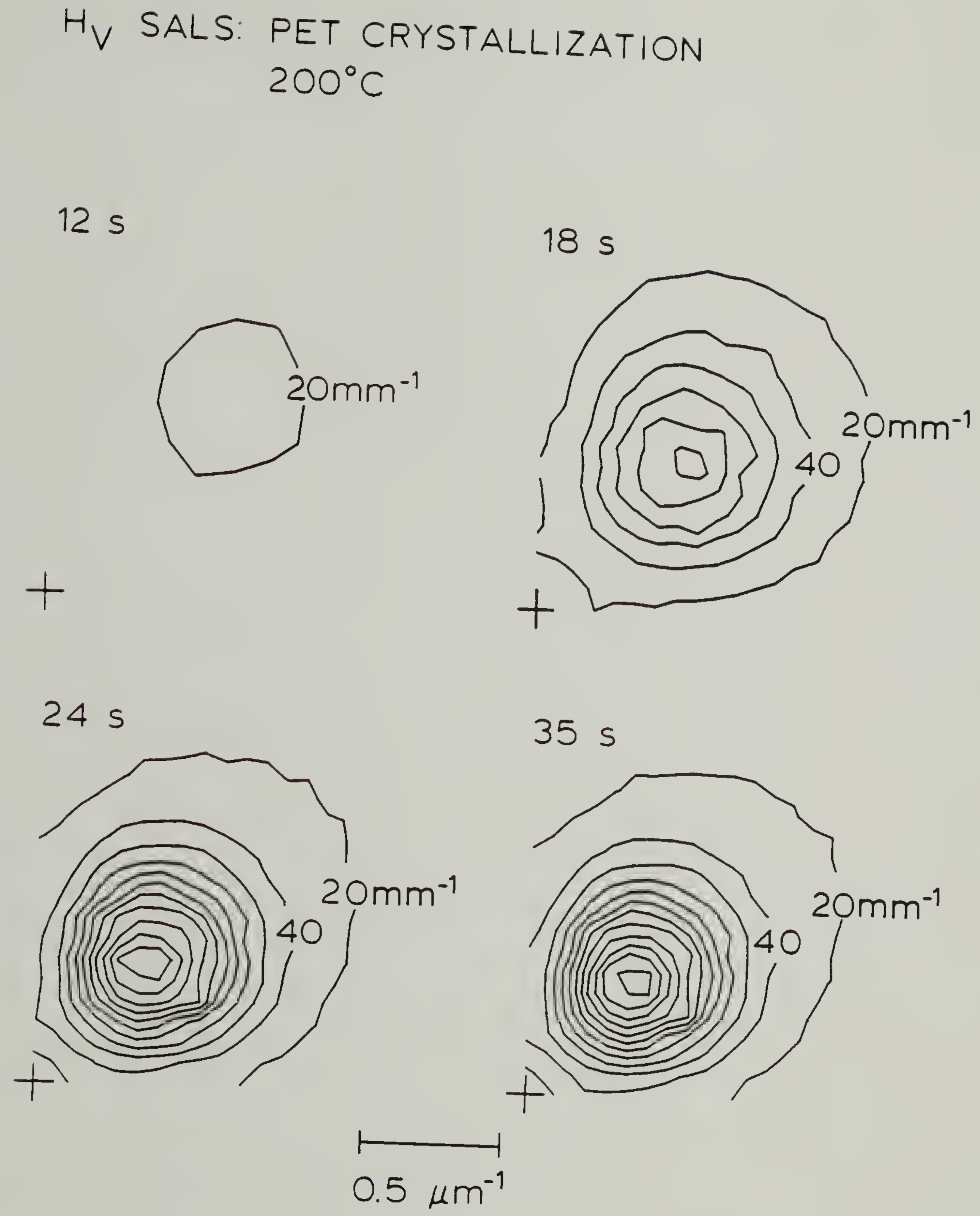

Fig. VI-2 Isointensity contours of single quadrant averaged H_v SALS patterns from PET crystallized from the melt at 200°C for 12, 18, 24, and 35 seconds. The contour levels are at intervals of 20 mm^{-1}.

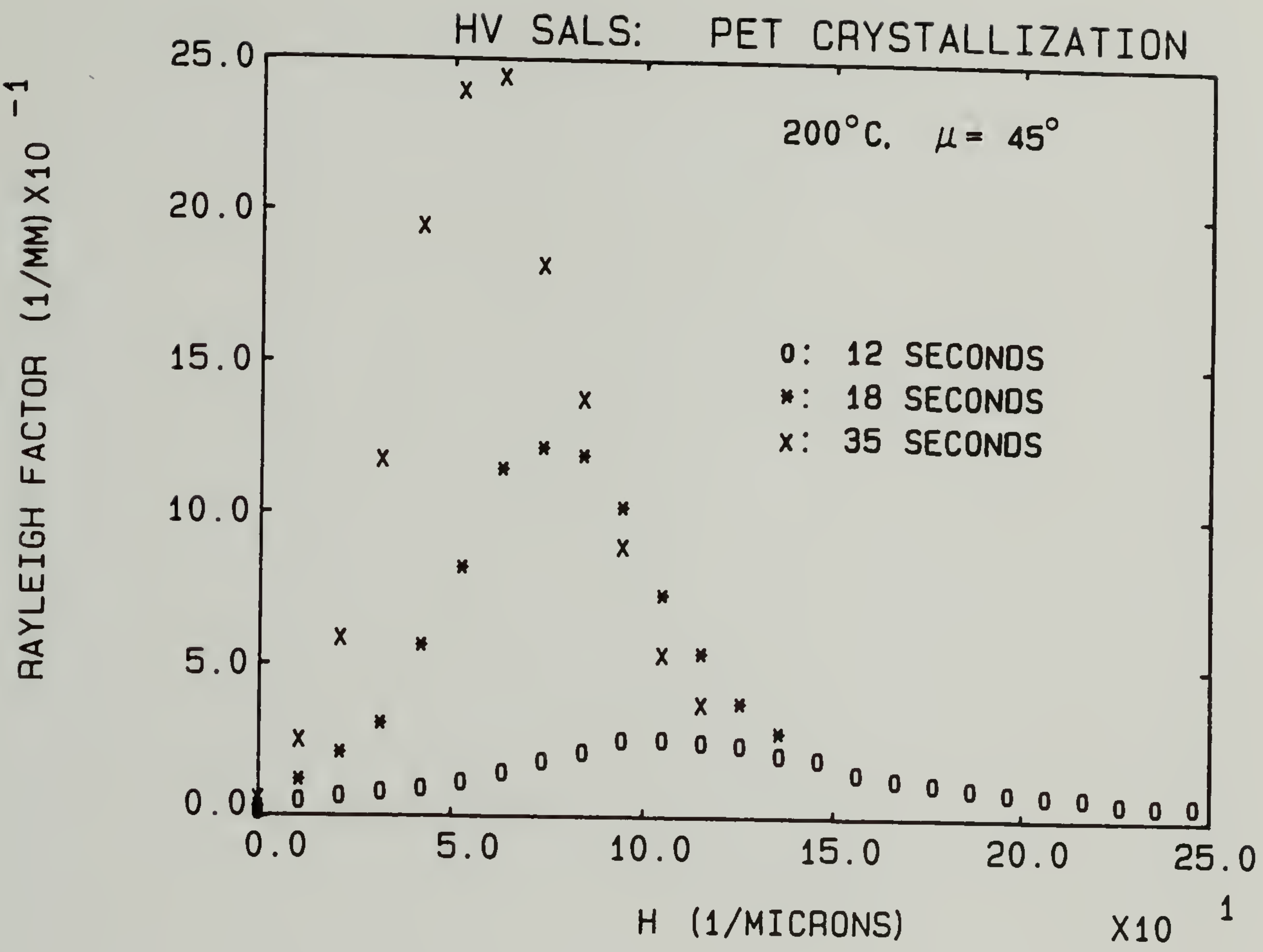

Fig. VI-3 H_v SALS intensity profiles at μ = 45°, as functions of the magnitude of the scattering vector, for different crystallization times.

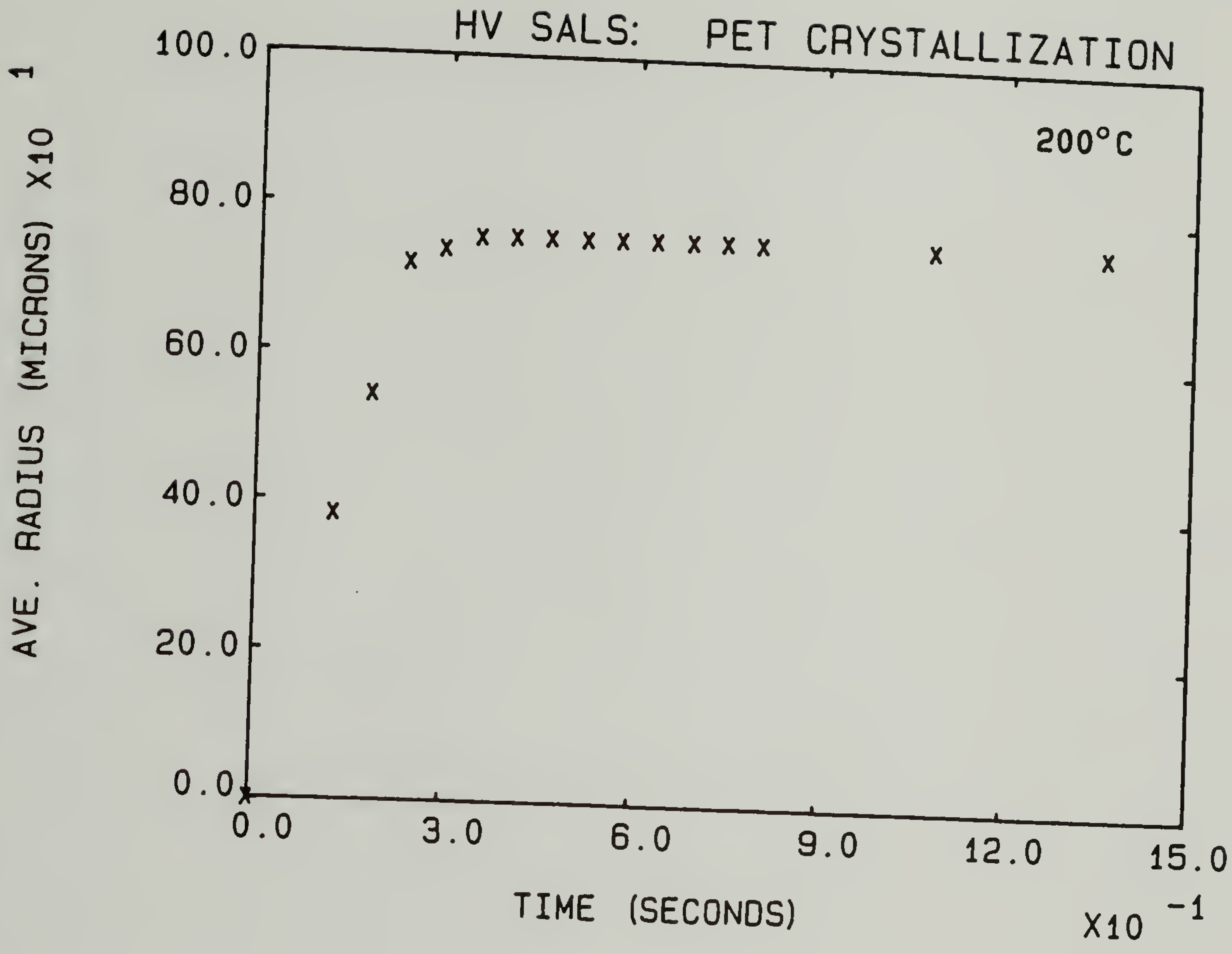

Fig. VI-4 Average spherulite radius, determined by H_v SALS, as a function of crystallization time.

initial slope of Figure VI-4 to be 0.30 ± 0.05 µm per second. The average spherulite radius after full growth was 7.6 ± 0.1 µm.

To further examine the H_v SALS theories and the morphology of the PET spherulites, intensity profiles as functions of the azimuthal angle, at the polar angle of maximum intensity, were determined for each crystallization time. Some of these profiles are given in Figure VI-5. The intensity at the maximum increases with crystallization time. The maxima of course occur near $\mu = 45°$. The breadth of the profiles is related to the multiple scattering of the sample, the internal disorder and the truncation. The corrected intensity at the maximum is related to several factors, including spherulite size, volume fraction and crystallinity. These effects will be examined in the discussion section.

Isointensity contour diagrams of the V_v SALS patterns are plotted in Figure VI-6 for six crystallization times. As described in previous examinations of V_v SALS patterns [2,9], the V_v patterns change during crystallization from circularly symmetric, to oval shaped to the dumbbell shape as the sample becomes filled with spherulites. An explanation of the V_v SALS pattern shape changes was given in Chapter II.

The isointensity contour levels are at the same intensity intervals for each plot in Figure VI-6. From these contours one can see that the V_v intensity increased during crystallization, reached a maximum, decreased to a new level and then remained approximately constant throughout the remainder of the experiment. These intensity changes are

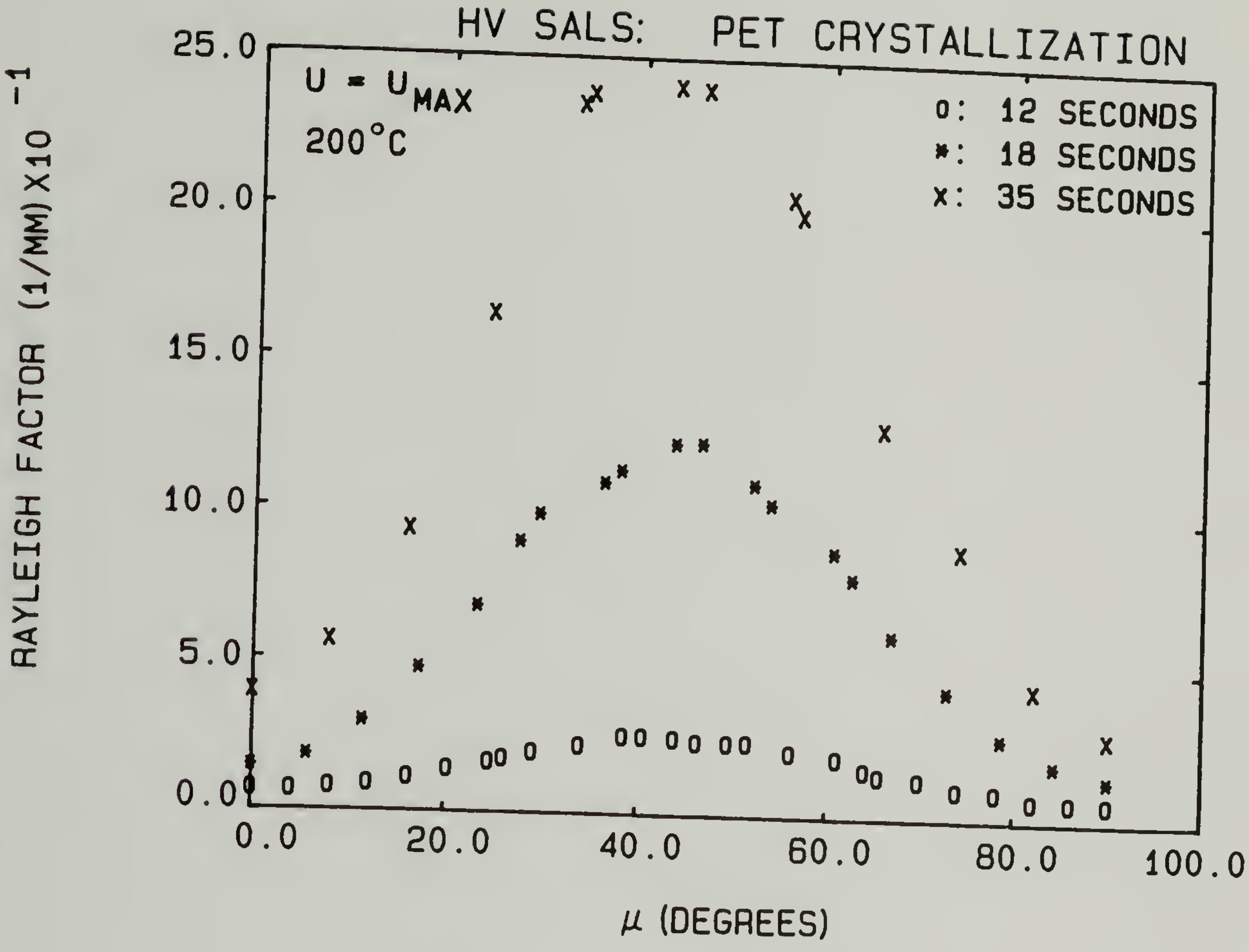

Fig. VI-5 H_v SALS intensity profiles at $U = U_{max}$, as functions of the azimuthal angle, for different crystallization times.

Fig. VI-6 Isointensity contours of four quadrant V_v SALS patterns from PET crystallized from the melt at 200°C for 2, 8, 13, 19, 25 and 36 seconds. The contour levels are at intervals of 70 mm^{-1}. The main beam is suppressed within the central hatched circle.

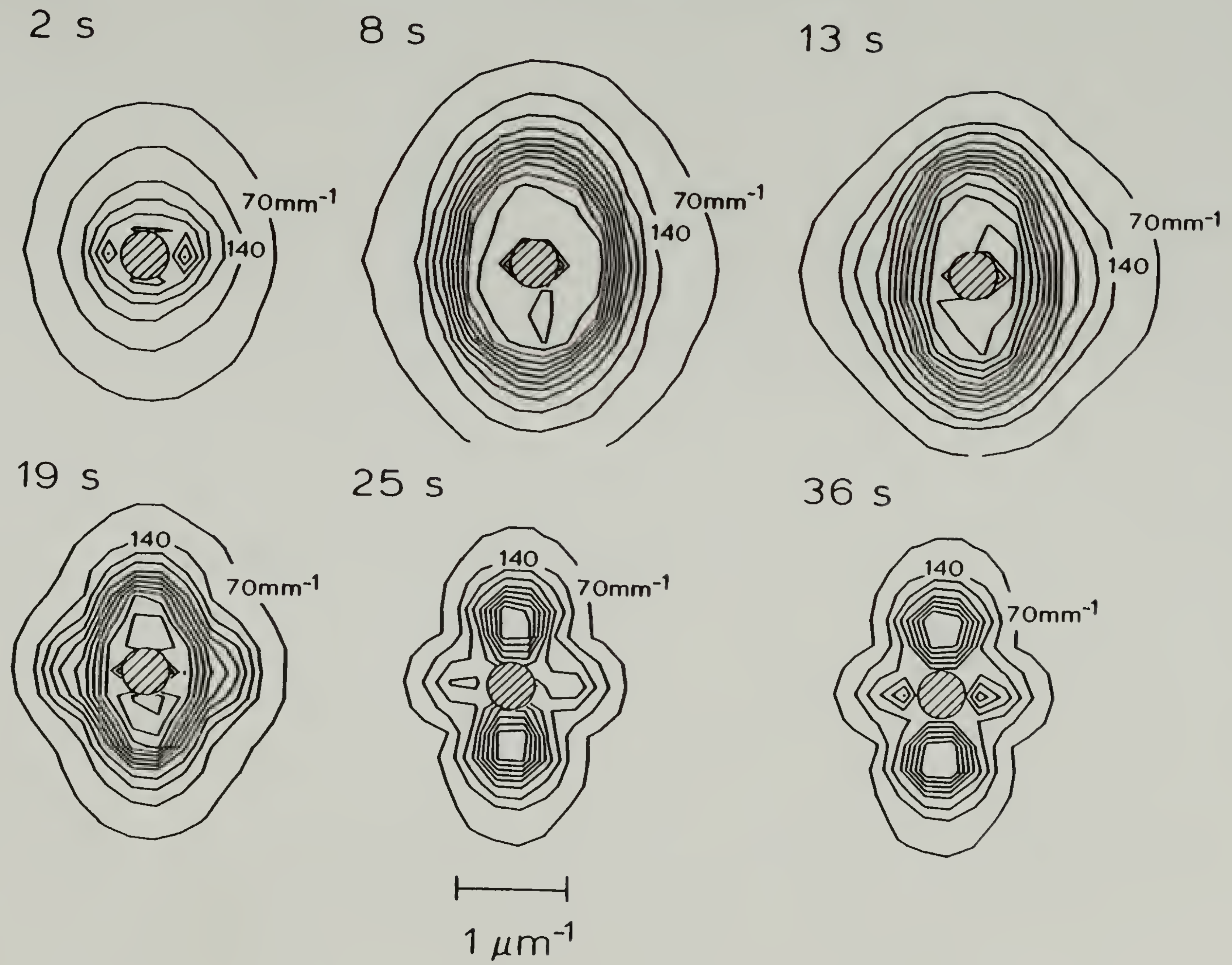

V_V SALS: PET CRYSTALLIZATION, 200°C

more apparent in Figure VI-7 where the V_v SALS intensities are plotted as functions of crystallization time at fixed polar and azimuthal scattering angle locations. (The V_v SALS intensity patterns were quadrant averaged before the constant angle analysis was performed. The values of $H = 0.53$ and $1.06\ \mu m^{-1}$ represent $U_\infty = 4$ and 8, respectively, where U_∞ is calculated using the spherulite size at full growth.) Chapter II presented the explanation of such intensity changes during polymer crystallization.

Transmission. The value of τd is plotted in Figure VI-8 as a function of the crystallization time. The turbidity of course behaved in a fashion similar to the V_v intensity: increasing rapidly, reaching a maximum, decreasing to a new level and remaining relatively constant. The values of τd were used to evaluate the volume fraction spherulites and the effects of multiple scattering.

Differential scanning calorimetry. The average weight fraction crystallinity, w_c, after crystallization in the OMA2 at 200°C, was 0.36 ± 0.03. The crystallinity was calculated from the area under the melting endotherm, being calibrated by the melting of a tin standard. The value of the heat of fusion of PET used was 30. cal/g [82].

Discussion

The SALS and transmission results indicate that the crystallization process for the PET was very rapid and the spherulite growth rate was high. The growth rate and the maximum average spherulite radius can be

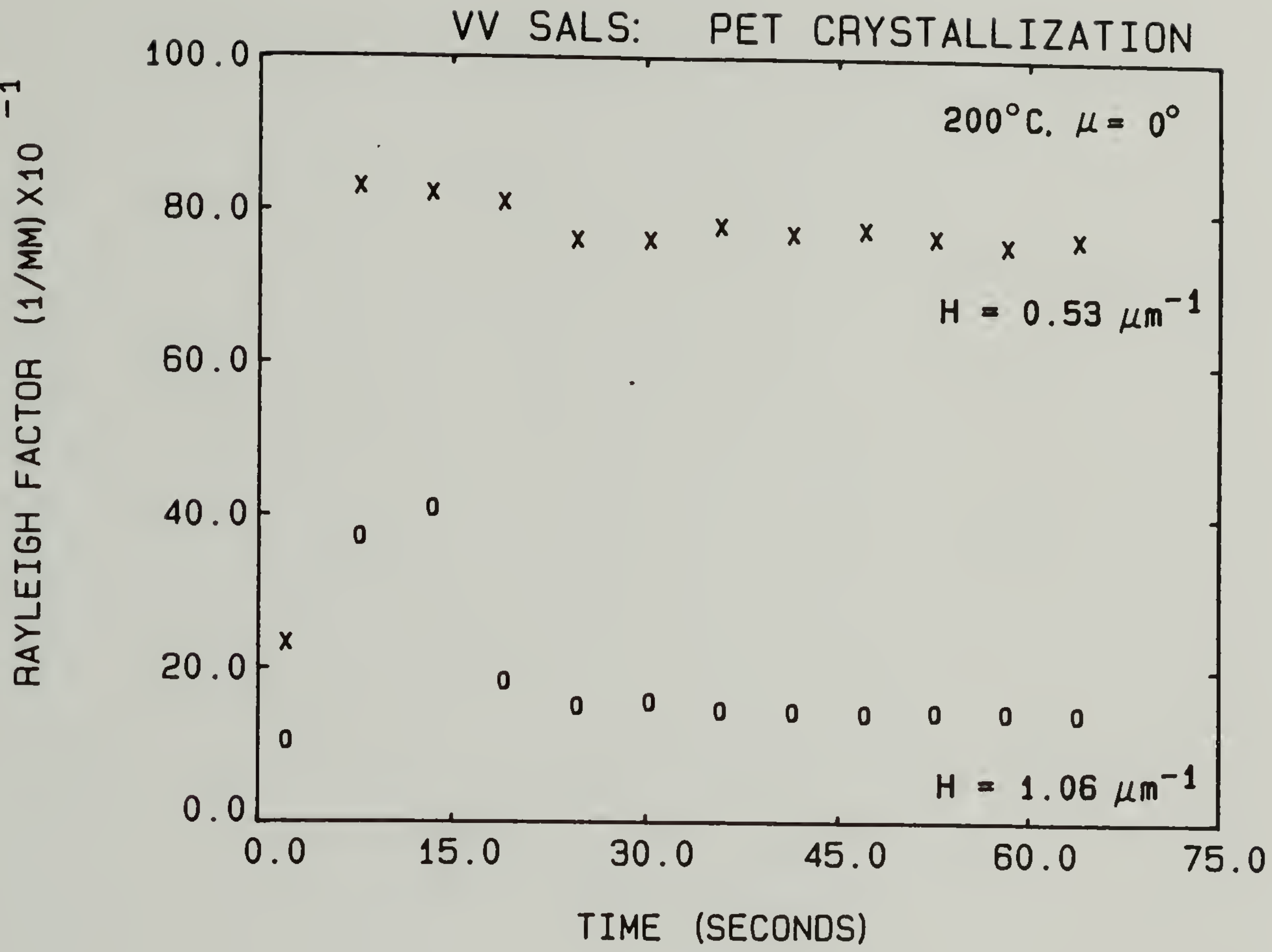

Fig. VI-7a V_v SALS intensities at (X) H = 0.53 and (O) H = 1.06 μm^{-1}, as functions of the crystallization time; $\mu = 0°$

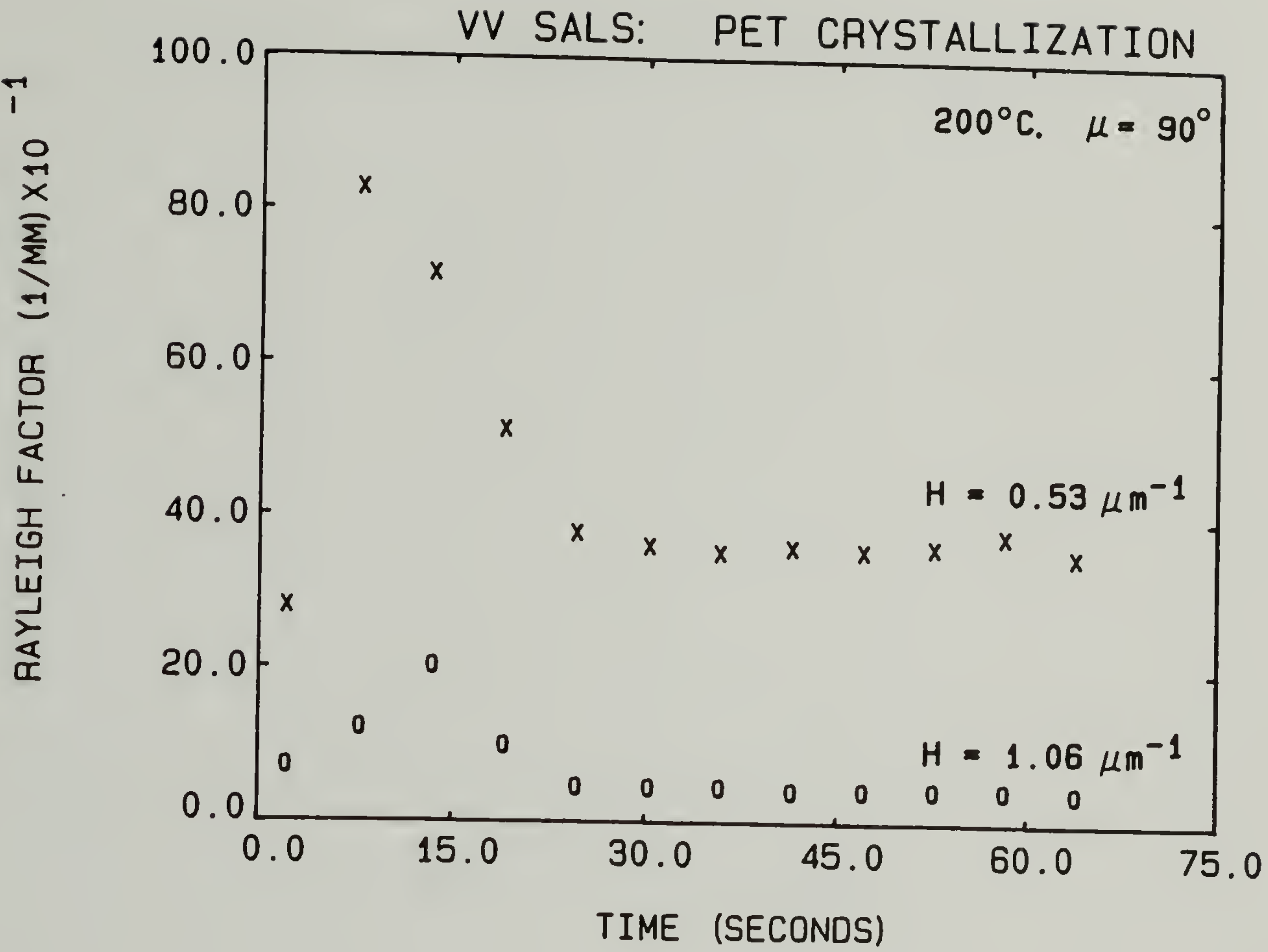

Fig. VI-7b V_v SALS intensities at (X) H = 0.53 and (O) H = 1.06 μm^{-1}, as functions of the crystallization time; μ = 90°.

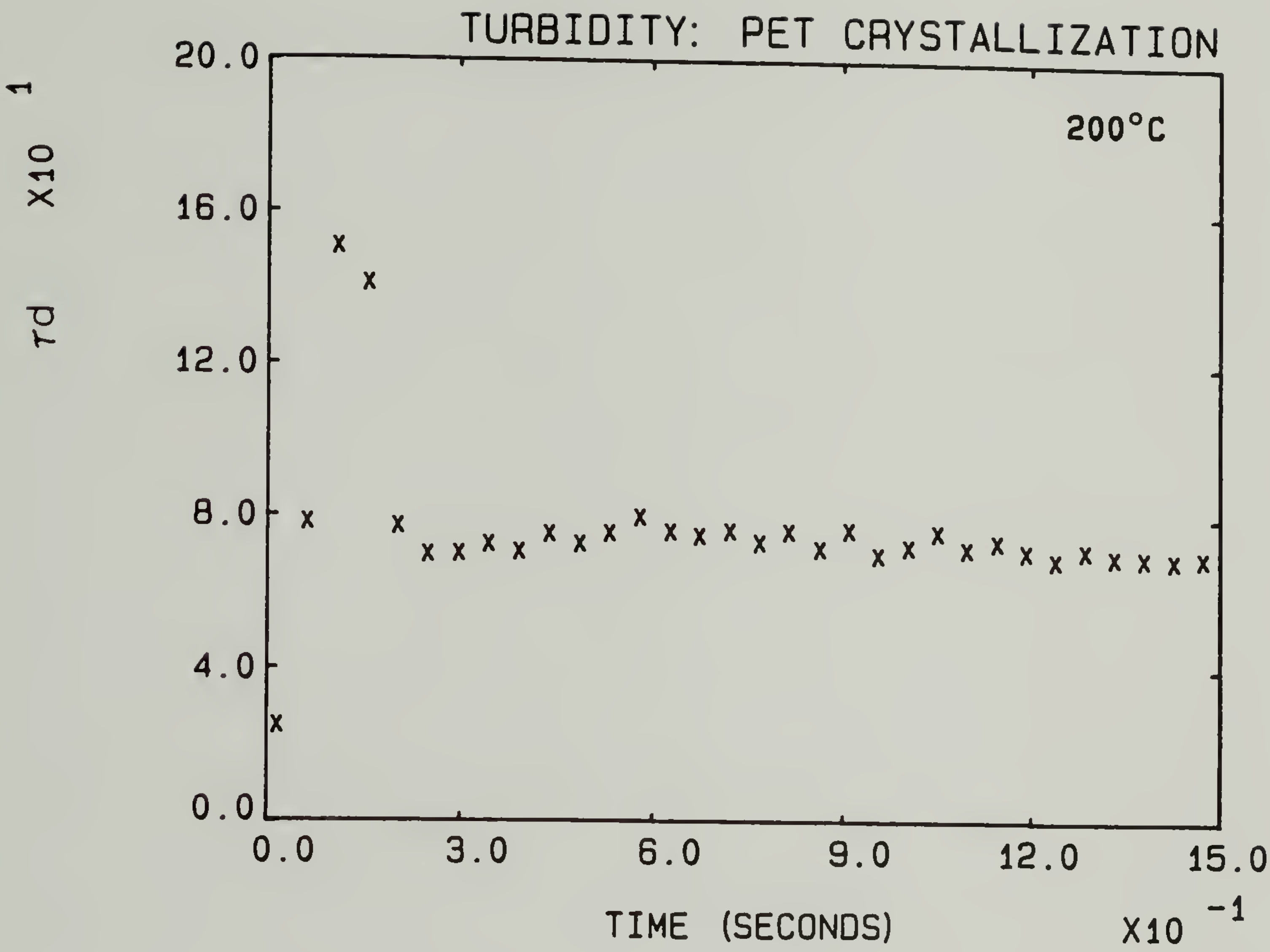

Fig. VI-8 τd as a function of crystallization time.

compared to the values measured from other studies of PET crystallization. van Antwerpen et al. [90] derived a relationship for the spherulite growth rate of PET crystallized from the melt, as a function of the number average molecular weight, M_N, and the crystallization temperature. M_N was not measured for the PET used in this study. Assuming that $M_N \approx 0.75\ M_v$ [94], M_N for the PET in this study was approximately 13,000. The van Antwerpen equation predicts a spherulite growth rate of 0.12 µm per second for PET of this molecular weight crystallized at 200°C. Baranov et al. [79] measured the spherulite growth rate of PET, $M_N = 13{,}000$ and crystallization temperature of 200°C, by H_v SALS to be about 0.07 µm per second. The spherulite growth rate of 0.30 µm per second measured in this study seems to have about the same order of magnitude, but is somewhat higher than these other reported values. Of course the growth rate may be influenced by factors other than M_N and temperature, such as sample purity, molecular weight distribution or material additives [90]. The maximum average spherulite radius of 7.6 µm was in the general size range predicted by van Antwerpen et al. [90], if one extrapolates their results to the low molecular weight used here.

The values of the polar angle of maximum H_v SALS intensity, θ_{max}, were determined from the scattering profiles at $\mu = 45°$, some of which are depicted in Figure VI-3. Using the value of θ_{max} after complete growth ($\theta_{max,\infty}$), θ_{max} at each crystallization time and the relationship represented in Figure III-24, the volume fraction spherulites, ϕ_s, was calculated. ϕ_s is plotted in Figure VI-9 as a function of

crystallization time. Since the relationship between ϕ_s and θ_{max} was derived in Chapter III assuming three dimensional spherulite growth following simultaneous nucleation, it would not be reasonable to perform an Avrami type analysis [55,56] on the data represented in Figure VI-9. Correspondence between the volume fraction spherulites given in Figure VI-9 with that determined from the V_v SALS and the transmission results would be a partial verification of the applicability of the model used. These comparisons are made later in this section.

The number of spherulites per volume, N_s, can be related to the average spherulite volume and the volume fraction spherulites by

$$N_s = \frac{\phi_s}{V} \quad . \tag{VI-4}$$

ϕ_s is given in Figure VI-9 as a function of crystallization time. V can be calculated from the values of $\bar{R}_n$ and ϕ_s (Figures VI-4 and VI-9) and the relationships between ϕ_s, $\bar{R}_n$ and V (Figure III-25 and equation (III-20)). One can then calculate N_s from these values and equation (VI-4). N_s is calculated in this system to have a constant value of $1.2 \cdot 10^6$ nuclei per mm^3. Of course the derivations of the relationship among θ_{max}, ϕ_s and V were made assuming three dimensional spherulite growth following simultaneous nucleation. Since this derivation assumes that N_s remains constant during spherulite growth, the analysis of any spherulitization by this procedure must yield a constant value of N_s.

Quantitative H_v SALS was carried out using the azimuthal scattering profiles at $U = U_{max}$ using equation (VI-3) and the correction procedures outlined in Chapter V. The azimuthal profiles were corrected for

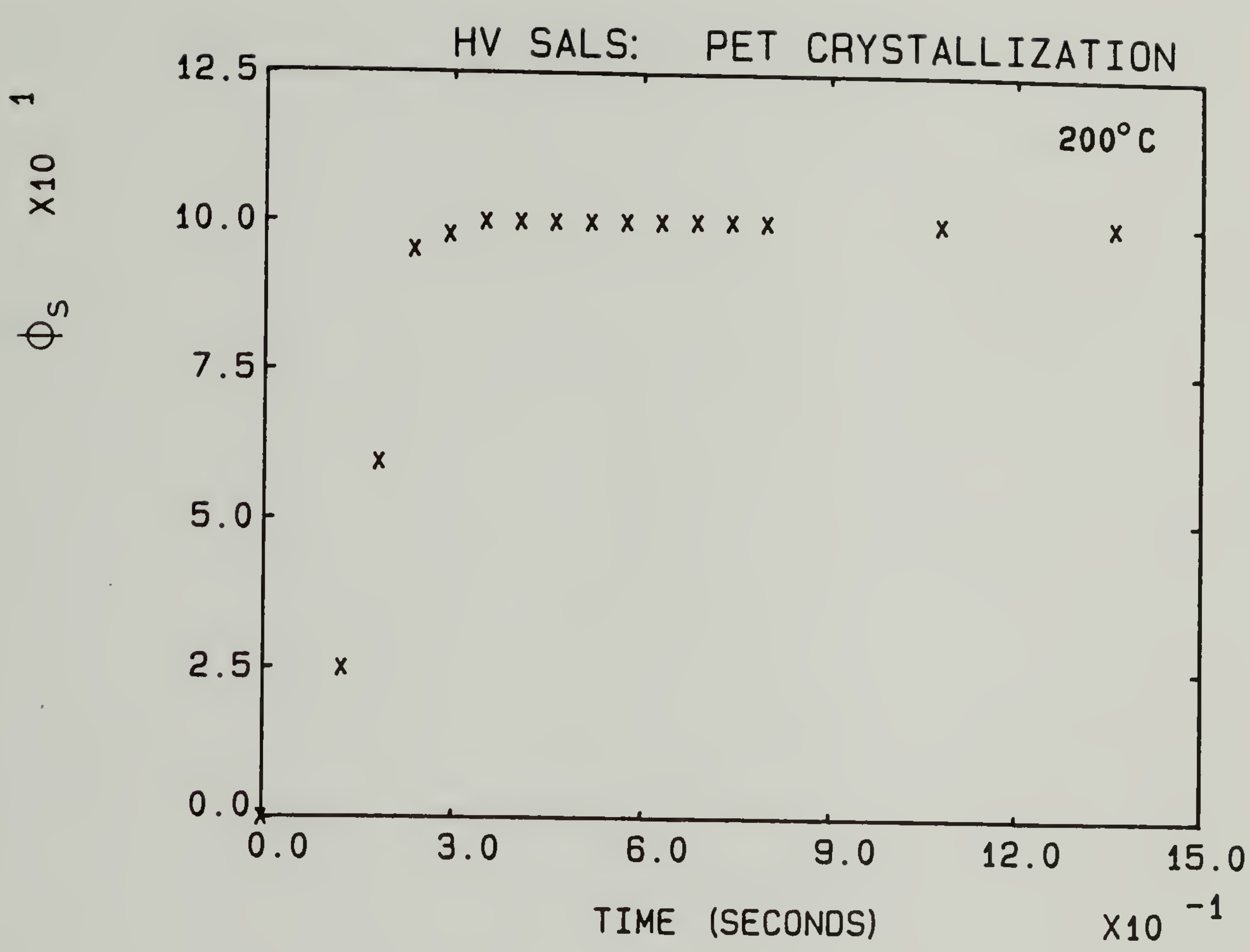

Fig. VI-9 Volume fraction spherulites, determined by H_v SALS, as a function of crystallization time.

multiple scattering at $\mu = 45$, 20, 10 and 0° using the τd values given in Figure VI-8 and the correction curves given in Figure V-1.

The analysis of internal disorder in the presence of varying amounts of truncation was also made following the techniqes outlined in Chapter V. Using the value of ϕ_s given in Figure VI-9 along with the H_V intensity ratios $R_{H_V}(U_{max},\mu)/R_{H_V}(U_{max},45)$ given in Figure III-23, the theoretical intensity ratios at $\mu = 20$, 10 and 0° were calculated for each crystallization time. These ratios were combined with similar ratios for several values of the internal disorder parameter (Figure V-3) to develop plots of the internal disorder parameter as functions of each of the three intensity ratios for each value of ϕ_s. The internal disorder parameter was then determined from these plots and the experimental intensity ratios, following the multiple scattering correction.

The calculated average internal disorder parameter is plotted as a function of crystallization time in Figure VI-10. The internal disorder decreases in the early stages of crystallization and then levels off. The value of δ became negative after about 20 seconds of crystallization time. Possible reasons for the low value of δ are similar to those presented in Chapter V for PET spherulite melting.

An initial decrease in the internal disorder during crystallization apparently differs from the results of Yuasa [39]. In that study δ was reported to remain relatively constant at a value of 0.22 during the crystallization. That study did not adjust the azimuthal profile breadth for the effects of truncation as was done in this study. Since

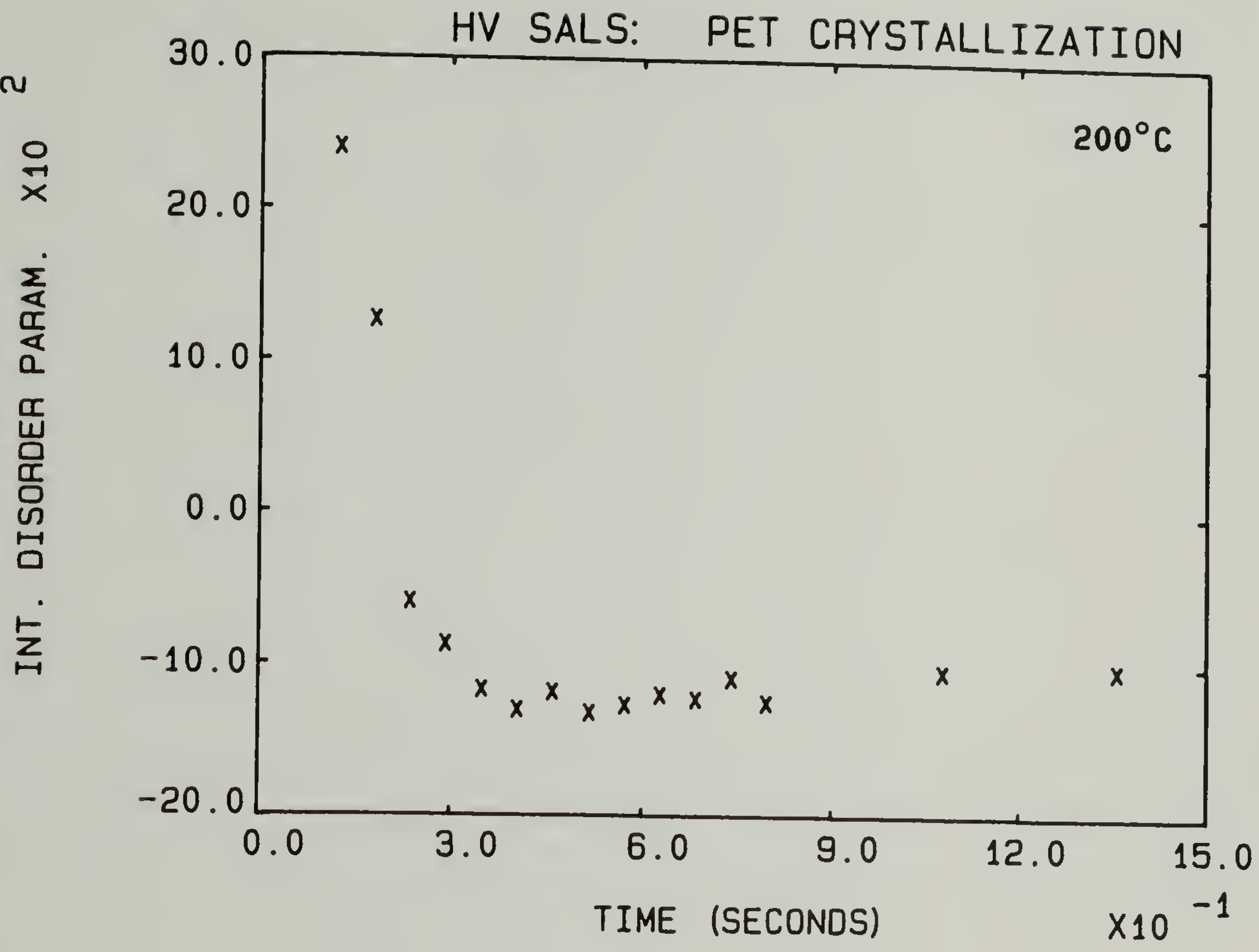

Fig. VI-10 Internal disorder parameter as a function of crystallization time.

the truncation effects are least in the early stages of growth and greatest near full growth, adjustment of the Yuasa results for the varying amounts of truncation would yield relatively higher values of δ for the early stages as opposed to the later stages, similar to the results of this study. Neglect of the profile broadening effects of truncation in the Yuasa study accounts for at least some of the difference between the generally high values of δ in that study and the low values in this study.

The values of $R_{H_{v,exp}}$ $(U_{max},45)$ have been fully corrected by applying the correcting factors C_{refl}, C_{refr}, C_T and C_D to the multiple scattering corrected values. The reflection and refraction corrections are as given in Chapter V: $C_{refl} = 1.05$ and $C_{refr} = 2.69$. The truncation correction, C_T was determined from the value of ϕ_s and from Figure III-22. The internal disorder correction, C_D, was determined from the value of δ and Figure V-5. (δ was assumed equal to 0 for the crystallization times where it was calculated to be negative.)

The fully corrected values of R_{H_v} $(U_{max},45)$ have been applied in equation (VI-3) to determine the value of the volume fraction crystallinity within the spherulites, ϕ_{cs}, during the crystallization. K_v in equation (VI-3) was determined using the values of ϕ_s and Figure III-25. ϕ_{cs} is plotted as a function of crystallization time in Figure VI-11. The crystallinity within the spherulites appears to decrease initially and then remain relatively constant.

Combination of the results in Figures VI-10 and VI-11 implies that the spherulites are initially more crystalline, but containing less well

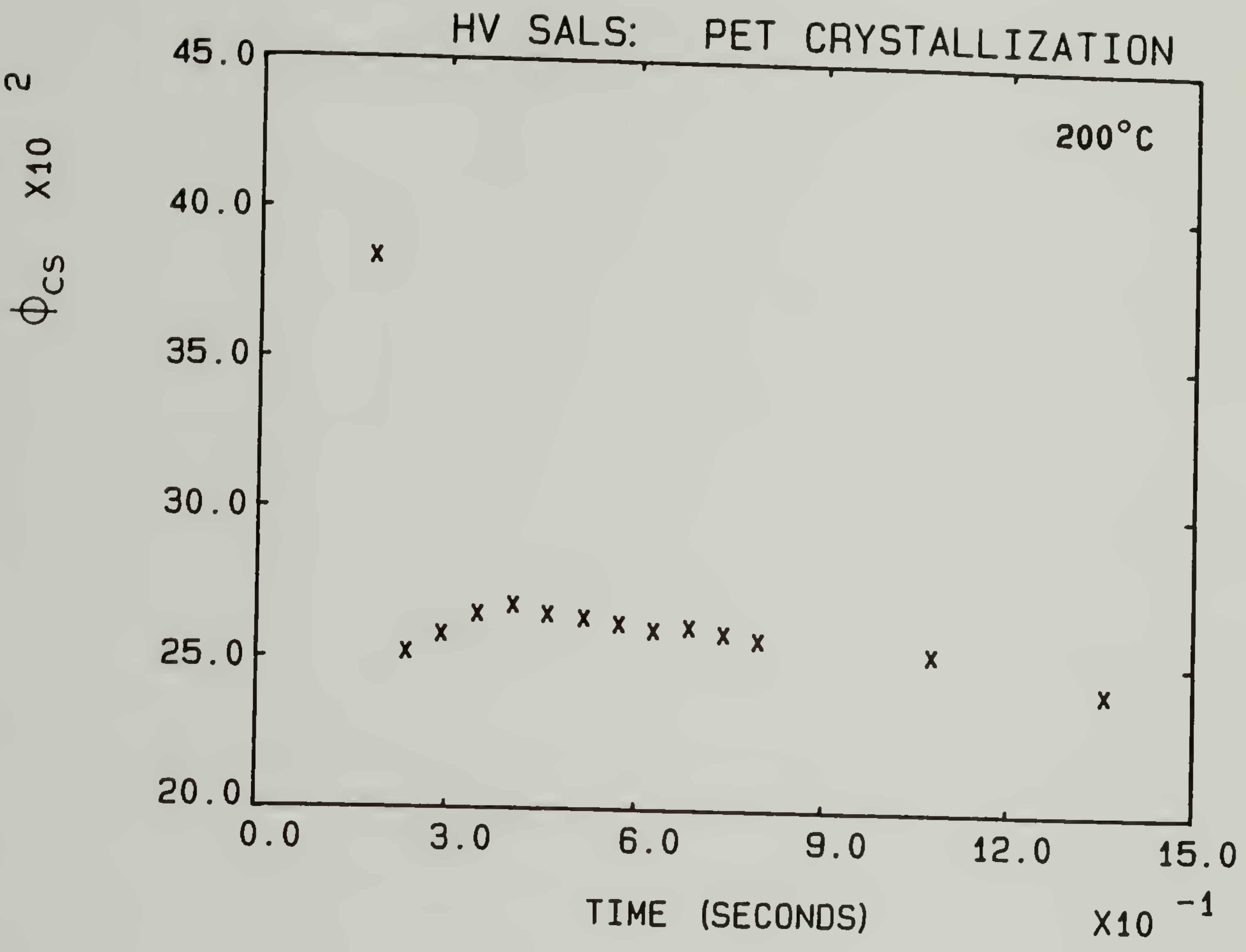

Fig. VI-11 Volume fraction crystallinity within the spherulites as a function of crystallization time.

oriented crystallites, than the more fully grown spherulites. It has often been proposed [95-98] that spherulites are the product of an evolution which includes a rodlike structure developing into a sheaflike structure which spreads to form a spherical structure. Spherical growth is maintained by the growth and branching of radial fibrils. Such an evolution implies that the crystallites of small spherulites would tend to be less well oriented with respect to the spherulite radius than larger spherulites. It would seem that this early morphology would become an insignificant factor in the SALS from the spherulite as the radial structure develops and the spherulite size increases since the larger structures scatter more strongly. This type of behavior is indicated in this study of PET crystallization by the initially decreasing, and then levelling value of the internal disorder parameter.

The decrease in spherulitic crystallinity is in agreement with a SALS study of isotactic polystyrene spherulites where it was found that the crystallinity within spherulites decreases radially [60]. The observation that ϕ_{cs} initially decreases and then remains constant may be indicative of the rejection of the low molecular weight components or other impurities by the growing crystal front. It has been observed [95,99] that the impurities can be rejected in such a fashion as to build up a relatively high concentration of the impurities at the crystal-melt interface. Such a buildup would imply a higher level of crystallinity in the spherulites during the early stages of growth than during the later stages. This type of behavior is indicated for this system by the values of ϕ_{cs} as a function of crystallization time in

Figure VI-11. The fact that the values of ϕ_{cs} become constant before the system becomes volume filling implies that the crystalline fraction of newly formed spherulitic material also reaches a constant level. This type of behavior may be due to inclusion of a consistent level of impurity in the interfibrillar region of the spherulites. The evidence from this study is sufficient only to speculate such a morphological development in this system.

A radial decrease in spherulite crystallinity is a significant deviation from the spherulites modelled by Stein et al. [2,11]. In these models it is assumed that the spherulite anisotropy, $(\alpha_r - \alpha_t)$, is not a function of position in the spherulites. If it can be generally shown that spherulite crystallinity changes with radial position as indicated in this study, then the model equations for SALS from spherulites should be modified to include this effect.

The fully corrected R_{H_v} $(U_{max},45)$ can be compared to the theoretically predicted R_{H_v} $(U_{max},45)$ as predicted by equation (VI-3). In the case of volume filling spherulites, ϕ_{cs} in equation (VI-3) can be replaced by ϕ_c, as was done in Chapter V. ϕ_c at full growth was determined by DSC to be 0.34 ± 0.03. From this value of ϕ_c the theoretically predicted H_v SALS intensity for volume filling spherulites would be

$$R_{H_{v,theor}} (U_{max},45) = 3300 \text{ mm}^{-1}.$$

The fully corrected experimental intensity for volume filling

spherulites was calculated to be

$$R^{c}_{H_{v,exp}}(U_{max},45) = 1860 \text{ mm}^{-1}.$$

The crystallinity at full growth was found from these H_v SALS experiments to be

$$\phi_{cs} = \phi_c = 0.25 \pm 0.02.$$

This level of agreement is gratifying considering all of the assumptions made. As discussed in Chapter V, two likely causes of the low value of the experimental intensity (or degree of crystallinity) are the use of a two dimensional disorder theory and the possible overestimation of the effects of spherulitic truncation.

The overall degree of crystallinity can be calculated as well, as a function of crystallization time, from the values of ϕ_{cs} and ϕ_s and equation (V-5), assuming all of the crystals occur within the spherulites ($\phi_{cm} = 0$). The crystallinity calculated in this fashion is plotted in Figure VI-12. From this plot is can be seen that the half time of crystallization is about 14 seconds. van Antwerpen et al. [90] reported a half time of 35 seconds for a higher molecular weight (M_N = 19,000) PET crystallized at 200°C. Cobbs and Burton [100] reported a half time of crystallization of 45 seconds for a higher molecular weight($[\eta]$ = 61 ml/g) PET crystallized at 200°C. The half time reported here is low, but not unreasonably low, considering the lower molecular weight of the polymer used in this experiment. The somewhat higher crystallization rate is in concurrence with the spherulite growth rate

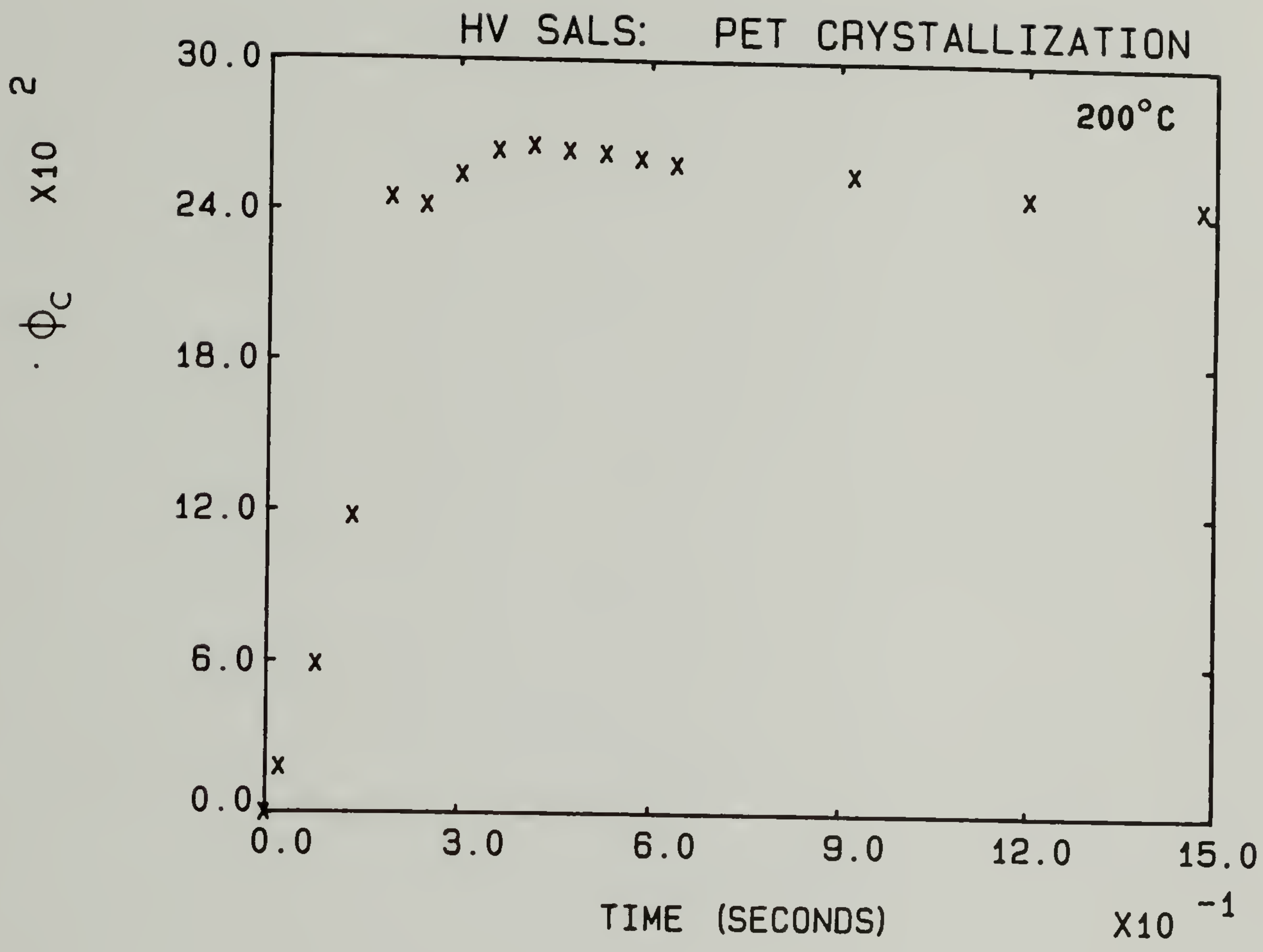

Fig. VI-12 Overall degree of crystallinity as a function of crystallization time.

which was also somewhat higher than the values reported in these other works.

From Figure VI-7 it can be seen that the V_v SALS intensity reaches a maximum at about 12 seconds of crystallization time. As discussed in Chapter II, the V_v SALS intensity should go through a maximum at about $\phi_s = 0.6$ [9]. From Figure VI-8 it can be seen that the turbidity also goes through a maximum at about the same time as the V_v SALS maximum, which is as expected. Figure VI-9 shows that ϕ_s, as calculated from θ_{max} assuming three dimensional, simultaneously nucleated spherulites, equals 0.6 at about 18 seconds of crystallization time. These crystallization times for $\phi_s = 0.6$ are in reasonable agreement considering the different methods of assigning the time = 0 for each experiment type. This agreement implies that the assumed model of three dimensional growth following simultaneous nucleation is reasonable for this crystallization process. The small number of data points available in the non-volume filling region of the crystallization curve limits one to accepting the implication only, not the confirmation, of the validity of the assumed model for this crystallization.

The spherulites become volume filling at about 30 seconds of crystallization time, as indicated by the maximum in the spherulite radius in Figure VI-5 and the levelling off of the V_v SALS intensities and the turbidity in Figures VI-7 and VI-8, respectively. After the system was volume filled, there were no signs of secondary crystallization, such as an increase in spherulite crystallinity, an increase in V_v or H_v intensity, an increase in the turbidity or a

decrease in internal disorder.

From the results from H_v SALS one can calculate the V_v SALS during crystallization using equations (VI-4) and (II-6). The polarizabilities (α_r, α_t, α_s and α_m) in these equations can be calculated using the values of ϕ_s, ϕ_{cs}, the refractive indices and the Lorenz-Lorentz equation [46]:

$$\frac{n^2 - 1}{n^2 + 2} = \frac{4}{3} \pi \alpha. \tag{VI-6}$$

The spherulite polarizabilities are calculated from

$$\alpha_{r,t} = \phi_{cs}\, \alpha^{o}_{r,t} + (1 - \phi_{cs})\, \alpha_m \tag{VI-7}$$

where $\alpha^{o}_{r,t}$ is the radial or tangential polarizability calculated from equation (VI-6) and the crystalline refractive indices. α_m is calculated from the amorphous refractive index of PET (1.576) [80], assuming that the nonspherulitic medium is completely amorphous. α_s is calculated from equation (II-4). These polarizabilities were determined and the V_v SALS intensities were calculated, assuming internally ordered spherulites.

The techniques of quantitative V_v SALS are much less developed than those of H_v SALS. The corrections for multiple V_v scattering have been calculated for only a limited number of scattering angles [38]. The effects of internal disorder and spherulitic truncation on V_v SALS have not been calculated.

In correcting the measured V_v SALS intensities for the experimental effects, the correction for reflection was again assumed to be equal to 1.05. The refraction correction, C_{refr}, was again assumed equal to n^2,

where the refractive index, n, of the sample is given by

$$n = \phi_c \, n_{crystal} + (1 - \phi_c) \, n_{amorphous}. \qquad \text{(VI-8)}$$

The crystalline ($n_{crystal}$) and amorphous ($n_{amorphous}$) refractive indices were as previously given. The V_v SALS intensities were measured at U = 4 and μ = 0 and 90° they were corrected for reflection, refraction [36] and multiple scattering [38]. Figure VI-13 plots the calculated and corrected experimental V_v SALS intensities as functions of the crystallization time. It can be seen in these plots that the agreement is good considering the lack of theoretical treatments available.

It was assumed in these calculations that the nonspherulitic material was completely amorphous. An assumption of the presence of some nonspherulitic crystalline material in the calculations would make the calculated and experimental agreements in Figure VI-13 more poor than those given. As an example, assuming that ϕ_{cm} = 0.2 leads to higher calculated values of R_{V_v} (4,0) and lower calculated values of R_{V_v} (4,90), for $\phi_s < 1$, than those given in Figure VI-13, thus widening the difference between the experimental and calculated intensities in this figure. This result implies that there was not significant nonspherulitic crystalline material present in this crystallization.

Conclusions

This study has examined the morphology of PET spherulites

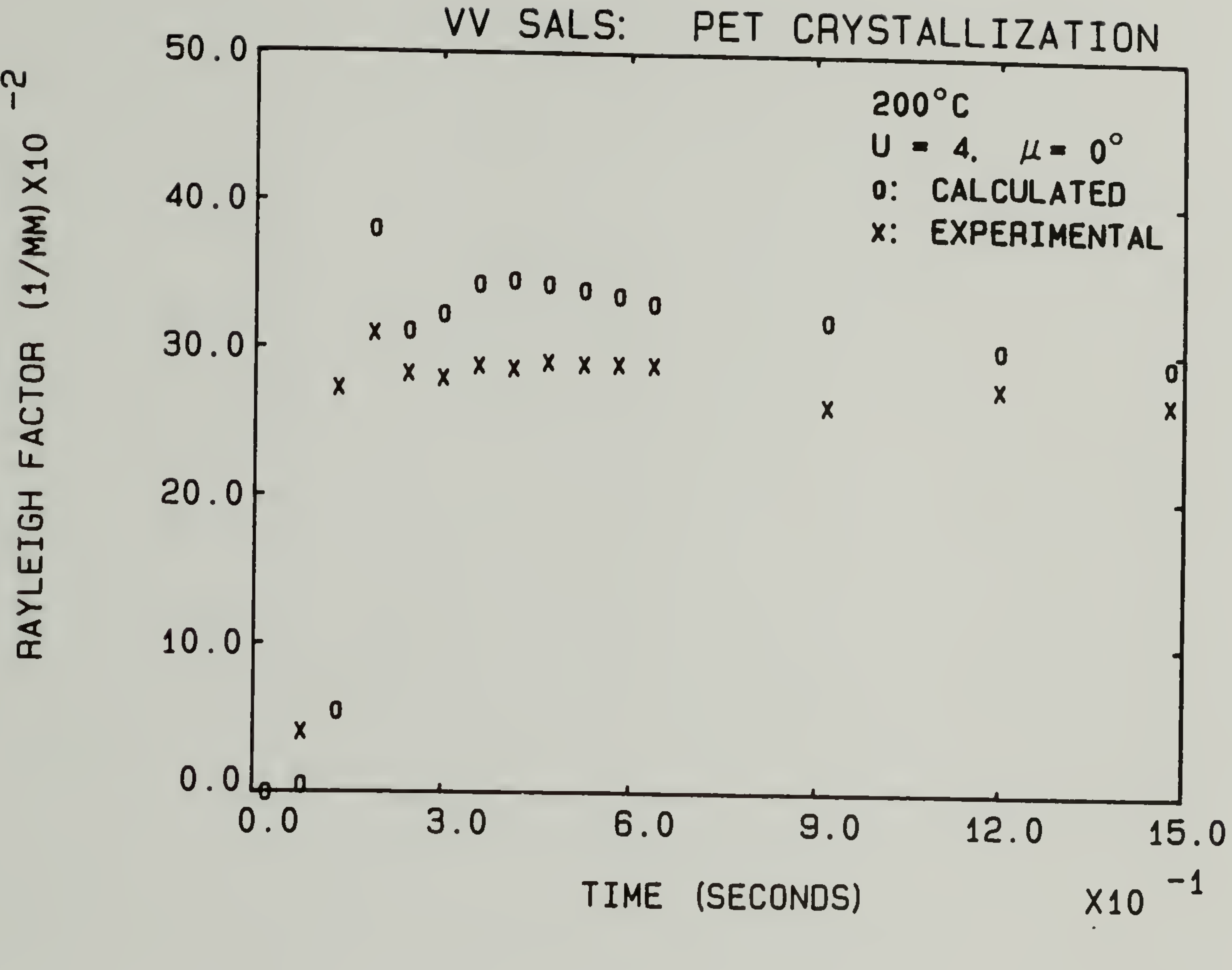

Fig. VI-13a V_v SALS intensity at U = 4 as a function of crystallization time: (X) corrected experimental intensities and (O) intensities calculated from H_v SALS results; $\mu = 0°$.

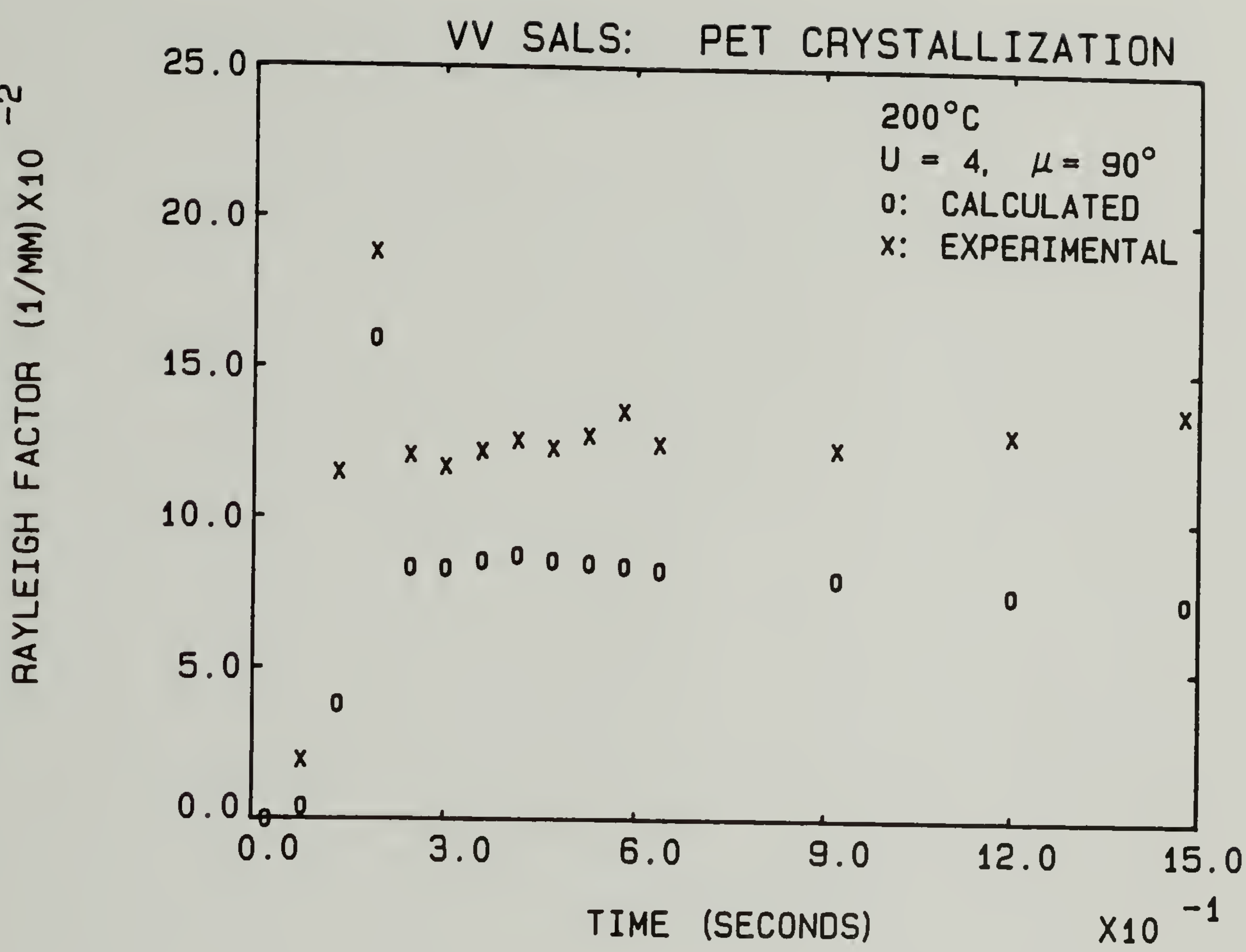

Fig. VI-13b V_v SALS intensity at U = 4 as a function of crystallization time: (X) corrected experimental intensities and (O) intensities calculated from H_v SALS results; $\mu = 90°$.

crystallization by SALS, as well as examined the SALS theory itself. It was found that when crystallized from the melt at 200°C, this PET material has the high spherulite growth rate of 0.30 µm per second. Quantitative examination of the H_v SALS has shown that there are initial decreases in both internal disorder and spherulite crystallinity during the crystallization; both of these properties level off to constant values. The spherlulite crystallinity reaches a constant value before the system becomes volume filled with spherulites. Quantitative examination of the V_v SALS intensities indicated that there was not significant nonspherulitic crystallization.

There was reasonable agreement between the volume fraction spherulites measured by H_v SALS, V_v SALS and sample transmission. The H_v SALS measurement of the volume fraction spherulites was dependent upon the truncation theories developed in Chapter III. The experimental and theoretical H_v intensities at full spherulite growth were in modest agreement. The lower value of the experimental intensity was again explained in terms of the lack of a suitable three dimensional internal disorder theory and possible overestimation of the effects of spherulitic truncation.

The OMA2 made it possible to examine such a rapidly crystallizing system by quantitative H_v and V_v SALS. A more thorough examination could be performed on a slightly less rapidly crystallizing system which would permit one to collect more SALS scans before the spherulites become volume filling. It would also be interesting to examine, in a similar fashion, a system which develops significant secondary

crystallization following full spherulite growth.

CHAPTER VII

STUDIES OF THE ELONGATION OF LOW DENSITY POLYETHYLENE AND POLYPROPYLENE

Introduction

The deformation behavior of polymer spherulites has been the subject of many studies [2,7,11,13,14,18,42,43,47,76,101-124]. Despite this fact, the mechanisms of spherulite deformation are not completely understood and there does not exist a well accepted model of spherulite deformation. An acceptable spherulite deformation model must be able to explain the experimental results obtained from spherulite deformation studies by many techniques. These techniques include optical microscopy [101-106], electron microscopy and diffraction [102,107,108], small and wide angle x-ray scattering [14,109-114], birefringence [103,110,115-117] and small and wide-angle light scattering [2,7,11,13,14,18,42,43,47,101,103,106,110,113,118-121].

The most basic models of spherulite deformation proposed often include the assumption of affine deformation of spherulites [11,13,14,42,43,47,109,114,116,117], that is, that the microscopic dimensions of the spherulite change during deformation proportionately to the macroscopic dimensions. Several studies have found that, at least over a limited deformation range, polymer spherulites elongate affinely [11,13,14,42,43,47,101,109,110,113,114,116,117]. Several other models and studies conclude that spherulite deformation is generally non-affine [103-106,108,122,123].

SALS techniques can be used to help understand the deformation mechanisms of polymer spherulites. Also, in order to develop quantitative SALS techniques for deformed spherulitic systems along the lines of that described earlier for undeformed systems, a valid model for the deformation mechanisms must be established. The development of the OMA2 greatly facilitates more thorough examinations of the anisotropic SALS patterns produced by deformed polymer spherulite systems. Therefore, a study of the deformation of polymer spherulites, using the OMA2, in order to evaluate spherulite deformation mechanisms and the SALS theories used to examine the deformation, is appropriate.

This chapter presents a study of the deformation of low density polyethylene (LDPE) and isotactic polypropylene (PP) by SALS. Complementary studies of the deformation by birefringence and infrared dichroism were also made to corroborate the SALS results. The SALS was carried out in the H_v, V_v and H_h polarization modes and the analysis was performed using the three dimensional, affine spherulite deformation models of van Aartsen and Stein [42,43]. Estimations of the compliance parameters defined in the models were made for the two polymers by an extensive comparison of the measured SALS intensities with that predicted by the models.

Experimental

Sample preparation.

LDPE. The LDPE used was supplied in pellet form by ARCO Chemical Company: ARCO 161-1. The films were formed by pressing for 15 minutes

at 150°C and then annealing 4 hours at 60°C. The films used for SALS, birefringence and infrared dichroism were approximately 70 μm thick. The films used for wide-angle x-ray diffraction (WAXD) were approximately 700 μm thick.

PP. The isotactic PP used was supplied in pellet form by Hercules Incorporated: Pro-fax 6331F. The films were formed by pressing for 10 minutes at 200°C and then quenching into a water bath at 45°C. The films used for SALS, birefringence and WAXD were approximately 70 μm thick. A stack of 4 films was used for the WAXD of PP.

Sample characterization. The characterization of the LDPE and PP, both the original materials and the pressed films, is given in Table VII-1. Table VII-1 includes the characterization of the original LDPE by the supplier and by Anderson [125]. It also includes the supplier's characterization of the original PP. In addition, the crystallinities of the LDPE and PP films, as determined by the method of Ruland [126,127] using WAXD and the computer program supplied by Anderson [125], are also given in the table.

Table VII-1
Physical Properties of LDPE and PP

	LDPE	PP
Density (g/cm³)	0.928$^{(a)}$, 0.927$^{(b)}$	—
M_N	$1.5 \cdot 10^4$ $^{(a)}$	$4.2 \cdot 10^4$ $^{(a)}$
M_W	$9.4 \cdot 10^4$ $^{(a)}$	$2.5 \cdot 10^5$ $^{(a)}$
M_W/M_N	6.3$^{(a)}$	6$^{(a)}$
Short chain branches (per 1000 c)	22.1$^{(a)}$	—
Long chain branches	1.45$^{(a)}$	—
Weight fraction crystallinity	0.48$^{(b)}$ 0.50$^{(c)}$	0.46$^{(c)}$

(a) data from supplier
(b) data from Anderson [125]
(c) data from this study

Birefringence. The birefringence of the samples was measured using a Zeiss polarizing microscope and a rotatable quartz compensator. The rectangular shaped (6 mm wide, 30 mm between grips) thin film samples were slowly elongated in a hand held mechanical stretcher by a turnscrew mechanism. While held at fixed length the birefringences of the LDPE and PP were measured at room temperature and 125°C, respectively. It was measured as a function of the uniaxial elongation ratio, λ_E, from $\lambda_E = 1.0$ to 2.0 for LDPE and from $\lambda_E = 1.0$ to 1.65 for PP.

Infrared dichroism. The infrared absorbances of the LDPE were measured at room temperature using a nicolet Fourier Transform Infrared Spectrometer. The samples were rectangular in shape (12 mm wide, 30 mm

long). They were elongated slowly and held at fixed length, allowing 1/2 hour for relaxation before infrared measurements. The absorbances were measured as functions of λ_E, from $\lambda_E = 1.0$ to 1.5, at several increments. The base lines chosen for the absorbance measurements were generaly unambiguous. In the cases of the 1303, 1352 and 1368 cm^{-1} absorbances, the base line method of Glenz and Peterlin was used [128].

WAXD. The crystallinities of the undeformed samples were determined as previously described using the Siemens D-500 Diffractometer and the Cu K_α radiation. 2θ intensity scans were made in transmission over the ranges of 4 - 46° for the LDPE and 5 - 35° for the PP. The results are included in Table VII-1.

Optical microscopy. The sign of the PP spherulites was examined using a Zeiss polarizing microscope at 710X and a quartz first order red plate.

SALS. The SALS experiments were performed using the OMA2 described in Chapter IV. The geometry of the OMA2 was chosen such that the intensity from all four quadrants of the scattering pattern was collected by the detector. The system was calibrated in terms of scattering angles, sensitivity and absolute intensity according to procedures outlined in Chapter IV. Scans were taken in the H_v, V_v and H_h modes of polarization for values of λ_E from 1.0 to 2.0, in increments of 0.1. The stretching direction was vertical. The samples were rectangular in shape (6 mm wide, 30 mm between grips). They were stretched slowly in a hand held stretcher by a turnscrew mechanism and held at fixed length. For LDPE, the stretching was performed at room temperature. For PP, the stretching was performed at 125°C; the samples were held stretched for

one minute at 125°C, quenched into water to room temperature and examined at room temperature.

Results

Birefringence and infrared dichroism. The birefringences of LDPE at room temperature and PP at 125°C are plotted in Figure VII-1. These values are in reasonable agreement with a previous study on similar materials [116]. The molecular orientations in LDPE are related to the infrared dichroism [76,129-131]. For a uniaxially oriented polymer sample, dichroic ratio, D, is given by

$$D = \frac{A_{||}}{A_{\perp}} \qquad \text{(VII-1)}$$

where $A_{||}$ is the absorbance measured with radiation polarized parallel to the stretching direction and $A_{\perp}$ is the absorbance measured with the radiation polarized perpendicular to the stretching direction. The dichroic ratio is related to the orientation function, f (defined in Chapter V, equation (V-3)), according to

$$f = \frac{(D - 1)}{(D + 2)} \frac{(D_o + 2)}{(D_o - 1)} \qquad \text{(VII-2)}$$

where the orientation measured is that of the molecular chain axis with respect to the stretching direction and D_o is defined as

$$D_o = 2 \cot^2 \Omega \qquad \text{(VII-3)}$$

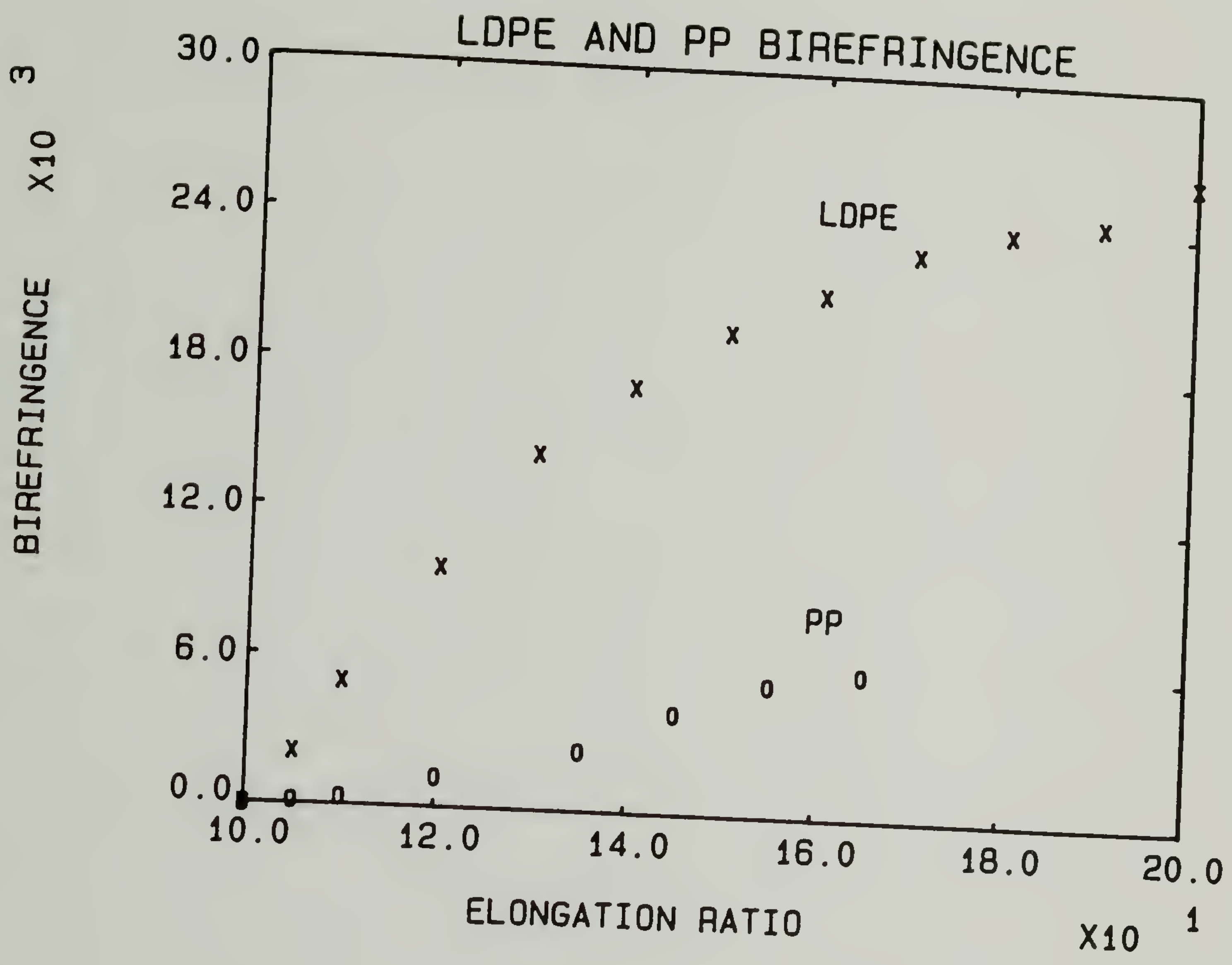

Fig. VII-1 Birefringences of: (X) LDPE and (O) PP as functions of the elongation ratio.

where Ω is the angle between the chain axis and the transition moment direction for the vibrational mode responsible for the infrared absorption.

Crystalline polyethylene has an orthorhombic unit cell [132]. Orientation of the different crystal unit cell directions, as well as that of the amorphous chains, can be obtained from the dichroic ratios due to the absorbance bands resulting from vibrational modes characteristic of the different molecular structures. The dichroic ratios of several absorbance bands in LDPE are given as functions of the uniaxial elongation ratio in Figure VII-2.

The following assignments of the vibrational modes responsible for the various bands will be used in this study:

730 cm^{-1}: This band arises from the crystalline phase. The transition moment has been found to be parallel to the crystalline a axis [131,133].

1303, 1352, 1368 cm^{-1}: These bands arise from the amorphous phase. Their transition moments are parallel to the chain axis [131,134].

1894 cm^{-1}: This band arises from the crystalline phase. The transition moment is perpendicular to the crystalline c axis [131,135].

The crystalline c axis orientation, f_c, was obtained from the 1894 cm^{-1} band and the crystalline a axis orientation, f_a, from the 730 cm^{-1} band. The b axis orientation, f_b, was obtained from the relationship derived for an orthorhombic unit cell [76]

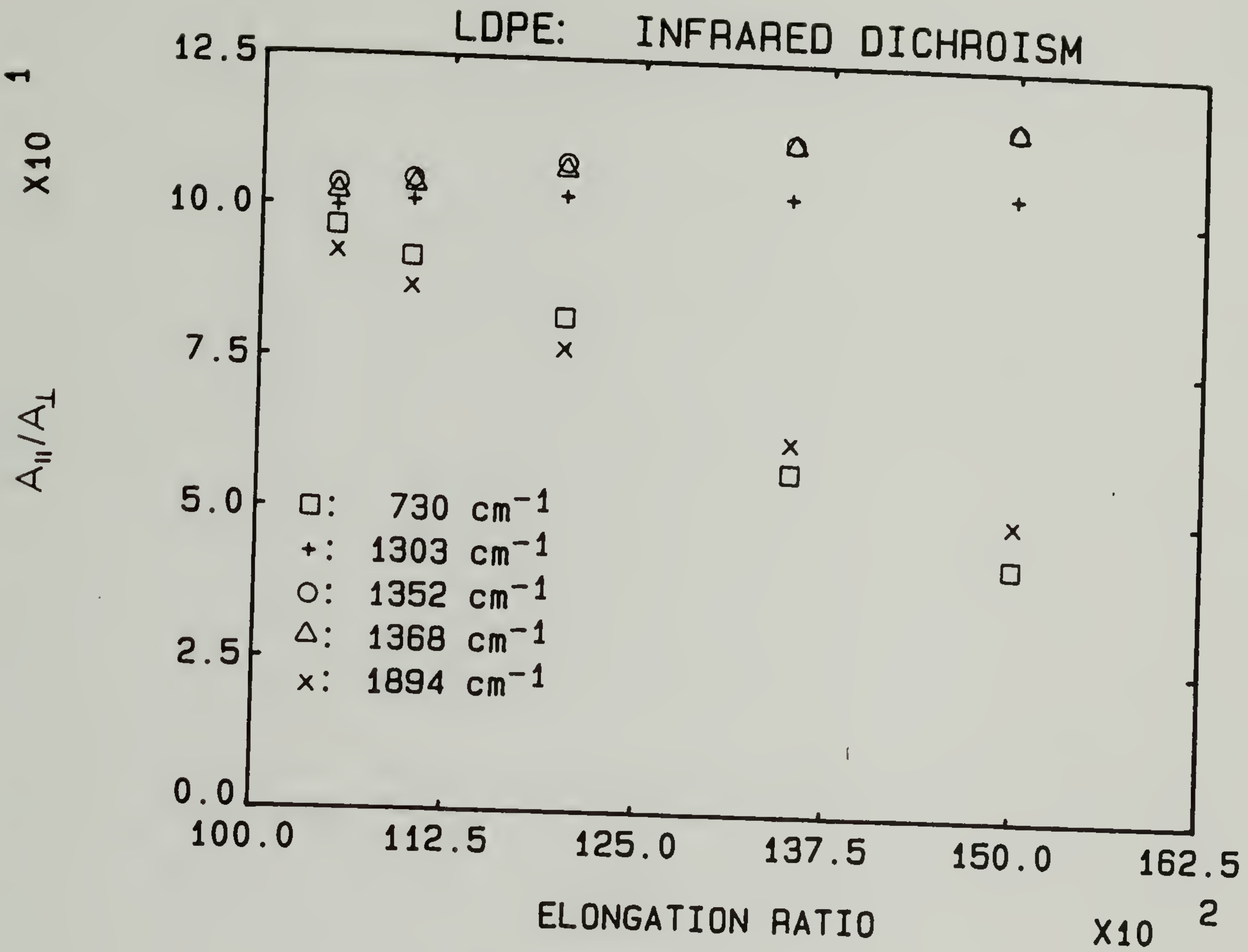

Fig. VII-2 Infrared dichroic ratios for LDPE as functions of the elongation ratio.

$$f_a + f_b + f_c = 0. \qquad \text{(VII-4)}$$

The amorphous orientation, f_{am}, was calculated from the average of the orientations calculated from the 1303, 1352, and 1368 cm^{-1} bands. The orientation functions for the LDPE, as functions of λ_E are given in Figure VII-3. These orientations are in good agreement with previous studies of the deformation of LDPE [76,109]. At deformation ratios greater than 1.3, the orientation of the a axis is more perpendicular to the stretching direction than that of the b axis. The birefringence of LDPE can be calculated from the orientation functions and the crystallinity according to [75]

$$\Delta = \phi_c \, \Delta_c^o \, f_c + (1 - \phi_c) \, \Delta_{am}^o \, f_{am} + \Delta F \qquad \text{(VII-5)}$$

where Δ_c^o and Δ_{am}^o are the intrinsic birefringences of the crystalline and amorphous phases, respectively, ΔF is the form birefringence and the other terms are as previously defined. The volume fraction crystallinity, ϕ_c, was calculated from the weight fraction crystallinity, w_c, for LDPE from Table VII-1, equation (V-13) and the crystalline and amorphous densities of LDPE: $\rho_c = 1.00$ [132] and $\rho_a = 0.855$ [136]. Therefore, ϕ_c (LDPE) = 0.46. Using the crystalline refractive indices of polyethylene [137], Δ_c^o was calculated to be 0.0585. Δ_{am}^o is given by Peiffer as 0.56 [138]. The measured values of the birefringence of LDPE are compared to those calculated using equation (VII-5) and the orientation functions determined by infrared dichroism in Figure VII-4. The agreement between the two measurements is excellent.

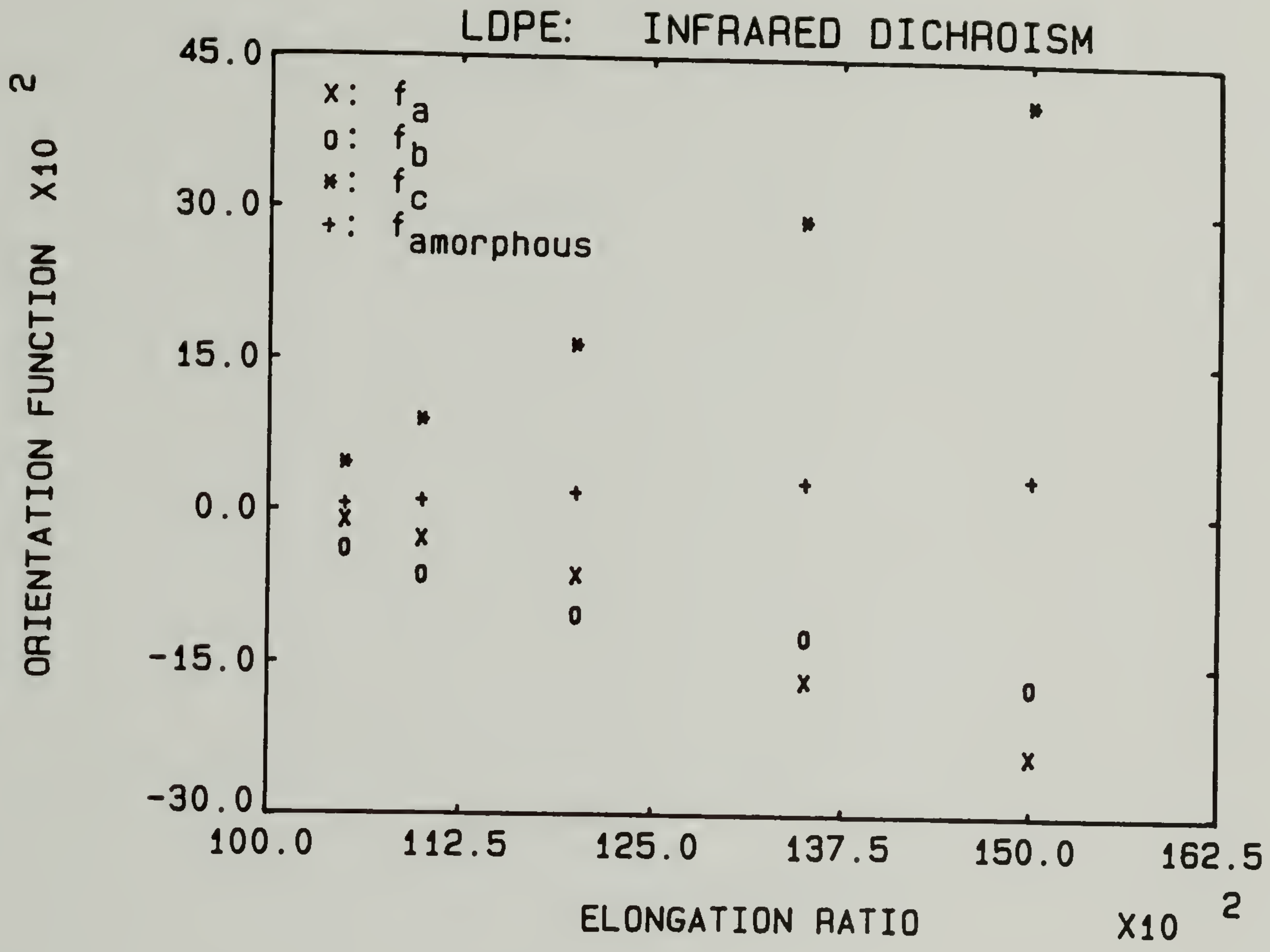

Fig. VII-3 Crystalline and amorphous orientation functions of LDPE as functions of the elongation ratio, as determined by infrared dichroism.

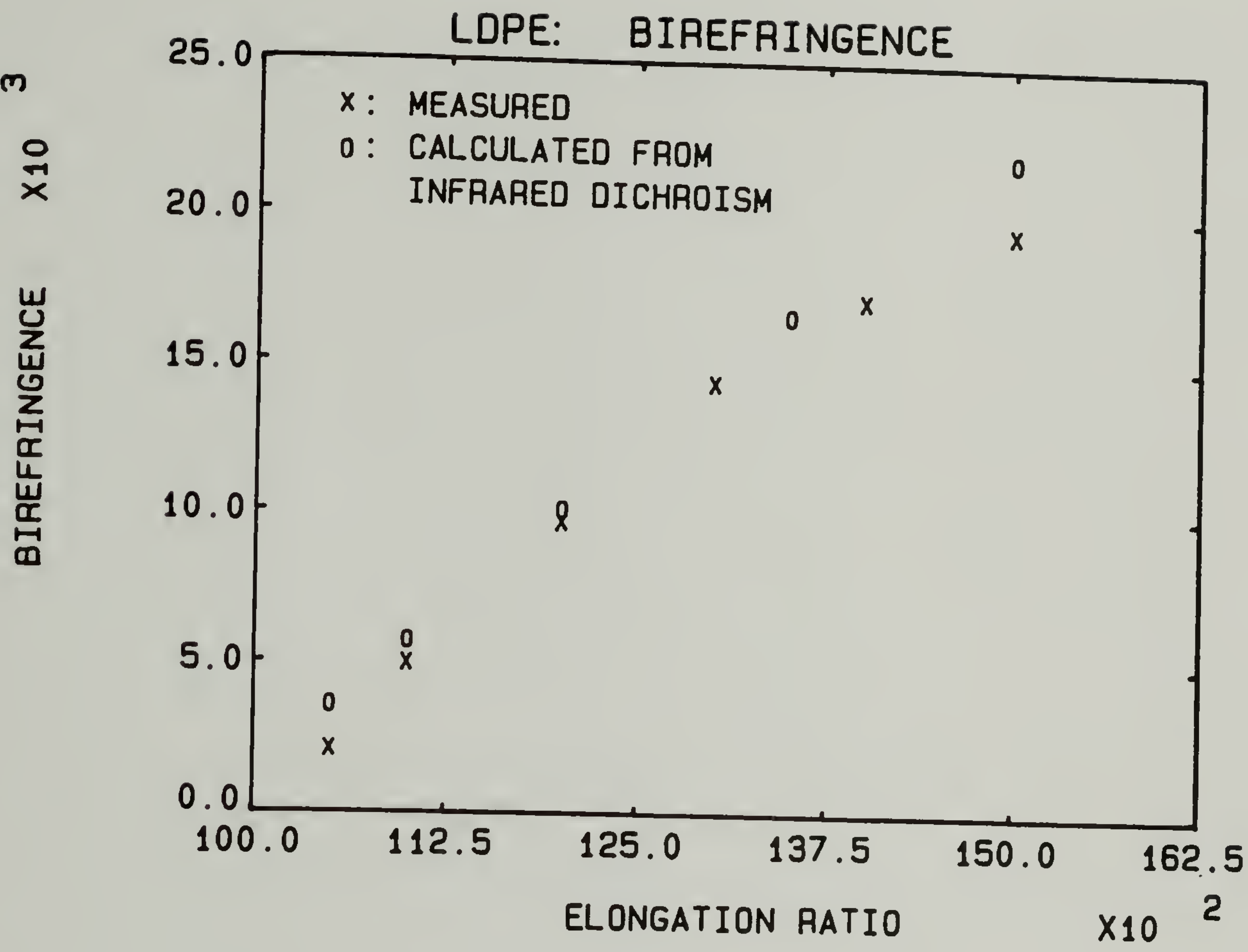

Fig. VII-4 Birefringence of LDPE as a function of the elongation ratio, as measured (X) and as calculated from infrared dichroism (O).

WAXD and optical microscopy. The crystallinities of the undeformed LDPE and PP films were determined by WAXD as previously described. The WAXD from the undeformed LDPE films was the usual polyethylene diffraction pattern resulting from the orthorhombic unit cell [76,139]. The WAXD from the undeformed PP films was typical of the α-form of the monoclinic crystal structure [140]. The PP spherulites which were distinguishable by optical microscopy were positively birefringent, indicating that they were Type I, according to the classification scheme of Keith and Padden [141,142].

SALS. Sample single quadrant averaged isointensity plots for H_v SALS from LDPE, for extension ratios of 1.0 and 1.3, are given in Figure VII-5. It is apparent in the figure that the azimuthal angle of maximum intensity, μ_{max}, increases from its initial value of 45° with elongation. This behavior is in agreement with the van Aartsen and Stein model [42,43], as indicated in Figure II-5.

μ_{max} also increased with elongation for PP. This behavior differs from the results and theories of Samuels [13,14,47], who found that μ_{max} remained constant up to $\lambda_E = 5$. Figure VII-6 plots μ_{max} as a function of the elongation ratio for LDPE and PP.

It appears from Figures VII-7 and VII-8 that the V_v SALS pattern of LDPE becomes more circularly symmetric, while the H_h pattern becomes horizontally elongated, with elongation. These observations are in agreement with the results of Stein and Rhodes [2]. The SALS patterns from PP were similar in appearance. These patterns are closely compared to the models in the next section.

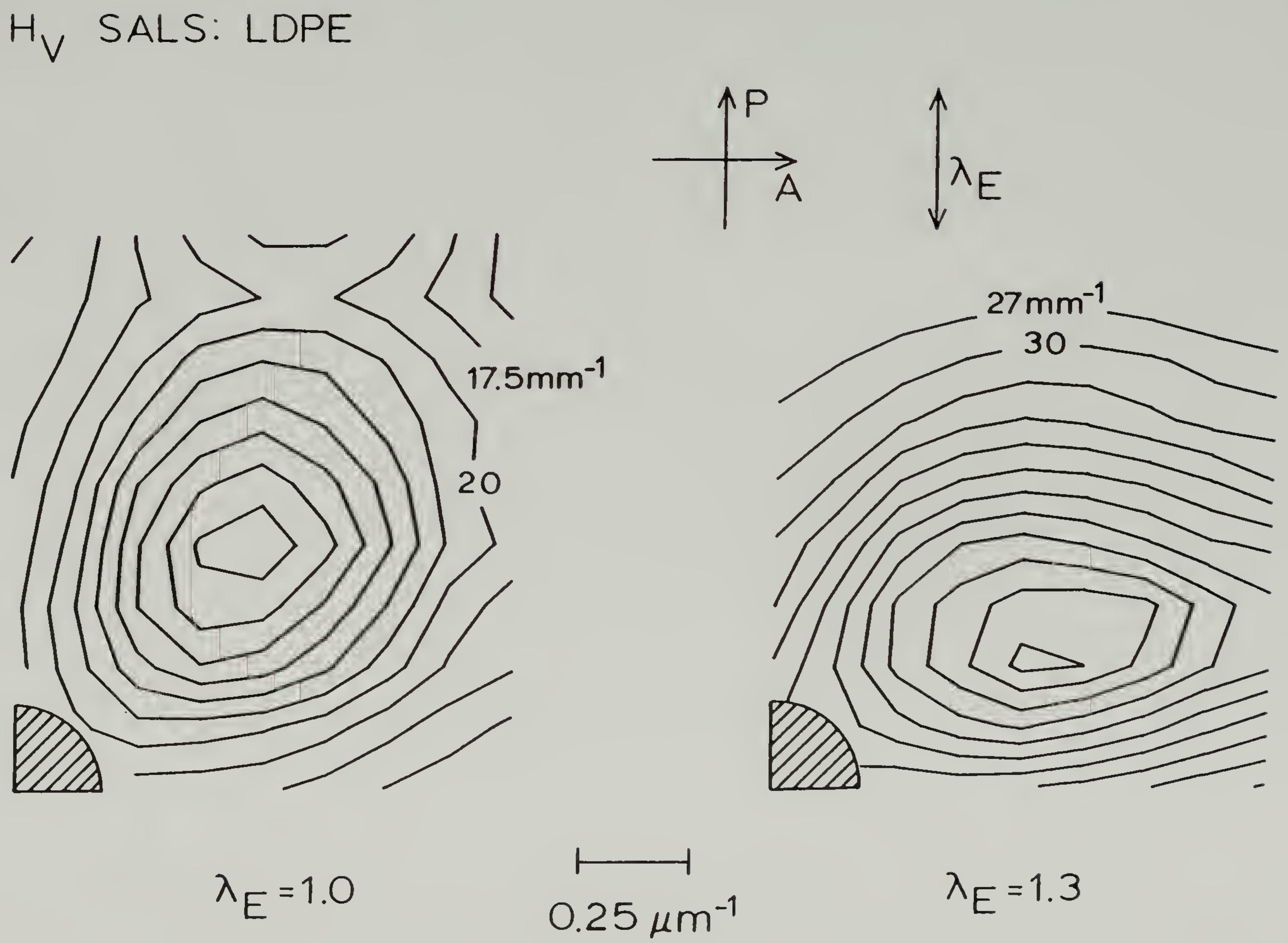

Fig. VII-5 Single quadrant averaged isointensity contour plots of H_v SALS from LDPE, undeformed and $\lambda_E = 1.3$. Stretching direction is vertical. Contour levels are at linear intervals. Main beam is suppressed in the hatched area.

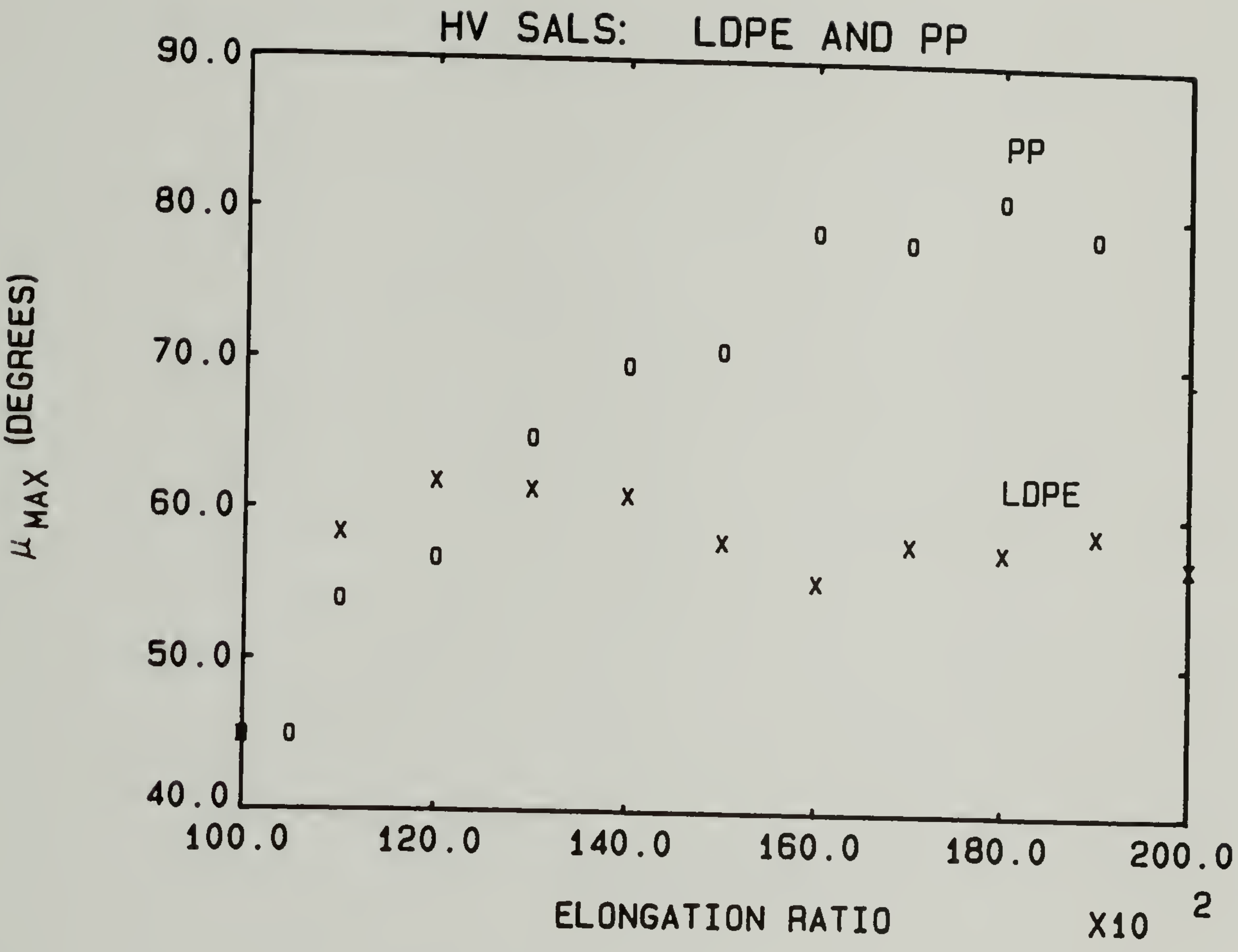

Fig. VII-6 Azimuthal angles of maximum H_v SALS intensity for (X) LDPE and (0) PP, as functions of the elongation ratio.

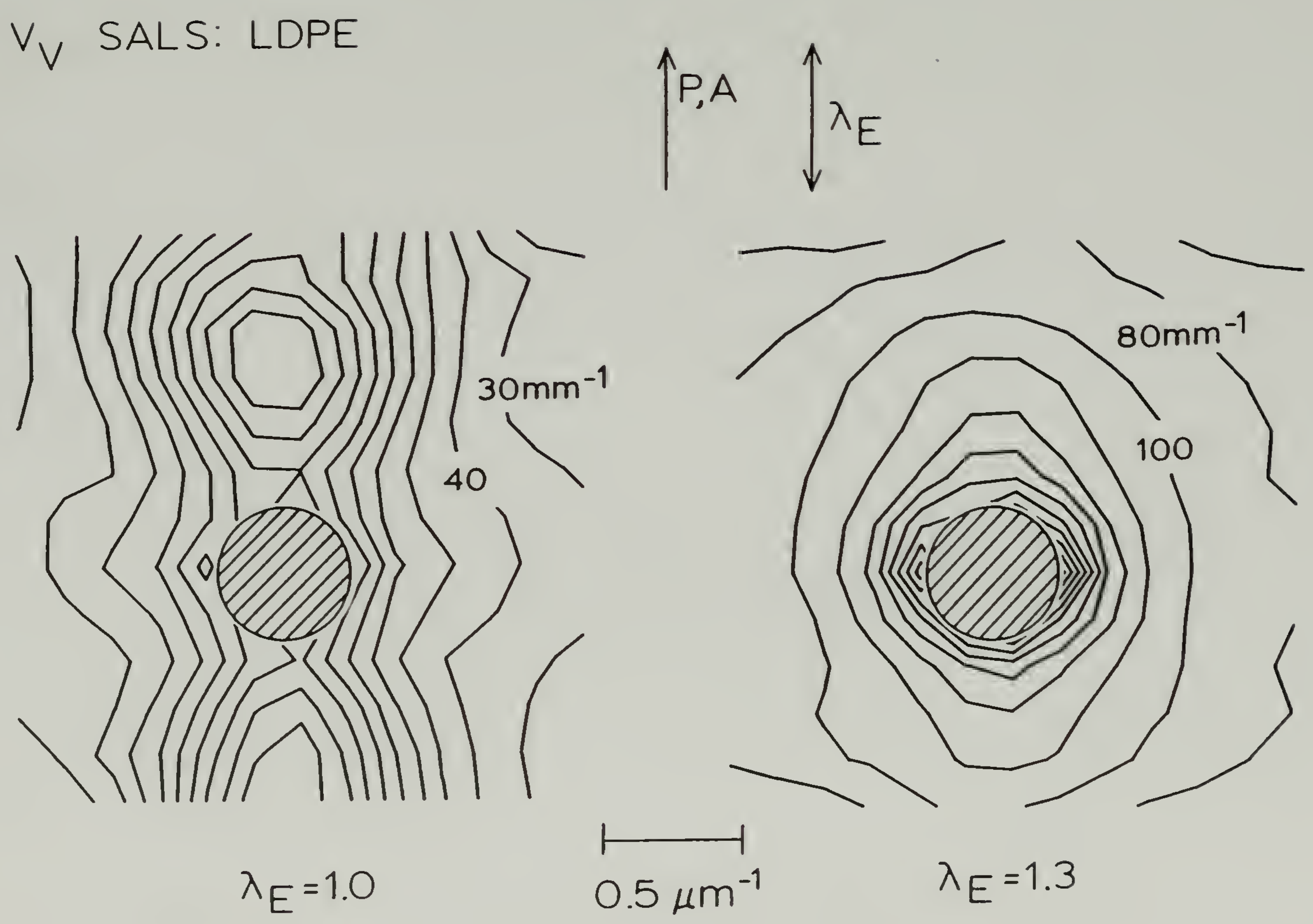

Fig. VII-7 Isointensity contour plots of V_v SALS from LDPE, undeformed and $\lambda_E = 1.3$. Stretching direction is vertical. Contour levels are at linear intervals. Main beam is suppressed in the hatched area.

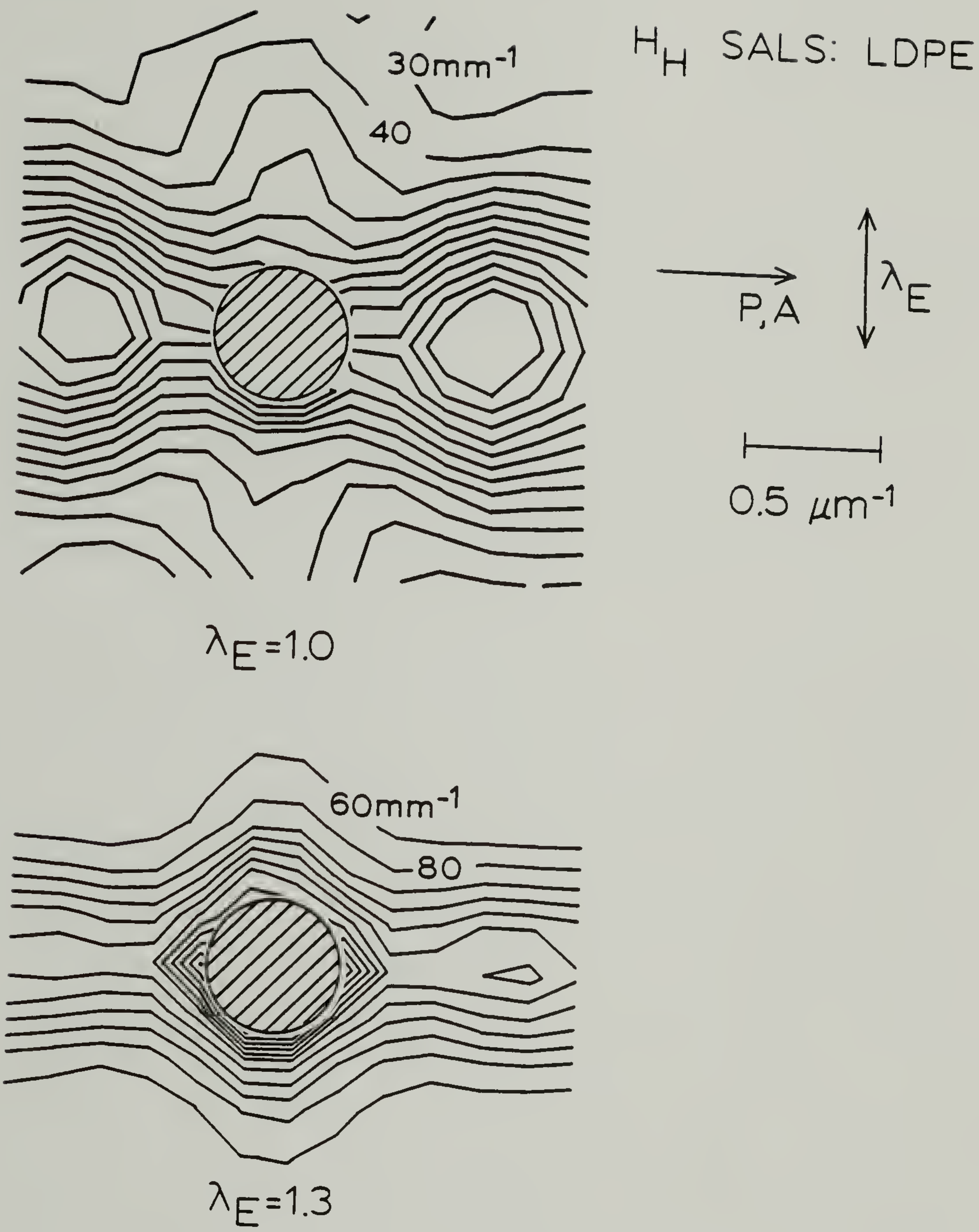

Fig. VII-8 Isointensity contour plots of H_h SALS from LDPE, undeformed and $\lambda_E = 1.3$. Stretching direction is vertical. Contour levels are at linear intervals. Main beam is suppressed in the hatched area.

Discussion

The van Aartsen and Stein spherulite deformation model [42,43] was described in Chapter II. This model involves two compliance parameters. The parameter, η, indicates the ease with which the optic axis rotates about the radius due to sample elongation. The parameter, κ, indicates the ease with which the optic axis tilts toward the stretching direction due to sample elongation. These parameters were evaluated in this study by a careful examination of the changes in the SALS patterns during deformation.

The changes in the SALS patterns were evaluated by examining the changes in the intensity ratio

$$T(U,\mu,\lambda_E) = \frac{R(U,\mu,\lambda_E)}{R(U,\mu,\lambda_E = 1.0)} \qquad \text{(VII-6)}$$

where $R(U,\mu,\lambda_E)$ is the Rayleigh factor, for a particular polarization condition, as a function of the scattering angles U and μ and the uniaxial elongation ratio λ_E. The intensity ratios, rather than the absolute intensities, were evaluated in order to minimize the effects on the deformation analysis of the deviation of the undeformed samples from the perfect spherulite model. These deviations are due to internal and external disorder and have been discussed in the earlier chapters. It is assumed in this analysis that these disorders are not affected by sample deformation. This assumption will be discussed later.

The intensity ratios were evaluated at various polar and azimuthal angular locations in the patterns. For H_V polarization, the ratios were

determined at U = 2 and 4 and μ = 45 and 60°. These angles were chosen since it is apparent from Figure II-5 that the scattered intensities are strong in these locations and that they change with elongation. For V_v and H_h polarization, the ratios were determined at U = 2 and 4 and μ = 0, 45 and 90°. Similar intensity ratios were calculated using the model [42]. The model and experimental intensity ratios were compared for each of the polarization conditions over the range of $\lambda_E = 1.0$ to $\lambda_E = 1.5$, in increments of 0.1.

The intensity ratios for the model are dependent upon the choices of η and κ. These ratios were calculated for values of η and κ ranging from 0.0 to 1.0, in increments of 0.1 for each elongation value. The values of η and κ which gave the best fit of the experimental data with the model were determined by a least squares analysis. The goodness of fit was determined by

$$\chi^2 = \left(\frac{T_e(U,\mu,\lambda_E) - T_m(U,\mu,\lambda_E)}{T_e(U,\mu,\lambda_E)}\right)^2 \qquad \text{(VII-7)}$$

where the subscripts e and m refer to experimental and model intensity ratios, respectively. The best values of η and κ were evaluated by minimizing χ^2. This evaluation was carried out for each of the polarization conditions (H_v, V_v and H_h) separately and for all three conditions combined.

The average deviation between the experimental intensities and the model intensities was calculated according to

$$\langle\sigma\rangle = \frac{1}{N} \Sigma\left(\left| \frac{T_e(U,\mu,\lambda_E) - T_m(U,\mu,\lambda_E)}{T_e(U,\mu,\lambda_E)} \right|\right) \times 100\% \qquad \text{(VII-8)}$$

where N is the number of data points considered. The summation in equation (VII-8) was performed for $\lambda_E = 1.1$ to 1.5. The best values of η and κ for LDPE and PP are given in Table VII-2 for each of the polarization conditions and for the combination of all three data sets. The average deviations are also given.

Table VII-2

SALS Anslysis of the Deformation of LDPE and PP

Polarization Conditions		η	κ	$\langle\alpha\rangle$
LDPE:	H_v	0.6	0.0	7%
	V_v	0.1	0.0	63
	H_h	0.1	0.1	32
	H_v, V_v, H_h combined	0.1	0.0	46
PP:	H_v	0.0	0.2	23%
	V_v	0.2	0.0	36
	H_h	0.1	0.1	43
	H_v, V_v, H_h combined	0.1	0.0	45

It is apparent from Table VII-2 that the average deviation between the experimental and model intensity ratios is large for most of the polarization conditions. The condition of least deviation for both LDPE

and PP is the H_v condition. In this condition, the value of η is larger than κ for LDPE and the reverse is true for PP. For the other polarization conditions, the values of η and κ are indistinguishable between the two polymers and the average deviation between the experiment and the model is large.

The results from the H_v mode are very encouraging. The values of η and κ indicate that the optic axis reorientation mechanism is LDPE is more dominated by optic axis rotation about the spherulite radius than optic axis tilting toward the stretching direction. Previous studies have concluded that rotation of the crystals about the radial b axis by lamellar detwisting is the dominating mechanism in crystal reorientations in polyethylene [102,124,143]. The H_v SALS results from this study are in agreement with these previous works.

The η and κ values from the H_v SALS study of PP elongation indicate that the optic axis reorientation is more dominated by a tilting mechanism rather than a rotation mechanism in PP spherulites. This result is reasonable since the morphology of PP spherulites does not lend itself to an easy crystal rotation about the radius. For the α-type crystal structure present in these PP films, the crystal a axis is most nearly radial [14,142]. The morphology is much more complex than that of polyethylene. PP spherulites are distinguished by much dendritic structure [141,142,144]. The deformation is also more complex. The crystal c axis reorientation occurs through a process of planar slip and rotation about the nonradial b axis [14]. Also the early deformation may be confined to the less ordered polymeric material

between the fibrils [145]. It is therefore rewarding to observe the different η and κ values determined from the H_v SALS of LDPE and PP deformation. These values appear to be in qualitative agreement with several previous studies of spherulite deformation of these two polymers.

This study found that μ_{max} increases with elongation for H_v SALS PP films. This result differs from that of Samuels [13,14,47]. Although the PP used in this study very closely resembled the PP used by Samuels, the different deformation techniques in the two studies may be responsible for the different results. The Samuels study used a hot rolling procedure to obtain deformation up to $\lambda_E = 5$. This study employed a simple uniaxial elongation at a similar temperature up to $\lambda_E = 2$. Since the various spherulitic morphologies possible in PP are thermal history dependent the differing results of the two studies may be due to differing morphologies [141,142]. A more detailed comparison of the materials used in the two studies in not possible.

The orientation of the optic axis with respect to the stretching direction can be calculated using selected values of η and κ and the van Aartsen and Stein model [109]. Figure VII-9 plots the orientation function of the optic axis, f_o, calculated for $\eta = 0.6$ and $\kappa = 0.0$, as a function of the elongation ratio. Also plotted in the same figure is the c axis orientation function, f_c, for LDPE as determined by infrared dichroism. The similarity between the two curves is encouraging. A more close match of the two curves can be obtained with the choice of a slightly larger value of η, for which the value of $\langle\sigma\rangle$ is not much worse

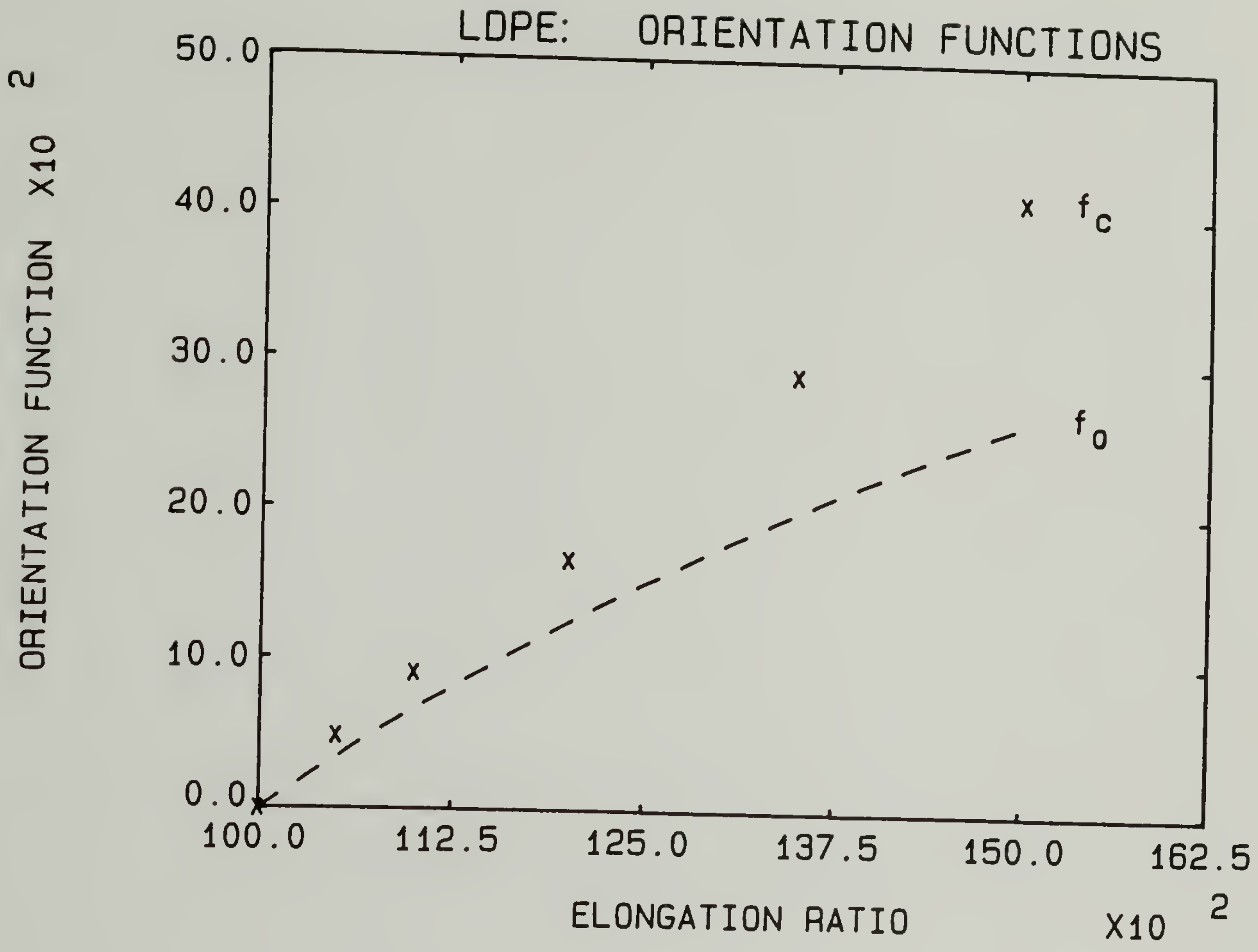

Fig. VII-9 Orientation functions as functions of the elongation ratio: (X) crystalline c axis of LDPE as determined by infrared dichroism and (dashed line) optic axis of a spherulite as calculated from SALS model with $\eta = 0.6$ and $\kappa = 0.0$.

than it is for $\eta = 0.6$.

It must be noted that the optic axis is not necessarily the same as the crystal c axis. An equivalence can be presumed for unoriented spherulites where the amorphous material is randomly oriented. Once the spherulite becomes deformed, the amorphous orientation becomes nonrandom and therefore the optic axis would be composed of both amorphous and crystalline components. The contributions of the amorphous chains to the SALS might be calculated using a model of amorphous orientation, such as that of Petraccone et al. [146]. Such a calculation is beyond the scope of this work.

The large average deviations in Table VII-2 for polarization conditions other than H_v are indicative of the simplicity of the model. The model assumes that the spherulite deformation is affine. The Wang micromechanics model of spherulite deformation concludes that the deformation is nonaffine and that the deformation in the equatorial portions of the spherulites is greater than that in the polar portions [123]. The H_v SALS experiment is most sensitive to the portions of the spherulite azimuthally midway between the polar and equatorial portions. If the spherulite deformation is actually nonaffine according to the Wang model, these portions of the spherulites may experience a more average deformation and therefore may appear to more closely follow an affine transformation. The V_v SALS is most sensitive to the equatorial portion of the spherulite, while the H_h SALS is most sensitive to the polar portion. The large deviation of the model V_v and H_h intensities from the experimental intensities may be indicative of the nonaffine

deformations in the polar and equatorial portions of the spherulites. Work is currently underway in our laboratory to incorporate features of the Wang model into the van Aartsen and Stein model.

Additionally, the approach followed in this study assumed that the internal and external disorders are not functions of the deformation. This assumption was necessary considering the current status of the theoretical studies of spherulitic disorder. The calculation techniques developed in Chapter III for the growth and truncation of spherulites should be useful in a more complete theoretical development of a SALS model of spherulite deformation. Modification of the programs to include deformations, either affine or nonaffine, and/or internal disorder should be a straightforward procedure.

There are other simplifications in the model which need further examination. It is assumed that the optic axis orientation can be described by two mechanisms which are described by somewhat arbitrary functions. The process of chain tilting and lamellar untwisting are well established deformation mechanisms. Although the functions describing the changes in β and ω with elongation have reasonable dependencies on spherulite position, these functions are still rather arbitrary. Other deformation mechanisms, such as planar slip and shear stress effects, might also need to be considered. The combination of crystalline and amorphous orientations into one optic axis orientation simplifies the SALS theoretical treatment, but makes comparison with other techniques, such as infrared dichroism, birefringence and WAXD, difficult.

Conclusions

This study has made the most complete comparison to date of the affine spherulite deformation model of van Aartsen and Stein with experimental SALS intensities. The comparisons were made for three modes of polarization: H_v, V_v and H_h. The SALS results were compared with results from infrared dichroism and birefringence. The SALS study was made possible by the development of the OMA2 detector system described in Chapter IV.

It was found that the model well describes the H_v SALS behavior of the deformation of LDPE and describes reasonably well that of PP. The crystal reorientation mechanisms indicated by the H_v SALS results are in good agreement with previous studies. The descriptions of V_v and H_h SALS from the two polymers were not satisfactory. It appears that the neglect of nonaffine deformation mechanisms may be significant for these polarization conditions. Some of the other simplifying assumptions of the model may also need further examination. Improvement of the models and further investigation of polymer spherulite deformation are underway in our laboratory.

CHAPTER VIII

EFFECT OF PARTICLE SIZE ON POLYMER FILM HAZE

Introduction

The optical clarity of polymer films has great significance in many commercial applications of polymers. Optical clarity may be aesthetically desirable for such applications as beverage containers and food wrappers. It is a necessity for applications such as safety face shields and windows.

While films made from single phase amorphous polymers are generally clear, such films may be unsatisfactory for certain applications due to other inadequacies such as brittleness, low glass transition temperature, poor aging characteristics, expense of production, etc. One can often achieve the other necessary properties in a polymer film with a polyphase polymer system such as a phase separated polymer blend or a semicrystalline polymer. These polyphase systems generally suffer from lack of optical clarity. Optical clarity can be improved in these systems by close control of such factors as the refractive index of the phases, the size and orientation of the phases and the surface smoothness of the film.

This chapter discusses the importance of these factors in achieving optical clarity and outlines the manner in which they should be controlled. A new relationship between polymer film haze and particle size has been developed. Two commercially available films made from

polyphase blends were evaluated for optical clarity. The contributing factors responsible for their degree of clarity (transparency) were evaluated by SALS.

Experimental

The samples were obtained from two nine ounce disposable beverage cups, referred to as samples 1 and 2. The cups are made of rubber-modified polystyrene compositions. Three specimens (approximately 6 x 15 mm) were cut from different positions in each cup, as described in Figure VIII-1.

Silicone oil was applied to the surface of the samples for the light scattering tests to minimize surface scattering effects. The light scattering was performed using the OMA2 described in Chapter IV. Photographs of the light scattering patterns were also obtained. The light transmission was measured, with and without silicone oil, using a photometer arranged to collect all of the light energy emitted at scattering angles less than 2 milliradians. All the light sources used were He-Ne lasers (wavelength = 632.8 nm) and no polarizers were used.

Results

Transmittance. The light transmittances for the six specimens, with and without silicone oil on the surfaces, are given in Table VIII-1. It can be seen from these results that sample 1 was more transparent in the "as

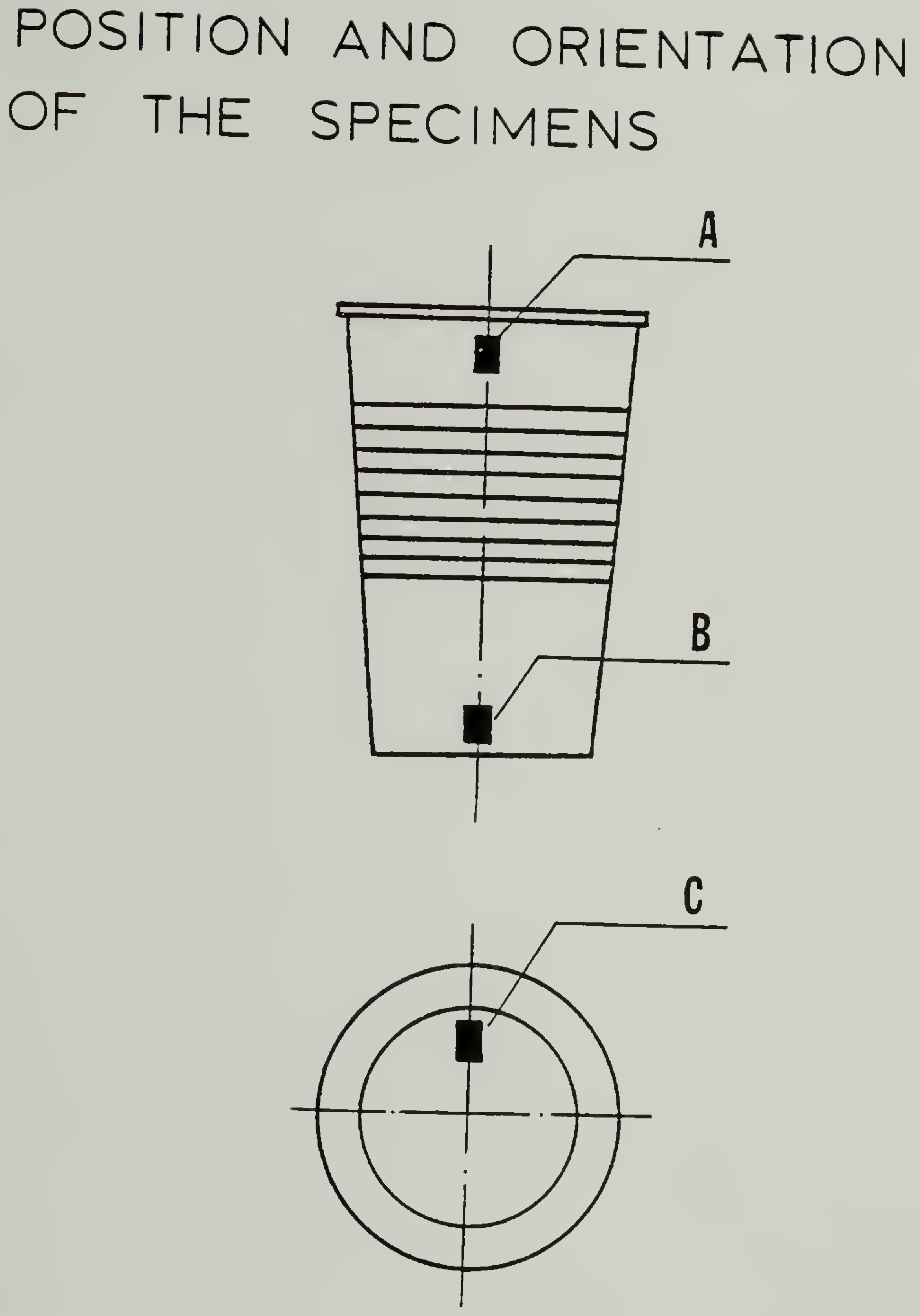

Fig. VIII-1 Diagram of the positions of the A-, B-, and C-position specimens in the beverage cups.

received" condition than sample 2. It can also be seen that the transparency of both samples was greatly enhanced by the silicone oil, indicating that there was a significant amount of surface scattering by both samples. Sample 1 had greater transparency than sample 2 for the oil-covered samples, except for the A-position specimens.

Table VIII-1

Sample Transmittances

(Aperture size = ± 2 milliradians λ_o = 632.8 nm)

Specimen	Transmittance as received (%)	Transmittance with silicone oil (%)
1-A	2	28
2-A	1	37
1-B	15	33
2-B	1	3
1-C	2	5
2-C	1	2

Photographic. Photographic light scattering patterns from the six specimens are presented in Figure VIII-2. The same photographic

Fig. VIII-2 Photographic light scattering patterns from samples 1 and 2, A-, B-, and C-position specimens. The exposure conditions are the same for the A- and B-position specimens. The two C-position specimens have the same exposure conditions, but different from the A- and B-positions.

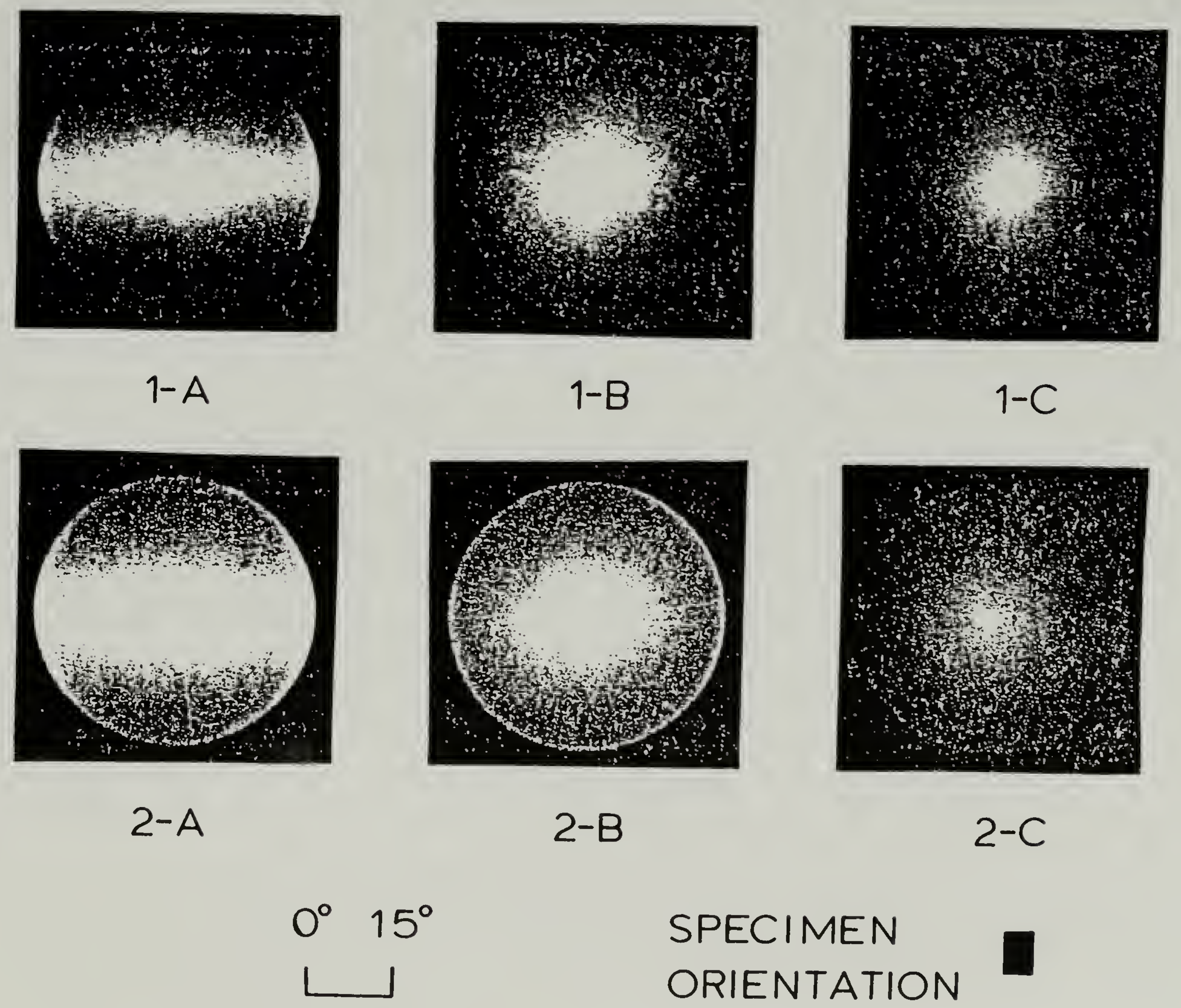
1-A
1-B
1-C
2-A
2-B
2-C
0° 15°
SPECIMEN ORIENTATION

conditions were used for the A- and B-position specimens. The same photographic conditions were used for both C-position specimens but these conditions differed from those for the A- and B-position specimens. Therefore, qualitative intensity comparisons can be made between samples 1 and 2 for any one specimen position.

The A-position specimen patterns are elongated in the horizontal direction, indicating elongation of the scattering structures in the vertical direction (the vertical direction in an upright sitting cup). This orientation is probably a result of the forming process of the cups. The intensity levels of the two A-position specimen patterns appear qualitatively similar.

The B- and C-position specimen patterns appear to be circularly symmetric, indicating no preferred orientation of the scattering structures in these specimens. It is apparent that sample 1 has greater low angle scattering (i.e. greater transparency) than sample 2 for both the B- and C-position specimens.

Position sensitive detector. Light scattering data from the six specimens obtained on the two dimensional position-sensitive detector are given in Figures VIII-3 to VIII-5. The four quadrant scattering patterns have been averaged into single quadrant patterns. Isointensity contours are shown for each specimen's scattering pattern. The main beam was suppressed within the hatched area in Figures VIII-3 to VIII-5. The experimental conditions were such that the intensities can be compared between samples (1 and 2) for any one specimen position (A, B, or C).

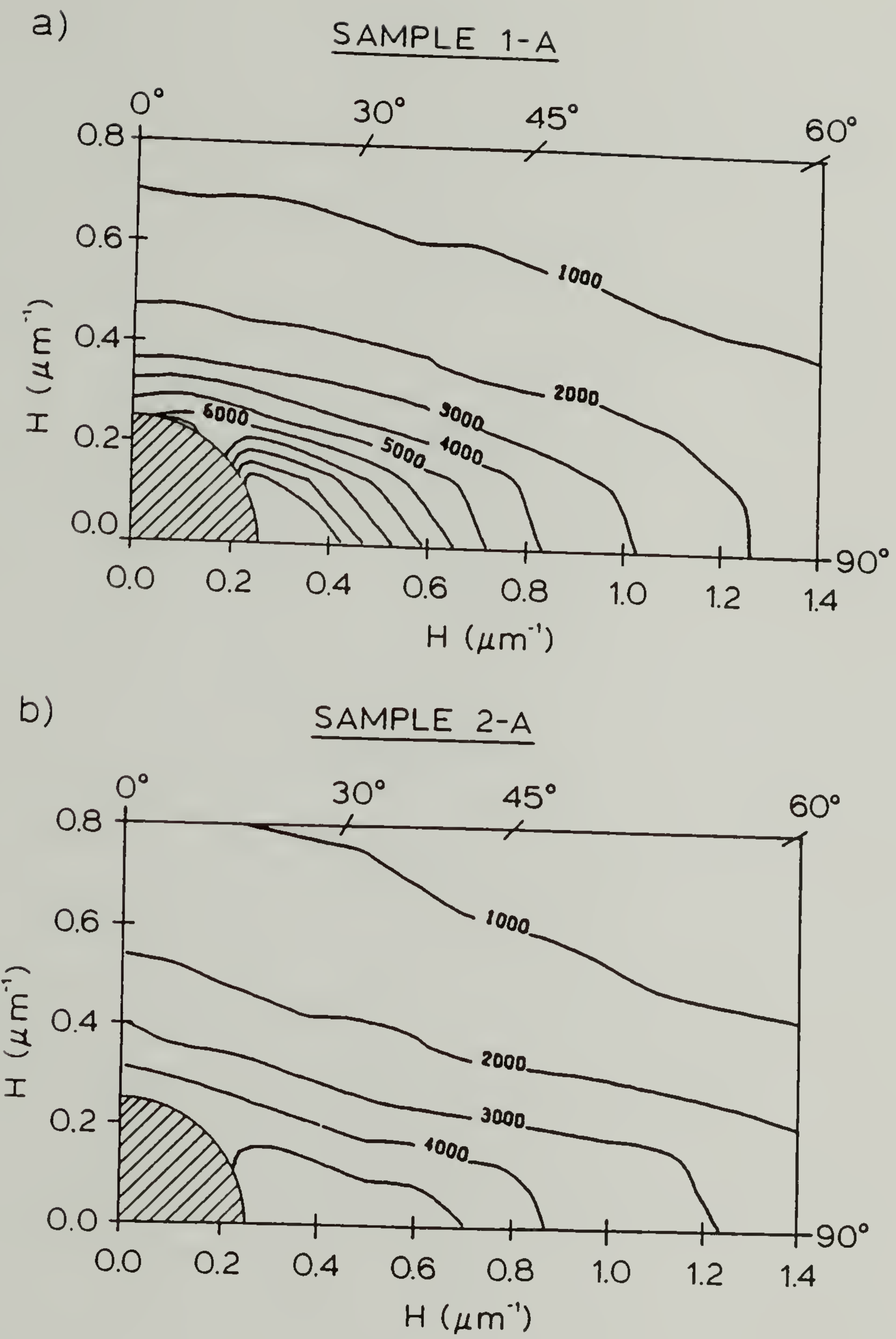

Fig. VIII-3 Two dimensional, single quadrant averaged SALS isointensity contours from the A-position specimens. Main beam stop is indicated by the hatched area.
a) sample 1-A, contours at every 1,000 intensity units, and
b) sample 2-A, contours at every 1,000 intensity units.

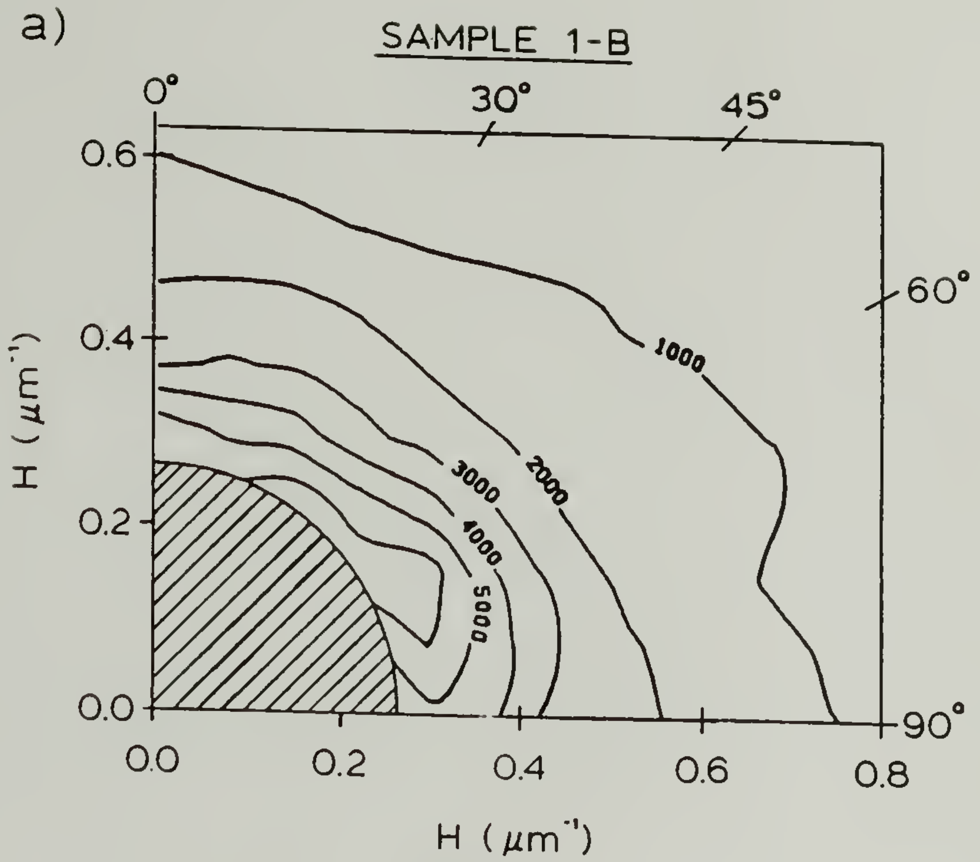

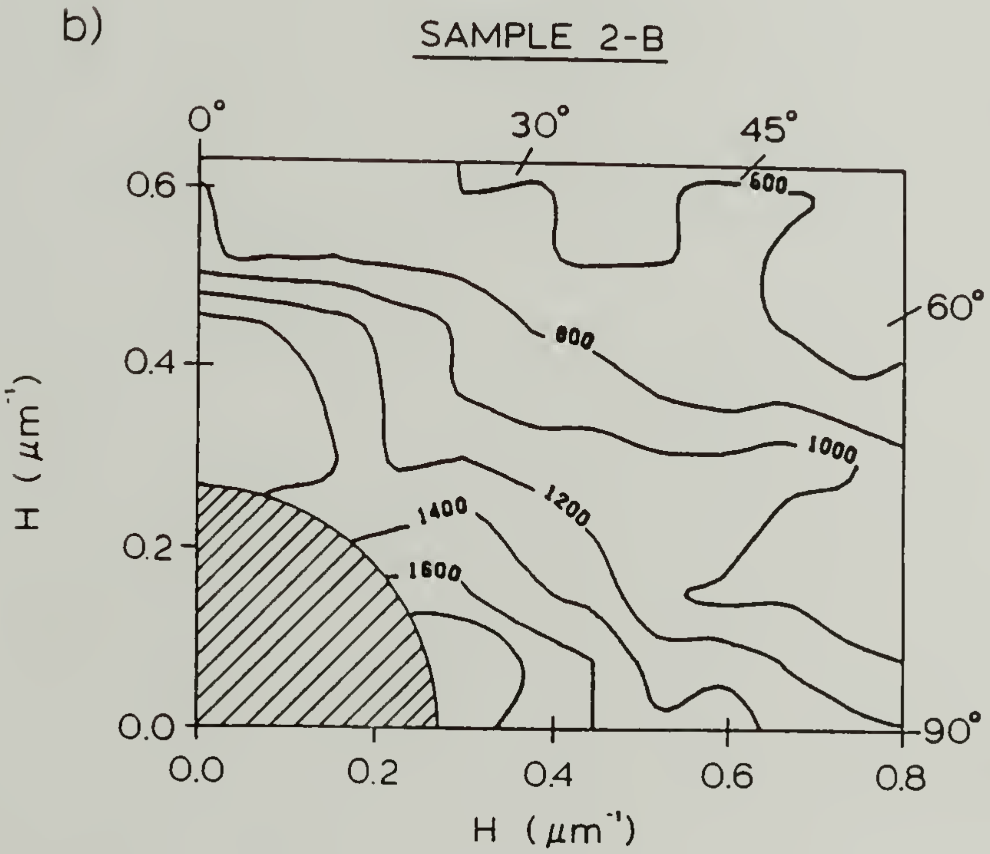

Fig. VIII-4 Two dimensional, single quadrant averaged SALS isointensity contours from the B-position specimens. Main beam stop is indicated by the hatched area.
a) sample 1-B, contours at every 1,000 intensity units, and
b) sample 2-B, contours at every 200 intensity units.

a) SAMPLE 1-C

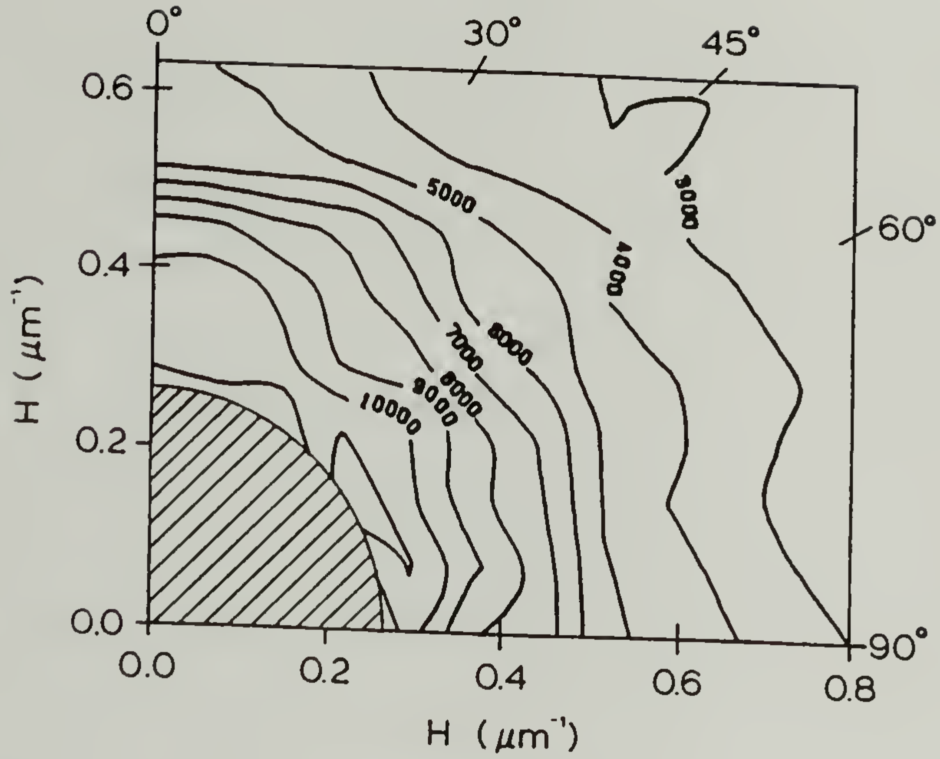

b) SAMPLE 2-C

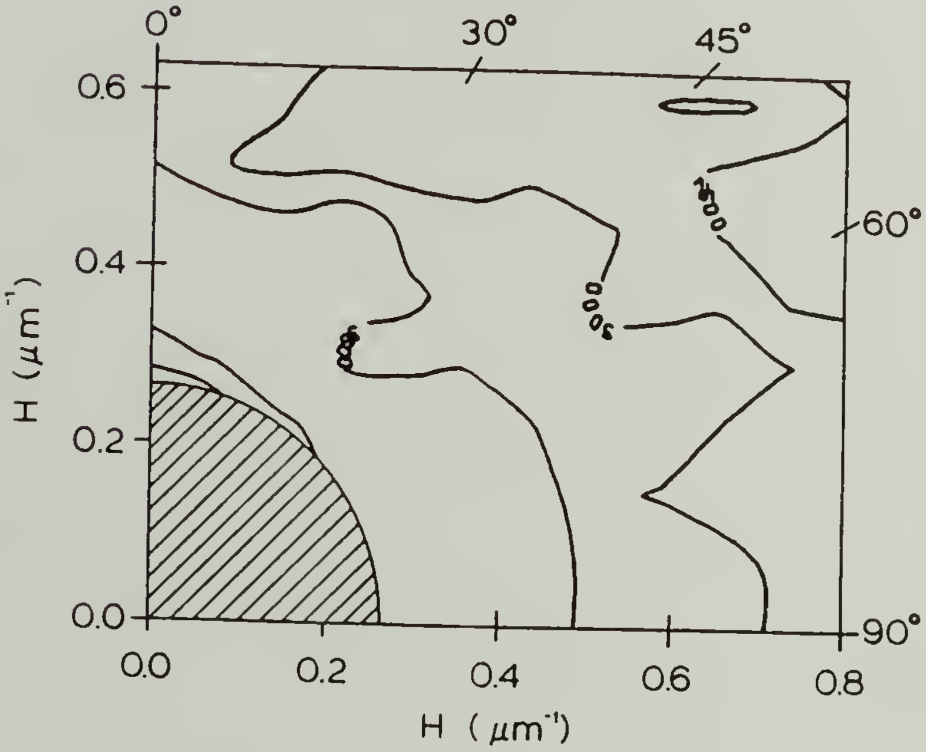

Fig. VIII-5 Two dimensional, single quadrant averaged SALS isointensity contours from the C-position specimens. Main beam stop is indicated by the hatched areas.
a) sample 1-C, contours at every 1,000 intensity units, and
b) sample 2-C, contours at every 500 intensity units.

The light scattering contours give quantitative confirmation of the results concluded from the photographic studies: The A-position specimens show structural elongation in the vertical direction, the B- and C-position specimen patterns are approximately circularly symmetric, sample 1 shows higher intensity levels of scattering at all angles measured.

The light scattering contours have been analyzed in the Guinier method [54] at various azimuthal angles. At small angles, random two phase systems follow the general scattering behavior of

$$I(H) = I(0)\ \exp\left(\frac{-\overline{R}_g^2 H^2}{3}\right) \qquad \text{(VIII-1)}$$

where I(H) is the scattered intensity at scattering vector magnitude H, $H = (4\pi/\lambda)\sin\ \theta/2$, λ is the wavelength of the light in the sample, is the polar scattering angle in the sample, I(0) is the extrapolated intensity H = 0, and R_g is the average radius of gyration of the inhomogeneities. Equation (VIII-1) can be rearranged to give

$$\ln\ I(H) = \ln\ I(0) - \left(\frac{\overline{R}_g^2 H^2}{3}\right). \qquad \text{(VIII-2)}$$

Therefore a plot of ln I(H) vs. H^2 gives a straight line at small H values with a slope = $-\overline{R}_g^2/3$ and an intercept of ln I(0).

The intensity at zero angle is given by [1]

$$I(0) = K\overline{\eta^2}V \qquad \text{(VIII-3)}$$

where K is a constant, $\overline{\eta^2}$ is the mean squared fluctuation in the refractive index and V is the average volume of the inhomogeneities ($V \sim \overline{R}_g^3$). For random two phase systems with sharp boundaries [46,73]

$$\overline{\eta^2} = \phi_1\phi_2(n_1 - n_2)^2 \qquad \text{(VIII-4)}$$

where ϕ_1 and ϕ_2 are the volume fractions of phases 1 and 2 and n_1 and n_2 are the refractive indices of phrases 1 and 2, respectively. I(0) can then be given as

$$I(0) = K'\ \phi_1\phi_2\ (n_1 - n_2)^2\overline{R}_g^3 \qquad \text{(VIII-5)}$$

where K' is a new constant. Since $\overline{R}_g^2$ is determined from the slope of the plot of I(H) vs. H^2, a term proportional to the mean squared fluctuation can be determined from the size-corrected intercept according to

$$I(0)/\overline{R}_g^3 = K'\ \phi_1\phi_2\ (n_1 - n_2)^2 = K'\ \overline{\eta^2}. \qquad \text{(VIII-6)}$$

The average R_g and $I(0)/\overline{R}_g^3$ were determined from the SALS data for the six specimens.

For the A-position specimens, radii of gyration in both the vertical and horizontal directions can be determined. The vertical radius of gyration ($\overline{R}_{g||}$) is determined from equation (VIII-2) using intensity values at an azimuthal angle of 0°. The horizontal radius of gyration

($\bar{R}_{g\perp}$) is determined using intensity values at an azimuthal angle of 90°. The elongation ratio (α) of the sample can be determined from

$$\frac{\bar{R}_{g||}}{\bar{R}_{g\perp}} = \alpha^{3/2} \qquad \text{(VIII-7)}$$

The light scattering profiles for azimuthal angles 0 and 90° are given in Figure VIII-6 for samples 1 and 2, A-position specimen. The linear regression lines indicated are for the low H range of the data. The size-corrected intercepts, radii of gyration and elongation of the A-position specimens are summarized in Table VIII-2.

Table VIII-2

Guinier Analysis of Specimen Type A

(from Figure VIII-6)

Sample	$\bar{R}_{g||}$ (μm)	$\bar{R}_{g\perp}$ (μm)	α	$I(0)/\bar{R}^3_{g||}$	$I(0)/\bar{R}^3_{g\perp}$
1	4.8	2.7	1.5	61	720
2	3.8	1.7	1.7	68	1300

The radii of gyration listed in Table VIII-2 indicate a larger particle size in both azimuthal directions for sample 1 as compared to sample 2. Sample 2 seems to show a slightly higher elongation ratio than sample 1. The size-corrected intercept values were higher for

Fig. VIII-6 Guinier type SALS plots from the A-position specimens: a) sample 1-A, azimuthal angle = 0°, b) sample 1-A, azimuthal angle = 90°, c) sample 2-A, azimuthal angle = 0°, and d) sample 2-A, azimuthal angle = 90°.

a)

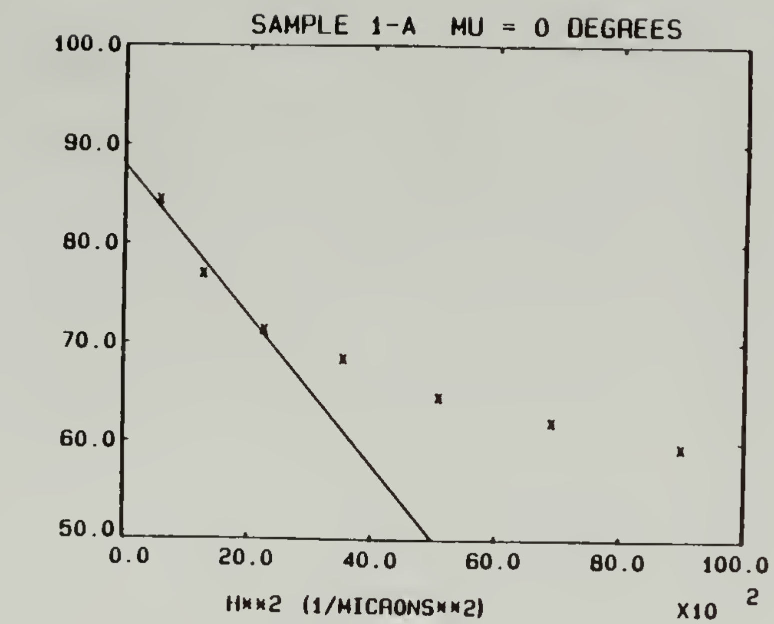
SAMPLE 1-A MU = 0 DEGREES
LN (INTENSITY)
X10 1
100.0
90.0
80.0
70.0
60.0
50.0
0.0
20.0
40.0
60.0
80.0
100.0
H**2 (1/MICRONS**2)
X10 2

b)

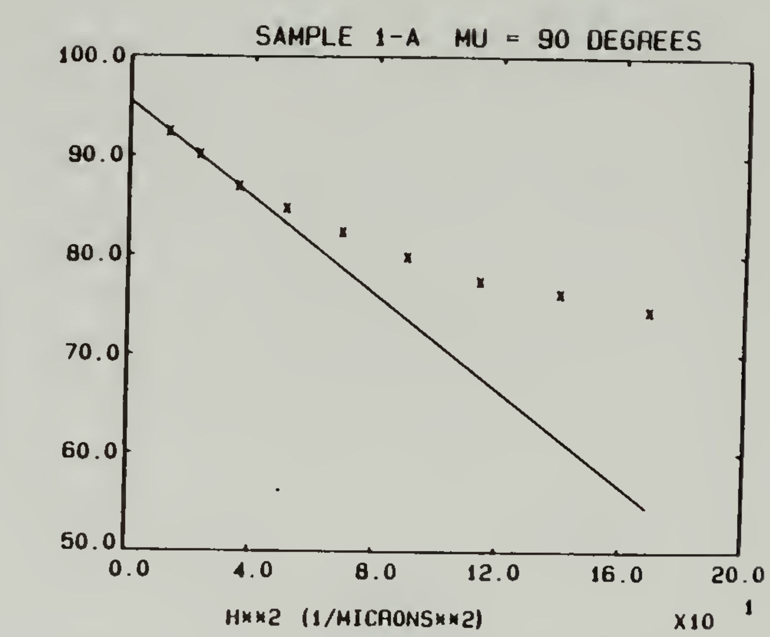
SAMPLE 1-A MU = 90 DEGREES
LN (INTENSITY)
X10 1
100.0
90.0
80.0
70.0
60.0
50.0
0.0
4.0
8.0
12.0
16.0
20.0
H**2 (1/MICRONS**2)
X10 1

c)

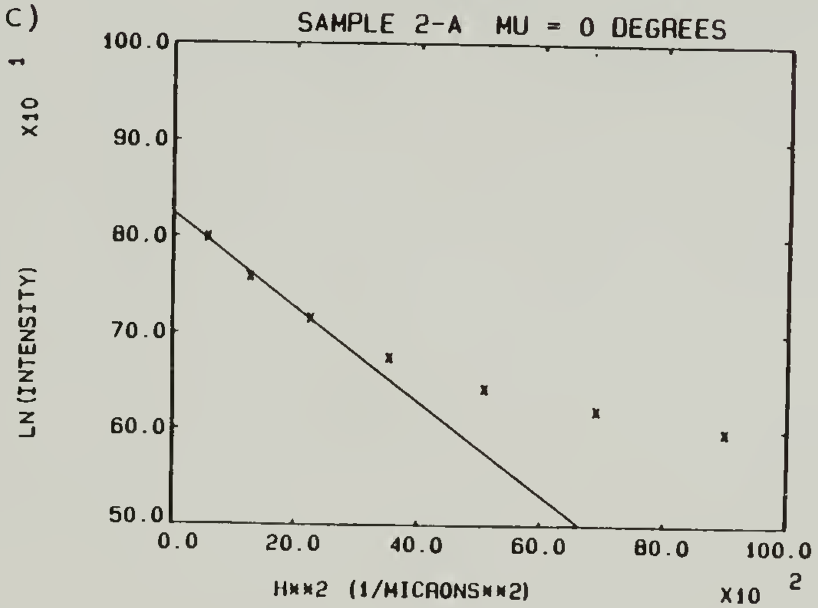
SAMPLE 2-A MU = 0 DEGREES
LN (INTENSITY)
X10 1
100.0
90.0
80.0
70.0
60.0
50.0
0.0
20.0
40.0
60.0
80.0
100.0
H**2 (1/MICRONS**2)
X10 2

d)

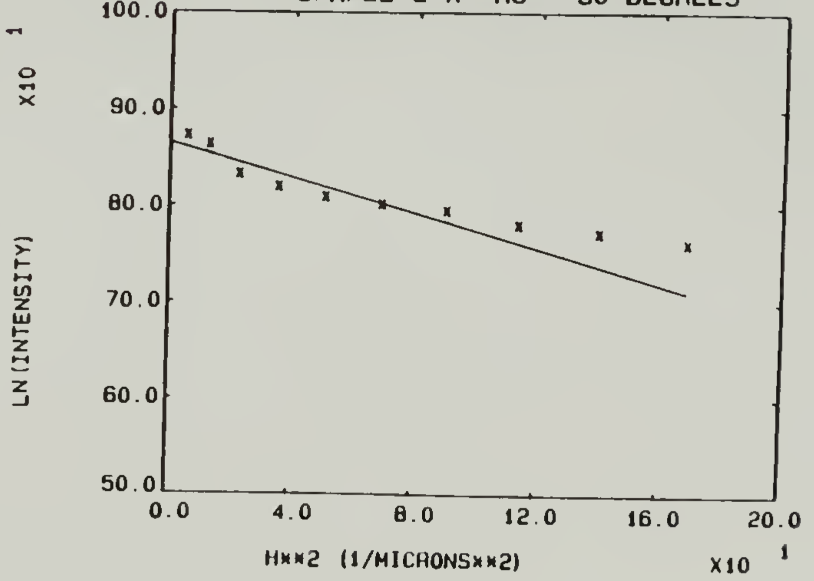
SAMPLE 2-A MU = 90 DEGREES
LN (INTENSITY)
X10 1
100.0
90.0
80.0
70.0
60.0
50.0
0.0
4.0
8.0
12.0
16.0
20.0
H**2 (1/MICRONS**2)
X10 1

sample 2 for each azimuthal angle.

B- and C-position specimens give approximately circularly symmetrical light scattering patterns (Figures VIII-4 and VIII-5). The light scattering data was therefore circularly averaged and then analyzed according to equations (VIII-2) and (VIII-6). The Guinier plots of the circularly averaged data are given in Figure VIII-7. Table VIII-3 summarizes this data. It is clear that sample 1 exhibits larger particle size than sample 2. Also sample 2 has equal or greater size-corrected intercept values for these B- and C-position specimens.

Table VIII-3

Guinier Analysis of B- and C-Position Specimens

(from Figure VIII-7)

Specimen	$\bar{R}_g$ (μm)	$I(0)/\bar{R}_g^3$
1-B	5.2	91
2-B	2.6	100
1-C	3.4	420
2-C	1.2	2000

Fig. VIII-7 Guinier type plots from circularly averaged SALS data: a) sample 1-B, b) sample 2-B, c) sample 1-C, and d) sample 2-C.

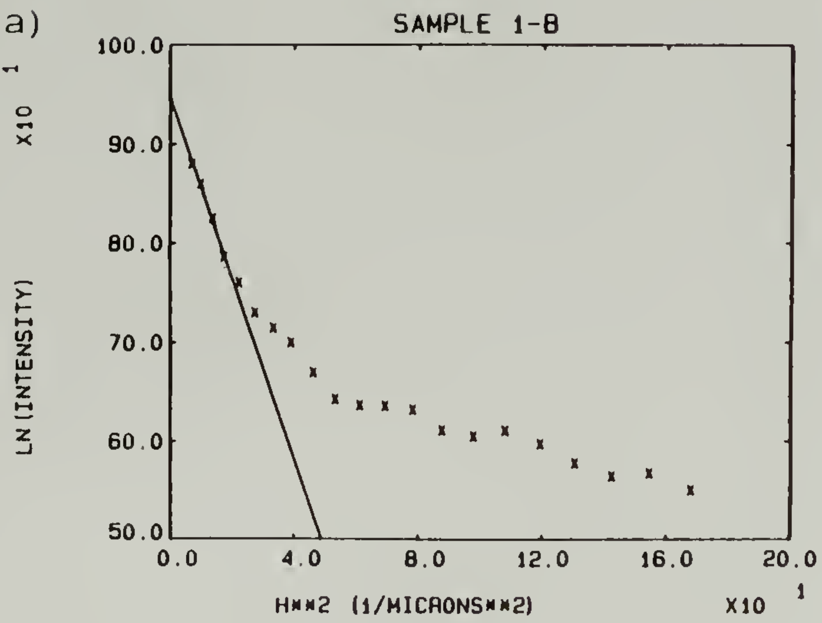
a)
SAMPLE 1-B
LN (INTENSITY)
X10 1
100.0
90.0
80.0
70.0
60.0
50.0
0.0
4.0
8.0
12.0
16.0
20.0
H**2 (1/MICRONS**2)
X10 1

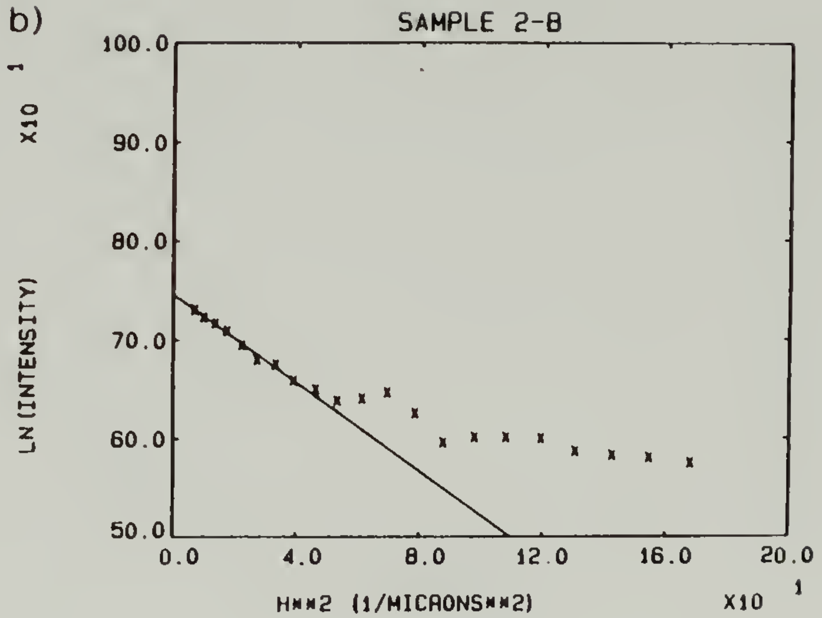
b)
SAMPLE 2-B
LN (INTENSITY)
X10 1
100.0
90.0
80.0
70.0
60.0
50.0
0.0
4.0
8.0
12.0
16.0
20.0
H**2 (1/MICRONS**2)
X10 1

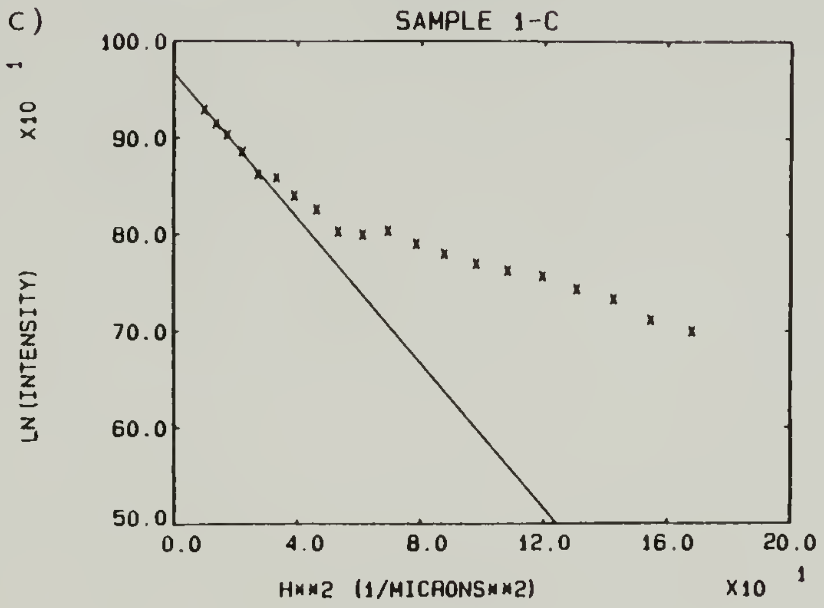
c)
SAMPLE 1-C
LN (INTENSITY)
X10 1
100.0
90.0
80.0
70.0
60.0
50.0
0.0
4.0
8.0
12.0
16.0
20.0
H**2 (1/MICRONS**2)
X10 1

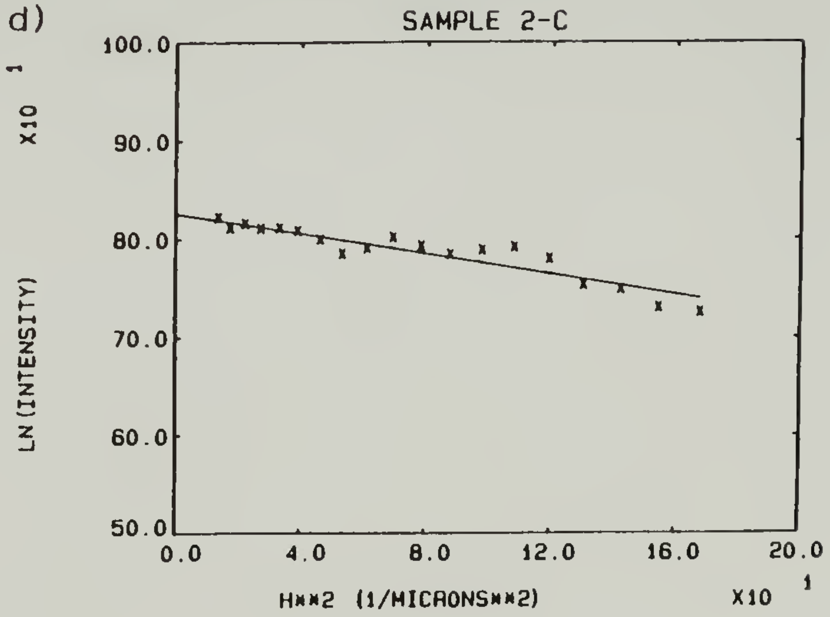
d)
SAMPLE 2-C
LN (INTENSITY)
X10 1
100.0
90.0
80.0
70.0
60.0
50.0
0.0
4.0
8.0
12.0
16.0
20.0
H**2 (1/MICRONS**2)
X10 1

Discussion

Sample 1 was more transparent than sample 2 for each specimen type in the "as received" condition. The light scattering studies can be used to analyze the reason for the transparency and to suggest means of controlling the transparency of such films. It is apparent from the transmission data from the oil-covered samples that control of surface smoothness may be a very significant means of improving the transparency of polyphase films. This conclusion is similar to the results of Stehling et al. [147]. They concluded that most of the haze of low density polyethylene was due to surface scattering.

The greater transparency of sample 1 can be analyzed in terms of the SALS results. The greater transparency of sample 1 may be due to its larger particle size. Although one generally associates larger particle size with greater haze, this may not be true for sufficiently larger particles. Diminished haze for larger particle size can be explained in terms of the Debye and Bueche [1] type analysis. They [1] and others [148,149] have shown that, for internal structures composed of isotropic, random inhomogeneities, the scattered light represented by the Rayleigh factor, $R(\theta)$, is given by:

$$R(\theta) = \frac{4\pi^3 \overline{\eta^2} a^3 (1 + \cos^2\theta)}{\varepsilon^2 \lambda^2 (1 + a^2 H^2)^2} \qquad \text{(VIII-8)}$$

where a is the correlation length (a measure of the average size of the inhomogeneities), ε is the average dielectric constant of the medium and the other terms are as previously defined.

Equation (VIII-8) describes the scattering of unpolarized, monochromatic light by a medium containing isotropic, random inhomogeneities. If the inhomogeneities are anisotropic (as polymer crystals or spherulites), one must consider the scattering from orientation fluctuations as well as density fluctuations [4]. We will consider only isotropic inhomogeneities in this discussion.

The turbidity (τ) arising from the internal structure is calculated by integrating equation (VIII-8) over all scattering angles:

$$\tau = 2\pi\int_0^\pi R(\theta)\ \sin\theta\ d\theta \qquad \text{(VIII-9)}$$

The turbidity is defined by the relation

$$I_t = I_o\ \exp(-\tau d) \qquad \text{(VIII-10)}$$

where I_t is the intensity transmitted by a sample of thickness d when the incident intensity is I_o. Integration of equation (VIII-9) leads to an expression relating the turbidity to the average size of the inhomogeneities and the radiation wavelength [1]:

$$\tau = \frac{32\pi^4\overline{\eta^2}a^3}{\varepsilon^2\lambda^4}\left[\frac{(b + 2)^2}{b^2(b + 1)} - \frac{2(b + 2)}{b^3}\ln\ (b + 1)\right] \qquad \text{(VIII-11)}$$

where $b = (16\pi^2/\lambda^2)a^2$. Equation (VIII-11) predicts that, for a given wavelength of light, the turbidity will increase as the average size of the inhomogeneities increases.

In practical polymer film usage, the light scattered at very small angles, as well as the transmitted light, contributes to clarity. This

very small angle scattering should not be included in the turbidity when analyzing the effects of internal structure on polymer clarity. Hazemeters, often used to assess polymer clarity, do not include in the measured haze the light scattered at $\theta' < 2.5°$, where θ' is the polar scattering angle in air [150]. (θ' is related to θ by Snell's law: $n \sin\theta = \sin\theta'$, where n is the refractive index of the medium; $n^2 = \varepsilon$). Standard light transmission tests also include some small angle scattering in the measurement of transmission [151].

Let us define turbidity (τ) as the amount of light that is scattered, at any angle. The incident and transmitted intensities are then related as in equation (VIII-10). Haze is here defined as being that portion of the scattered light intensity which does not contribute to clarity. Haze ($\tau'(\theta_{min})$) is calculated by excluding the very small angles from the integration of equation (VIII-9):

$$\tau'(\theta_{min}) = 2\pi\int_{\theta_{min}}^{\pi} R(\theta) \sin\theta \, d\theta \qquad \text{(VIII-12)}$$

where θ_{min} is the minimum angle of the scattered light to be included in the haze. In practice, θ_{min} is dependent upon the distance between the light source and the film and the distance between the observer and the film. Effectively, θ_{min} tends to decrease as either of these distances are increased. Integration of equation (VIII-12) yields:

$$\tau'(\theta_{min}) = \frac{32\pi^4\overline{\eta^2}a^3}{\varepsilon^2\lambda^4} \left[\left(\frac{1}{b} + \frac{2}{b^2} + \frac{2}{b^3}\right)\left(\frac{1}{F} - \frac{1}{b+1}\right)\right.$$

$$\left. - \frac{2(b+2)}{b^3} \ln\left(\frac{b+1}{F}\right) + \frac{2}{b^3}(1 + b - F)\right] \qquad \text{(VIII-13)}$$

where $F = 1 + \frac{b}{2}(1-\cos\theta_{min})$. Equation (VIII-13) leads to equation (VIII-11) in the case of $\theta_{min} = 0$.

For a given $\theta_{min} > 0$ and a given wavelength of light, equation (VIII-13) predicts that, as a function of the inhomogeneity size a, $\tau'(\theta_{min})$ reaches a maximum at a critical value of a ($a = a_c$). For $\theta_{min} = 1.67°$ ($\theta'_{min} = 2.5°$, refractive index = 1.5) and $\lambda_o = 0.6328$ (λ_o = wavelength in air), $a_c = 2.3$ µm. For reasonably small minimum angles ($\theta_{min} < 7°$), the critical inhomogeneity size is related to the minimum angle according to

$$a_c H_{min} = 1.0 \qquad \text{(VIII-14)}$$

where $H_{min} = 4\pi/\lambda \sin \theta_{min}/2$. Figure VIII-8 shows the effect of the inhomogeneity size on $\tau'(\theta_{min})$ for various values of θ_{min}.

The analysis of haze arising from the internal structure of polymer films can be made using equations (VIII-13) and (VIII-14). These equations indicate that haze is not necessarily reduced by reducing the size of the inhomogeneities in the polymer film, but that there is a critical size where the haze is a maximum. This phenomenon is dependent upon the exclusion of some small angle scattering from the measurement of haze. Since larger particles scatter more at small angles, the choice of a non-zero θ_{min} will tend to exclude some of the scattering due to large particles from the measurement of haze. It is this exclusion which leads to the critical size phenomenon. Since equations (VIII-13) and (VIII-14) were derived for a fixed wavelength of light,

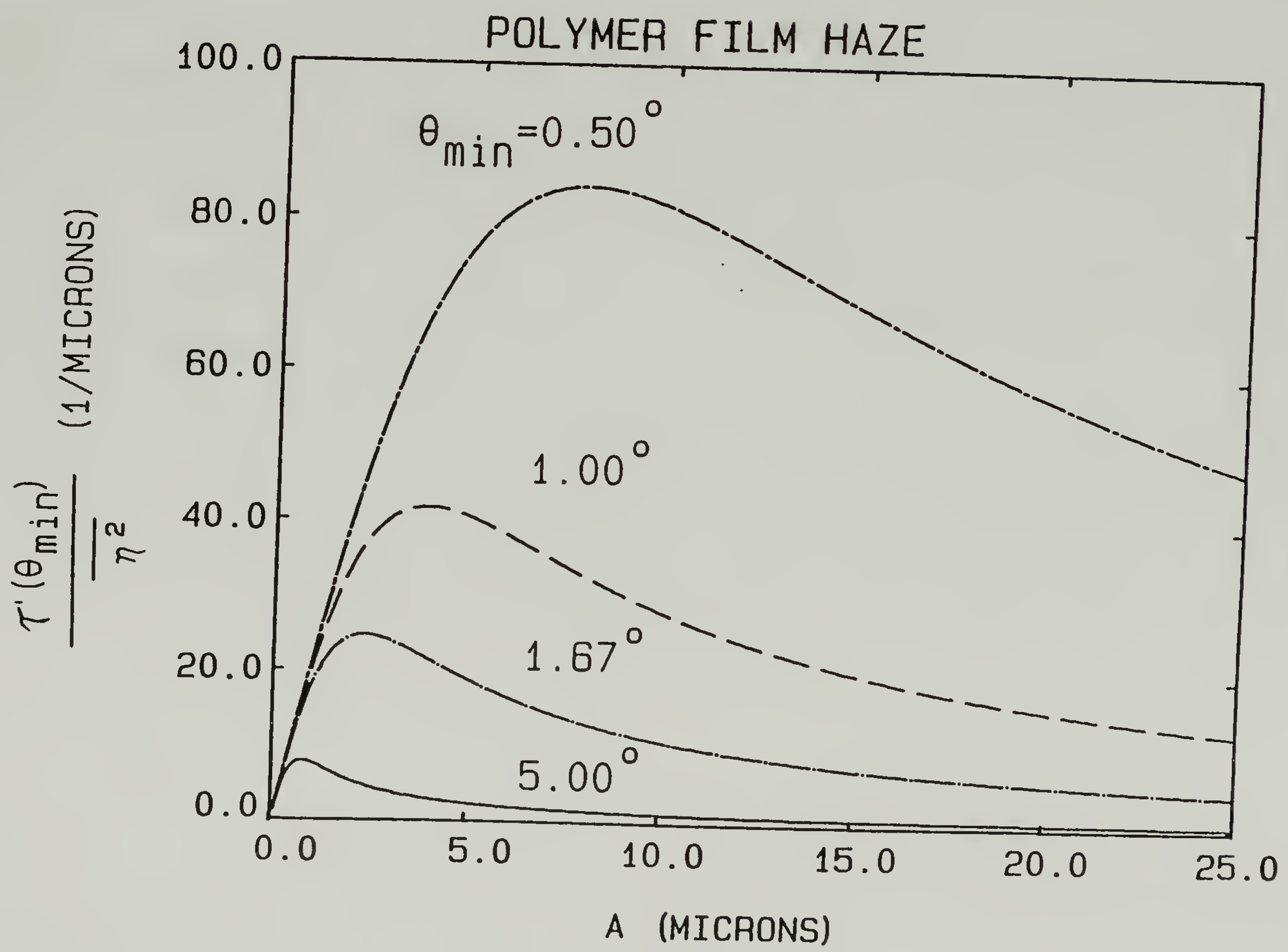

Fig. VIII-8 Haze as a function of inhomogeneity size a, for various values of θ_{min}. $\lambda' = 0.6328$ µm, $n = 1.5$.

haze from white light can be determined by integrating the haze as given in equation (VIII-13) over the visible spectrum. One must also assess the surface effects when evaluating haze from polymer films. In order to separate the surface and internal effects, one can eliminate the surface effects by performing the scattering experiments using a matching refractive index immersion fluid on the surface of the film.

It appears that in our systems we may be beyond the critical value of a such that the systems with the larger inhomogeneities have a greater transparency. Since the radius of gyration determined by scattering is weighted towards the larger radii of gyration [1], the scattering will be sensitive to the distribution of the sizes of the inhomogeneities as well as the average size.

Apparently, the B-position specimens have a larger particle size than the C-position specimens from the same sample number. The Guinier analysis used assumed spherically symmetrical particles. The size difference could be due to the particles in the B-position specimens being oblate spheroids in the plane of the film, being thinner in the direction perpendicular to the film than the C-position specimens. Such a shape difference would allow the B- and C-position particles to have the same volume, but different $\bar{R}_g$ as measured by SALS.

To examine the possibility of such a shape change, similar SALS experiments were performed on samples which were tilted 45° relative to the incident beam. There was no apparent elongation of the SALS patterns due to the tilting. Tilting of oblate spheroids would produce an elongated pattern. The size difference between B- and C-position

specimens may be due to different phase growth for the different specimens due to the different thermal and mechanical history of the two different positions in the cups during their molding.

The intensity of the SALS is also dependent upon the value of $\overline{\eta^2}$. The size-corrected intercept values reported in Tables VIII-2 and VIII-3 are proportional to $\overline{\eta^2}$. The results show that the size-corrected intercepts for sample 2 are equal to or larger than those for sample 1, indicating that $\overline{\eta^2}$ is larger for sample 2 than sample 1. The larger value of $\overline{\eta^2}$ for sample 2 may be due to a larger volume fraction of rubber particles or a larger refractive index difference between the two phases in sample 2 as compared to sample 1. Since we have no further information on these systems, we cannot distinguish between these two effects. The greater transparency of sample 1 may be due to its lower value of $\overline{\eta^2}$ alone or it may also be due to the larger inhomogeneity size. Our data does not allow us to decide whether the larger values for sample 2 are sufficient to cause its greater scattering of if the size effect is also important.

Conclusions

This study has demonstrated the use of SALS techniques and a two dimensional position sensitive light scattering detector to evaluate the cause of transparency in very practical polyphase systems. The principal factors found to be affecting the transparency of these hi-impact polystyrene products are the surface roughness, the volume fractions of the phases, the difference of the refractive indices of the

phases and the size of the phases. The thickness of the material is also important. The control of these factors in the manufacturing of these products should lead to the control of the transparency of these products. The extension of the inhomogeneities due to processing were also determined by these techniques.

It was also shown that the haze from polyphase polymer films does not monotonically increase with particle size. An additional factor affecting haze is the maximum scattering angle that one includes in a transmission measurement. When the factor is considered, there is a critical particle size for which the haze is a maximum.

CHAPTER IX

SUMMARY

General Conclusions

This dissertation has presented studies of the advancement and utilization of the techniques of SALS to investigate the morphology of deformed and undeformed spherulitic semi-crystalline polymers. The technique advancements were made in both the theoretical and instrumental aspects of SALS. The utilization of the latest techniques was made in studies of the melting, crystallization and elongation of spherulitic polymers and the study of haze from phase separated polymer blends.

The determination of the effects of spherulitic truncation on H_v SALS was the major theoretical advancement of SALS made in this work. A method of computer simulation of spherulite nucleation and growth in both two and three dimensions was used. The changes in the H_v SALS patterns due to spherulitic truncation have been determined as functions of the volume (or area) fraction of spherulites and the type of nucleation. The meaning of the "average" size of spherulites as measured by H_v SALS is now more well understood. Several terms in the model equations for H_v SALS are now more readily calculable in terms of experimental results. The application of the model equations for truncated spherulitic systems has been developed and outlined. The calculated results from this study make it a straightforward procedure

to quantitatively analyze H_v SALS data from spherulitic polymers. The results can also be applied to quantitative V_v SALS analysis.

The computer simulation method of nucleation, growth and truncation is useful, not only in the results calculated and presented in this dissertation, but also as a general modelling technique. The computer simulation method is general and can be extended to the SALS study of several other morphological phenomena. A very large data base and several programs have been developed. With only very minor changes to the data base or a program, one could examine: the effects of deformation on truncated spherulites, the combined effects of internal disorder and spherulitic truncation, the effects on V_v and H_h SALS, or spherulitic growth under nonrandom nucleating conditions, for example. More significant modifications of the programs would permit one to model internally disordered, truncated, deformed spherulites. The method is also amendable to certain nonspherulitic nucleation and growth phenomena, such as phase separation.

The major instrumental advancement made in this work was the development of the OMA2: a two dimensional, position sensitive SALS detector. This device permits one to rapidly collect and analyze quantitative, two dimensional SALS data. Quantitative, two dimensional SALS intensity data is necessary to carry out the type of analysis of SALS from polymer spherulites described and developed elsewhere in this work. The two dimensional nature of the device makes it useful to examine SALS from anisotropic systems, such as deformed spherulites. The device is also useful for isotropic SALS patterns, such as that from

phase separated polymer blends. The OMA2 was essential for the experimental portions of this work and is essential for that of several other workers in our laboratory.

The theoretical and instrumental advances made were utilized in four experimental SALS studies: the melting of PET, the crystallization of PET, the deformation of LDPE and PP and the evaluation of haze from phase separated polymer blends. The melting and crystallization studies utilize both the theoretical and instrumental advances in quatitative SALS studies of changes in PET spherulites during melting and crystallization. The study of LDPE and PP spherulite deformation and the study of film haze both utilize the OMA2 and its features.

In the study of PET melting, it was found that the spherulites melt over a range of about 20°C without change in spherulite size, number or internal disorder (optic axis misorientation). The decrease in H_V SALS intensity is due to a continuous decrease in spherulite crystallinity. The fully corrected experimental H_V SALS intensities are lower than, but in modest agreement with, the theoretically predicted intensities. The intensity differences have been attributed to: lack of suitable three dimensional internal disorder theory, possible overestimation of the effects of truncation and/or nonrandom amorphous orientation following the melting of crystals.

In the study of PET crystallization, it was found from the quantitative H_V SALS that, as the spherulites grow, there was an initial decrease and then a levelling off of both the internal disorder and the spherulite crystallinity. The quantitative V_V SALS results indicated

that there was not significant nonspherulitic crystallization. The rapid detection capabilities of the OMA2 were utilized to follow the spherulitic growth of a rapidly crystallizing polymer. The measurement of the volume fraction spherulites by H_v SALS, V_v SALS and sample turbidity were in reasonable agreement. The relationships between the corrected experimental and the theoretical H_v SALS intensities were similar to that found in the melting study.

The study of the deformation elongation of LDPE and PP spherulites was the most comprehensive examination to date of the van Aartsen and Stein affine model of spherulite deformation. It was found that the model adequately described the H_v SALS of LDPE and PP, but failed in the description of V_v and H_h SALS. The deformation mechanisms indicated by the H_v SALS were reasonable for LDPE and PP.

The study of polymer film haze from phase separated polymer blends demonstrated the use of SALS and the OMA2 to analyze a very practical polymer problem. It was found, and explained in terms of the Debye-Bueche theory, that the haze from a film of a phase separated polymer blend does not increase monotonically with particle size. There exists a critical particle size where the haze is maximum.

This dissertation combined theoretical, instrumental and experimental efforts in SALS from polymer films. The theoretical and instrumental advances were essential precursors for the quantitative SALS of spherulitic polymer melting and crystallization. The theoretical and instrumental advances will also assist future studies in this area. The instrumental advances facilitated the studies of

spherulite deformation and film haze.

Suggestions for Further Research

It has often been suggested that good research uncovers more unsolved questions than it solves. This dissertation has indicated several interesting future studies and has laid the necessary groundwork for many of these studies. The development in this dissertation of theories, procedures and instrumentation for quantitative and nonquantitative SALS studies is at least as important as the experimental results achieved. The following few suggestions for further research are not only appropriate and interesting research topics, but they have also been made much more feasible by the results of this dissertation.

Theoretical studies. Several theoretical investigations of the effects changing morphologies on the SALS have been made possible by the theoretical methods developed in this dissertation. These investigations can combine several of the complexities of polymer morphology into the more simplified models.

Truncation of spherulites. The programs have been developed for computer simulated spherulite growth and truncation. The results presented may have overestimated the effects of truncation since random nucleation was assumed. Optical microscopic investigations of the nucleation of large spherulites, such as those from polyethylene oxide or poly-1-butene, could be made to establish an experimental nuclei

distribution. Such a distribution can be readily inserted into the existing programs in order to calculate the resulting spherulite shapes and their H_v SALS. Such a study would determine whether the random results could be applied to the melting and crystallization studies carried out here, or to similar studies.

Internally disordered and truncated spherulites. One can edit the program which calculates the H_v SALS from a truncated spherulite assuming a perfectly ordered spherulite to include the effects of internal disorder. The routines for calculating the effects of internal disorder are available from D.Y. Yoon. The programs of nucleation, spherulite growth and truncation analysis would be unaffected. The PDP 11/34 in our laboratory would be adequate for such a study. This study would combine the effects of internal disorder and spherulitic truncation and eliminate the need for assuming the additivity of these effects. The results could be applied to the melting and crystallization studies here, or to similar studies.

Deformed, truncated spherulites. The spherulite data bases already generated can be transformed, by affine or nonaffine methods, to develop data bases for deformed, truncated spherulites. The H_v SALS program can then be used to calculate the resulting intensity distributions. These calculations could be carried out for internally disordered and truncated spherulites as well. Other polarization modes could be examined by development of the appropriate programs. Such a study is necessary to develop a procedure for quantitative SALS from deformed systems.

Other impinging growth studies. The methods and/or programs developed here could be extended to calculate the SALS from: the nucleation and growth of separated phases in polymer blends or the oriented crystal structure developed during stress induced crystallization, for example. The techniques can also be generalized to small-angle scattering from other radiation.

Three dimensional internal disorder. Further advancements of the techniques of quantitative SALS from polymer spherulites are impeded by the absence of the calculations of the effects of internal disorder in three dimensional spherulites on the H_v SALS azimuthal profiles. Such calculations could best be made in cooperation with D.Y. Yoon. The results could be applied to the melting and crystallization studies here, or to similar studies.

Radial variation of spherulite crystallinity. The H_v and V_v SALS intensity equations were derived for model spherulites with constant crystallinity within the spherulites. It was found here that the crystallinity within the spherulite decreases radially. If this type of behavior can be generally shown to be true, one should rederive the SALS equations to include this effect.

Spherulite deformation. Studies are necessary to develop the features of nonaffine deformation into the SALS models of spherulite deformation.

Experimental studies. The experimental studies in this dissertation provided some interesting results about spherulite melting, crystallization and deformation, as well as polymer film haze. Several

new studies are appropriate.

Spherulite melting. Assuming that the discrepancy between the corrected experimental and theoretical H_v SALS intensities before melting can be rectified by the further studies of internal disorder and spherulitic truncation, the experimental H_v SALS intensity decrease during melting lags behind the theoretical intensity. The theoretical intensity assumes no amorphous contributions to the scattering. The amorphous contributions could be assessed by examining the melting by H_v SALS as a function of heating rate. For extremely slow heating rates, the amorphous material should have time to relax to its random configurations. It would be interesting to see if the experimental H_v SALS intensity decrease still lags behind the theoretical intensity at slow heating rates.

Crystallization. The results of this study determined the changes in internal disorder and spherulite crystallinity with spherulite growth rate as large as 0.3 µm/sec, only a limited number of scans were taken before the system was volume filled with spherulites. One should examine crystallization by SALS in a slightly slower crystallization rate region, such as high temperature or with a higher molecular weight, for PET for example. Crystallization kinetics should be examined over a range of temperatures and/or molecular weights. The internal disorder and spherulite crystallinity effects are probably dependent on these variables. The crystallization rate in this study is approximately the limiting rate at which one can obtain full intensity scans and analysis using this apparatus. The theory and equipment is available for such

studies.

Crystallinity measurement device. Quantitative SALS from spherulitic polymers has the potential of measuring the degree of crystallinity of polymers, literally with the "speed of light". This measurement could be of great practical importance in the on-line monitoring of crystallinity during polymer fabrication processes. The results of this study are encouraging for the development of a SALS crystallinity detector. The three dimensional internal disorder and improved truncation theories may be necessary predecessors to such a device. One can examine the spherulite crystallinities by SALS of several polymer films, with varying choices of polymer, molecular weight and crystallization conditions. These results can be compared to crystallinities measured by density, DSC and WAXD to test the general applicability of the methods developed here.

Spherulite deformation of PP. This study examined the deformation of one spherulitic form of PP. Three other forms can be grown by proper choices of crystallization conditons. One could examine the SALS from films with other spherulite type to see if the van Aartsen and Stein model distinguishes the differences in their deformation morphologies.

Spherulite deformation, orientation functions. This study showed reasonable agreement between the c axis orientation measured by infrared dichroism and the optic axis orientation calculated from the H_v SALS results. The optic axis orientation should be further compared with other orientation measurements, such as by WAXD. In this way one might examine the deformation mechanism, the validity of the models and the

relationships among the orientation functions of the optic axis, the crystalline a, b and c axes and the amorphous orientation. Birefringence studies would be useful in this work as well.

References

1. P. Debye and A.M. Bueche, J. Appl. Phys., 20, 518 (1949).
2. R.S. Stein and M.B. Rhodes, J. Appl. Phys., 31, 1873 (1960).
3. M. Goldstein and E.R. Michalik, J. Appl. Phys., 26, 1450 (1955).
4. R.S. Stein and P.R. Wilson, J. Appl. Phys., 33, 1914 (1962).
5. R.S. Stein, P. Erhardt, S. Clough and G. Adams, J. Appl. Phys., 37, 3980 (1966).
6. J.J. van Aartsen, J. Colloid Interface Sci., 39, 583 (1972).
7. R.S. Stein and T. Hotta, J. Appl. Phys., 35, 2237 (1964).
8. T. Hashimoto and R.S. Stein, J. Polym. Sci., A2, 8, 1127 (1970).
9. D.Y. Yoon and R.S. Stein, J. Polym. Sci., Polym. Phys. Ed., 12, 735 (1974).
10. S. Clough, M.B. Rhodes and R.S. Stein, J. Polym. Sci., C, 18, 1 (1967).
11. S. Clough, J.J. van Aartsen and R.S. Stein, J. Appl. Phys., 36, 3072 (1965).
12. R.J. Samuels, J. Polym. Sci., 9, 2165 (1971).
13. R.J. Samuels, Structured Polymer Properties, J. Wiley, New York (1974).
14. R.J. Samuels, J. Polym. Sci., A2, 6, 1101 (1968).
15. R.S. Stein, in Structure and Properties of Polymer Films, R.W. Lenz and R.S. Stein, eds., Plenum Press, N.Y. (1973).
16. R.S. Stein, Applied Polymer Symp., 20, 347 (1973).
17. R.S. Stein, A. Misra, T. Yuasa and F. Khambatta, Pure and Appl. Chem., 49, 915 (1977).

18. R.E. Prud'homme, Ph.D. Dissertation, University of Massachusetts, Amherst, MA (1973).

19. R.S. Stein and M.B. Rhodes, J. Appl. Phys., 39, 4903 (1968).

20. R.E. Prud'homme and R.S. Stein, J. Polym. Sci., Polym. Phys. Ed., 12, 1805 (1974).

21. R.S. Stein and W. Chu, J. Polym. Sci., A2, 8, 1137 (1970).

22. R.E. Prud'homme and R.S. Stein, Europ. Polym. J., 13, 365 (1977).

23. R.S. Stein, M.B. Rhodes, P.R. Wilson and S.N. Stidham, Pure and Appl. Chem., 4, 219 (1962).

24. M. Motegi, T. Oda, M. Moritani and H. Kawai, Polymer Journal (Japan) 1, 209 (1970).

25. R.E. Prud'homme and R.S. Stein, J. Polym. Sci., Polym. Phys. Ed., 11, 1357 (1973).

26. R.S. Stein and C. Picot, J. Polym. Sci., 8, 1955 (1970).

27. C. Picot, R.S. Stein, R.H. Marchessault, J. Borch and A. Sarko, Macrom., 4, 467 (1971).

28. I.T. Moneva, Y.W. Brestkin, B.M. Ginsburg and S.Y. Frenkel, Europ. Polym. J., 8, 1033 (1972).

29. R.E. Prud'homme and R.S. Stein, J. Polym. Sci., Polym. Phys. Ed., 11, 1683 (1973).

30. R.S. Stein and C. Picot, J. Polym. Sci., A2, 8, 2127 (1970).

31. R.J. Tabar, A. Wasiak, S.D. Hong, T. Yuasa and R.S. Stein, J. Polym. Sci., Polym. Phys. Ed., 19, 49 (1981).

32. R.S. Stein and T. Hashimoto, J. Polym. Sci., A2, 9, 1747 (1971).

33. R.E. Prud'homme, D. Yoon and R.S. Stein, J. Polym. Sci., Polym. Phys. Ed., 11, 1047 (1973).

34. D.Y. Yoon and R.S. Stein, J. Polym. Sci., Polym. Phys. Ed., 12, 763 (1974).

35. D.Y. Yoon, private communication.

36. R.S. Stein and J. Keane, J. Polym. Sci., 17, 21 (1955).

37. R.E. Prud'homme, L. Bourland, R.T. Natarajan and R.S. Stein, J. Polym. Sci., Polym. Phys. Ed., 12, 1955 (1974).

38. R.T. Natarajan, R.E. Prud'homme, L. Bourland and R.S. Stein, J. Polym. Sci., Polym. Phys. Ed., 14, 1541 (1976).

39. T. Yuasa, M.S. Thesis, University of Massachusetts, Amherst, MA (1975).

40. P. Leite-James, M.S. Thesis, University of Massachusetts, Amherst, MA (1979).

41. R.T. Natarajan, D.Y. Yoon, R.E. Prud'homme and R.S. Stein, unpublished.

42. J.J. van Aartsen and R.S. Stein, ONR Technical Report No. 83 (1966).

43. J.J. van Aartsen and R.S. Stein, J. Polym. Sci., A2, 9, 295 (1971).

44. W. Kuhn and F. Grün, Kolloid Z., 101, 248 (1942).

45. L.R.G. Treloar, The Physics of Rubber Elasticity, second edition, Clarendon Press, Oxford (1958).

46. R.S. Stein, Rubber Chem. Technol., 49, 458 (1976).

47. R.J. Samuels, J. Polym. Sci., C, 13, 37 (1966).

48. A. Misra, R.E. Prud'homme and R.S. Stein, J. Polym. Sci., Polym. Phys. Ed., 12, 1235 (1974).

49. T. Ishikawa and R.S. Stein, Polym. J. (Japan), 8, 369 (1976).

50. A. Galeski, J. Polym. Sci., Polym. Phys. Ed., 19, 721 (1981).

51. A. Galeski and E. Piorkowska, J. Polym. Sci., Polym. Phys. Ed., 19, 731 (1981).

52. A. Galeski and E. Piorkowska, private communication.

53. R. Lutz and D.L. Handlin, private communication.

54. A. Guinier and G. Fournet, Small-Angle Scattering of X-Rays, Wiley, New York (1955).

55. M. Avrami, J. Chem. Phys., 7, 1103 (1939).

56. M. Avrami, J. Chem. Phys., 8, 212 (1940).

57. A.E.M. Keijzers, Ph.D. Dissertation, Technological University of Delft, Delft, The Netherlands (1967).

58. M.B. Rhodes, D.A. Keedy and R.S. Stein, J. Polym. Sci., 62, 573 (1962).

59. R.S. Stein, F.H. Norris and A. Plaza, J. Polym. Sci., 24, 455 (1957).

60. A.E.M. Keijzers, J.J. van Aartsen and W. Prins, J. Am. Chem. Soc., 90, 3107 (1968).

61. F. van Antwerpen and D.W. van Krevelen, J. Polym. Sci. A2, 10, 2409 (1972).

62. T. Pakula and Z. Soukup, J. Polym. Sci., Polym. Phys. Ed., 12, 2437 (1974).

63. C.O. Ruud, J. Metals, 10 (June, 1979).

64. D.A. Steffen and C.O. Ruud, in Advances in X-Ray Analysis, Vol. 21, Plenum Press, New York (1978).

65. M.R. James and J.B. Cohen, in Advances in X-Ray Analysis, Vol. 19, Kendall/Hunt, Dubuque, Iowa (1976).

66. G.T. Reynolds, J.R. Milch and S.M. Gruner, Rev. Sci. Instrum., 49, 1241 (1978).

67. T. Hashimoto, S. Suehiro, M. Shibayama, K. Saijo and H. Kawai, Polym. J. (Japan) 13, 501 (1981).

68. A. Wasiak, D. Peiffer and R.S. Stein, J. Polym. Sci., Polym. Lett. Ed., 14, 381 (1976).

69. R.J. Tabar, R.S. Stein and M.B. Long, J. Polym. Sci., Polym. Phys. Ed., 20, 2041 (1982).

70. T.P. Russell, J. Koberstein, R. Prud'homme, A. Misra, R.S. Stein, J.W. Parsons and R.L. Rowell, J. Polym. Sci., Polym. Phys. Ed., 16, 1879 (1978).

71. M. Born and E. Wolf, Principles of Otics, Pergamon Press, New York (1964).

72. J. Gilmer, N. Goldstein and R.S. Stein, submitted for publication.

73. J. Koberstein, T.P. Russell and R.S. Stein, J. Polym. Sci., Polym. Phys. Ed., 17, 1719 (1979).

74. M.K. Parpart, Ph.D. Dissertation, University of Massachusetts, Amherst, MA (1979).

75. R.S. Stein and F.H. Norris, J. Polym. Sci., 21, 381 (1956).

76. R.S. Stein, J. Polym. Sci., 31, 327 (1958).

77. J.J. Hermans, P.H. Hermans, D. Vermaas and A. Weidynger, Rec. Trav. Chem. Pays-Bas., 65, 427 (1946).

78. L.E. Alexander, S. Ohlberg and G.R. Taylor, J. Appl. Phys., 26, 1068 (1955).

79. V.G. Baranov, A.V. Kenarov and T.I. Volkov, J. Polym. Sci., C, 30, 271 (1970).

80. Polymer Handbook, J. Brandrup and E.H. Immergut, eds., second edition, Wiley-Interscience, New York (1975).

81. W.R. Moore and D. Sanderson, Polymer, 9, 153 (1968).

82. B. Wunderlich, Macromoleclar Physics Volume 1 Crystal Structure, Morphology, Defects, Academic Press, New York (1973).

83. A. Keller, J. Polym. Sci., 17, 291 (1955).

84. A. Keller, J. Polym. Sci., 17, 351 (1955).

85. N.C. Watkins and D. Hansen, Text. Res. J., 38, 388 (1968).

86. H.J. Biangardi and H.G. Zachman, Makromol. Chem., 177, 1173 (1976).

87. R. de P. Daubeny, C.W. Bunn and C.J. Brown, Proc. Roy. Soc. (London) A226, 531 (1954).

88. N. Sakaguchi, T. Oda, A. Nakai and H. Kawai, J. of the Society of Fiber Science and Technology (Japan), 33, 499 (1977).

89. H.H. Dumbleton, J. Polym. Sci., A2, 6, 795 (1968).

90. F. van Antwerpen and D.W. van Krevelen, J. Polym. Sci., Polym. Phys. Ed., 10, 2423 (1972).

91. T. Ishibashi, Y. Tani, O. Yoskizaki and E. Nagai, Kobunshi Kagaku (Chem. High Polymers), 23, 205 (1966).

92. T. Ishibashi and Y. Tani, Int. Chem. Eng., 10, 294 (1970).

93. T. Pakula and M. Kryszewski, Europ. Polym. J., 12, 47 (1976).

94. C.H. Bamford, W.G. Barb, A.D. Jenkins and P.F. Onyon, Kinetics of Vinyl Polymerization by Radical Mechanisms, Butterworths, London (1958).

95. H.D. Keith and F.J. Padden, Jr., J. Appl. Phys., 34, 2409 (1963).

96. C. Picot, R.S. Stein, M. Motegi and H. Kawai, J. Polym. Sci., A2, 8, 2115 (1970).

97. A. Misra and R.S. Stein, J. Polym. Sci., B, 10, 473 (1972).

98. R.S. Stein and A. Misra, J. Polym. Sci., Polym. Phys. Ed., 11, 109 (1973).

99. H.D. Keith and F.J. Padden, Jr., J. Appl. Phys., 35, 1270 (1964).

100. W.H. Cobbs and R.L. Burton, J. Polym. Sci., 10, 275 (1953).

101. K. Sasaguri, M.B. Rhodes and R.S. Stein, J. Polym. Sci., B, 1, 571 (1963).

102. I.L. Hay and A. Keller, Kolloid Z. Polymer, 204, 43 (1965).

103. R. Yang and R.S. Stein, J. Polym. Sci., A2, 5, 939 (1967).

104. T. Oda, N. Sakaguchi and H. Kawai, Chem. of High Polymers (Japan), 281, 588 (1968).

105. K. Kataoka, T. Takahashi and I. Tsujimoto, Sen-I-Gakkaishi, 28, 336 (1972).

106. T. Pakula, A. Galeski and M. Kryszewski, J. Polym. Sci., Symp., 42, 743 (1973).

107. K. Shimamura, S. Murakami and K. Katayama, Makromol. Chem., Rapid Commun., 3, 199 (1982).

108. W.W. Adams, Ph.D. Dissertation, University of Massachusetts, Amherst, MA (1983).

109. D.Y. Yoon, C. Chang and R.S. Stein, J. Polym. Sci., Polym. Phys. Ed., 12, 2091 (1974).

110. M. Matsuo, M. Tamada, T. Terada, C. Sawatari and M. Niwa, Macrom., 15, 988 (1982).

111. K. Fujita, S. Suehiro, S. Nomura and H. Kawai, Polym. J. (Japan), 14, 545 (1982).

112. S. Nomura, M. Matsuo and H. Kawai, J. Polym. Sci., Polym. Phys. Ed., 10, 2489 (1972).

113. M. Matsuo, Y. Seino, T. Watanabe, S. Moriguchi, F. Ozaki and T. Ogita, Polym. J. (Japan), 13, 755 (1981).

114. T. Oda, S. Nomura and H. Kawai, J. Polym. Sci., A, 3, 1993 (1965).

115. K. Sasaguri and R.S. Stein, J. Polym. Sci., C, 5, 139 (1964).

116. K. Sasaguri, S. Hoshino and R.S. Stein, J. Appl. Phys., 35, 47 (1964).

117. K. Sasaguri, R. Yamada and R.S. Stein, J. Appl. Phys., 35, 3188 (1964).

118. P. Erhardt, K. Sasaguri and R.S. Stein, J. Polym. Sci., C, 5, 179 (1964).

119. T. Hashimoto, Ph.D. Dissertation, University of Massachusetts, Amherst, MA (1970).

120. S. Nomura, M. Matsuo and H. Kawai, J. Polym. Sci., Polym. Phys. Ed., 12, 1371 (1974).

121. A. Todo, T. Hashimoto and H. Kawai, Polym. J. (Japan), 11, 59 (1979).

122. Z.W. Wilchinsky, Polymer, 5, 271 (1964).

123. T.T. Wang, J. Polym. Sci., Polym. Phys. Ed., 12, 145 (1974).

124. R.S. Moore, J. Polym.Sci., A2, 5, 711 (1967).

125. D.P. Anderson, Ph.D. Dissertation, University of Massachusetts, Amherst, MA (1981).

126. W. Ruland, Acta Cryst., 14, 1180 (1961).

127. C.G. Vonk, J. Appl. Cryst., 6, 148 (1973).

128. W. Glenz and A. Peterlin, J. Macromol. Sci., B4, 473 (1970).

129. R. Zbinden, Infrared Spectroscopy of High Polymers, Academic Press, New York (1964).

130. B. Jasse and J.L. Koenig, J. Macromol. Sci. Rev. Macromol. Chem., C17, 61 (1979).

131. B.E. Read and R.S. Stein, Macromol., 1, 116 (1968).

132. C.W. Bunn, Trans. Faraday Soc., 35, 482 (1939).

133. S. Krimm, Fortschr. Hochpolym.-Forsch., 2, 51 (1960).

134. R.G. Snyder, J. Chem. Phys., 47, 1316 (1967).

135. J.R. Nielson and A.H. Woolett, J. Chem. Phys., 26, 1391 (1957).

136. G. Allen, G. Gee and G.J. Wilson, Polymer, 1, 456 (1960).

137. C.W. Bunn and R. de P. Daubeny, Trans. Faraday Soc., 50, 1173 (1954).

138. D.G. Peiffer, Ph.D. Dissertation, University of Massachusetts, Amherst, MA (1976).

139. C.R. Desper and R.S. Stein, J. Appl. Phys., 37, 3990 (1966).

140. A. Turner-Jones, J.M. Aizlewood and D.R. Beckett, Makromol. Chem., 75, 134 (1964).

141. F.J. Padden, Jr. and H.D. Keith, J. Appl. Phys., 30, 1479 (1959).

142. H.D. Keith, F.J. Padden, Jr., N.M. Walter and H.W. Wyckoff, J. Appl. Phys., 30, 1485 (1959).

143. R.J. Cembrola, T. Kyu, R.S. Stein, S. Suehiro and H. Kawai, accepted, J. Polym. Sci., Polym. Phys. Ed., (1983).

144. M. Inoue, J. Polym. Sci., 60, 81 (1962).

145. H.D. Keith and F.J. Padden, Jr., J. Polym. Sci., 41, 525 (1959).

146. V. Petraccone, I.C. Sanchez and R.S. Stein, J. Polym. Sci., Polym. Phys. Ed., 13, 1991 (1975).

147. F.C. Stehling, C.S. Speed and L. Westerman, Macromol., 14, 698 (1981).

148. P. Debye, H.R. Anderson, Jr. and H. Brumberger, J. Appl. Phys., 28, 679 (1957).

149. J.T. Koberstein and R.S. Stein, J. Polym. Sci., Polym. Phys. Ed., 18, 199 (1980).

150. "Standard Test Method for Haze and Luminous Transmittance of Transparent Plastics", ASTM D1003, 1980 Annual Book of ASTM Standards, Part 35, American Society for Testing and Materials, Easton, MD, 1980.

151. "Standard Test Method for Transparency of Plastic Sheeting", ASTM D1746, 1980 Annual Book of ASTM Standards, Part 35, American Society for Testing and Materials, Easton, MD, 1980.

APPENDIX

Polynomial Equations

In order to help automate the use of the analytical plots in this dissertation which are useful to future studies of quantitative SALS from spherulitic polymers, the calculated data has been fit to polynomial equations by the least squares method. These equations are presented to assist the experimenter; no presumption of any significance to the polynomial fitting is being made.

The general form of the polynomial equation is:

$$y = a_o + a_1 X + a_2X^2 \ldots + a_nX^n \qquad \text{(A-1)}$$

The tables of the a_i coefficients can be used with equation (A-1) in place of graphical determination of the values. The following definitions apply to the tables:

C_T: truncation correction at $U = U_{max}$ and $\mu = 45°$

ϕ_s: area or volume fraction spherulites

$R_{H_v}(U_{max},\mu)$: H_v intensity at $U = U_{max}$ and $\mu = \mu$

$\theta_{max,\infty}$: polar scattering angle of maximum H_v intensity, after infinite growth time (volume filling spherulites)

θ_{max}: polar scattering angle of maximum H_v intensity

K_v: parameter in $V = K_v\bar{R}_n^3$

V: average spherulite volume

$\bar{R}_n$: average spherulite radius, as determined by H_v SALS

K_A: parameter in $A = K_A \bar{R}_n^2$

A: average spherulite area

$C_M(U_{max},\mu)$: multiple scattering correction correction and $U = U_{max}$ and $\mu = \mu$

τd: product of turbidity and thickness of sample

δ: internal disorder parameter

C_D: internal disorder correction at $U = U_{max}$ and $\mu = 45°$.

Table A-1

Truncation Correction for Two Dimensional Spherulite Growth

(From Figure III-18)

y	x	a_o	a_1	a_2	a_3	a_4	a_5	a_6	a_7
C_T (simultaneous nucleation)	ϕ_s	1.000	-0.2390	9.910	-45.35	97.10	-97.59	37.99	0.0000
C_T (sporadic nucleation)	ϕ_s	1.522	-1.953	4.323	41.99	-221.5	437.8	-393.3	134.1

Table A-2

Azimuthal H_V SALS Intensity Ratios for Two Dimensional Spherulite Growth and Simultaneous Nucleation

(From Figure III-19)

y	x	a_o	a_1	a_2	a_3	a_4	a_5	a_6
$\frac{R_{H_v}(U_{max},20)}{R_{H_v}(U_{max},45)}$	ϕ_s	0.4132	0.991	-0.2332	1.128	1.915	1.112	0.0000
$\frac{R_{H_v}(U_{max},15)}{R_{H_v}(U_{max},45)}$	ϕ_s	0.2500	0.1144	-0.1381	0.8716	-1.668	1.063	0.0000
$\frac{R_{H_v}(U_{max},10)}{R_{H_v}(U_{max},45)}$	ϕ_s	0.1170	0.1552	-0.3200	1.415	-2.310	1.343	0.0000
$\frac{R_{H_v}(U_{max},0)}{R_{H_v}(U_{max},45)}$	ϕ_s	0.0000	0.1506	0.3218	-2.380	6.420	-7.245	3.050

Table A-3

Azimuthal H_V SALS Intensity Ratios for Two Dimensional Spherulite Growth and Sporadic Nucleation

(From Figure III-20)

y	x	a_o	a_1	a_2	a_3	a_4	a_5	a_6
$\frac{R_{H_v}(U_{max},20)}{R_{H_v}(U_{max},45)}$	ϕ_s	0.4132	-0.930	2.318	-10.53	19.90	-16.94	5.522
$\frac{R_{H_v}(U_{max},15)}{R_{H_v}(U_{max},45)}$	ϕ_s	0.2500	-0.1173	2.731	-12.55	24.59	-21.87	7.441
$\frac{R_{H_v}(U_{max},10)}{R_{H_v}(U_{max},45)}$	ϕ_s	0.1170	-0.1273	2.769	-12.60	25.23	-23.09	8.074
$\frac{R_{H_v}(U_{max},0)}{R_{H_v}(U_{max},45)}$	ϕ_s	0.0000	-0.2430	2.762	-10.72	21.65	-20.95	7.773

Table A-4

Area Fraction Spherulites for Two Dimensional Spherulite Growth

(From Figure III-21)

y	x	a_o	a_1	a_2	a_3	a_4	a_5	a_6
ϕ_s (simultaneous nucleation)	$\frac{\theta_{max,\infty}}{\theta_{max}}$	0.0000	-0.0707	3.455	-5.097	7.811	-8.525	3.421
ϕ_s (sporadic nucleation)	$\frac{\theta_{max,\infty}}{\theta_{max}}$	0.0000	-0.1792	2.032	-6.389	19.84	-22.16	7.851

Table A-5

Truncation Correction for Three Dimensional Spherulite Growth and Simultaneous Nucleation

(From Figure III-22)

y	x	a_o	a_1	a_2	a_3	a_4	a_5	a_6	a_7
C_T	ϕ_s	1.000	-0.1608	6.002	-26.97	58.51	-58.96	22.73	0.0000

Table A-6

Azimuthal H_V SALS Intensity Ratios for Three Dimensional Spherulite Growth and Simultaneous Nucleation

(From Figure III-23)

y	x	a_o	a_1	a_2	a_3	a_4	a_5	a_6
$\frac{R_{H_v}(U_{max},20)}{R_{H_v}(U_{max},45)}$	ϕ_s	0.4132	-0.0161	0.6471	-2.897	5.953	-5.610	2.017
$\frac{R_{H_v}(U_{max},15)}{R_{H_v}(U_{max},45)}$	ϕ_s	0.2500	-0.0078	0.6858	-3.098	6.427	-6.104	2.211
$\frac{R_{H_v}(U_{max},10)}{R_{H_v}(U_{max},45)}$	ϕ_s	0.1170	0.0055	0.6254	-2.824	5.927	-5.700	2.093
$\frac{R_{H_v}(U_{max},0)}{R_{H_v}(U_{max},45)}$	ϕ_s	0.0000	0.0108	0.5275	-2.159	4.474	-4.364	1.646

Table A-7

Volume Fraction Spherulates for Three Dimensional Spherulite Growth and Simultaneous Nucleation

(From Figure III-24)

y	x	a_o	a_1	a_2	a_3	a_4	a_5	a_6
ϕ_s	$\frac{\theta_{max,\infty}}{\theta_{max}}$	0.000	-0.4509	4.243	-13.33	27.78	-25.15	7.907

Table A-8

Average Spherulite Volume for Three Dimensional Spherulite Growth and Simultaneous Nucleation

(From Figure III-25)

y	x	a_o	a_1	a_2	a_3	a_4	a_5
K_v	ϕ_s	4.189	-0.7891	-4.402	8.571	-7.395	1.794

Table A-9

Average Spherulite Area for Two Dimensional Spherulite Growth

(From Figure III-26)

y	x	a_o	a_1	a_2	a_3	a_4
K_A (simultaneous nucleation)	ϕ_s	3.142	-1.654	-0.2861	1.340	-1.293
K_A (sporadic nucleation)	ϕ_s	1.390	0.4457	-4.685	9.928	-6.051

Table A-10

Multiple Scattering Correction

(From Figure V-1, $\delta = 0.2$)

y	x	a_o	a_1	a_2	a_3
$C_M\ (U_{max},45)$	τd	1.000	0.4265	0.0777	0.0538
$C_M\ (U_{max},20)$	τd	1.000	0.3453	0.0915	0.0244
$C_M\ (U_{max},10)$	τd	1.000	0.2152	0.1047	-0.0093
$C_M\ (U_{max},0)$	τd	1.000	0.0977	0.0736	-0.0128

Table A-11

Azimuthal H_V SALS Intensity Ratios for Internally Disordered, Nontruncated, Two Dimensional Spherulites

(From Figure V-3)

y	x	a_o	a_1	a_2
$\frac{R_{H_v}(U_{max},20)}{R_{H_v}(U_{max},45)}$	ϕ_s	0.4132	0.0198	1.708
$\frac{R_{H_v}(U_{max},15)}{R_{H_v}(U_{max},45)}$	ϕ_s	0.2500	-0.0782	2.628
$\frac{R_{H_v}(U_{max},10)}{R_{H_v}(U_{max},45)}$	ϕ_s	0.1170	-0.1513	3.267
$\frac{R_{H_v}(U_{max},0)}{R_{H_v}(U_{max},45)}$	ϕ_s	0.0000	-0.0508	2.772

Table A-12

Azimuthal H_V SALS Intensity Ratios for Internally Disordered, Fully Grown, Three Dimensional Spherulites Resulting from Simultaneous Nucleation

(From Figure V-4)

y	x	a_o	a_1	a_2
δ	$\frac{R_{H_V}(U_{max},20)}{R_{H_V}(U_{max},45)}$	-1.072	2.095	-0.7874
δ	$\frac{R_{H_V}(U_{max},15)}{R_{H_V}(U_{max},45)}$	0.0697	0.4058	-0.1577
δ	$\frac{R_{H_V}(U_{max},10)}{R_{H_V}(U_{max},45)}$	0.3771	0.0166	-0.0272
δ	$\frac{R_{H_V}(U_{max},0)}{R_{H_V}(U_{max},45)}$	0.4816	-0.0682	0.0003

Table A-13

Internal Disorder Correction for Two Dimensional Spherulites

(From Figure V-5)

y	x	a_o	a_1	a_2	a_3
$\ln(C_D)$	δ	0.0000	1.975	3.872	226.5

OMA2 Analysis Software

The flow diagram in Figure A-1 summarizes the interrelationships among the computer programs available for SALS data collection and analysis using the OMA2. The functions of the programs are summarized as follows:

OMA2: controls the detector, monitors, data collection and storage;

SALS: converts raw x-y intensity data to absolute intensities as functions of the polar and azimuthal scattering angles;

CIRCLE: circularly averages a SALS data set;

QUAD: performs single quadrant averaging of a SALS data set;

SCAN: determines azimuthal or polar angle profiles of a SALS data set;

READS: reads the binary output files from SALS or QUAD and prints the results or sends them to a specified location;

CONDNS: condenses the output files from SALS or QUAD into fewer data points by averaging neighboring points together;

The plotting can be carried out using the PDP 11/34 and the associated software developed by C.T. Murray.

Copies of the SALS (with subroutines), CIRCLE, QUAD, SCAN, READS and CONDNS programs follow. The documentation included in the programs should assist the user. The OMA2 program is too voluminous to be reproduced here. It can be obtained from M.B. Long of the Department of Engineering and Applied Science at Yale University.

OMA2 PROGRAMS:

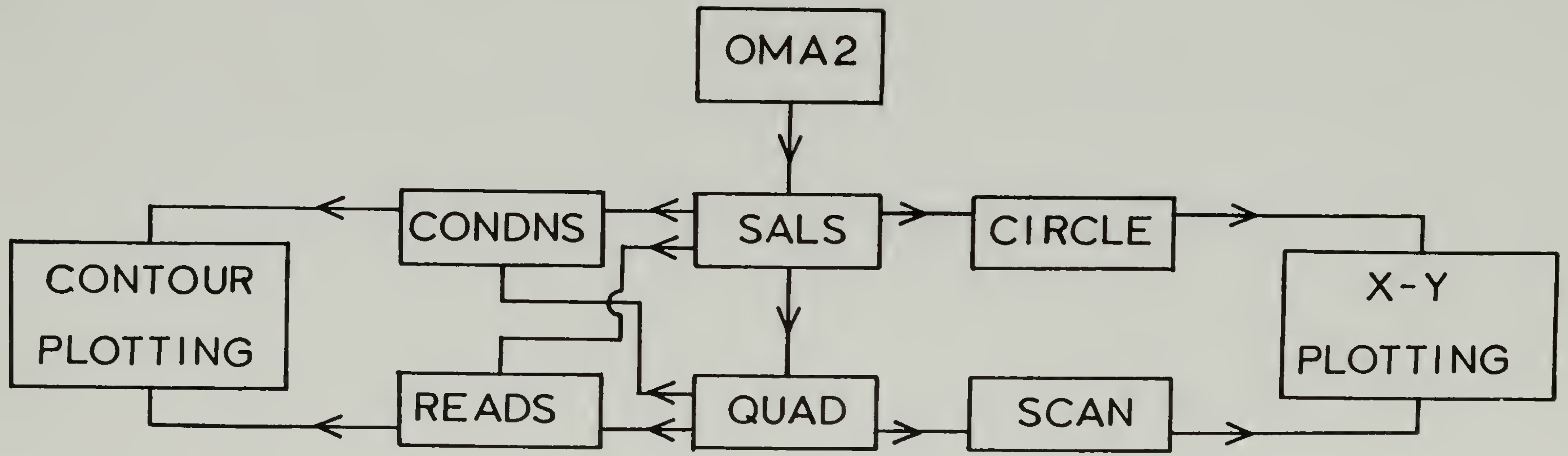

Fig. A-1 Flow diagram of the computer programs for SALS data collection and analysis using the OMA2.

```
      PROGRAM SALS
C ---------------------------------------------------------------------
C      THIS PROGRAM CORRECTS LIGHT SCATTERING DATA FROM THE OMA2 FOR
C      EXPERIMENTAL CONDITIONS.  IT CORRECTS FOR THE SENSITIVITY OF
C      THE DETECTOR AND THE NEUTRAL DENSITY FILTERS USED.
C      IT CALCULATES ABSOLUTE INTENSITTES (IN 1/MM) USING
C      THE SCATTERED INTENSITY FROM THE
C      LAMBERTIAN DIFFUSER AS A STANDARD.  THIS PROGRAM
C      CALIBRATES THE SCATTERING ANGLES FROM DIFFRACTION GRATING DATA.
C      THE OMA2 DATA IS IN BINARY FILES WHICH ARE READ INTO THIS
C      PROGRAM USING SUBROUTINE READBN.  THE OUTPUT FILE FROM THIS
C      PROGRAM IS ALSO IN BINARY.  IT CAN BE READ USING THE PROGRAM
C      READS.  THE OUTPUT FILE IS ALSO READY FOR FURTHER ANALYSIS
C      USING PROGRAMS QUAD AND CIRCLE.  THE OUTPUT DATA CAN BE PLOTTED
C      AS AN ISOINTENSITY CONTOUR MAP USING THE PROGRAM CONDNS AND
C      THE CONTOUR PLOTTING PROGRAMS ON THE PDP  11/34.
C      THIS PROGRAM CALLS SUBROUTINES DIFGRT, FILTER, READBN AND
C      CORSEN.
C      DEFINITIONS OF VARIABLES FOR SALS AND THE 4 SUBROUTINES:
C              ITID(I)= EXPERIMENT IDENTIFICATION INFORMATION
C              IOUTFL= NAME OF OUTPUT FILE
C              ISAMFL= SAMPLE DATA FILE NAME
C              ISENFL= SENSITIVITY DATA FILE NAME
C              IGRAFL= DIFFRACTION GRATING DATA FILE NAME
C              IBLNFL= BLANK SAMPLE FILE NAME
C              TDATA(I)= TEMPORARY INTENSITY VALUE BEING READ INTO
C                        OR FROM A BINARY FILE
C              CAL(IC,IT)= DIFFRACTION GRATING, SENSITIVITY OR BLANK
C                          SAMPLE INTENSITY AT CHANNEL IC AND TRACK IT
C              DATA(IC,IT)= SAMPLE INTENSITY AT CHANNEL IC AND TRAK IT
C              IBLOCK(I)= TEMPORARY DATA VARIABLE READ FROM BINARY FILE
C              IUNIT= UNIT NUMBER OF INPUT FILE
C              NCHAN= NUMBER OF CHANNELS IN EACH SCAN
C              NTRAK= NUMBER OF TRACKS IN EACH SCAN
C              THETA1= SCATTERING ANGLE (DEGREES) OF THE FIRST ORDER
C                      PEAK FROM THE DIFFRACTION GRATING
C              MAINC= CHANNEL LOCATION OF THE MAIN BEAM
C              MAINT= TRACK LOCATION OF THE MAIN BEAM
C              CHNCAL= CHANNEL CALIBRATION FACTOR FOR CONVERTING
C                      CHANNEL POSITIONS TO SCATTERING ANGLE
C              F015,F030,= FILTER FACTORS FOR THE 0.15, 0.30, 0.60,
C              F060,F100  1.00, 2.00, 3.00 AND 4.00 FILTERS
C              F200,F300
C              AND F400
C              DATMIN= MINIMUM INTENSITY VALUE
C              DATMAX= MAXIMUM INTENSITY VALUE
C              SAMFF= FILTER FACTOR FOR SAMPLE SCAN
```

```
C               SENFF= FILTER FACTOR FOR SENSITIVITY SCAN
C               BLNFF= FILTER FACTOR FOR BLANK SAMPLE SCAN
C               RGTG= (RAYLEIGH FACTOR)*(THICKNESS) FOR THE LAMBERTIAN
C                     DIFFUSER AT ZERO ANGLE (UNITLESS)
C               INSTBL= Y IF A BLANK SAMPLE IS USED
C                       N IF ONE IS NOT USED
C               TRANS= TRANSMITTANCE OF THE SAMPLE, RELATIVE TO THE
C                      BLANK SAMPLE
C               INST= Y IF THE OPERATOR NEEDS INSTRUCTIONS
C                     N IF INSTRUCTIONS ARE NOT NEEDED
C               RI= SAMPLE REFRACTIVE INDEX
C               AMUX= AZIMUTHAL ANGLE OF THE X AXIS OF THE MONITOR
C                     SCREEN
C               ANATT= ANALYZER ATTENUATION FACTOR (BETWEEN 0. & 1.)
C               TSAMP= SAMPLE THICKNESS IN MICRONS
C               INSTDG= Y IF A DIFFRACTION GRATING ANALYSIS IS TO
C                         BE DONE ON THIS RUN
C                       N IF IT IS NOT TO BE DONE
C               FRONT= FACTOR USED TO CALCULATE THE SCATTERING VECTOR
C                      H, ASSUMING THE WAVELENGTH=0.6328 MICRONS
C               INDEX= VARIABLE USED FOR COUNTING DATA POINTS IN A
C                      BINARY FILE RECORD
C               IDELC= CHANNELS AWAY FROM THE MAIN BEAM
C               IDELCA= EQUIVALENT CHANNEL LOCATION LOCATION IN
C                       THE FIRST QUADRANT
C               IDELT= TRACKS AWAY FROM THE MAIN BEAM
C               IDELTA= EQUIVALENT TRACK LOCATION IN THE FIRST
C                       QUADRANT
C               H= SCATTERING VECTOR (1/MICRONS)
C               AMU= AZIMUTHAL ANGLE
C               THETEX= SCATTERING ANGLE IN AIR, IN RADIANS
C               X= VARIABLE USED TO DETERMINE THETA
C               THETA= SCATTERING ANGLE IN THE SAMPLE, IN RADIANS
C               NUMREC= RECORD NUMBER IN A BINARY FILE
C               THEMAX= SCATTERING ANGLE AT THE MAXIMUM INTENSITY
C               HMAX= SCATTERING VECTOR AT THE MAXIMUM INTENSITY
C               AMUMAX= AZIMUTHAL ANGLE AT THE MAXIMUM INTENSITY
C               GMAX= MAXIMUM INTENSITY FROM THE DIFFRACTION GRATING
C               FOFMAX= INTENSITY AT FIRST ORDER PEAK
C               MAX1C= CHANNEL NUMBER OF RIGHT HAND FIRST ORDER PEAK
C               MAX1T= TRACK NUMBER OF RIGHT HAND FIRST ORDER PEAK
C               IMAX1C= CHANNEL SEPARATION OF THE MAIN BEAM AND THE
C                       RIGHT HAND FIRST ORDER PEAK
C               IMAX1T= TRACK SEPARATION OF THE MAIN BEAM AND THE
C                       RIGHT HAND FIRST ORDER PEAK
C               FILNUM= FILTER NUMBER USED IN A SCAN
C       WRITTEN BY R.J. TABAR 8-APR-81
C ---------------------------------------------------------------------
```

```
        DIMENSION ITID(70),IOUTFL(8),ISAMFL(8),ISENFL(8),IGRAFL(8)
        DIMENSION TDATA(8),IBLNFL(8)
        COMMON/ABLOCK/CAL(50,50),DATA(50,50),IBLOCK(256),
     +  IUNIT,NCHAN,NTRAK
        COMMON/BBLOCK/THETA1,MAINC,MAINT,CHNCAL
        COMMON/FBLOCK/F015,F030,F060,F100,F200,F300,F400
        DATA DATMIN,DATMAX/1.E+30,0./
        DATA F015,F030,F060/1.652,2.476,7.123/
        DATA F100,F200,F300,F400/20.294,190.52,1772.6,24736./
C ---------------------------------------------------------------------
C       ENTERING THE INPUT PARAMETERS
C ---------------------------------------------------------------------
        TYPE*,' DO YOU WANT INSTRUCTIONS, [Y/N]?'
        ACCEPT 100,INST
100     FORMAT(A1)
        IF(INST.NE.'Y')GO TO 302
        TYPE*,' ENTER 2 LINES OF DESCRIPTION FOR THIS RUN, '
        TYPE*,' LEAVE A SPACE AT THE BEGINNING OF EACH LINE:'
302     ACCEPT 303,(ITID(IJ),IJ=1,35)
        ACCEPT 303,(ITID(IJ),IJ=36,70)
303     FORMAT(35A2)
        IF(INST.NE.'Y')GO TO 311
        TYPE 310
310     FORMAT(' ENTER THE SAMPLE FILE NAME AND THE SENSITIVITY',
     +  ' FILE NAME',/,' ON SEPARATE LINES:')
311     ACCEPT 312,ISAMFL
312     FORMAT(8A2)
        ACCEPT 312,ISENFL
        IF(INST.NE.'Y')GO TO 452
        TYPE*,' ENTER THE OUTPUT FILE NAME:'
452     ACCEPT 312,IOUTFL
C ---------------------------------------------------------------------
C       SET UP FOR BLANK SAMPLE, IF USED
C ---------------------------------------------------------------------
        IF(INST.NE.'Y') GO TO 510
        TYPE*,' DO YOU WANT TO SUBTRACT A BLANK SAMPLE, [Y/N]?'
510     ACCEPT 100,INSTBL
        IF(INSTBL.NE.'Y') GO TO 600
        IF(INST.NE.'Y') GO TO 520
        TYPE*,' ENTER THE FILE NAME OF THE BLANK SAMPLE:'
520     ACCEPT 312,IBLNFL
        IF(INST.NE.'Y') GO TO 530
        TYPE*,' ENTER THE SAMPLE TRANSMISSION RELATIVE TO THE BLANK'
        TYPE*,' (REAL NUMBER BETWEEN 0. AND 1.):'
530     ACCEPT *,TRANS
C ---------------------------------------------------------------------
C       DETERMINE THE SAMPLE, SENSITIVITY AND BLANK RUNS' FILTER FACTORS
C ---------------------------------------------------------------------
```

```
600      IF(INST.NE.'Y')GO TO 610
         TYPE*,' ENTER THE FILTER NUMBERS USED.'
         TYPE*,' (REAL NUMBERS, ONE FILTER PER LINE, LAST LINE ',
     +   'MUST BE 0.)'
         TYPE*,'      SAMPLE RUN FILTERS:'
610      CALL FILTER(SAMFF)
         IF(INST.NE.'Y') GO TO 620
         TYPE*,'      SENSITIVITY RUN FILTERS:'
620      CALL FILTER(SENFF)
         IF(INSTBL.NE.'Y')GO TO 690
         IF(INST.NE.'Y') GO TO 630
         TYPE*,'      BLANK RUN FILTERS:'
630      CALL FILTER(BLNFF)
C ---------------------------------------------------------------------
C        READ IN MORE PARAMETERS
C ---------------------------------------------------------------------
690      IF(INST.NE.'Y')GO TO 106
         TYPE 103
103      FORMAT(' ENTER THE SAMPLE REFRACTIVE INDEX',/,' AND THE ',
     +   'AZIMUTHAL ANGLE, IN DEGREES, AT WHICH THE X AXIS')
         TYPE 104
104      FORMAT(' OF THE MONITOR SCREEN IS LOCATED (REAL NUMBERS):')
106      ACCEPT*,RI,AMUX
         IF(INST.NE.'Y') GO TO 550
         TYPE*,' ENTER THE ANALYZER ATTENUATION FACTOR'
         TYPE*,' (REAL NUMBER BETWEEN 0. AND 1.),'
         TYPE*,' THE SAMPLE THICKNESS (REAL, IN MICRONS) AND'
         TYPE*,' THE RGTG VALUE FOR THE GLASS DIFFUSER (REAL):'
550      ACCEPT*,ANATT,TSAMP,RGTG
         TSAMP=TSAMP/1000.
         IF(INST.NE.'Y')GO TO 108
         TYPE*,' DO YOU WANT A DIFFRACTION GRATING ANALYSIS, [Y/N]?'
108      ACCEPT 100,INSTDG
         IF(INSTDG.EQ.'Y')GO TO 120
         IF(INST.NE.'Y')GO TO 110
         TYPE 109
109      FORMAT(' ENTER THE CHANNEL AND TRACK NUMBERS OF THE MAIN ',
     +   'BEAM (INTEGERS)',/,' AND CHANNEL CALIBRATION FACTOR (REAL):')
110      ACCEPT*,MAINC,MAINT,CHNCAL
         GO TO 130
120      IF(INST.NE.'Y')GO TO 314
         TYPE 313
313      FORMAT(' ENTER THE DIFFRACTION GRATING FILE NAME:')
314      ACCEPT 312,IGRAFL
         IF(INST.NE.'Y')GO TO 112
         TYPE 111
111      FORMAT(' ENTER THE SCATTERING ANGLE, IN DEGREES, OF THE ',/,
     +   ' FIRST ORDER DIFFRACTION PEAK (REAL):')
```

```
112     ACCEPT*,THETA1
        THETA1=THETA1/57.29578
C ----------------------------------------------------------------------
C       GO DO DIFFRACTION GRATING ANALYSIS, IF NECESSARY
C ----------------------------------------------------------------------
        CALL DIFGRT(IGRAFL)
130     FRONT=19.85836*RI
C ----------------------------------------------------------------------
C       READ IN THE SAMPLE DATA
C ----------------------------------------------------------------------
        IUNIT=2
        CALL READBN(ISAMFL)
C ----------------------------------------------------------------------
C       SUBTRACT BLANK SAMPLE, IF USED
C ----------------------------------------------------------------------
        IF(INSTBL.NE.'Y') GO TO 700
        IUNIT=1
        CALL READBN(IBLNFL)
        DO 720 IT=1,NTRAK
        DO 720 IC=1,NCHAN
        DATA(IC,IT)=(DATA(IC,IT)*SAMFF - CAL(IC,IT)*BLNFF*TRANS)/SAMFF
720     CONTINUE
C ----------------------------------------------------------------------
C       GO CALIBRATE THE SAMPLE DATA IN TERMS OF THE LAMBERTIAN
C       DIFFUSER SCATTERING
C ----------------------------------------------------------------------
700     CALL CORSEN(ISENFL,SAMFF,SENFF,RGTG,TSAMP,ANATT)
        INDEX=0
        DO 3 IT=1,NTRAK
        DO 4 IC=1,NCHAN
C ----------------------------------------------------------------------
C       DETERMINE POLAR AND AZIMUTHAL SCATTERING ANGLES FOR EACH POINT
C ----------------------------------------------------------------------
        IDELC=IC-MAINC
        IDELCA=IABS(IDELC) + 1
        IDELT=IT-MAINT
        IDELTA=IABS(IDELT) + 1
C ----------------------------------------------------------------------
C       WATCH OUT FOR INDETERMINATE AZIMUTHAL ANGLE CALCULATIONS
C ----------------------------------------------------------------------
        IF(IDELT.NE.0)GO TO 401
        IF(IDELC.NE.0)GO TO 402
        AMU=0.
        H=0.
        THETA=0.
        GO TO 180
402     IF(IDELC.LT.0)GO TO 403
        AMU=90.
```

```
      GO TO 405
403   AMU=270.
      GO TO 405
C ----------------------------------------------------------------------
C     CALCULATION OF THE AZIMUTHAL ANGLES FROM THE CHANNEL
C     AND TRACK LOCATION OF EACH DATA POINT
C ----------------------------------------------------------------------
401   AMU=ATAN(IDELC/(1.*IDELT))
      IF(IDELT.LT.0) AMU=AMU + 3.14159
C ----------------------------------------------------------------------
C     CONVERT AZIMUTHAL ANGLES TO DEGREES IN THE RANGE OF 0 TO 360
C     AND CORRECT FOR THE AZIMUTHAL ANGLE ORIENTATION OF THE DETECTOR
C ----------------------------------------------------------------------
      AMU=AMU*57.29578
405   AMU=AMU + AMUX - 90.
      IF(AMU.LT.0.)AMU=AMU + 360.
      IF(AMU.GE.360.)AMU=AMU - 360.
C ----------------------------------------------------------------------
C     CALCULATION OF THE SCATTERING VECTOR H
C ----------------------------------------------------------------------
      THETEX=ATAN((SQRT((IDELC*1.)**2 + IDELT**2))/CHNCAL)
      X=(SIN(THETEX))/RI
      THETA=ATAN(X/SQRT(1-X**2))
      H=FRONT*SIN(THETA/2.)
      THETA=THETA*57.29578
C ----------------------------------------------------------------------
C     WRITING OUT THE DATA
C ----------------------------------------------------------------------
180   IF(IT.NE.1.OR.IC.NE.1)GO TO 170
      OPEN(UNIT=4,NAME=IOUTFL,FORM='UNFORMATTED',ACCESS='DIRECT',
     + RECORDSIZE=8)
      WRITE(4'1) NCHAN,NTRAK,RI,CHNCAL,MAINC,MAINT,AMUX
      NUMREC=1
      DO 5 L=1,57,14
      L13=L+13
      NUMREC=NUMREC+1
      WRITE(4'NUMREC) (ITID(M),M=L,L13)
5     CONTINUE
170   IF(DATA(IC,IT).LE.DATMAX) GO TO 171
      DATMAX=DATA(IC,IT)
      THEMAX=THETA
      HMAX=H
      AMUMAX=AMU
171   IF(DATA(IC,IT).LT.DATMIN) DATMIN=DATA(IC,IT)
      INDEX=INDEX + 1
      TDATA(INDEX)=DATA(IC,IT)
      IF(INDEX.LT.8)GO TO 4
      NUMREC=NUMREC + 1
```

```
      WRITE(4'NUMREC) (TDATA(L),L=1,8)
      INDEX=0
4     CONTINUE
3     CONTINUE
      IF(INDEX.EQ.0) GO TO 165
      NUMREC=NUMREC + 1
      WRITE(4'NUMREC) (TDATA(L),L=1,INDEX)
      CLOSE(UNIT=4)
C ---------------------------------------------------------------------
C     SEND INFORMATION TO THE TERMINAL
C ---------------------------------------------------------------------
165   TYPE 166, DATMIN,DATMAX
166   FORMAT(/,' THE MINIMUM INTENSITY =',E14.7,/' THE MAXIMUM',
    + ' INTENSITY =',E14.7,'; IT OCCURS AT:')
      TYPE 167, THEMAX,HMAX,AMUMAX
167   FORMAT(10X,'THETA =',F7.4,' DEGREES',/,10X,'H =',F7.4,
    + ' 1/MICRONS',/10X,'MU =',F6.2,' DEGREES.',//)
      STOP
      END


      SUBROUTINE DIFGRT(IGRAFL)
      DIMENSION IGRAFL(8)
      COMMON/ABLOCK/CAL(50,50),DATA(50,50),IBLOCK(256),
    + IUNIT,NCHAN,NTRAK
      COMMON/BBLOCK/THETA1,MAINC,MAINT,CHNCAL
C ---------------------------------------------------------------------
C     THIS SUBROUTINE USES DIFFRACTION GRATING INTENSITY DATA
C     TO DETERMINE THE CHANNEL AND TRACK LOCATION OF THE MAIN BEAM
C     AND TO DETERMINE THE CALIBRATION OF THE SCAN IN TERMS OF
C     CHANNELS OR TRACKS PER DEGREE OF SCATTERING ANGLE:
C     CHNCAL*TAN(THETA)= NUMBER OF CHANNELS AWAY FROM THE MAIN BEAM.
C     THIS SUBROUTINE IS CALLED FROM PROGRAM SALS.  IT CALLS
C     SUBROUTINE READBN TO READ IN THE BINARY DIFFRACTION GRATING
C     DATA FILE.
C ---------------------------------------------------------------------
C
C     READ IN THE DIFFRACTION GRATING DATA
C ---------------------------------------------------------------------
      IUNIT=1
      CALL READBN(IGRAFL)
C ---------------------------------------------------------------------
C     DETERMINING THE CHANNEL AND TRACK NUMBERS OF THE MAIN BEAM
C ---------------------------------------------------------------------
      GMAX=0.
      MAINC=1
      MAINT=1
```

```
        DO 3 IT=1,NTRAK
        DO 4 IC=1,NCHAN
        IF(CAL(IC,IT).LE.GMAX)GO TO 4
        GMAX=CAL(IC,IT)
        MAINC=IC
        MAINT=IT
4       CONTINUE
3       CONTINUE
        TYPE 200,MAINC,MAINT
200     FORMAT(/,' THE CHANNEL AND TRACK NUMBERS OF THE MAIN BEAM',
     +  ' ARE:',I3,I4)
C ----------------------------------------------------------------------
C       FINDING THE FIRST ORDER PEAK RIGHT OF THE MAIN BEAM
C ----------------------------------------------------------------------
        FOPMAX=0.
        MAX1C=1
        MAX1T=1
        DO 5 IT=MAINT,NTRAK
        DO 6 IC=MAINC+5,NCHAN
        IF(CAL(IC,IT).LE.FOPMAX)GO TO 6
        FOPMAX=CAL(IC,IT)
        MAX1C=IC
        MAX1T=IT
6       CONTINUE
5       CONTINUE
        TYPE 105,MAX1C,MAX1T
105     FORMAT(/,' THE CHANNEL AND TRACK NUMBERS OF THE RIGHT HAND',/,
     +  ' FIRST ORDER PEAK ARE:',I3,I4)
        IMAX1C=IABS(MAX1C-MAINC)
        IMAX1T=IABS(MAX1T-MAINT)
        CHNCAL=((COS(THETA1))/SIN(THETA1))*(SQRT((IMAX1C*1.)**2 +
     +  IMAX1T**2))
30      TYPE 110,CHNCAL
110     FORMAT(/,' THE CHANNEL CALIBRATION FACTOR IS:',F10.5)
        RETURN
        END


        SUBROUTINE FILTER(FILFAC)
        COMMON/FBLOCK/F015,F030,F060,F100,F200,F300,F400
C ----------------------------------------------------------------------
C       THIS SUBROUTINE DETERMINES THE FILTER FACTOR FOR A DATA FILE.
C       THIS SUBROUTINE IS CALLED BY THE PROGRAM SALS.
C ----------------------------------------------------------------------
        FILFAC=1.
20      ACCEPT 10,FILNUM
10      FORMAT(F5.2)
```

```
      IF(FILNUM.NE.0.) GO TO 1015
      RETURN
1015  IF(FILNUM.NE.0.15) GO TO 1030
      FILFAC=FILFAC*F015
      GO TO 20
1030  IF(FILNUM.NE.0.3) GO TO 1060
      FILFAC=FILFAC*F030
      GO TO 20
1060  IF(FILNUM.NE.0.6) GO TO 1100
      FILFAC=FILFAC*F060
      GO TO 20
1100  IF(FILNUM.NE.1.0) GO TO 1200
      FILFAC=FILFAC*F100
      GO TO 20
1200  IF(FILNUM.NE.2.0) GO TO 1300
      FILFAC=FILFAC*F200
      GO TO 20
1300  IF(FILNUM.NE.3.0) GO TO 1400
      FILFAC=FILFAC*F300
      GO TO 20
1400  IF(FILNUM.NE.4.0) GO TO 1500
      FILFAC=FILFAC*F400
      GO TO 20
1500  TYPE*,'....INVALID FILTER NUMBER, TRY AGAIN...'
      GO TO 20
      RETURN
      END


      SUBROUTINE READBN(IFLNAM)
      DIMENSION IFLNAM(8)
      COMMON/ABLOCK/CAL(50,50),DATA(50,50),IBLOCK(256),
     + IUNIT,NCHAN,NTRAK
C ----------------------------------------------------------------
C     THIS SUBROUTINE READS THE OMA2 DATA FROM THE BINARY FILES.
C     IT IS CALLED FROM THE PROGRAM SALS AND THE SUBROUTINES
C     CORSEN AND DIFGRT.
C     THE NAME OF THE FILE BEING READ IS IFLNAM, PASSED FROM THE
C     CALLING PROGRAM.
C ----------------------------------------------------------------
      OPEN(UNIT=IUNIT,NAME=IFLNAM,TYPE='OLD',READONLY,
     + FORM='UNFORMATTED',ACCESS='DIRECT',RECORDSIZE=128)
C ----------------------------------------------------------------
C     READ SCAN PARAMETERS FROM THE FIRST RECORD
C ----------------------------------------------------------------
      READ(IUNIT'1) (IBLOCK(I),I=1,256)
C ----------------------------------------------------------------
```

```
C       DEFINE SCAN PARAMETERS
C -----------------------------------------------------------------------
        NCHAN=IBLOCK(8)
        NTRAK=IBLOCK(9)
C -----------------------------------------------------------------------
C       READ IN THE DATA
C -----------------------------------------------------------------------
        NUMREC=1
        INDEX=256
        DO 100 I=1,NTRAK
        DO 50 J=1,NCHAN
        INDEX=INDEX+1
        IF(INDEX.LE.256)GO TO 55
        NUMREC=NUMREC+1
        READ(IUNIT'NUMREC) (IBLOCK(K),K=1,256)
        INDEX=1
55      IF(IUNIT.EQ.1) CAL(J,I)=FLOAT(-IBLOCK(INDEX) -1)
        IF(IUNIT.EQ.2) DATA(J,I)=FLOAT(-IBLOCK(INDEX) - 1)
50      CONTINUE
100     CONTINUE
        CLOSE(UNIT=IUNIT)
        RETURN
        END


        SUBROUTINE CORSEN(ISENFL,SAMFF,SENFF,RGTG,TSAMP,ANATT)
        DIMENSION ISENFL(8)
        COMMON/BBLOCK/THETA1,MAINC,MAINT,CHNCAL
        COMMON/ABLOCK/CAL(50,50),DATA(50,50),IBLOCK(256),
     +  IUNIT,NCHAN,NTRAK
C -----------------------------------------------------------------------
C       THIS SUBROUTINE READS IN THE SENSITIVITY DATA.  IT NORMALIZES
C       THE SENSITIVITY FILE ASSUMING THE LAMBERTIAN DIFFUSER
C       SCATTERS AS THE COS(THETA).  IT CALCULATES THE ABSOLUTE
C       SCATTERING INTENSITY.  IT CALLS THE SUBROUTINE READBN TO
C       READ THE BINARY SENSITIVITY DATA FILE.  CORSEN
C       IS CALLED BY THE PROGRAM SALS.
C -----------------------------------------------------------------------
        IUNIT=1
        CALL READBN(ISENFL)
        DO 1 IT=1,NTRAK
        IDELT=IT-MAINT
        DO 2 IC=1,NCHAN
        IDELC=IC-MAINC
        THETA=ATAN(SQRT((IDELC*1.)**2 + IDELT**2)/CHNCAL)
        CAL(IC,IT)=CAL(IC,IT)/COS(THETA)
        DATA(IC,IT)=DATA(IC,IT)*SAMFF*RGTG/
```

```
     +  (CAL(IC,IT)*SENFF*TSAMP*ANATT)
2       CONTINUE
1       CONTINUE
        RETURN
        END
```

```
      PROGRAM CIRCLE
C ------------------------------------------------------------------------
C      THIS PROGRAM PERFORMS CIRCULAR AVERAGING ON OMA2 LIGHT
C      SCATTERING DATA.  IT AVERAGES ALL THE DATA FOR EACH SCATTERING
C      ANGLE, NEGLECTING AZIMUTHAL ANGLES.  THE INPUT FILE IS
C      THE BINARY OUTPUT FILE FROM THE RUNNING OF THE PROGRAM SALS.
C      OF EACH DATA POINT, AS DEFINED IN THE OUTPUT FILE
C      DEFINITIONS OF THE VARIABLES:
C              DATA(IC,IT)= INTENSITY AT CHANNEL IC AND TRACK IT
C                           ((IC,IT)=(IT,IC))
C              NUM(IC,IT)= THE NUMBER OF ACTUAL DATA POINTS AT
C                          POSITION (IC,IT), LATER USED AS A
C                          MEASURE OF DISTANCE FROM MAIN BEAM
C              ITID(I)= EXPERIMENT IDENTIFICATION
C              IINFL= NAME OF INPUT FILE
C              IOUTFL= NAME OF OUTPUT FILE
C              TDATA(I)= TEMPORARY VARIABLE FOR INTENSITY VALUES
C                        READ FROM THE BINARY INPUT FILE
C              IDCMAX= NUMBER OF CHANNELS IN THE SCAN (EQUIVALENT
C                      FIRST QUADRANT)
C              IDTMAX= NUMBER OF TRACKS IN THE SCAN (EQUIVALENT
C                      FIRST QUADRANT)
C              NPTS= NUMBER OF DATA POINTS RESULTING FROM THE
C                    CIRCULAR AVERAGING
C              ITEST= TEST VALUE USED TO SORT THE CIRCULAR DATA
C                     IN ASCENDING ANGLE ORDER
C              DATMAX= MAXIMUM INTENSITY VALUE
C              DATMIN= MINIMUM INTENSITY VALUE
C              INST= Y IF THE OPERATOR WANTS INSTRUCTIONS
C                    N IF INSTRUCTIONS ARE NOT NEEDED
C              NCHAN= TOTAL NUMBER OF CHANNELS IN ORIGINAL SCAN
C              NTRAK= TOTAL NUMBER OF TRACKS IN ORIGINAL SCAN
C              RI= REFRACTIVE INDEX OF THE SAMPLE
C              CHNCAL= CALIBRATION FACTOR FOR CONVERTING CHANNEL
C                      POSITIONS TO SCATTERING ANGLE
C              MAINC= CHANNEL LOCATION OF THE MAIN BEAM
C              MAINT= TRACK LOCATION OF THE MAIN BEAM
C              FRONT= FACTOR USED TO CALCULATE THE SCATTERING VECTOR,
C                     ASSUMING THE WAVELENGTH= 0.6328 MICRONS
C              NUMREC= RECORD NUMBER IN THE BINARY INPUT FILE
C              INDEX= VARIABLE FOR COUNTING DATA POINTS IN A RECORD
C              IDELT= TRACKS AWAY FROM THE MAIN BEAM
C              IDELTA= EQUIVALENT FIRST QUADRANT TRACK LOCATION
C              IDELC= CHANNELS AWAY FROM THE MAIN BEAM
C              IDELCA= EQUIVALENT FIRST QUADRANT CHANNEL LOCATION
C              ITEMP= VARIABLE FOR TEMPORARILY STORING IDELT
C              IFIX= CHANNEL NUMBER
```

```
C                 JFIX= TRACK NUMBER
C                 THETEX= SCATTERING ANGLE IN AIR (RADIANS)
C                 X= VARIABLE USED TO DETERMINE THETA
C                 THETA= SCATTERING ANGLE IN THE SAMPLE
C                 H= SCATTERING VECTOR (I/MICRONS)
C                 THEMAX= SCATTERING ANGLE AT THE MAXIMUM INTENSITY
C                 HMAX= SCATTERING VECTOR AT THE MAXIMUM INTENSITY
C       WRITTEN BY R.J. TABAR  24-JUN-81
C       MODIFIED BY D.P.LEFEBVRE 17-DEC-82
C ----------------------------------------------------------------------
        DIMENSION DATA(65,65),NUM(65,65),ITID(70)
        DIMENSION IINFL(8),IOUTFL(8),TDATA(8)
        INTEGER A
C ----------------------------------------------------------------------
C       INITIALIZING SOME VARIABLES
C ----------------------------------------------------------------------
        DATA NUM,IDCMAX,IDTMAX,NPTS,ITEST/4228*0,30000/
        DATA DATA,DATMAX,DATMIN/4226*0.,1.E+30/
C ----------------------------------------------------------------------
C       OPEN UP THE INPUT FILE
C       AND READ IN THE PARAMETERS FOR THIS SCAN
C ----------------------------------------------------------------------
        TYPE 200
200     FORMAT(' DO YOU WANT INSTRUCTIONS, [Y/N]?')
        ACCEPT 205,INST
205     FORMAT(A1)
        IF(INST.NE.'Y') GO TO 215
        TYPE 210
210     FORMAT(' ENTER THE NAME OF THE INPUT FILE:')
215     ACCEPT 99,IINFL
99      FORMAT(8A2)
        OPEN(UNIT=1,NAME=IINFL,TYPE='OLD',READONLY,FORM='UNFORMATTED',
     +  ACCESS='DIRECT',RECORDSIZE=8)
        READ(1'1) NCHAN,NTRAK,RI,CHNCAL,MAINC,MAINT
        FRONT=RI*19.85836
C ----------------------------------------------------------------------
C       READ IN THE EXPERIMENT IDENTIFICATION INFORMATION
C ----------------------------------------------------------------------
        NUMREC=1
        DO 199 L=1,57,14
        L13=L+13
        NUMREC=NUMREC+1
        READ(1'NUMREC) (ITID(M),M=L,L13)
199     CONTINUE
C ----------------------------------------------------------------------
C       READ IN THE INTENSITY VALUES
C ----------------------------------------------------------------------
        INDEX=8
```

```
      DO 2 IT=1,NTRAK
      DO 3 IC=1,NCHAN
      IDELT=IT-MAINT
      IDELTA=IABS(IDELT) + 1
      IDELC=IC-MAINC
      IDELCA=IABS(IDELC) + 1
      INDEX=INDEX+1
      IF(INDEX.LE.8) GO TO 270
      NUMREC=NUMREC+1
      READ(1'NUMREC) (TDATA(L),L=1,8)
      INDEX=1
C -----------------------------------------------------------------------
C     CONSIDER POINTS (IDELCA,IDELTA)=(IDELTA,IDELCA): SO SWITCH
C     COORDINATES IF IDELTA IS LARGER THAN IDELCA
C -----------------------------------------------------------------------
270   IF(IDELCA.LE.IDELTA) GO TO 40
      ITEMP=IDELTA
      IDELTA=IDELCA
      IDELCA=ITEMP
40    DATA(IDELCA,IDELTA)=DATA(IDELCA,IDELTA) + TDATA(INDEX)
      NUM(IDELCA,IDELTA)=NUM(IDELCA,IDELTA) + 1
C -----------------------------------------------------------------------
C     DETERMINE HOW MANY CHANNELS AND TRACKS ARE IN THE FIRST
C     QUADRANT
C -----------------------------------------------------------------------
      IF(IDELTA.GT.IDTMAX)IDTMAX=IDELTA
3     CONTINUE
2     CONTINUE
      CLOSE(UNIT=1)
C -----------------------------------------------------------------------
C     BEGIN PROCESSING OF EQUIVALENT DATA
C     AVERAGE THE INTENSITIES WITH THE SAME SCATTERING ANGLE
C -----------------------------------------------------------------------
      DO 4 I=1,IDCMAX
      DO 5 J=I,IDTMAX
      NPTS=NPTS+1
      DATA(I,J)=DATA(I,J)/NUM(I,J)
      NUM(I,J)=I**2 + J**2
5     CONTINUE
4     CONTINUE
C -----------------------------------------------------------------------
C     OPEN UP THE OUTPUT FILE; WRITE OUT THE TITLES
C -----------------------------------------------------------------------
      IF(INST.NE.'Y') GO TO 410
      TYPE 405
405   FORMAT(' ENTER THE OUTPUT FILE NAME:')
410   ACCEPT 99,IOUTFL
      OPEN(UNIT=2,NAME=IOUTFL)
```

```
300     FORMAT(35A2)
        WRITE(2,300) (ITID(K),K=1,35)
        WRITE(2,300) (ITID(K),K=36,70)
        WRITE(2,140)
140     FORMAT(/,'   CIRCULARLY AVERAGED LIGHT SCATTERING RESULTS:')
        WRITE(2,150)
150     FORMAT(/,T10,'SCATTERING',T26,'SCATTERING',/,T13,'ANGLE',
     +  T28,'VECTOR',T43,'INTENSITY')
        WRITE(2,151)
151     FORMAT(T11,'(DEGREES)',T25,'(1/MICRONS)',/)
C -----------------------------------------------------------------------
C       WRITE OUT THE RESULTS IN THE ORDER OF SCATTERING ANGLES,
C       SMALLEST ANGLES FIRST
C -----------------------------------------------------------------------
        A=IDCMAX**2+IDTMAX**2
        DO 7 K=1,A
        DO 8 I=0,IDCMAX
        DO 9 J=I,IDTMAX
        ITEST=I**2+J**2
        IF(K.EQ.ITEST) GO TO 10
9       CONTINUE
8       CONTINUE
        GO TO 11
10      CONTINUE
        IDELC=I
        IDELT=J
        IFIX=I+1
        JFIX=J+1
C -----------------------------------------------------------------------
C       CALCULATE THE SCATTERING ANGLES
C -----------------------------------------------------------------------
        THETEX=ATAN((SQRT((IDELC*1.)**2 + IDELT**2))/CHNCAL)
        X=(SIN(THETEX))/RI
        THETA=ATAN(X/SQRT(1-X**2))
        H=FRONT*SIN(THETA/2.)
        THETA=THETA*57.29578
        IF(DATA(IFIX,JFIX).LE.DATMAX)GO TO 171
        DATMAX=DATA(IFIX,JFIX)
        THEMAX=THETA
        HMAX=H
171     IF(DATA(IFIX,JFIX).LT.DATMIN) DATMIN=DATA(IFIX,JFIX)
        IF(DATA(IFIX,JFIX).EQ.0.) GO TO 11
C -----------------------------------------------------------------------
C       WRITE OUT THE RESULTS
C -----------------------------------------------------------------------
        WRITE(2,160) THETA,H,DATA(IFIX,JFIX)
160     FORMAT(T12,F7.4,T27,F7.4,T40,E14.7)
11      CONTINUE
```

```
7       CONTINUE
        CLOSE(UNIT=2)
C ----------------------------------------------------------------------
C       SEND INFORMATION TO THE TERMINAL
C ----------------------------------------------------------------------
        TYPE 165,NPTS
165     FORMAT(/,' THE CIRCULARLY AVERAGED FILE CONTAINS',I5,
     +  ' POINTS.')
        TYPE 166,DATMIN,DATMAX
166     FORMAT(/,' THE MINIMUM INTENSITY=',E14.7,/,' THE MAXIMUM ',
     +  'INTENSITY=',E14.7,'; IT OCCURS AT:')
        TYPE 167,THEMAX,HMAX
167     FORMAT(10X,'THETA=',F7.4,' DEGREES',/,10X,'H= ',F7.4,
     +  ' (1/MICRONS)')
        STOP
        END
```

```
      PROGRAM QUAD
C ----------------------------------------------------------------------
C     THIS PROGRAM TAKES THE SCATTERING DATA DETERMINED BY PROGRAM
C     SALS AND AVERAGES IT ALL INTO THE FIRST QUADRANT.  IT CONVERTS
C     CHANNEL AND TRACK LOCATIONS TO THE EQUIVALENT LOCATIONS IN
C     THE FIRST QUADRANT WITH THE MAIN BEAM LOCATED AT (1,1).
C     THE INPUT AND OUTPUT FILES ARE BINARY.  THE OUTPUT FILE CAN
C     BE READ BY RUNNING THE PROGRAM READS.  THE OUTPUT DATA CAN BE
C     PLOTTED AS AN ISOINTENSITY CONTOUR MAP USING THE PROGRAM
C     CONDNS AND THE CONTOUR PLOTTING PROGRAMS ON THE PDP 11/34.
C     DEFINTIONS OF VARIABLES:
C             DATA(IC,IT)= INTENSITY AT CHANNEL IC AND TRACK IT
C             ITID(I)= EXPERIMENT DESCRIPTION INFORMATION
C             NUM(IC,IT)= NUMBER OF DATA POINTS WITH FIRST QUADRANT
C                         EQUIVALENT POSITIONS OF CHANNEL IC AND
C                         TRACK IT
C             IINFL= NAME OF INPUT FILE
C             IOUTFL= NAME OF OUTPUT FILE
C             TDATA(I)= TEMPORARY INTENSITY VALUE BEING READ
C                       INTO OR FROM THE BINARY FILES
C             IDCMAX= NUMBER OF EQUIVALENT FIRST QUADRANT CHANNELS
C                     IN THE SCAN
C             IDTMAX= NUMBER OF EQUIVALENT FIRST QUADRANT TRACKS
C                     IN THE SCAN
C             DATMIN= MINIMUM INTENSITY VALUE
C             DATMAX= MAXIMUM INTENSITY VALUE
C             INST= Y IF THE OPERATOR NEEDS INSTRUCTIONS
C                   N IF INSTRUCTIONS ARE NOT NEEDED
C             NCHAN= ACTUAL NUMBER OF CHANNELS IN THE SCAN
C             NTRAK= ACTUAL NUMBER OF TRACKS IN THE SCAN
C             RI= SAMPLE REFRACTIVE INDEX
C             CHNCAL= CHANNEL CALIBRATION FACTOR FOR CONVERTING
C                     CHANNEL POSITIONS TO SCATTERING ANGLE
C             MAINC= CHANNEL LOCATION OF MAIN BEAM
C             MAINT= TRACK LOCATION OF MAIN BEAM
C             NUMREC= BINARY FILE RECORD NUMBER
C             INDEX= VARIABLE FOR COUNTING DATA POINTS IN A
C                    BINARY FILE RECORD
C             FRONT= FACTOR USED TO CALCULATE THE SCATTERING VECTOR
C                    H, ASSUMING THE WAVELENGTH=0.6328 MICORNS
C             IDELT= TRACKS AWAY FROM THE MAIN BEAM
C             IDELTA= EQUIVALENT FIRST QUADRANT CHANNEL LOCATION
C             IDELC= CHANNELS AWAY FROM THE MAIN BEAM
C             IDELCA= EQUIVALENT FIRST QUADRANT TRACK LOCATION
C             AMU= AZIMUTHAL ANGLE
C             H= SCATTERING VECTOR (1/MICRONS)
C             THETEX= SCATTERING ANGLE IN AIR (RADIANS)
```

```
C                X= VARIABLE USED TO DETERMINE THETA
C                THETA= SCATTERING ANGLE IN THE SAMPLE
C                THEMAX= SCATTERING ANGLE AT THE MAXIMUM INTENSITY
C                HMAX= SCATTERING VECTOR AT THE MAXIMUM INTENSITY
C                AMUMAX= AZIMUTHAL ANGLE AT THE MAXIMUM INTENSITY
C         WRITTEN BY R.J. TABAR 16-JUN-81
C ----------------------------------------------------------------------
          DIMENSION DATA(65,65),ITID(70),NUM(65,65)
          DIMENSION IINFL(8),IOUTFL(8),TDATA(8)
C ----------------------------------------------------------------------
C         INITIALIZE SOME VARIABLES, READ IN SCAN PARAMETERS FROM THE
C         INPUT FILE
C ----------------------------------------------------------------------
          DATA NUM,IDCMAX,IDTMAX/4227*0/
          DATA DATA,DATMAX,DATMIN/4226*0.,1.E+30/
          TYPE 600
600       FORMAT(' DO YOU WANT INSTRUCTIONS, [Y/N]?')
          ACCEPT 605,INST
605       FORMAT(A1)
          IF(INST.NE.'Y') GO TO 611
          TYPE 610
610       FORMAT(' ENTER THE NAME OF THE INPUT FILE:')
611       ACCEPT 620,IINFL
620       FORMAT(8A2)
          OPEN(UNIT=1,NAME=IINFL,TYPE='OLD',READONLY,FORM='UNFORMATTED',
     +    ACCESS='DIRECT',RECORDSIZE=8)
          READ(1'1)NCHAN,NTRAK,RI,CHNCAL,MAINC,MAINT
          IF(INST.NE.'Y') GO TO 615
          TYPE*,'ENTER THE NAME OF THE OUTPUT FILE:'
615       ACCEPT 620,IOUTFL
C ----------------------------------------------------------------------
C         READ IN THE EXPERIMENT IDENTIFICATION INFORMATION
C ----------------------------------------------------------------------
          NUMREC=1
          FRONT=RI*19.85836
          DO 50 L=1,57,14
          L13=L+13
          NUMREC=NUMREC+1
          READ(1'NUMREC) (ITID(M),M=L,L13)
50        CONTINUE
          INDEX=8
C ----------------------------------------------------------------------
C         READ IN THE INTENSITY VALUES FROM THE INPUT FILE
C ----------------------------------------------------------------------
          DO 2 IT=1,NTRAK
          IDELT=IT-MAINT
          IDELTA=IABS(IDELT) + 1
          DO 3 IC=1,NCHAN
```

```
      IDELC=IC-MAINC
      IDELCA=IABS(IDELC) + 1
      INDEX=INDEX+1
      IF(INDEX.LE.8) GO TO 800
      NUMREC=NUMREC+1
      READ(1'NUMREC) (TDATA(L),L=1,8)
      INDEX=1
800   DATA(IDELCA,IDELTA)=TDATA(INDEX) + DATA(IDELCA,IDELTA)
      NUM(IDELCA,IDELTA)=NUM(IDELCA,IDELTA) + 1
3     CONTINUE
2     CONTINUE
      CLOSE(UNIT=1)
C ---------------------------------------------------------------------
C     DETERMINE HOW MANY CHANNELS AND TRACKS IN THE AVERAGED
C     FIRST QUADRANT
      IDCMAX=NCHAN-MAINC+1
      IF(MAINC.GT.IDCMAX) IDCMAX=MAINC
      IDTMAX=NTRAK-MAINT+1
      IF(MAINT.GT.IDTMAX)IDTMAX=MAINT
      INDEX=0
C ---------------------------------------------------------------------
C     CALCULATE ANGLE LOCATIONS AND AVERAGE INTENSITIES
C ---------------------------------------------------------------------
      DO 4 J=1,IDTMAX
      IDELT=J-1
      DO 5 I=1,IDCMAX
      IDELC=I-1
      DATA(I,J)=DATA(I,J)/NUM(I,J)
      IF(IDELT.NE.0) GO TO 401
      IF(IDELC.NE.0) GO TO 402
      AMU=0.
      H=0.
      THETA=0.
      GO TO 180
402   AMU=90.
      GO TO 500
401   AMU=ATAN(IDELC/(1.*IDELT))
      AMU=AMU*57.29578
500   THETEX=ATAN((SQRT((IDELC*1.)**2 + IDELT**2))/CHNCAL)
      X=(SIN(THETEX))/RI
      THETA=ATAN(X/SQRT(1-X**2))
      H=FRONT*SIN(THETA/2.)
      THETA=THETA*57.29578
180   IF(I.NE.1.OR.J.NE.1)GO TO 170
C ---------------------------------------------------------------------
C     WRITE OUT THE EXPERIMENT IDENTIFICATION INFORMATION
C     TO THE OUTPUT FILE
C ---------------------------------------------------------------------
```

```
        OPEN(UNIT=2,NAME=IOUTFL,FORM='UNFORMATTED',ACCESS='DIRECT',
     +  RECORDSIZE=8)
        WRITE(2'1) IDCMAX,IDTMAX,RI,CHNCAL
        NUMREC=1
        DO 820 L=1,57,14
        L13=L+13
        NUMREC=NUMREC+1
        WRITE(2'NUMREC) (ITID(M),M=L,L13)
820     CONTINUE
170     IF(DATA(I,J).LE.DATMAX)GO TO 171
        DATMAX=DATA(I,J)
        THEMAX=THETA
        HMAX=H
        AMUMAX=AMU
171     IF(DATA(I,J).LT.DATMIN) DATMIN=DATA(I,J)
C ----------------------------------------------------------------------
C       WRITE OUT THE FIRST QUADRANT RESULTS TO THE OUTPUT FILE
C ----------------------------------------------------------------------
        INDEX=INDEX+1
        TDATA(INDEX)=DATA(I,J)
        IF(INDEX.LT.8) GO TO 5
        NUMREC=NUMREC+1
        WRITE(2'NUMREC) (TDATA(L),L=1,8)
        INDEX=0
5       CONTINUE
4       CONTINUE
        IF(INDEX.EQ.0) GO TO 850
        NUMREC=NUMREC+1
        WRITE(2'NUMREC) (TDATA(L),L=1,INDEX)
850     CLOSE(UNIT=2)
C ----------------------------------------------------------------------
C       WRITE OUT THE MINIMUM AND MAXIMUM INTENSITY INFORMATION
C       TO THE TERMINAL
C ----------------------------------------------------------------------
        TYPE 166,DATMIN,DATMAX
166     FORMAT(/,' THE MINIMUM INTENSITY=',E14.7,/,' THE MAXIMUM ',
     +  'INTENSITY=',E14.7,'; IT OCCURS AT:')
        TYPE 167,THEMAX,HMAX,AMUMAX
167     FORMAT(10X,'THETA=',F7.4,' DEGREES',/,10X,'H=',F7.4,
     +  ' 1/MICRONS',/,10X,'MU=',F6.2,' DEGREES.')
        TYPE 168,IDCMAX,IDTMAX
168     FORMAT(/,' THERE ARE ',I3,' FIRST QUADRANT CHANNELS',
     +  ' AND ',I3,' TRACKS.')
        STOP
        END
```

```
      PROGRAM SCAN
C ----------------------------------------------------------------------
C      THIS PROGRAM TAKES DATA FILES FROM THE FIRST QUADRANT AVERAGING
C      PROGRAM QUAD AND ALLOWS THE USER TO PRODUCE A SCAN OF LIGHT
C      SCATTERING INTENSITIES HOLDING ANY OF THE THREE VARIABLES
C      CONSTANT:  THE SCATTERING ANGLE IN THE SAMPLE (CTHETA), THE
C      AZIMUTHAL ANGLE (CAMU), OR THE SCATTERING VECTOR (CH).  LINEAR
C      INTERPOLATION IS USED TO CALCULATE THE INTERMEDIATE VALUES.
C      THE INPUT FILES ARE BINARY.
C      DEFINITIONS OF OTHER VARIABLES:
C              ITID(I)= EXPERIMENT IDENTIFICATION INFORMATION
C              THETA(I)= CALCULATED SCATTERING ANGLE VALUE
C              AMU(I)= CALCULATED AZIMUTHAL ANGLE
C              H(I)= CALCULATED SCATTERING VECTOR
C              SCATIN(I)= SCATTERING INTENSITY VALUES CALCULATED IN THE
C                         PROGRAM FOR A SPECIFIC ANGULAR POSITION
C              DATA(IC,IT)= ORIGINAL DATA VALUES READ FROM INPUT
C                           FILE(S), WHERE:
C                              IC= DELTA CHANNEL INDEX
C                              IT= DELTA TRACK INDEX
C              IINFL= NAME OF FIRST INPUT FILE
C              IOUTFL= NAME OF OUTPUT FILE
C              TDATA(I)= TEMPORARY VARIABLE FOR INTENSITY VALUES
C                        READ FROM THE INPUT FILE
C              INST= Y IF THE USER WANTS INSTRUCTIONS FOR ENTERING
C                      THE DATA AT THE TERMINAL
C                    N IF USER DOES NOT WANT INSTRUCTIONS
C              IFILE= 1 IF OUTPUT IS WANTED ON THE TERMINAL ONLY
C                     2 IF A FLOPPY DISK FILE ONLY IS WANTED
C                     3 IF BOTH THE TERMINAL AND FLOPPY DISK OUTPUTS
C                       ARE WANTED
C              NCHAN= NUMBER OF CHANNELS IN THE INPUT FILE
C              NTRAK= NUMBER OF TRACKS IN THE INPUT FILE
C              RI= SAMPLE REFRACTIVE INDEX
C              CHNCAL= CALIBRATION FACTOR RELATING CHANNEL AND TRACK
C                      POSITION WITH POLAR ANGLE POSITION
C              FRONT= FACTOR USED IN CALCULATING  SCATTERING VECTOR;
C                     (4*PI*RI/WAVELENGTH)
C              NUMREC= RECORD NUMBER IN BINARY INPUT DATA FILE
C              INDEX= VARIABLE USED FOR COUNTING DATA POINTS IN A
C                     RECORD
C              KONST= 1 IF SCATTERING ANGLE (THETA) IS TO BE
C                       HELD CONSTANT
C                     2 IF AZIMUTHAL ANGLE (AMU) IS TO BE HELD CONSTANT
C                     3 IF SCATTERING VECTOR (H) IS TO BE HELD CONSTANT
C              CONST= CONSTANT VALUE ENTERED FOR CTHETA,CAMU, OR CH
C              THETEX= CTHETA IN AIR
```

```
C                 NMAX= MAXIMUM TRACK OR CHANNEL NUMBER POSSIBLE FOR
C                       THE CTHETA VALUE CHOSEN
C                 A=VARIABLE USED TO CALCULATE THETEX OR THETA
C                 NPTS= NUMBER OF DATA POINTS IN THE CONSTANT ANGLE SCAN
C                 X= INTERPOLATED CHANNEL POSITION
C                 Y= INTERPOLATED TRACK POSITION
C                 RATIO= INTERPOLATION FACTOR
C                 IRUN= Y TO MAKE ANOTHER SCAN, N TO EXIT
C
C        THIS PROGRAM WRITTEN BY D.E. ROSE 23-JUL-81
C        MODIFIED BY R.J. TABAR 4-OCT-81
C -----------------------------------------------------------------------
         DIMENSION ITID(70),THETA(100),AMU(100),H(100),SCATIN(100)
         DIMENSION DATA(65,65),IINFL(8),IOUTFL(8),TDATA(8)
C -----------------------------------------------------------------------
C        ENTERING THE PARAMETERS FOR THIS RUN
C -----------------------------------------------------------------------
         TYPE 1
1        FORMAT(' DO YOU WANT INSTRUCTIONS, [Y/N]?')
         ACCEPT 799,INST
799      FORMAT(A1)
         IF(INST.NE.'Y') GOTO 3
         TYPE 2
2        FORMAT(' ENTER THE NAME OF THE QUADRANT AVERAGED INPUT FILE:')
C -----------------------------------------------------------------------
C        OPEN UP THE DATA FILES AND READ IN SOME SCAN PARAMETERS
C -----------------------------------------------------------------------
3        ACCEPT 4,IINFL
    4    FORMAT(8A2)
         OPEN(UNIT=1,NAME=IINFL,TYPE='OLD',READONLY,FORM='UNFORMATTED',
     +   ACCESS='DIRECT',RECORDSIZE=8)
         IF(INST.NE.'Y')GO TO 401
         TYPE 399
399      FORMAT(' CHOOSE SCAN PROGRAM TYPE OF OUTPUT.  ENTER:',/,5X,
     +   '1 FOR TERMINAL OUTPUT ONLY,')
         TYPE 400
400      FORMAT(5X,'2 FOR FLOPPY DISK FILE OUTPUT ONLY OR',/,5X,
     +   '3 FOR BOTH TERMINAL AND FLOPPY DISK FILE OUTPUT:')
401      ACCEPT *,IFILE
         IF(IFILE.EQ.1) GO TO 420
         IF(INST.NE.'Y') GO TO 431
         TYPE 430
430      FORMAT(' ENTER THE OUTPUT FILE NAME:')
431      ACCEPT 4,IOUTFL
         OPEN(UNIT=2,NAME=IOUTFL)
420      READ(1'1) NCHAN,NTRAK,RI,CHNCAL
         FRONT=RI*19.85836
C -----------------------------------------------------------------------
```

```
C       READ IN AND WRITE OUT THE EXPERIMENT IDENTIFICATION INFORMATION
C -----------------------------------------------------------------------
        NUMREC=1
        DO 210 L=1,57,14
        L13=L+13
        NUMREC=NUMREC+1
        READ(1'NUMREC) (ITID(M),M=L,L13)
210     CONTINUE
750     FORMAT(35A2)
        IF(IFILE.NE.2)TYPE 750, (ITID(I),I=1,35)
        IF(IFILE.NE.2)TYPE 750, (ITID(I),I=36,70)
        IF(IFILE.NE.1) WRITE(2,750) (ITID(I),I=1,35)
        IF(IFILE.NE.1) WRITE(2,750) (ITID(I),I=36,70)
C -----------------------------------------------------------------------
C       READ IN THE DATA FROM THE INPUT FILE
C -----------------------------------------------------------------------
        INDEX=8
        DO 310 IT=1,NTRAK
        DO 310 IC=1,NCHAN
        INDEX=INDEX+1
        IF(INDEX.LE.8) GO TO 300
        NUMREC=NUMREC+1
        READ(1'NUMREC) (TDATA(L),L=1,8)
        INDEX=1
300     DATA(IC,IT)=TDATA(INDEX)
310     CONTINUE
        CLOSE(UNIT=1)
5       IF(INST.NE.'Y') GO TO 7
        TYPE 6
    6   FORMAT(1H ,'WHICH VARIABLE DO YOU WISH TO HOLD CONSTANT?',/,
     +  1X,'TYPE 1 FOR THETA, 2 FOR MU, AND 3 FOR SCATTERING VECTOR H:')
    7   ACCEPT *,KONST
        IF(INST.NE.'Y') GOTO 9
        GO TO (501,502,503),KONST
501     TYPE 601
601     FORMAT(' ENTER CONSTANT THETA VALUE (REAL NUMBER, IN DEGREES',
     +' IN THE SAMPLE):')
        GO TO 9
502     TYPE 602
602     FORMAT(' ENTER CONSTANT AZIMUTHAL ANGLE (REAL NUMBER, IN',
     +  ' DEGREES):')
        GO TO 9
503     TYPE 603
603     FORMAT(' ENTER CONSTANT SCATTERING VECTOR (REAL NUMBER,',
     +  ' IN 1/MICRONS):')
    9   ACCEPT *,CONST
C -----------------------------------------------------------------------
C       SET CONSTANT VALUE; MAKE DEG/RAD AND THETA/H CONVERSIONS
```

```
C -----------------------------------------------------------------
        GOTO (10,11,12),KONST
   10   CTHETA=CONST*0.0174533
        GOTO 13
   11   CAMU=CONST*0.0174533
        GOTO 13
   12   CTHETA=2.*(ATAN((CONST/FRONT)/SQRT(1.-(CONST/FRONT)**2)))
13      GO TO (18,21,18), KONST
C -----------------------------------------------------------------
C       THIS SECTION OF PROGRAM FOR CONSTANT THETA SCAN
C -----------------------------------------------------------------
   18   A=SIN(CTHETA)
        THETEX=ATAN((A*RI)/SQRT(1.-(A*RI)**2.))
        NMAX=INT(SQRT((SIN(THETEX)/COS(THETEX))**2. * CHNCAL**2.))
        I=1
C -----------------------------------------------------------------
C       FIND AND INTERPOLATE ALL POINTS AT TRACK INTERSECTIONS
C -----------------------------------------------------------------
        DO 19 IT=1,NMAX
        X=SQRT((SIN(THETEX)/COS(THETEX))**2.*CHNCAL**2-(IT-1.)**2.)
        IF(X+1.GT.FLOAT(NCHAN)) GOTO 19
        IC=INT(X)+1
        RATIO=X-INT(X)
        SCATIN(I)=DATA(IC,IT)+RATIO*(DATA(IC+1,IT)-DATA(IC,IT))
        IF(IT.EQ.1)GOTO 100
        AMU(I)=ATAN(X/(IT-1.))
        GOTO 99
100     AMU(I)=90.*0.0174533
   99   I=I+1
   19   CONTINUE
C -----------------------------------------------------------------
C       FIND AND INTERPOLATE ALL POINTS AT CHANNEL INTERSECTIONS
C -----------------------------------------------------------------
        DO 20  IC=1,NMAX
        Y=SQRT(((SIN(THETEX)/COS(THETEX)))**2.*CHNCAL**2.-(IC-1.)**2.)
        IF(Y+1.GT.FLOAT(NTRAK)) GOTO 20
        IT=INT(Y)+1
        RATIO=Y-INT(Y)
        SCATIN(I)=DATA(IC,IT)+RATIO*(DATA(IC,IT+1)-DATA(IC,IT))
        IF(IC.EQ.1)GOTO 105
        AMU(I)=ATAN((IC-1.)/Y)
        GOTO 104
  105   AMU(I)=0.
  104   I=I+1
   20   CONTINUE
        GOTO 30
C -----------------------------------------------------------------
C       THIS SECTION OF PROGRAM FOR CONSTANT MU SCAN
```

```
C -----------------------------------------------------------------------
C       SET VALUES OF INITIAL (ORIGIN) POINT
C -----------------------------------------------------------------------
   21   SCATIN(1)=DATA(1,1)
        THETA(1)=0.0
        H(1)=0.0
        I=2
C -----------------------------------------------------------------------
C       HANDLE SPECIAL CASES MU=0, 90, OR 45 DEGREES
C -----------------------------------------------------------------------
        IF(CONST.NE.0.) GOTO 23
        DO 22 I=2,NTRAK
        THETEX=ATAN((SQRT((I-1.)**2.))/CHNCAL)
        A=(SIN(THETEX))/RI
        THETA(I)=ATAN(A/SQRT(1.-A**2.))
   22   SCATIN(I)=DATA(1,I)
        NPTS=NTRAK
        GOTO 130
   23   IF(CONST.NE.90.) GOTO 25
        DO 24 I=2,NCHAN
        THETEX=ATAN((SQRT((I-1.)**2.))/CHNCAL)
        A=(SIN(THETEX))/RI
        THETA(I)=ATAN(A/SQRT(1.-A**2.))
   24   SCATIN(I)=DATA(I,1)
        NPTS=NCHAN
        GOTO 130
   25   IF(CONST.NE.45.) GOTO 27
        IF(NCHAN.GT.NTRAK) NPTS=NTRAK
        IF(NCHAN.LE.NTRAK) NPTS=NCHAN
        DO 26 I=2,NPTS
        ABC=SQRT((I-1.)**2+(I-1.)**2)
        THETEX=ATAN((ABC/CHNCAL))
        A=(SIN(THETEX))/RI
        THETA(I)=ATAN(A/SQRT(1.-A**2))
   26   SCATIN(I)=DATA(I,I)
        GOTO 130
C -----------------------------------------------------------------------
C       FIND AND INTERPOLATE ALL POINTS AT TRACK INTERSECTIONS
C -----------------------------------------------------------------------
   27   NMAX=NTRAK-1
        DO 28 IT=2,NMAX
        X=(IT-1)*(SIN(CAMU)/COS(CAMU))
        IF(X+1.GT.FLOAT(NCHAN)) GOTO 28
        IC=INT(X)+1
        RATIO=X-INT(X)
        SCATIN(I)=DATA(IC,IT)+RATIO*(DATA(IC+1,IT)-DATA(IC,IT))
        THETEX=ATAN((SQRT(X**2. + (IT-1.)**2.))/CHNCAL)
        A=(SIN(THETEX))/RI
```

```
      THETA(I)=ATAN(A/SQRT(1.-A**2.))
      I=I+1
   28 CONTINUE
C ----------------------------------------------------------------------
C     FIND AND INTERPOLATE ALL POINTS AT CHANNEL INTERSECTIONS
C ----------------------------------------------------------------------
      NMAX=NCHAN-1
      DO 29 IC=2,NMAX
      Y=(IC-1)/(SIN(CAMU)/COS(CAMU))
      IF(Y+1.GT.FLOAT(NTRAK)) GOTO 29
      IT=INT(Y)+1
      RATIO=Y-INT(Y)
      SCATIN(I)=DATA(IC,IT)+RATIO*(DATA(IC,IT+1)-DATA(IC,IT))
      THETEX=ATAN((SQRT(Y**2. + (IC-1.)**2.))/CHNCAL)
      A=(SIN(THETEX))/RI
      THETA(I)=ATAN(A/SQRT(1.-A**2.))
      I=I+1
   29 CONTINUE
C ----------------------------------------------------------------------
C     SORT ALL POINTS IN ASCENDING ORDER OF THETA OR AZIMUTHAL VALUES
C ----------------------------------------------------------------------
   30 NPTS=I-1
      NMI=NPTS-1
      DO 31 I=1,NMI
      K=I+1
      DO 31 J=K,NPTS
      IF(KONST.EQ.2.AND.THETA(J).GT.THETA(I)) GOTO 31
      IF(KONST.NE.2.AND.AMU(J).GT.AMU(I)) GOTO 31
      TEMP=THETA(I)
      THETA(I)=THETA(J)
      THETA(J)=TEMP
      TEMP=SCATIN(I)
      SCATIN(I)=SCATIN(J)
      SCATIN(J)=TEMP
      TEMP=AMU(I)
      AMU(I)=AMU(J)
      AMU(J)=TEMP
   31 CONTINUE
C ----------------------------------------------------------------------
C     CALCULATE H VALUES AND MAKE RAD/DEG CONVERSIONS
C ----------------------------------------------------------------------
  130 DO 32 I=1,NPTS
      IF(KONST.NE.2) THETA(I)=CTHETA
      H(I)=FRONT*SIN(THETA(I)/2.)
      AMU(I)=AMU(I)/0.0174533
   32 THETA(I)=THETA(I)/0.0174533
33    GO TO (34,42,38),KONST
C ----------------------------------------------------------------------
```

```
C       WRITE OUT RESULTS TO TERMINAL AND FILE (IF DESIRED)
C -----------------------------------------------------------------------
34      IF(IFILE.NE.2)TYPE 35, CONST
        IF(IFILE.NE.1) WRITE(2,35) CONST
   35   FORMAT(1H ,10X,'THETA =',F9.5,' DEGREES')
        IF(IFILE.NE.2)TYPE 36
        IF(IFILE.NE.1)WRITE(2,36)
   36   FORMAT(1H ,/,13X,'INTENSITY',14X,'H',12X,'MU')
        IF(IFILE.NE.2)TYPE 37,(SCATIN(L),H(L),AMU(L),L=1,NPTS)
        IF(IFILE.NE.1) WRITE(2,37) (SCATIN(L),H(L),AMU(L),L=1,NPTS)
   37   FORMAT(1H ,9X,E14.7,8X,F7.4,6X,F8.4)
        GOTO 46
38      IF(IFILE.NE.2)TYPE 39,CONST
        IF(IFILE.NE.1) WRITE(2,39) CONST
   39   FORMAT(1H ,10X,'H =',F9.5,' 1/MICRONS')
        IF(IFILE.NE.2)TYPE 40
        IF(IFILE.NE.1) WRITE(2,40)
   40   FORMAT(1H ,/,13X,'INTENSITY',12X,'THETA',8X,'MU')
        IF(IFILE.NE.2)TYPE 41, (SCATIN(L),THETA(L),AMU(L),L=1,NPTS)
        IF(IFILE.NE.1) WRITE(2,41) (SCATIN(L),THETA(L),AMU(L),L=1,NPTS)
   41   FORMAT(1H ,9X,E14.7,8X,F7.4,7X,F7.4)
        GOTO 46
42      IF(IFILE.NE.2)TYPE 43, CONST
        IF(IFILE.NE.1) WRITE(2,43) CONST
   43   FORMAT(1H ,10X,'MU =',F9.5,' DEGREES')
        IF(IFILE.NE.2)TYPE 44
        IF(IFILE.NE.1) WRITE(2,44)
   44   FORMAT(1H ,/,13X,'INTENSITY',11X,'THETA',11X,'H')
        IF(IFILE.NE.2)TYPE 45, (SCATIN(L),THETA(L),H(L),L=1,NPTS)
        IF(IFILE.NE.1) WRITE(2,45) (SCATIN(L),THETA(L),H(L),L=1,NPTS)
   45   FORMAT(1H ,9X,E14.7,8X,F7.4,7X,F7.4)
        IF(IFILE.NE.2)TYPE 650
650     FORMAT(//)
        TYPE 145,NPTS
145     FORMAT(/,' THIS SCAN CONTAINS',I4,' DATA POINTS.')
46      IF(INST.NE.'Y') GOTO 48
        TYPE 47
47      FORMAT(' DO YOU WANT TO RUN THIS PROGRAM AGAIN, [Y/N]?')
   48   ACCEPT 799,IRUN
        IF(IRUN.EQ.'Y') GOTO 5
        IF(IFILE.NE.1)CLOSE(UNIT=2)
        STOP
        END
```

```
      PROGRAM READS
C ---------------------------------------------------------------------
C     THIS PROGRAM IS USED TO READ THE BINARY OUTPUT FILES FROM THE
C     SALS AND QUAD PROGRAMS.  THE OUTPUT FILE FROM THIS PROGRAM
C     GIVES THE SCATTERED LIGHT INTENSITY IN TERMS OF THE CHANNEL
C     LOCATION, TRACK LOCATION, POLAR SCATTERING ANGLE, SCATTERING
C     VECTOR H AND THE AZIMUTHAL ANGLE.  THE OUTPUT CAN BE SENT TO
C     A FLOPPY DISK FILE, THE TERMINAL, THE LINE PRINTER, THE LS:
C     DEVICE, ETC.
C     DEFINITIONS OF THE VARIABLES:
C             IINFL(I)= INPUT FILE NAME
C             IOUTFL(I)= OUTPUT FILE NAME
C             ITID(I)= EXPERIMENT IDENTIFICATION INFORMATION
C             DATA(IC,IT)= INTENSITY VALUE AT CHANNEL IC AND TRACK IT
C             INST= Y IF THE OPERATOR WANTS INSTRUCTIONS
C                   N IF INSTRUCTIONS ARE NOT NEEDED
C             IQUAD= 1 IF THE FILE BEING READ IS A QUADRANT AVERAGED
C                      FILE
C                    2 IF IT IS FROM THE PROGRAM SALS
C             NCHAN= NUMBER OF CHANNELS OR EQUIVALENT FIRST QUADRANT
C                    AVERAGED CHANNELS
C             NTRAK= NUMBER OF TRACKS OR EQUIVALENT FIRST QUADRANT
C                    AVERAGED TRACKS
C             RI= SAMPLE REFRAVTIVE INDEX
C             CHNCAL= CALIBRATION FACTOR TO CONVERT CHANNEL AND
C                     TRACK LOCATIONS TO ANGULAR LOCATIONS
C             MAINC= CHANNEL LOCATION FO THE MAIN BEAM
C             MAINT= TRACK LOCATION OF THE MAIN BEAM
C             AMUX= AZIMUTHAL ANGLE OF THE X AXIS ON THE MONITOR
C                   H, ASSUMING WAVELENGTH= 632.8NM
C             NUMREC= RECORD NUMBER IN THE INPUT FILE
C             FRONT= FACTOR USED TO CALCULATE THE SCATTERING VECTOR
C             IDELT= TRACKS AWAY FROM THE MAIN BEAM
C             IDELTA= EQUIVALENT FIRST QUADRANT TRACK LOCATION
C             IDELC= CHANNELS AWAY FROM THE MAIN BEAM
C             IDELCA= EQUIVALENT FIRST QUADRANT CHANNEL LOCATION
C             AMU= AZIMUTHAL ANGLE
C             H= SCATTERING VECTOR (1/MICRONS)
C             THETEX= SCATTERING ANGLE IN AIR, IN RADIANS
C             X= VARIABLE USED TO DETERMINE THETA
C             THETA= SCATTERING ANGLE IN THE SAMPLE, IN RADIANS
C     WRITTEN BY R.J. TABAR 27-SEP-81
C ---------------------------------------------------------------------
      DIMENSION IINFL(8),IOUTFL(8),ITID(70),TDATA(8),DATA(65,65)
C ---------------------------------------------------------------------
C     ENTER PARAMETERS FOR THIS RUN
C ---------------------------------------------------------------------
```

```
      TYPE 100
100   FORMAT(' DO YOU WANT INSTRUCTIONS, [Y/N]?')
      ACCEPT 101,INST
101   FORMAT(A1)
      IF(INST.NE.'Y') GO TO 105
      TYPE*,' ENTER THE INPUT FILE NAME:'
105   ACCEPT 110,IINFL
110   FORMAT(8A2)
      IF(INST.NE.'Y') GO TO 115
      TYPE*,' ENTER 1 IF YOU ARE READING A QUADRANT AVERAGED FILE'
      TYPE*,' 2 IF THE FILE IS FROM THE SALS PROGRAM:'
115   ACCEPT*,IQUAD
      IF(INST.NE.'Y') GO TO 125
      TYPE*,' ENTER THE OUTPUT FILE NAME OR DEVICE:'
125   ACCEPT 110,IOUTFL
C -----------------------------------------------------------------------
C     OPEN UP INPUT AND OUTPUT FILES
C -----------------------------------------------------------------------
      OPEN(UNIT=1,NAME=IINFL,TYPE='OLD',READONLY,FORM='UNFORMATTED',
     + ACCESS='DIRECT',RECORDSIZE=8)
      OPEN(UNIT=2,NAME=IOUTFL)
      IF(IQUAD.EQ.1)READ(1'1) NCHAN,NTRAK,RI,CHNCAL
      IF(IQUAD.EQ.2) READ(1'1) NCHAN,NTRAK,RI,CHNCAL,MAINC,MAINT,AMUX
      NUMREC=1
      FRONT=19.85836*RI
C -----------------------------------------------------------------------
C     READ AND WRITE THE EXPERIMENT IDENTIFICATION INFORMATION
C -----------------------------------------------------------------------
      DO 50 L=1,57,14
      L13=L+13
      NUMREC=NUMREC + 1
      READ(1'NUMREC) (ITID(M),M=L,L13)
50    CONTINUE
      IF(IQUAD.EQ.2) WRITE(2,20) NCHAN,NTRAK,RI,CHNCAL
20    FORMAT(1X,2I4,2X,F5.3,2X,F10.5,/)
      IF(IQUAD.EQ.1) WRITE(2,21) NCHAN,NTRAK,RI,CHNCAL
21    FORMAT(1X,2I4,2X,F5.3,2X,F10.5,'  SINGLE QUADRANT AVERAGED',
     + ' RESULTS',/)
      WRITE(2,300) (ITID(I),I=1,35)
      WRITE(2,300) (ITID(I),I=36,70)
300   FORMAT(35A2)
      IF(IQUAD.EQ.2) WRITE(2,200)
200   FORMAT(/,T28,'DELTA',T35,'DELTA',T41,'SCATTERING',T52,
     + 'SCATTERING',T63,'AZIMUTHAL')
      IF(IQUAD.EQ.1) WRITE(2,201)
201   FORMAT(/,T3,'DELTA',T10,'DELTA',T28,'DELTA',T35,'DELTA',
     + T41,'SCATTERING',T52,'SCATTERING',T63,'AZIMUTHAL')
      WRITE(2,202)
```

```
202   FORMAT(T2,'CHANNEL',T10,'TRACK',T16,'INTENSITY',T27,'CHANNEL',
     + T35,'TRACK',T43,'ANGLE',T53,'VECTOR',T65'ANGLE')
      WRITE(2,203)
203   FORMAT(T41,'(DEGREES)',T17,'(1/MM)',T51,'(1/MICRONS)',
     + T63,'(DEGREES)',/)
      INDEX=8
C ----------------------------------------------------------------------
C     READ IN THE DATA
C ----------------------------------------------------------------------
      DO 1 J=1,NTRAK
      DO 2 I=1,NCHAN
      INDEX=INDEX+1
      IF(INDEX.LE.8) GO TO 600
      NUMREC=NUMREC+1
      READ(1'NUMREC) (TDATA(L),L=1,8)
      INDEX=1
600   DATA(I,J)=TDATA(INDEX)
2     CONTINUE
1     CONTINUE
      CLOSE(UNIT=1)
      IF(IQUAD.EQ.1) GO TO 400
C ----------------------------------------------------------------------
C     DETERMINE POLAR AND AZIMUTHAL SCATTERING ANGLES FOR EACH POINT
C     IN A SALS TYPE INPUT FILE
C ----------------------------------------------------------------------
      DO 3 IT=1,NTRAK
      IDELT=IT-MAINT
      IDELTA=IABS(IDELT) + 1
      DO 4 IC=1,NCHAN
      IDELC=IC-MAINC
      IDELCA=IABS(IDELC) + 1
      IF(IDELT.NE.0) GO TO 301
      IF(IDELC.NE.0) GO TO 302
      AMU=0.
      H=0.
      THETA=0.
      GO TO 350
302   IF(IDELC.LT.0) GO TO 303
      AMU=90.
      GO TO 305
303   AMU=270.
      GO TO 305
301   AMU=ATAN(IDELC/(1.*IDELT))
      IF(IDELT.LT.0) AMU=AMU + 3.14159
      AMU=AMU*57.29578
305   AMU=AMU + AMUX -90.
      IF(AMU.LT.0.) AMU=AMU+360.
      IF(AMU.GE.360.) AMU=AMU-360.
```

```
        THETEX=ATAN((SQRT((IDELC*1.)**2 + IDELT**2))/CHNCAL)
        X=(SIN(THETEX))/RI
        THETA=ATAN(X/SQRT(1-X**2))
        H=FRONT*SIN(THETA/2.)
        THETA=THETA*57.29578
C -------------------------------------------------------------------
C       WRITE OUT THE RESULTS TO THE OUTPUT FILE OR DEVICE
C -------------------------------------------------------------------
350     WRITE(2,360) IC,IT,DATA(IC,IT),IDELCA,IDELTA,THETA,H,AMU
360     FORMAT(T4,I3,T10,I3,T14,E14.7,T29,I3,T36,I3,T42,F7.4,T53,F7.4,
     +  T64,F6.2)
4       CONTINUE
3       CONTINUE
        GO TO 500
C -------------------------------------------------------------------
C       DETERMINE POLAR AND AZIMUTHAL SCATTERING ANGLES FOR EACH POINT
C       IN A QUADRANT AVERAGED TYPE INPUT FILE
C -------------------------------------------------------------------
400     DO 5 IT=1,NTRAK
        IDELT=IT-1
        DO 6 IC=1,NCHAN
        IDELC=IC-1
        IF(IDELT.NE.0) GO TO 401
        IF(IDELC.NE.0) GO TO 402
        AMU=0.
        H=0.
        THETA=0.
        GO TO 450
402     AMU=90.
        GO TO 405
401     AMU=ATAN(IDELC/(1.*IDELT))
        AMU=AMU*57.29578
405     THETEX=ATAN((SQRT((IDELC*1.)**2 + IDELT**2))/CHNCAL)
        X=(SIN(THETEX))/RI
        THETA=ATAN(X/SQRT(1 - X**2))
        H=FRONT*SIN(THETA/2.)
        THETA=THETA*57.29578
C -------------------------------------------------------------------
C       WRITE OUT THE RESULTS TO THE OUTPUT FILE OR DEVICE
C -------------------------------------------------------------------
450     WRITE(2,360) IC,IT,DATA(IC,IT),IC,IT,THETA,H,AMU
6       CONTINUE
5       CONTINUE
C -------------------------------------------------------------------
C       PLACE 99 FLAG AT THE END FOR CYBER CONTOUR PLOTTING
C -------------------------------------------------------------------
500     WRITE(2,700)
700     FORMAT(T32,'99')
```

```
      CLOSE(UNIT=2)
      STOP
      END
```

```
      PROGRAM CONDNS
C ---------------------------------------------------------------------
C     THIS PROGRAM CONDENSES THE OUTPUT FILES FROM SALS OR QUAD INTO
C     FEWER DATA POINTS BY AVERAGING NEIGHBORING POINTS TOGETHER.
C     IT WILL GATHER 1, 4, 9, 16, ETC. POINTS TOGETHER SUCH THAT THERE
C     ARE NO MORE THAN 990 POINTS.
C     ONE CAN ALSO CHOOSE THE LEVEL OF CONDENSATION.
C     THE CONDENSED FILE IS GOOD FOR CONTOUR PLOTTING USING THE
C     PDP 11/34.
C     DEFINITIONS OF THE VARIABLES:
C             DATA(IC,IT)= INTENSITY AT CHANNEL IC AND TRACK IT
C             NUMBER= NUMBER OF DATA POINTS BEING AVERAGED INTO
C                     A DATA POINT
C             IINFL= INPUT FILE NAME
C             IOUTFL= OUTPUT FILE NAME
C             TDATA(I)= TEMPORARY VARIABLE FOR THE INTENSITY VALUES
C                       READ FROM THE INPUT FILE
C             DATSUM= VARIABLE USED FOR SUMMING INTENSITY VALUES
C             NCHAN= TOTAL NUMBER OF CHANNELS IN ORIGINAL DATA FILE
C             NTRAK= TOTAL NUMBER OF TRACKS IN ORIGINAL DATA FILE
C             NUMREC= RECORD NUMBER IN BINARY INPUT FILE
C             ICHOS= Y IF THE OPERATOR WANTS TO CHOOSE INT
C                    N IF INT IS CHOSEN TO GIVE LESS THAN 990 POINTS
C             INT= INT**2 IS THE NUMBER OF DATA POINTS TO COLLECT
C                  INTO ONE DATA POINT
C             INDEX= VARIABLE USED TO COUNT THE NUMBER OF POINTS
C                    IN A RECORD
C             INET= NUMBER OF CONDENSED CHANNELS
C             JNET= NUMBER OF CONDENSED TRACKS
C     WRITTEN BY R.J. TABAR 10-OCT-81
C ---------------------------------------------------------------------
      DIMENSION DATA(50,50),NUM(50,50),IINFL(8),IOUTFL(8),TDATA(8)
      DATA DATSUM/0./
      DATA NUMBER/0/
C ---------------------------------------------------------------------
C     OPEN UP THE INPUT AND OUTPUT FILES
C ---------------------------------------------------------------------
      TYPE*,'ENTER THE INPUT FILE NAME ON ONE LINE AND'
      TYPE*,'THE OUTPUT FILE OR DEVICE NAME (AS LP: OR LS:)',
     + 'ON THE NEXT LINE:'
10    FORMAT(8A2)
      ACCEPT 10,IINFL
      ACCEPT 10,IOUTFL
      OPEN(UNIT=1,NAME=IINFL,TYPE='OLD',READONLY,FORM='UNFORMATTED',
     + ACCESS='DIRECT',RECORDSIZE=8)
      OPEN(UNIT=2,NAME=IOUTFL)
      READ(1'1) NCHAN,NTRAK
```

```
C -----------------------------------------------------------------------
C       CHOOSE HOW MUCH TO CONDENSE THE DATA OR ALLOW THE PROGRAM
C       TO CONDENSE TO LESS THAN 990 POINTS
C -----------------------------------------------------------------------
        TYPE*,' DO YOU WANT TO CHOOSE THE CONDENSATION LEVEL [Y/N]:'
        ACCEPT 15,ICHOS
15      FORMAT(A1)
        IF(ICHOS.NE.'Y')GO TO 25
        TYPE*,' ENTER INT, WHERE INT**2 WILL BE HOW MANY POINTS'
        TYPE*,' WILL BE GATHERED INTO 1 POINT (INTEGER):'
        ACCEPT*,INT
        GO TO 220
25      DO 200 I=1,9
        ITEST=(IFIX((NCHAN-1)/I)+1)*(IFIX((NTRAK-1)/I)+1)
        IF(ITEST.GT.990)GO TO 200
        INT=I
        GO TO 220
200     CONTINUE
220     WRITE(2,20) IINFL
20      FORMAT(' CONDENSED VERSION OF FILE: ',8A2)
C -----------------------------------------------------------------------
C       READ IN THE DATA
C -----------------------------------------------------------------------
        NUMREC=6
        INDEX=8
        DO 30 IT=1,NTRAK
        DO 40 IC=1,NCHAN
        INDEX=INDEX+1
        IF(INDEX.LE.8)GO TO 100
        NUMREC=NUMREC+1
        READ(1'NUMREC) (TDATA(L),L=1,8)
        INDEX=1
100     DATA(IC,IT)=TDATA(INDEX)
40      CONTINUE
30      CONTINUE
        CLOSE(UNIT=1)
C -----------------------------------------------------------------------
C       CONDENSE THE DATA TO INT**2 POINTS PER POINT
C -----------------------------------------------------------------------
        DO 1 J=1,NTRAK,INT
        JPLUS=J + INT - 1
        JNET=IFIX((J-1)/INT) + 1
        DO 2 I=1,NCHAN,INT
        IPLUS=I + INT - 1
        INET=IFIX((I-1)/INT) + 1
        DO 3 J2=J,JPLUS
        DO 4 I2=I,IPLUS
        IF(I2.GT.NCHAN.OR.J2.GT.NTRAK)GO TO 4
```

```
         DATSUM=DATSUM + DATA(I2,J2)
         NUMBER=NUMBER + 1
4        CONTINUE
3        CONTINUE
         DATA(INET,JNET)=DATSUM/NUMBER
C -----------------------------------------------------------------------
C        WRITE OUT THE CONDENSED DATA
C -----------------------------------------------------------------------
         WRITE(2,50) INET,JNET,DATA(INET,JNET)
50       FORMAT(T4,I3,T10,I3,T14,E14.7)
         DATSUM=0.
         NUMBER=0
2        CONTINUE
1        CONTINUE
C -----------------------------------------------------------------------
C        PLACE 99 FLAG AT THE END FOR CYBER CONTOUR PLOTTING
C -----------------------------------------------------------------------
         WRITE(2,60)
60       FORMAT(T32,'99')
         CLOSE(UNIT=2)
C -----------------------------------------------------------------------
C        SEND INFORMATION TO THE TERMINAL
C -----------------------------------------------------------------------
         TYPE 70,IOUTFL,INET,JNET
70       FORMAT(/,' THE CONDENSED FILE HAS BEEN PASSED TO: ',8A2,/,
     +   ' IT CONTAINS',I3,' CHANNELS AND',I3,' TRACKS.',/)
         STOP
         END
```

Three Dimensional Internal Disorder

In an unpublished work Yoon has calculated the effects of three dimensional internal disorder on the H_v SALS from model spherulites [35]. He has calculated the effects on the polar scattering angle profile at $\mu = 45°$. These results were not used in this study due to the problems discussed earlier regarding polar scattering angle scans. The results of Yoon are documented here in order to assist future workers in this subject area. Combination of the Yoon theories with the spherulite growth and truncation techniques developed in Chapter III seems to be the most reasonable comprehensive method for theoretically assessing the H_v SALS from the most common polymeric spherulitic condition: three dimensional, disordered spherulites.

In this work, the three dimensional lattices were 50 layers, ω was random, $C_1 = 0.01$ and $\mu = 45°$. The reader is urged to consult the original work [34] for explanation of the model and its parameters. Figure A-2 plots the logarithm of the H_v SALS intensity as a function of the magnitude of the reduced scattering vector, U, at $\mu = 45°$, for 5 values of the internal disorder parameter, δ. The profiles were drawn by Yoon as smooth curves approximating the peaks of the higher order maxima, when present. It is apparent in the figure that the polar profile is broadened as the value of δ increases.

The internal disorder parameter has been identified in terms of the polar profile broadening. Table A-14 lists the values of the internal disorder parameter, both from the two and three dimensional theory, as a

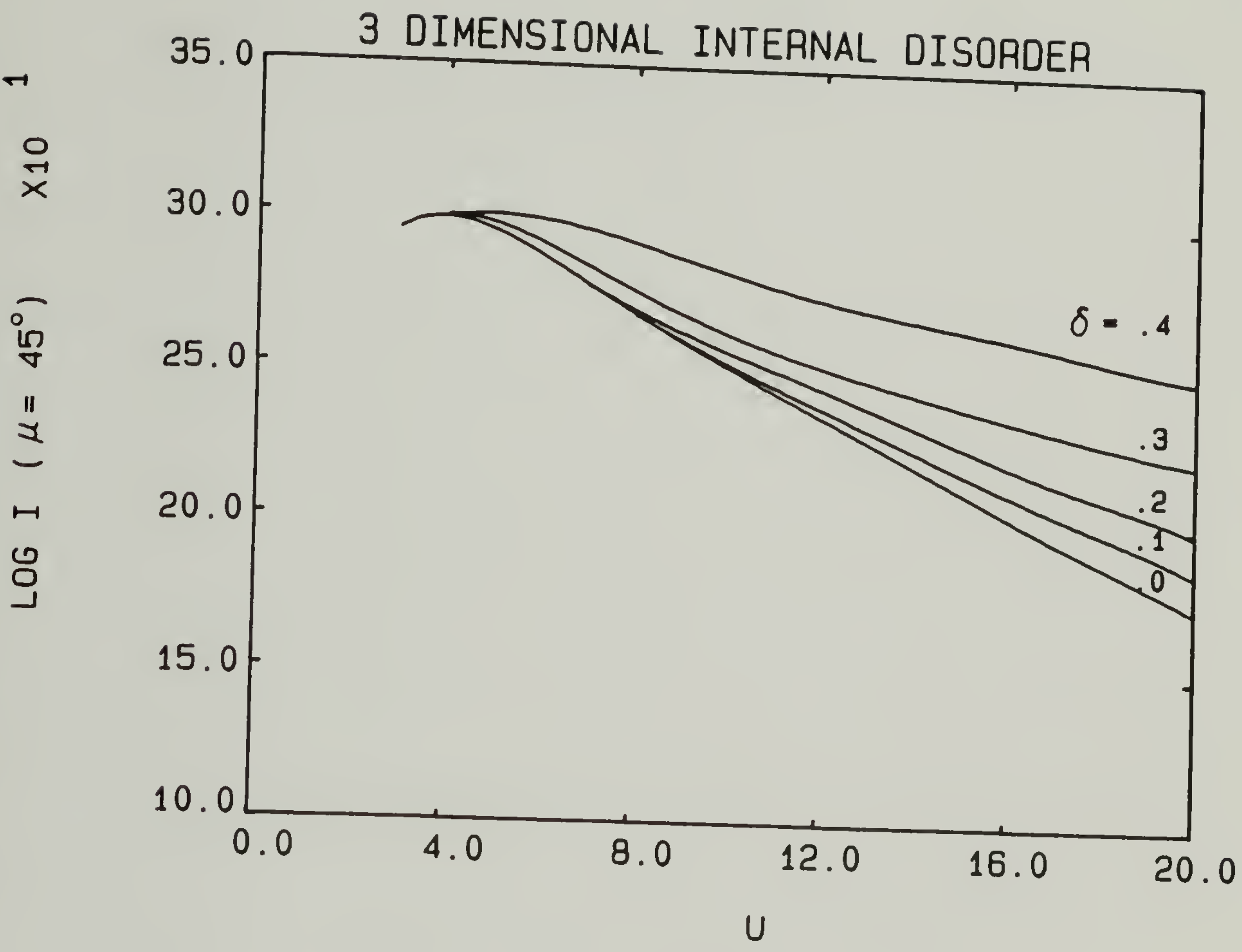

Fig. A-2 Polar scattering angle profiles from three dimensional spherulites, at μ = 45°, for various values of the internal disorder parameter.

function of the profile breadth, as measured at $U = 4$ and 15, at $\mu = 45^\circ$. Breadths at other values of U for three dimensional spherulites can be determined from Figure A-1 and related to δ.

The correction factors at the intensity maxima for internal disorder, C_D, are also listed in Table A-14 for both the two and three dimensional calculations. The two dimensional results are from the original work [34].

Table A-14

Two and Three Dimensional Internal Disorder

$\frac{R_{H_v} (U = 4, \mu = 45^\circ)}{R_{H_v} (U = 15, \mu = 45^\circ)}$	Two Dimensional		Three Dimensional	
	δ	C_D	δ	C_D
500	--	--	0.07	1.1
100	--	--	0.28	7.0
50	0.18	6	0.34	23
25	0.20	10	0.38	60
10	0.22	20	0.43	260
5	0.24	70	0.46	700

It is apparent from the table that the same polar profile broadening from the three dimensional model leads to a larger correction factor of the intensity maximum than that from the two dimensional model. These results should be useful to one attempting to combine the effects of truncation and internal disorder.